

AMORPHOUS HYDROGENATED BORON CARBIDE FOR
SOLID-STATE DIRECT-CONVERSION
THERMAL NEUTRON DETECTION

A DISSERTATION IN
Physics
and
Chemistry

Presented to the Faculty of the University
of Missouri-Kansas City in partial fulfillment of
the requirements for the degree

DOCTOR OF PHILOSOPHY

by

GYANENDRA BHATTARAI

B.Sc., Tribhuvan University, 1998
M.Sc., Tribhuvan University, 2007
M.S., University of Missouri-Kansas City, 2015

Kansas City,
Missouri 2021

© 2021
GYANENDRA BHATTARAI
ALL RIGHTS RESERVED

AMORPHOUS HYDROGENATED BORON CARBIDE FOR
SOLID-STATE DIRECT-CONVERSION
THERMAL NEUTRON DETECTION

Gyanendra Bhattarai, Candidate for the Doctor of Philosophy Degree

University of Missouri-Kansas City, 2021

ABSTRACT

Amorphous hydrogenated boron carbide (a-BC:H) is one of a very limited number of neutron-sensitive materials. It has been studied over the last three decades for solid-state thermal neutron detection due to its high resistivity, moderate bandgap, high neutron absorption cross-section, and high stability under harsh physical and chemical environment. However, its success has been hindered by its poor and/or not well understood charge transport properties as well as fabrication challenges. This study focuses on obtaining thick and stable a-BC:H films using plasma-enhanced chemical vapor deposition (PECVD) and optimizing their charge transport properties for potential application in solid-state direct-conversion thermal neutron detection.

We have investigated the effect of single-carrier transport and low charge carrier mobility, which are expected in a-BC:H films, on detection efficiency and spectral performance of a thin-film B₄C detector using numerical Monte Carlo calculations. Experimentally, we have used space-charge-limited current (SCLC) analysis to extract

the charge carrier mobility in a-BC:H thin films. To better describe the extracted charge carrier mobility, we have presented an extension of SCLC theory to include negative field-dependence in mobility as well as a theory to check self-consistency of the extracted mobility.

Toward obtaining stable thick films and optimizing the charge transport metrics, we have deposited multiple series' of a-BC:H thin films using an *ortho*-carborane precursor with varying PECVD process parameters, including substrate temperature, RF power, process pressure, carrier gas flow rate, and partial precursor flow. Films grown using higher substrate temperature and higher RF power demonstrated higher charge carrier mobility. Partial precursor flow was found to correlate significantly with film growth rate and film properties. The precursor flow rate was found to be very sensitive to the precursor bubbler temperature, which allowed us to fine-tune the precursor flow and produce films with predictable growth rate and film properties. With optimized growth conditions, we demonstrated a 3 μm thick and stable film deposited on copper foil exhibiting a carrier mobility value of $8 \times 10^{-6} \text{ cm}^2 \cdot \text{V}^{-1} \cdot \text{s}^{-1}$ and a resistivity value of $\sim 10^{12} \Omega \cdot \text{cm}$. With this film thickness and carrier mobility, our Monte Carlo calculations suggested that a neutron detector using an integration time of $\geq 5 \mu\text{s}$ can detect neutrons for a carrier lifetime $> 10 \mu\text{s}$, and the intrinsic detection efficiency saturates to $\sim 10\%$ for a carrier lifetime $\geq 100 \mu\text{s}$.

APPROVAL PAGE

The faculty listed below, appointed by the Dean of the College of Arts and Sciences have examined a dissertation titled “Amorphous Hydrogenated Boron Carbide for Solid-State Direct-Conversion Thermal Neutron Detection,” presented by Gyanendra Bhattarai, candidate for the Doctor of Philosophy degree, and certify that in their opinion it is worthy of acceptance.

Supervisory Committee

Anthony N. Caruso, Ph.D., Committee Chair
Department of Physics and Astronomy

Michelle M. Paquette, Ph.D., Research Advisor
Department of Physics and Astronomy

J. David Van Horn, Ph.D.
Department of Chemistry

Paul M. Rulis, Ph.D.
Department of Physics and Astronomy

Nathan A. Oyler, Ph.D.
Department of Chemistry

TABLE OF CONTENTS

ABSTRACT	iii
LIST OF ILLUSTRATIONS	xii
LIST OF TABLES	xxvii
ACKNOWLEDGEMENTS	xxxii
CHAPTER 1 INTRODUCTION	1
1.1. Motivation and Objectives	4
1.1.1. Applications of Neutrons and Neutron Detectors	4
1.1.2. Need for Helium-3 Alternatives	6
1.1.3. Boron-10 Compounds for Direct-Conversion Semiconductor Neutron Detection	9
1.1.4. Amorphous Boron Carbide Thermal Neutron Detectors	10
1.2. Fundamentals of Neutron Detection	12
1.2.1. Interaction of Neutrons with Matter	12
Neutron Scattering	14
Neutron Absorption	18
1.2.2. Neutron Detection	20
1.2.3. Solid-State (Semiconductor) Neutron Detectors	22
1.3. Amorphous Hydrogenated Boron Carbide (a-BC:H) for Direct-Conversion Thermal Neutron Detection: A Brief History	27

1.4. Scope of Dissertation	31
CHAPTER 2 DEVICE FABRICATION AND CHARACTERIZATION: THEORY AND EXPERIMENTS	33
2.1. Device Fabrication	33
2.1.1. PECVD Chamber.....	33
2.1.2. Substrate Temperature Calibration	38
2.1.3. Precursor Bubbler	40
2.1.4. Substrate Preparation	42
2.1.5. Film Growth.....	44
2.1.6. Electrical Contact Deposition	47
2.1.7. Device Wiring.....	49
2.2. Basic Characterization.....	52
2.2.1. Spectroscopic Ellipsometry	52
2.2.2. UV-Visible Reflection and Transmission Spectroscopy	55
2.2.3. Film Stress	59
2.3. Charge Transport Characterization	62
2.3.1. Dielectric Constant	62
2.3.2. Steady-State Current–Voltage Measurements	64
2.3.3. Transient Photoconductivity	80

CHAPTER 3 SINGLE-CARRIER CHARGE COLLECTION IN THIN DIRECT- CONVERSION SEMICONDUCTOR NEUTRON DETECTOR: A NUMERICAL SIMULATION.....	88
3.1. Introduction	88
3.2. Interaction of Thermal Neutrons with B ₄ C	93
3.3. Theory: Direct-Conversion Neutron Detection.....	96
3.4. Simulation Setup	101
3.4.1. Detector Geometry, and Contacts.....	101
3.4.2. Energy Deposition by Primary Reaction Products	102
3.4.3. Charge Carrier Excitation and Collection (Signal Generation).....	103
3.4.4. Simulation Process.....	106
3.5. Results and Discussion.....	108
3.5.1. Total Energy Deposition: The Case of 100% Charge Collection of Both Types of Charge Carriers	108
3.5.2. Charge Collection Efficiency: Effect of Charge Transport Properties and Device Thickness	111
3.5.3. Detection Efficiency: Effect of Charge Transport Properties and Device Thickness.....	116
3.5.4. Pulse Height Spectra: Effect of Charge Transport Properties, Integration Time, and Device Thickness	121
3.5.5. Energy Scaling of the Pulse Height Spectra	131

3.5.6. Boron Carbide Detector: An Example.....	138
3.6. Conclusions	141
CHAPTER 4 SPACE-CHARGE-LIMITED CURRENT IN DISORDERED MATERIALS: NEGATIVE FIELD DEPENDENCE IN MOBILITY	145
4.1. Introduction	145
4.2. Space-Charge-Limited Current	147
4.3. Field Dependence of Carrier Mobility	149
4.4. Results and Discussion.....	150
4.5. Conclusions	160
CHAPTER 5 MOBILITY EXTRACTION USING SPACE-CHARGE-LIMITED CURRENT ANALYSIS: EFFECT OF COMPETING CHARGE TRANSPORT PHENOMENA	162
5.1. Introduction	162
5.2. Ohmic Charge Transport with Poole–Frenkel Emission or Field-Dependent Mobility.....	163
5.2.1. Poole–Frenkel Emission	163
5.2.2. Field-Dependent Mobility	169
5.2.3. Experimental Considerations.....	171
5.3. Space-Charge-Limited Current with Continuous Distribution of Traps	176
5.4. Mobility Extraction of Selected Films	180

5.4.1. PCITO Series Films: Films Grown at Low Temperature and Low RF Power	181
5.4.2. V and AA Series Films: Films Grown at High Temperature and High RF Power	182
5.4.3. Thickness Dependence Test for Space-Charge-Limited Current ..	194
5.5. Conclusions	203
CHAPTER 6 CHARGE TRANSPORT OPTIMIZATION OF AMORPHOUS HYDROGENATED BORON CARBIDE FILMS	205
6.1. Mobility Measurement and Optimization	205
6.1.1. Gentle Growth Conditions: Low RF Power and Low Substrate Temperature	206
6.1.2. Harsh Growth Conditions: High RF Power and Substrate Temperature	212
6.2. Photoconductivity Measurements	226
6.2.1. Mobility-Lifetime Product Measurement: Steady-State Photoconductivity	226
6.2.2. Carrier Lifetime Measurements: Transient Photoconductivity	234
6.3. Thick Films and Film Stability	237
6.3.1. Growth Rate Inconsistency of Previous Films	237
6.3.2. Delamination of Thicker Films	239
6.3.3. Film Stress Measurement	241

6.3.4. Thickness Reproducibility	272
6.3.5. Properties of the NS18, PC18, FT18 and PP18 Series Films	290
6.4. Discussions: Film Properties and Correlations	300
6.5. Mobility and Thickness Optimization Revisited.....	304
CHAPTER 7 CONCLUSION AND FUTURE WORK.....	310
APPENDIX A BAND ALIGNMENT OF DIFFERENT METALS WITH AMORPHOUS HYDROGENATED BORON CARBIDE FOR DIFFERENT VALUES OF BANDGAP	323
REFERENCES	329
VITA.....	366

LIST OF ILLUSTRATIONS

Figure 1.1 Interaction of a neutron with ^{10}B , resulting in the emission of an alpha (α) particle, a lithium ion, and a gamma (γ) photon.	4
Figure 1.2. Total neutron cross-sections of selected neutron-sensitive isotopes [97]. .	13
Figure 1.3. Neutron elastic scattering cross-sections of selected neutron-sensitive isotopes [97]......	15
Figure 1.4 Elastic scattering of a neutron from the nucleus. The kinetic energy of the recoiled nucleus and the scattered neutron depends on the scattering angle θ	16
Figure 1.5. A ^{10}B -based planar indirect-conversion semiconductor neutron detector. Here, a conversion layer absorbs the incident neutron and emits primary reaction products (α particle and Li ion). Only one of the reaction products enters the semiconductor and excites electron-hole pairs.....	23
Figure 1.6. A direct-conversion semiconductor neutron detector. Here, the semiconductor material itself absorbs the incident neutron and emits primary reaction products. Both of the reaction products excite electron-hole pairs inside the detector.	26
Figure 2.1 A schematic of the PECVD chamber. The substrate holder is attached under the substrate heater with a rotating arm.	34
Figure 2.2 (a) A substrate holder with cleaned silicon substrates, and (b) after securing the substrates with a substrate cover.	35
Figure 2.3. A schematic of the sputtering deposition system.	37

Figure 2.4. A schematic of the substrate heating system with a K-type thermocouple resting on quartz window.....	39
Figure 2.5. a) Actual substrate temperature recorded over time for different set temperature values (the numbers below the curve are set temperatures in °C), and b) a graph of substrate temperature as a function of set temperature values.	41
Figure 2.6. A schematic of the solid-state precursor bubbler.	42
Figure 2.7. Cooling of substrates using two methods. Natural cooling resulted in a very rapid decrease in temperature at the beginning, potentially resulting in thermal shock in the films. Slow cooling was achieved using a ramp-down protocol.....	47
Figure 2.8. Types of bottom contact deposited on substrates.	48
Figure 2.9. Schematic of an a-BC:H film deposited on transparent substrate connected to Faraday cage.	50
Figure 2.10. A Faraday cage designed to connect thin-film devices for electrical characterization (top) and its backside (bottom).....	51
Figure 2.11. Alpha-SE spectroscopic ellipsometer.....	53
Figure 2.12. Spectroscopic ellipsometry data fitting with CompleteEASE™ software using Cauchy model for transparent films.	54
Figure 2.13. An example extraction of the optical bandgap using a Tauc analysis. The energy (2.13 eV) at which the dashed fit line (red) intersects the $h\nu$ -axis is the optical bandgap.	56
Figure 2.14. HP 8453 UV-Vis spectrometer.....	57

Figure 2.15. An example absorption graph with reflection oscillations in the low-energy spectrum. The circular points represent the minimum reflection data points.59

Figure 2.16. a) MTI Microtrak II laser/detector triangulation unit and b) custom-built profilometer for wafer curvature measurement.60

Figure 2.17. Wafer curvature data for a-BC:H sample Q32 (I), after silicon background correction.62

Figure 2.18. An MIS device placed on a MDC mercury probe station for capacitance–voltage and current–voltage measurements.64

Figure 2.19. Schematic of current–voltage measurement setup. A device under test (DUT) is connected in series with a voltage sourcemeter and a picoammeter.65

Figure 2.20. Band alignment of a-BC:H with nickel demonstrating the expected formation of a hole injecting contact.67

Figure 2.21. Band alignment of a-BC:H with tungsten demonstrating the expected formation of a neutral contact.68

Figure 2.22. Band alignment between a-BC:H and zirconium demonstrating the expected formation of a hole-blocking contact.69

Figure 2.23. An example of current–voltage data obtained from an a-BC:H film.73

Figure 2.24. Extraction of resistivity of device AB6 using Ohm’s law. The red line represents the fit to Equation (2.14).73

Figure 2.25. Extraction of resistivity and carrier mobility from I–V measurements in the Ohmic and SCLC current regimes.76

Figure 2.26. Experimental setup for steady-state photoconductivity experiments.....	80
Figure 2.27. Example TOF signal with dispersive transport of carriers. The figure is taken from reference [177].....	84
Figure 2.28. A schematic of transient photocurrent measurement setup.....	86
Figure 2.29. Experimental setup for the transient photoconductivity experiment.....	87
Figure 3.1 (a) Surface excitation by short-penetration-depth radiation: only one type of carrier contributes to total charge collection. (b) Excitation within the detector volume: both carriers contribute to total charge collection.....	90
Figure 3.2. Microscopic neutron cross-sections for the constituent nuclei of B ₄ C for dominant thermal neutron interaction processes. The absorption of neutrons by ¹⁰ B is significantly higher than any other interaction process.	94
Figure 3.3 Thermal neutron absorption probability of natural B ₄ C and ¹⁰ B-enriched B ₄ C thin film as a function of detector thickness.	96
Figure 3.4 Schematic of neutron absorption and energy deposition in a direct-conversion neutron detector.	97
Figure 3.5 Stopping powers of 1.47 MeV α particle (■), 1.78 MeV α particle (●), 0.84 MeV Li ion (▲), and 1.02 MeV Li ion (▼) emitted from neutron- ¹⁰ B interaction in B ₄ C.	102
Figure 3.6 (a) Energy deposition pulse height spectra for B ₄ C devices with thicknesses of 1–5 μm and (b) 750–2000 keV region of the pulse height spectra for devices with thicknesses of 5–25 μm.....	109

Figure 3.7. (a) Charge collection efficiency for B₄C detectors 1–25 μm thick as a function of $\mu\tau E/d$ assuming a single type of charge carrier for $t_i \geq d/\mu E$. (b) Maximum charge collection efficiency possible as a function of $\mu t_i E/d$ with high enough $\mu\tau$ product.114

Figure 3.8. The variation of charge collection efficiency (CCE) as a function of $\mu\tau E/d$ and $\mu t_i E/d$ for a 25 μm thick device.115

Figure 3.9. Neutron detection efficiency as a function of $\mu\tau E/d$ at different values of $\mu t_i E/d$ for (a) a 1 μm device and (b) a 25 μm thick device. The detection threshold is set at 10 fC.118

Figure 3.10. Maximum detection efficiency as a function of detector thickness for $\mu t_i E/d = 0.3$ (■), $\mu t_i E/d = 1.0$ (●), and their percentage difference (▲).121

Figure 3.11. Intensity-normalized pulse height spectra of B₄C detectors with thicknesses of 1, 5, 10, and 25 μm for long integration time ($\mu t_i E/d \geq 1.0$) for $\mu\tau E/d = 0.1$ (—), $\mu\tau E/d = 1$ (—), $\mu\tau E/d = 10$ (—), and $\mu\tau E/d = 100$ (—). The p-0 and p-1 peaks are assigned to incomplete charge collection of the 840 keV Li ions and 1470 keV α particles arising from neutrons absorbed close to the collecting electrode of the device. Peak p-2 arises from partial energy deposition in very thin devices, which can be seen even if both types of charge carriers are mobile, as shown in Figure 3.6a. The peaks at 2310 keV and 2800 keV are the sum peaks from Equation (3.1).123

Figure 3.12. Intensity map of normalized pulse height spectra of a 10 μm thick B₄C device as a function of $\mu\tau E/d$ for long integration time ($\mu t_i E/d \geq 1.0$). The discrete

shifts in color represent the steps in the pulse height spectra corresponding to the individual peaks, with the red representing the sum peak at 2310 keV.....125

Figure 3.13. The evolution of the pulse height spectra of a B₄C detector as a function of detector thickness for $\mu\tau E/d \gg 10$, and integration time longer than transit time ($\mu tiE/d \geq 1.0$). The pulse height spectra are normalized to intensity. The dashed lines are visual guidelines for the shift of the individual peaks.126

Figure 3.14. Normalized pulse height spectra of devices with thicknesses of 1, 5, and 25 μm for $\mu\tau E/d = 1$ and 10 as a function of $\mu tiE/d$130

Figure 3.15. Schematic of neutron absorption in a ¹⁰B-based direct conversion detector showing the regions that correspond to the specific spectral peaks obtained, considering only the first branch of the ¹⁰B nuclear reaction (Equation (3.1)).132

Figure 3.16. Intensity map of normalized pulse height spectra of a 10 μm thick detector overlapped with fit curves for charge collection.....134

Figure 3.17. Charge collection efficiency (CCE) defined by Equation (3.24) obtained for the sum peaks (2310 keV* and 2800 keV*) as a function of $\mu\tau E/d$ for different values of $\mu tiE/d$. Graphs corresponding to $\mu tiE/d = 0.9$ and 1.0 are not included as distinct sum peaks were not observed for thinner devices with larger values of $\mu\tau E/d$. The charge collection efficiencies are independent of device thickness.137

Figure 3.18. Minimum charge carrier mobility required to achieve neutron detection in a planar B₄C detector as a function of device thickness for different integration times when carrier lifetime is sufficiently long. For an order of magnitude decrease in

integration time, the required minimum carrier mobility increases by an order of magnitude.....139

Figure 3.19. Theoretical detection efficiency as a function of mobility–lifetime product ($\mu\tau$) for different charge carrier mobilities of a 5 μm thick B_4C neutron detector taking 10 fC of charge ($\sim 25\%$ of total energy deposition) as the lower level discriminator and 10 μs as the integration time.141

Figure 4.1. Variation of ηy against the normalized electric field z for positive field dependence. The integral I (shaded portion) is obtained by subtracting the area of the unshaded portion from the rectangle of area ηz_0154

Figure 4.2. Variation of normalized current density (η) against normalized applied voltage (ξ) obtained from the exact solution derived here in comparison to pure SCLC (Mott and Gurney), Murgatroyd’s original solution, and Barbe’s analytical solution for (a) $\xi < 500$ and (b) $\xi > 500$157

Figure 4.3. Plotting the variation of $\ln\eta/\xi^2$ against ξ yields a straight line, which supports the exponential dependence of the normalized current (η) on the square root of the normalized voltage ξ158

Figure 5.1. Minimum and maximum electric field as a function of the device constant C (Equation (5.7)) for Poole–Frenkel emission and SCLC to co-exist. E_0 is the cross-over field between Ohmic and SCLC charge transport in the absence of Poole–Frenkel emission. The colored region represents the allowed electric field region.....167

Figure 5.2. Device constant as a function of device thickness for different values of thermal equilibrium concentration. The low- and high-frequency dielectric constants assumed are 5 and 4, respectively. The dotted line in a is the limiting device constant (0.736) beyond which SCLC with Poole–Frenkel is not possible.....168

Figure 5.3. Theoretical current-voltage data of a 700 nm device with carrier concentration $n_0 = 10^{14} \text{ cm}^{-3}$, carrier mobility $\mu = 10^{-7} \text{ cm}^2 \cdot \text{V}^{-1} \cdot \text{s}^{-1}$, low-frequency dielectric constant $\kappa = 5$, and high-frequency dielectric constant $\epsilon = 4$ under different charge transport phenomena. The slope of the current–voltage data is 2 in the shaded regions of corresponding curves.172

Figure 5.4. Current–voltage data of Figure 5.3 plotted in the format of Equations (5.15) and (5.16). Only Ohmic charge transport with Poole–Frenkel emission or field-dependent mobility produces straight line in the format of Equation (5.15), and only the SCLC enhanced by Poole–Frenkel emission or field-dependent mobility produces straight line in the format of Equation (5.16), which, along with the device constant calculated from the fit parameters, helps in determining whether SCLC is present or not.174

Figure 5.5. Current–voltage data of the PCITO series films plotted in the format of Murgatroyd's equation. The dashed lines at the end of data are the trend lines of the fit.182

Figure 5.6. Current–voltage data of the V series films plotted in the format of Murgatroyd's equation.183

Figure 5.7. Current–voltage data of the AA series films a) films that potentially fit to Murgatroyd's Equation (5.16) in the shaded region and b) films that do not fit to Murgatroyd's equation.....186

Figure 5.8. Current–voltage data of the V and AA series plotted in the standard Poole–Frenkel format (Equation (5.15)). The shaded portion represents the electric field region where the data produces nearly straight lines.189

Figure 5.9. Current–voltage data of the AA and V series films plotted in the format of Equation (5.24), describing SCLC with exponential distribution of traps.191

Figure 5.10. Current–voltage data for the AA and V series films (a) plotted in the format of Equation (5.26) and (b) a zoomed section where data fit to straight lines.193

Figure 5.11. Thickness of the TD1703 films determined by spectroscopic ellipsometry before and after $C_2F_6 + O_2$ plasma etching.195

Figure 5.12. Graph of J/E^2 against E of the film TD1703 with different thicknesses achieved after C_2F_6 etching. The vertical bar at $\sim 10^7$ V/m (0.1 MV/cm) represents the field region at which the curves attain the minima.196

Figure 5.13. Resistivity of TD1703 films as a function of their film thickness.199

Figure 5.14. Current–voltage data of the TD1703 films plotted in the format of a) Ohmic current enhanced by Poole–Frenkel emission, b) SCLC with exponential distribution of traps, and c) SCLC with uniform distribution of traps.202

Figure 6.1. Charge carrier mobility of a-BC:H thin-films as a function of hydrogen concentration observed in previous studies within the group. Lower/higher hydrogen concentration correspond to harsh/gentle growth conditions.206

Figure 6.2. Refractive index and low-frequency dielectric constant of the PCITO series films as a function of growth rate for substrate temperature of 125 °C and 225 °C...210

Figure 6.3. Resistivity and carrier mobility of the PCITO series films as a function of growth rate for substrate temperature of 125 °C and 225 °C.....211

Figure 6.4. Refractive index and dielectric constant of the AA, AB and V series films as a function of growth rate.221

Figure 6.5. Iso-absorption energy gap (E_{04}) and Urbach energy of AA and V series films as a function of growth rate.223

Figure 6.6. Resistivity and carrier mobility values of a-BC:H films in the AA, AB and V series films as a function of growth rate.224

Figure 6.7. Photocurrent measurements of film PC1703 using a new approach where the current values in the dark and light were measured successively at each voltage interval. The high current spikes in the dark are the capacitive charging current spikes observed when the bias voltage was increased to the next value.228

Figure 6.8. Photocurrent–voltage data for films PC1703, PC1705, and PC1710. The terms “plus” and “minus” represent the polarity of the voltage applied to the transparent ITO/FTO contacts.230

Figure 6.9. Photocurrent–voltage data for films PC1704, PC1709, PC1712, and PC1713. The terms “plus” and “minus” represent the polarity of the voltage applied to the transparent FTO contacts. Only the photocurrents with “FTO plus” show saturation in limited electric field regimes.231

Figure 6.10. Hecht photocurrent fit of film PC1704.....233

Figure 6.11. Photocurrent transient of PC1713 with 20 ns laser pulse at 351 nm for different applied biasing voltages. The dashed lines of corresponding color (top) indicate exponential fits to obtain carrier lifetime.235

Figure 6.12. Buckling-based delamination observed in a-BC:H films grown at 350 °C, typically accelerated by higher humidity conditions.240

Figure 6.13. Wafer curvature measurement of the ST1701 film grown on a 4-inch silicon wafer.248

Figure 6.14. Wafer curvature measurement of the ST1703 film grown on a 4-inch silicon wafer.249

Figure 6.15. Wafer curvature measurement of the ST1704 film grown on a 4-inch silicon wafer250

Figure 6.16. Step height measurement of the ST1705 film using KLA Tenkor P-7 profilometer.....251

Figure 6.17. Aluminum film peeling off of silicon substrate during film growth.253

Figure 6.18. Delamination of ITO and FTO bottom contacts on films (a) PC1706 and (b) PC1708 compared to other substrates.253

Figure 6.19. Current–voltage data of the film PC1707 grown on a glass/TiW substrate.	254
Figure 6.20. The beginning stages of delamination of the TD1709 film. The film was grown with 1% hydrogen and 99% argon as carrier gases.	257
Figure 6.21. Films grown with 10% methane and 90% argon as carrier gas showing “ribbon” delamination pattern during PECVD growth.....	258
Figure 6.22. (a) Cross-sectional view of the AL1705 film obtained with scanning electron microscope, (b) Film AL1705 showing wrinkles, (c) film AL1701 rolled up after cutting from a large piece of foil, (d) film grown on tungsten, and (e) film grown on zirconium. The spots at the center of the films grown on tungsten and zirconium are sputtered top contacts.....	263
Figure 6.23. a-BC:H films grown on copper foil: a) CU1801, b) backside of CU1801 showing wrinkles on the copper foil, and c) CU1802.	264
Figure 6.24. IV characteristics of film AL1702. a) The film was stable up to 100 V in the first run. b) Electrical breakdown of the device in the second run.	265
Figure 6.25. Current–voltage characteristics of CU1801 and CU1802 films grown on copper foil.	265
Figure 6.26. a-BC:H on glass after 3 h in 1% KOH (left); a-BC:H on glass (AA14) in 10% KOH after 3 days (right).....	267
Figure 6.27. CU-18-01 film covered with PMMA in (a) FeCl ₃ solution, (b) after etching the copper foil, and (c) broken into pieces when washing PMMA with acetone.	269

Figure 6.28. Pressed pellet made from a-BC:H flakes obtained by dissolving a film on aluminum foil.....271

Figure 6.29. Installed MKS 1152 solid-state vapor-source mass flow controller.274

Figure 6.30. Saturated vapor pressure of *ortho*-carborane as a function of temperature determined by thermogravimetric analysis.....275

Figure 6.31. Variation of growth rate of NS18 series film. The bubbler was initially loaded with 10 g of *ortho*-carborane. The film growth rate increased, on average, by ~9 nm/min per sequential growth until the precursor started to deplete after the 10th growth. We observed a similar trend after refilling the bubbler with 2 g of *ortho*-carborane.277

Figure 6.32. Fluctuation in substrate temperature as a function of time (a) before tuning the PID controller and (b) after tuning the PID controller. The numbers below the curves represent the set temperature, while the y-axis values represent the actual substrate temperature.281

Figure 6.33. The growth rate of the FT18 and PP18 series films: (a) regular films and (b) central films, as a function of bubbler temperature. The colored arrows show the direction of increasing parameter values. Data points without corresponding arrows are obtained for carrier line temperature of 100 °C, precursor partial flow of 1.00, and process pressure of 0.2 Torr.....287

Figure 6.34. Refractive index and bandgap of NS18 series films as a function of growth rate compared to the AA series films.....291

Figure 6.35. Iso-absorption energy gap (E_{04}) and Urbach energy of NS18 series films as a function of growth rate compared to the AA series films.....292

Figure 6.36. Refractive indices and dielectric constants of the AA, PC18, FT18, and PP18 series films grown at 500 °C as a function of growth rate. The dashed lines are only for visual guidance.....296

Figure 6.37. Iso-absorption energy gap and Urbach energy of the AA, PC18, FT18, and PP18 series films grown at 500 °C as a function of growth rate.298

Figure 6.38. Electrical resistivity and carrier mobility of the AA, PC18, FT18, and PP18 series films grown at 500 °C as a function of growth rate. The dashed lines are for visual guidance only.....299

Figure 6.39. Variation of iso-absorption energy gap with the refractive index for high-temperature films.302

Figure 6.40. Film CU1803 deposited on 100 μm thick copper foil. The smaller films on the left were expected to be 3 μm thick, while the large film on the right was expected to be 5 μm thick based on the growth rate of films placed at the center of the substrate holder. All of the films in this batch were stable for a long time in the atmosphere. .305

Figure 6.41. Current–voltage characteristics of CU1803 devices (a) obtained with a Ti/W top contact, and (b) obtained with Hg probe.307

Figure 6.42. Current–voltage characteristics of the CU1804 film grown on p-type silicon.....307

Figure 6.43. Current–voltage characteristics of the CU1803 (top) and CU1804 (bottom) films in log-log scale.....309

LIST OF TABLES

Table 3.1. Position of the deposited charge packets that contribute to their associated spectral peaks in single-carrier B ₄ C neutron detector.....	134
Table 5.1. Parameters extracted from the Murgatroyd fit for the V series films. Symbols μ_0 , n , and ϵr represent respectively the carrier mobility, carrier concentration, and the high-frequency dielectric constant.....	185
Table 5.2. Parameters extracted from the Murgatroyd fit of current–voltage data of the selected V and AA series films. Symbols μ_0 , n , and ϵr represent respectively the carrier mobility, carrier concentration, and the high-frequency dielectric constant.	187
Table 5.3. Field-dependence factor and high-frequency dielectric constant extracted from the Poole–Frenkel fit of the AA and V series films.	190
Table 5.4. Minimum carrier mobility and the trap density extracted from the SCLC analysis of the AA and V series films. Symbols μ_{\min} and N_t represent the minimum carrier mobility and trap density, respectively.....	194
Table 5.5. Parameters extracted from the Murgatroyd fit of current–voltage data for the TD1703 films. Symbols μ_0 , n , and ϵr represent respectively the carrier mobility, carrier concentration, and the high-frequency dielectric constant.	198
Table 5.6. Minimum carrier mobility, maximum carrier concentration, and trap density in the TD1703 films extracted using SCLC with the uniform distribution of traps model.	201

Table 6.1. 2^2 factorial experiment design for a-BC:H film growth in the low-power/low-temperature regime. Other process conditions were held constant at a power of 15 W, pressure of 0.2 Torr, and total carrier gas flow rate of 200 sccm.207

Table 6.2. Growth conditions for the PCITO series films. The films PCITO 10, 11, 13, and 14 were grown for the 2^2 factorial experiments, as given in Table 6.1, and the film PCITO12 was grown using the growth conditions of a previously grown film N25. 207

Table 6.3. Properties of the PCITO series films. Symbols RI , κ , ρ , μ_0 , E_g , and EU are respectively the refractive index, low-frequency dielectric constant, resistivity, low-field mobility, bandgap, and Urbach energy.....208

Table 6.4. 2^2 factorial experiment design for film growth at high temperature and high power.....213

Table 6.5. Growth conditions for V series films grown according to the 2^2 factorial experiment design outlined in Table 6.4. The films were grown at 500 °C and 40 W at a pressure of 0.2 Torr for 20 minutes.....213

Table 6.6. Properties of V series thin films grown with the growth conditions given in Table 6.5. Symbols RI , κ , ρ , μ_0 , E_{04} , and EU are respectively the refractive index, low-frequency dielectric constant, resistivity, low-field mobility, iso-absorption gap, and Urbach energy.214

Table 6.7. Growth conditions of the AA series films. The process pressure was set at 0.2 Torr.217

Table 6.8. Properties of the AA series a-BC:H films.218

Table 6.9. Properties of AB series films. The symbols RI , κ , ρ , μ , and Nt are respectively the refractive index, dielectric constant, resistivity, minimum mobility, and trap density.....	219
Table 6.10. PC17 series films grown for photoconductivity measurements and their status. Films were grown with RF power of 40 W, process pressure of 0.2 Torr, total flow rate of 200 sccm, and precursor partial flow of 100%.....	227
Table 6.11. Effective mobility lifetime products and other properties of some PC17 series films. A uniform absorption of light is considered for mobility–lifetime estimation.....	232
Table 6.12. Mobility–lifetime product and other properties of some of the PC17 series films. A uniform absorption of light is considered for mobility–lifetime estimation.	233
Table 6.13. Growth rates for PCITO12 series films with longer growth times. The films were grown at substrate temperature of 100 °C, RF power of 10 W, total pressure of 0.2 Torr, total flow of 200 sccm and partial precursor pressure of 1.....	238
Table 6.14. Growth conditions of the B4 and Q32 films grown for stress measurements.	241
Table 6.15. Measured thickness and stress values in the B4 and Q32 films. A positive/negative stress value represents tensile/compressive stress.	242
Table 6.16. Growth conditions and film stress values of the ST series films.....	245
Table 6.17. Summary of attempted thick film growths on various substrates.....	262

Table 6.18. Growth conditions, film thickness, and growth rate of NS18 series films. The films were grown at 500 °C substrate temperature, 40 W RF power, and 200 sccm of carrier gas (argon) flow rate.276

Table 6.19. Growth time, thickness, and growth rate of the PC18 series films. The films were grown at a substrate temperature of 500 °C, RF power of 40 W, total argon flow of 200 sccm, and process pressure of 0.2 Torr. Bubbler temperature was set at 80 °C.282

Table 6.20. $3^1 \times 2^1$ factorial experiment design for FT18 series film growth.283

Table 6.21. Growth conditions, thickness, and growth rates of the FT18 series films grown according to the $3^1 \times 2^1$ factorial experiment design from Table 6.20. Films were grown for 5 minutes at a substrate temperature of 500 °C, RF power of 40 W, a total flow rate of 200 sccm, partial precursor flow of 100%, and process pressure of 0.2 Torr.284

Table 6.22. 2^3 factorial experiment design for PP18 series film growth.285

Table 6.23. Growth conditions of PP-18 series films grown according to the 2^3 factorial experiment design from Table 6.22. The films were grown for 10 minutes at a substrate temperature of 500 °C, RF power of 40 W, a total flow rate of 200 sccm, and carrier line temperature of 100 °C. The rows are shaded to separate different film batches .286

Table 6.24. Optical and electronic properties of NS-18 series films grown using new vapor source mass flow controller.290

Table 6.25. Optical, electronic, and electrical properties of PC18, FT18, and PP18 series films. The symbols RI , κ , ρ , μ_0 , E_{04} , and EU are respectively the refractive index, dielectric constant, resistivity, low-field mobility, iso-absorption energy gap, and Urbach energy.295

ACKNOWLEDGEMENTS

I would like to express my deep and sincere gratitude to my advisors, Professor Michelle M. Paquette and Professor Anthony N. Caruso for their invaluable guidance, support, motivation, and patience throughout my research. I will forever be grateful to them.

I would like to thank Professors J. David Van Horn, Nathan A. Oyler, and Paul M. Rulis for serving on my committee. I appreciate their dedication and time in providing valuable suggestions and insights.

My wife **Alija Pokharel** deserves special thanks for always giving me love, support and encouragement I needed to get to this day, especially, for her strength in holding me and guiding our daughter **Vedanti Bhattarai** alone to bring us out of a painful time during this research work. Alija, this is your achievement.

I am grateful to my parents Mr. Tulashi Ram Bhattarai and Mrs. Yashoda Devi Bhattarai for their continuous love, prayers, care, and sacrifices to educate me and prepare my future. I would like to thank my sisters and brothers-in-law for their constant support and motivation.

I cannot forget all my friends and colleagues, and the entire MIDE team for creating a friendly and encouraging environment. Shailesh Dhungana, Rupak Thapa, and Thuong Nguyen deserve special thanks for their help in research and beyond, especially to keep moving my apartment, not to mention the move a few days before my defense. Mark Pederson and Sai Pinepalli should get thanks for helping me with

their creative ideas. This work would not be in this shape today without a stress release platform, and Steve Young deserves thanks for setting it up. Steve, you owe me a can of beer.

At last, I want to thank my advisors Professor Michelle M. Paquette and Professor Anthony N. Caruso once again for everything and anything that I forgot to mention. I feel blessed to be working with them.

This work has been supported by the Defense Threat Reduction Agency under Grant No. HDTRA1-15-1-0020 and by funds provided through the University of Missouri-Kansas City School of Graduate Studies Research Grant program.

Dedicated to my daughter Vedanti

CHAPTER 1

INTRODUCTION

Matter is composed of tiny unbreakable particles. Written evidence indicates that people from as early as 5th century BC [1] maintained such a concept and referred to these tiny unbreakable particles as *atoms*. However, modern visualization of atoms began with Dalton's atomic theory of matter [2], and it took more than a century to see what an atom looks like. A complete portrait of the atom was revealed only after the 1932 discovery of *neutrons*, the neutral particles within the atomic nucleus, by James Chadwick [3]. *Electrons* (the negatively charged particles orbiting the nucleus), and *protons* (the positively charged particles within the nucleus) were already discovered by J. J. Thomson and Ernest Rutherford in 1897 and 1919, respectively.

Protons in the nucleus repel each other via the long-range Coulomb force and attract each other via the strong nuclear force, which acts only at a very short range of about one femtometer (10^{-15} m). The stability of a nucleus under the repulsive Coulomb force was not understood until the discovery of the neutron. The presence of neutrons with size and mass equal to those of protons increases the attractive nuclear force and overcomes the repulsive Coulomb force, lending stability to the nucleus. For this reason, heavy stable atoms always have more neutrons than protons in their nuclei.

When neutrons are added to an atom beyond a certain limit, known as the band of stability [4], the short-range nuclear force fails to balance the repulsive Coulomb force due to a large nuclear size. The unstable nucleus then finds one of two ways to

stabilize itself: (a) an internal conversion of a neutron into a proton with the emission of a negatively charged beta (β^-) particle, converting the original nucleus into a more stable nucleus and (b) breaking the nucleus into smaller stable nuclei, famously known as nuclear fission. A nuclear fission event releases many different kinds of radiation along with a large amount of energy, a phenomenon that humans have been exploiting for both survival and destruction. Neutrons not only give us the stability required for our physical existence but also play a fundamental role in our sociopolitical relationships.

Similar to light and other types of radiation such as X-rays, γ -rays, and electrons, neutrons can be used as a tool to probe everything from the microscopic world to the cosmos. Neutrons are also used for therapeutic purposes to treat certain cancers. However, because of the unique properties of neutrons such as electrical neutrality, high penetrating power, and a very short de Broglie wavelength, their applications can be extended well beyond the scope of other types of radiation. Some important applications of neutrons are the detection of uranium, plutonium, and their isotopes, known as *special nuclear materials* (SNMs) [5], the structural characterization of materials at the sub-nanometer scale, and the detection and imaging of hydrogenous materials (water, oil) on Earth and in outer space. However, all these uses of neutrons come with one caveat: neutrons are one of the most challenging types of radiation to detect.

Radiation can be detected if it interacts with the detector medium. Only a handful of elements (^1H , ^3He , ^6Li , ^{10}B , ^{28}Si , ^{113}Cd , ^{157}Gd , and ^{235}U) have a significant neutron

interaction probability, and materials composed of these elements can be used for neutron detection. However, the most efficient and widely used detectors at present exploit ^3He , a rare isotope of the balloon gas, whose scarcity has recently been of global concern [6], [7]. So, while we are in a state where neutrons are becoming more and more useful, we are losing our ability to talk to them. This work is an effort to understand a novel material, *boron carbide*, as a potential replacement of ^3He in neutron detection applications. With dedicated efforts, this refractory material, which has been used traditionally as a protective coating in armor and power tools due to its toughness under harsh environmental conditions, may find another home in scientific applications spanning our everyday life to cosmic explorations.

1.1. Motivation and Objectives

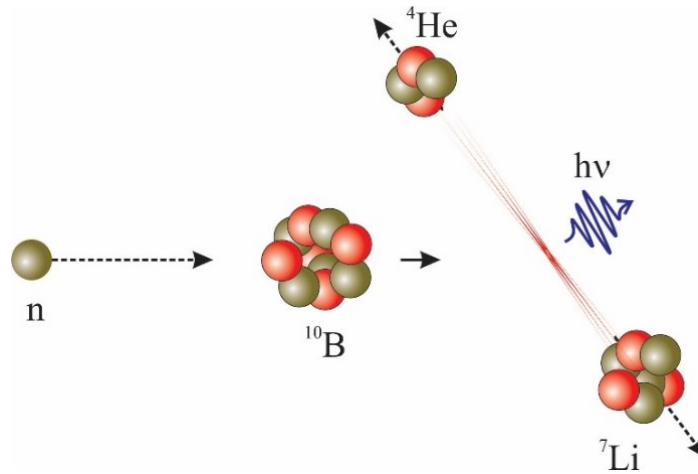


Figure 1.1 Interaction of a neutron with ${}^{10}\text{B}$, resulting in the emission of an alpha (α) particle, a lithium ion, and a gamma (γ) photon.

1.1.1. Applications of Neutrons and Neutron Detectors

After the discovery of neutrons, Goldhaber observed an unusually high probability of neutron capture by ${}^{10}\text{B}$ in 1934 [8]. This nuclear capture reaction, which results in the emission of an alpha (α) particle, a lithium ion, and a gamma (γ) photon, was shortly exploited for therapeutic use, and boron–neutron capture therapy (BNCT) was introduced in 1936 [9]. In BNCT, neutron radiation is concentrated with the help of localized boron drugs in tumor cells. The charged particles emitted from the boron–neutron interaction, which have a total energy of 2.33 MeV and a combined range of 12–13 μm in body tissues, can destroy tumor cells at the cellular level, leaving the healthy tissues minimally damaged. For some kinds of brain tumors [10], BNCT is to

date still the only effective treatment available, and its success greatly relies on precise control of the neutron flux/dose given to the patient.

With the discovery of induced fission in 1938 by Otto Hahn [11], neutrons became the trigger for nuclear bombs [12] and nuclear reactors [13]. The precise measurement of neutron flux to achieve a sustained nuclear reaction is critical for the safety of nuclear reactors, which currently provide nearly ten percent of electricity worldwide [14]. Neutrons are also used to obtain the information of fusion-energy and remaining fuel in fusion reactors, the so-called “infinite source of clean energy,” which are hoped to light up the world within the next five to fifteen years [15].

The discovery of neutron diffraction (elastic scattering of neutrons) in 1945 [16] by Wollan, Shull, and Clifboard made neutrons an integral part of materials research, especially in the structural characterization of bulk materials composed of light elements such as hydrogen, carbon, and oxygen, where X-ray diffraction could not provide sufficient information because of their poor X-ray sensitivity. However, these light elements have high neutron scattering cross-sections, which allow neutrons to be used in identifying these materials in many industrial applications such as oil well logging [17], coal mining [18], neutron imaging [19], industrial quality control (e.g., evaluation of cracks in turbines and cracks in wings of air planes) [20], as well as the search for water, carbon dioxide, and extraterrestrial life on other planets [21], [22].

Thermal neutrons, which have a de Broglie wavelength of about 2 Å, can be used to study the atomic motion in protein molecules [23]–[25], and have been used in

the study of the protein malformation responsible for Alzheimer's and Parkinson's diseases [23], [26]. A recent publication on the structure of an intrinsically disordered protein (obtained with neutron scattering combined with computer simulation [27] shows the possibility and importance of neutron physics in understanding the structural complexity of disordered materials.

Neutrons penetrate materials much deeper than any other type of radiation and interact only with the nuclei, which results in the emission of secondary radiation. This process, known as neutron activation, enables neutrons to be used for elemental analysis of a large quantity of material. Neutron activation analysis is used to study the composition of rocks and cancer cells, and to detect explosives and chemical weapons with very high precision [28]. The penetrating property of neutrons also helps in detecting special nuclear materials (SNMs) used to make nuclear weapons. Neutrons are emitted from SNM either by spontaneous fission or by active interrogation (induced fission by an active bombardment of these materials by neutrons). The detection of these fission neutrons then provides a unique signature of the SNM, providing a reliable means for its detection.

1.1.2. Need for Helium-3 Alternatives

It is clear that for applications ranging from the study of materials at the sub-nanometer scale to the study of the deep cosmos, neutrons have become a powerful probing tool. However, to date, neutron detection mostly relies on traditional detection

techniques based on ^3He gas-filled neutron detectors, which have many limitations in terms of fabrication and applications.

^3He is a helium isotope that has the highest neutron interaction probability among gases, but is very rare in the Earth (1.37 ppm) [7]. In the United States, ^3He is only available through the US nuclear weapons program, where it is obtained as a decay product of tritium. Tritium is a heavy isotope of hydrogen which is used in nuclear warheads to enhance their yield. As tritium production halted as of 1988 [29], the availability of ^3He has been dependent on remaining tritium from dismantled nuclear warheads and the ^3He stockpile [7]. Apart from its use in neutron detection, ^3He has many other important applications, including as a contrast material in magnetic resonance imaging of lungs [30] and a cryogenic material in many low-temperature physics experiments [31], [32]. With the increasing importance of these applications, the demand for ^3He is rising, while the widespread implementation of neutron detectors in radiation portal monitoring systems (RPMs) along the US border after the September 11, 2001 attack has depleted the ^3He stockpile at an alarming rate [7], [33]. Since 2009, the supply of ^3He for radiation portal monitoring systems has been limited [7], [33], and different programs have been initiated for the search of ^3He alternatives [6], [34].

While the shortage of ^3He is one reason for the increased demand for alternative neutron detection technologies, their development is also necessary for many emerging neutron detection applications where ^3He -filled tube detectors may not be suitable. Gas-filled detectors may not provide sufficient spatial resolution in many applications such

as BNCT, neutron imaging, and neutron scattering/diffraction experiments because of their bulky size. $^{10}\text{BF}_3$ -filled tube detectors [35], and boron-lined tube and straw detectors [36], [37] have been developed as alternatives to ^3He -filled detectors for radiation portal monitoring systems. However, they do not provide the same level of efficiency, stability, reliability, and gamma rejection [37].

Detectors with spatial resolutions in the sub-micrometer to tens of micrometer range with digital interfacing are necessary to take full advantage of neutron tomography [38], phase contrast imaging [39], real-time neutron imaging [40], as well as neutron diffraction and scattering experiments. Most of these applications currently use scintillation-based detectors [20], [41] for real-time monitoring and ^3He -filled tube detectors for neutron flux monitoring. Although pixelated scintillation detectors [42], [43] can provide high spatial resolution, they have inherently low efficiency and require complex optical coupling [44].

Fast and efficient neutron detectors with high energy and spatial resolution can take full advantage of intense neutron sources such as spallation neutron sources [45]. They can significantly reduce experiment/exposure time of many applications while increasing image/structural quality. Efficient and high spatial resolution detectors can be used to control neutron flux precisely in boron–neutron capture therapy and many other experiments. The only technology that can provide all of these neutron detection requirements is semiconductor technology.

1.1.3. Boron-10 Compounds for Direct-Conversion Semiconductor Neutron Detection

Detection of neutrons require neutron sensitive materials. Semiconductor neutron detector use these neutron sensitive materials in two ways. In an indirect-conversion detector, the neutron sensitive material is used as a capture layer on traditional semiconductor material, which absorbs neutrons and emits ionizing particles that the detector can detect. In contrast, a direct-conversion detector itself is made of the neutron sensitive material and performs better than the indirect-conversion detectors (*vide infra*)

Among the neutron-sensitive semiconductors, ^{10}B -based solid materials have the best combination of high thermal neutron cross-section and high energy release (Q-value) of neutron–nucleus interaction necessary for neutron detection. Direct-conversion devices using crystalline compounds of ^{10}B have been proposed since 1956 [46], with the most researched ^{10}B materials being boron phosphide [47], [48], boron nitride [49]–[54], boron arsenide [55]–[57], boron selenide [58], [59], and boron carbide [60]–[71]. Historically, neutron detectors based on these crystalline materials never gained traction due to the lack of material processing techniques. Despite the introduction of advanced low-temperature thin-film deposition techniques in the late 1980s, which provided great control in tuning the charge transport properties of semiconductors, these crystalline materials did not show promise until a recent success of achieving >50% neutron detection efficiency in a hexagonal boron nitride (hBN)

detector [50], [72]. This success highlights the promise of this class of neutron detectors to replace ^3He -based technology.

1.1.4. Amorphous Boron Carbide Thermal Neutron Detectors

Boron carbide is an important refractory material with excellent mechanical, electrical, and chemical stability [73]–[75]. Due to its toughness and large neutron absorption cross-section, it has been used traditionally in many industrial applications, such as armor coatings, abrasive materials, and control rods in nuclear reactors [11]. For semiconductor device applications, such as diodes, transistors, and detectors, it appeared as a candidate material only after low-temperature ($<400\text{ }^\circ\text{C}$) PECVD methods to produce amorphous thin films of this material were introduced in the early 1990s [76]–[78]. Following the trend of amorphous semiconductors set by amorphous silicon, and with continued efforts to understand the material for more than a decade [76], [79]–[87], Robertson et al. [88] reported a first direct-conversion thermal neutron detector based on plasma-enhanced chemical vapor deposition (PECVD) grown amorphous boron carbide (B_5C) on n-type silicon in 2002. Although the device had very low detection efficiency due to its very thin B_5C layer, and its performance was questioned for not showing the spectral characteristics of a direct-conversion neutron detector [89]–[91], the study prompted enough interest within the scientific community such that amorphous hydrogenated boron carbide (a-BC:H) continued to dominate direct-conversion neutron detection research [60]–[71], [92] for the last three decades.

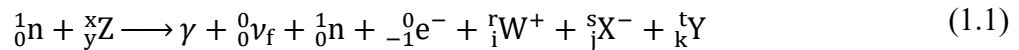
Amorphous hydrogenated boron carbide possesses many important properties for a semiconductor detector, including high electrical resistivity [77], [93]–[95], a moderately wide bandgap [77], [93]–[95], as well as high mechanical, radiation, and thermal stability. Because of the high neutron absorption cross-section of ^{10}B , a 25 μm thick film of ^{10}B -enriched a-BC:H can provide >60% theoretical detection efficiency. By exploiting its amorphous nature, simple fabrication techniques such as PECVD can produce large-area and flexible detector panels similar to the flat panel televisions and displays we see nowadays.

Despite the many encouraging properties of a-BC:H, the deposition of thick films beyond a couple of μm , and optimization of charge transport properties in this material remain challenging. For all direct-conversion semiconductor detectors, the most critical material properties are (a) the charge carrier mobility (μ) and (b) the charge carrier lifetime (τ), which together determine the efficiency of charge collection in a detector. However, both of these material parameters in amorphous boron carbide are either considered low or are not well understood. Thus, comprehensive studies of these properties are necessary to develop neutron detectors based on this material and resolve controversies regarding detector performance. This work aims to characterize and optimize the charge transport properties of PECVD-grown a-BC:H thin films and fabricate thick (5–10 μm) films with optimized properties for their use in direct-conversion solid-state thermal neutron detectors.

1.2. Fundamentals of Neutron Detection

1.2.1. Interaction of Neutrons with Matter

Neutrons are electrically neutral and do not interact with electrons or electric fields. Since the majority of the volume of an atom is occupied by electrons (the volume of an atom/electronic cloud in an atom is nearly 15 orders of magnitude larger than the volume of the atomic nucleus), neutrons can travel long distances in most materials without showing even a single trace of their presence. For example, in lead, the most common material used in radiation shielding, neutrons emitted from special nuclear materials (SNMs) such as uranium and plutonium, can travel more than 50 centimeters. Thus, any material looks like empty space for a neutron until it strikes an atomic nucleus. The neutron then either deviates off its original path, giving off some of its energy to the nucleus, or gets absorbed into the nucleus and induces a nuclear reaction. The interaction of a neutron with matter can be described as



where the primary reaction products on the right-hand side of Equation (1.1) can be gamma rays, neutrinos, neutrons, electrons, charged ions, and/or neutral atoms.

The interaction probability of a neutron with an atom is very small because it only interacts with the tiny nucleus. The term ‘microscopic cross-section’ generally quantifies the interaction probability. It can be understood as an effective area subtended by a material target such that an incident particle entering that area undergoes a

particular type of interaction. Thus, for different types of nuclear interactions, corresponding types of interaction cross-sections can be defined. When summed up for all possible interactions, the total area, known as the ‘total microscopic cross-section,’ gives the total probability that an incident particle can undergo a nuclear interaction.

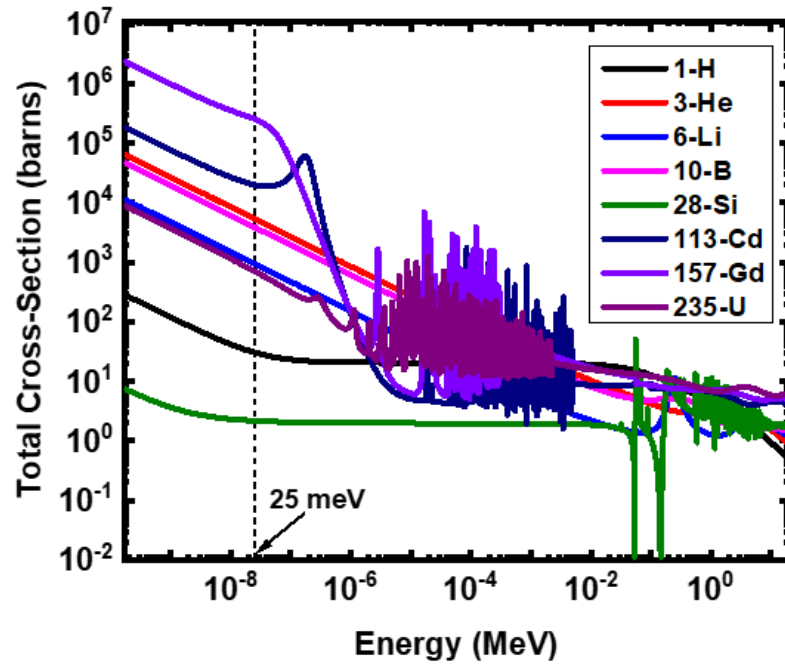


Figure 1.2. Total neutron cross-sections of selected neutron-sensitive isotopes [96].

Figure 1.2. shows the total microscopic neutron cross-sections of selected isotopes having relatively high neutron interaction probability as a function of incident neutron energy. We can see that the total cross-section falls off rapidly with increasing neutron energy. As the neutron–matter interaction is essential for neutron detection, the low interaction probability of high-energy neutrons explains the difficulty associated

with fast neutron detection in general. Based on the primary reaction products of neutron–matter interaction, neutron interactions can be placed in two broad categories: scattering and absorption.

Neutron Scattering

In the scattering of neutrons by a nucleus, the neutron transfers some fraction of its kinetic energy to the nucleus and deviates toward a different direction with lower kinetic energy. If the energy lost by an incident neutron in a scattering event is transferred only to the kinetic energy of the nucleus, it is known as elastic scattering. However, if the energy lost by the incident neutron is partially transferred to the kinetic energy of the nucleus and other forms of energy such as heat and light, it is known as inelastic scattering.

Figure 1.3 shows the neutron elastic scattering cross-sections for selected isotopes with higher interaction probabilities. Comparing the elastic scattering cross-section (Figure 1.3) with the total cross-section (Figure 1.2), we can see that the elastic scattering dominates the neutron interaction, particularly above 0.1 MeV, and this property is used to thermalize fast neutrons in many applications. As neutrons scatter from multiple nuclei, they lose their energy progressively and come to thermal equilibrium with the system. The energy transferred to the recoil nucleus (E_R) in an elastic scattering event depends on the mass of the target nucleus and the scattering angle of the recoil nucleus, given as

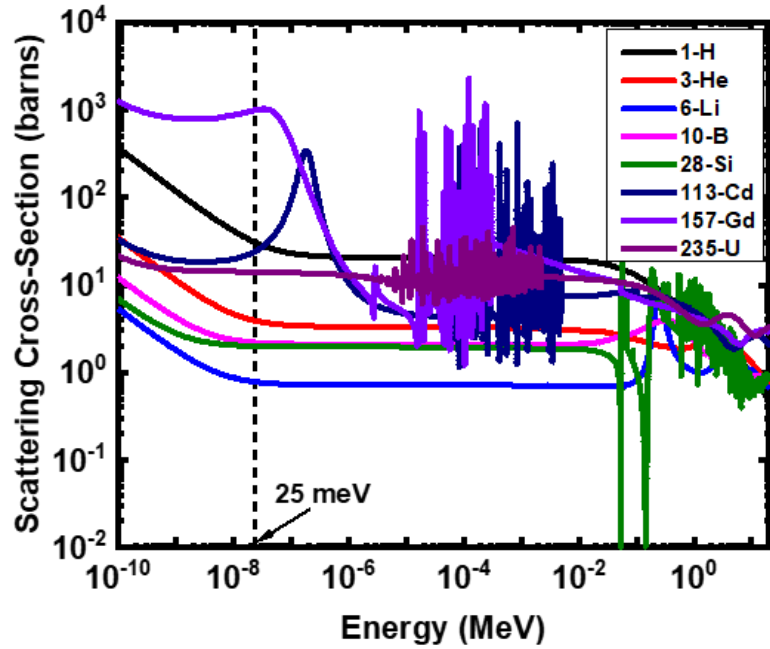


Figure 1.3. Neutron elastic scattering cross-sections of selected neutron-sensitive isotopes [96].

$$E_R = \frac{4A}{(1+A)^2} \cos^2 \theta E_n \quad (1.2)$$

where A is the ratio of the mass of the target nucleus to the mass of a neutron, E_n is the energy of the incident neutron, and θ is the scattering angle of the recoil nucleus, as shown in Figure 1.4.

Equation 1.2 tells us that the recoil nucleus can have a continuous range of energy from zero to the energy of the incident neutron in an elastic scattering event. The energy transfer will reach a maximum when the mass of the target nucleus becomes equal to that of a neutron ($A = 1$). Because hydrogen has an atomic mass equal to that

of a neutron, materials containing hydrogen are very efficient in slowing down fast neutrons.

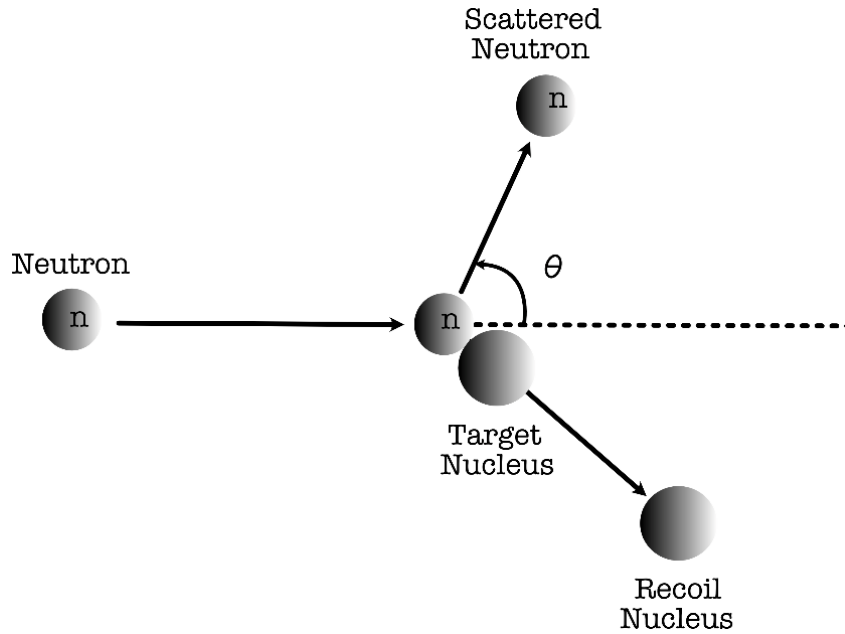


Figure 1.4 Elastic scattering of a neutron from the nucleus. The kinetic energy of the recoiled nucleus and the scattered neutron depends on the scattering angle θ .

When a fast neutron transfers enough energy to knock the positively charged nucleus off an atom in an elastic scattering event, the ejected nucleus (known as a recoil nucleus) can ionize and/or excite the medium via the Coulomb interaction with the electrons. This type of interaction, particularly with hydrogen, deuterium, and helium, has been used to detect fast neutrons [97]. In the case of hydrogen, the recoil nucleus is the positively charged proton, and the detectors that utilize the recoil proton are known as proton recoil detectors [97]. However, this type of interaction is not suitable for detecting slow neutrons because they do not have sufficient energy to transfer.

Inelastic scattering between a neutron and nucleus is possible if the energy of the neutron is high enough. In this case, the recoil nucleus gets excited into a higher energy state. The excited nucleus then decays quickly to a stable ground state, giving off a gamma photon. Similar to elastic scattering, inelastic scattering also helps in slowing down fast neutrons. However, the gamma photon emitted in inelastic scattering complicates fast neutron detection using recoil nuclei.

Besides its role in fast neutron detection utilizing recoil nuclei, scattering, in general, plays a vital role in many nuclear and neutron detection applications. In nuclear power plants, the energies of neutrons emitted from the fission of nuclear fuel such as ^{235}U and ^{240}Pu should be reduced to thermal energies before they can be reabsorbed to achieve a sustained chain reaction. The process of reducing neutron energy is known as moderation, which can be achieved by exploiting the high elastic scattering of neutrons by light nuclei. Because hydrogen and hydrogen-containing materials are the most efficient neutron moderators, more than 75% of the world's nuclear power plants use regular water (H_2O) as the neutron moderator [98]. Similarly, for neutron detection, when neutrons are slowed down sufficiently to thermal energies by using moderators, the probability of their absorption increases significantly. The absorption of these slow neutrons (also known as thermal neutrons) by atomic nuclei results in the subsequent emission of secondary radiation. Neutron detection using this secondary radiation is the most common method among all available techniques.

Neutron Absorption

The absorption of neutrons by a nucleus can happen in any range of neutron energy. For most of the neutron-sensitive elements, neutron absorption is the dominant mechanism of neutron interaction at lower energies. In some materials, the absorption of a neutron requires additional energy. For example, in silicon, a widely used semiconductor material, absorption of a neutron requires at least 2.66 MeV of energy [99]. Therefore, only fast neutrons with energy higher than the threshold energy can be absorbed by this element. Regardless of the energetics of the absorption process, a nucleus always becomes unstable immediately after neutron absorption. The unstable nucleus then undergoes many types of nuclear reactions, and in all cases, emits one or more types of secondary radiation. Based on the resulting radiation and the final nuclei, four main types of neutron absorption reactions are defined:

Radiative Capture

A target nucleus absorbs an incident neutron in radiative capture and gets excited to a higher nuclear energy state. The unstable nucleus then immediately de-excites to its ground state energy by emitting a gamma photon. As the nucleus has acquired one more neutron, it is then transmuted to a different stable isotope of the same element. The reaction is denoted as



One type of neutron detector that uses this gamma activation mechanism is the activation detector [97]. Here, a material with a high radiative capture cross-section is

placed in a neutron field for a certain time to activate the nuclei. The presence of neutrons is then determined by measuring the induced radioactivity (gamma photons) from the material. However, because the radiative capture cross-section is generally high only for thermal neutron energies, this method does not apply to fast neutrons. These detectors are not suitable for real-time neutron detection due to the long time required for activation.

Neutron Multiplication

In neutron multiplication, neutron absorption by a nucleus results in more than one fast neutron emission. Because fast neutrons are already difficult to detect, this reaction is not particularly helpful in neutron detection.

Charged Particle Emission

The absorption of a neutron by lighter nuclei results in the emission of charged particles such as electrons, protons, and alpha particles, along with a positively charged energetic residual nucleus. The energetic nucleus and the emitted charged particle both ionize the medium, exciting the charge carriers that can be detected. Because charged particle emission is the dominant mechanism of neutron absorption in the low neutron energy spectrum, it is the most widely used neutron transduction method in the most efficient thermal neutron detectors.

Induced Fission

Some heavy radioactive nuclei, such as the isotopes of uranium and plutonium, can break into two fragment nuclei when they absorb neutrons, commonly known as nuclear fission. A nuclear fission event releases a large amount of energy (≈ 200 MeV) and emits gamma photons and energetic neutrons. This large amount of released energy makes these heavy elements attractive for neutron detector materials. However, the increasing radioactivity of heavy nuclei with detector thickness leads to a tradeoff between electrical noise and neutron detection efficiency. The only heavy isotope considered for this type of neutron detection to date is ^{238}U . However, due to its small thermal neutron absorption cross-section, direct-conversion neutron detectors based on ^{238}U -containing materials are suitable only for fast neutron detection.

1.2.2. Neutron Detection

The detection of neutrons can, in principle, be achieved either by using their intrinsic properties such as linear momentum, suggested electrical dipole moment, and spin magnetic moment, or by using the primary reaction products of neutron–matter interactions as described by Equation (1.1). The direct detection of neutrons using their intrinsic properties is impractical for general applications, even with the state-of-the-art measurement techniques available today [21]. Of the possible primary reaction products described in Equation (1.1), neutrinos are even more challenging to detect than neutrons [100], [101]. The recoil neutral atoms knocked off by the incident neutrons have minimal momentum to produce a detectable mechanical force. Thus, only the high-

energy electrons, recoil protons, gamma rays, and light and heavy charged nuclei are suitable reaction products for neutron detection. These primary reaction products interact with and ionize the detector medium, exciting free/mobile charge carriers (electrons, holes, and ions) either directly or via some higher-order interaction processes. Neutron detection is then possible by detecting these excited charge carriers.

In most cases, neutron detection is an indirect process in which the energy and momentum information of the incident neutron is lost. The amount of excitation energy does not depend on the incident neutron energy but rather on the nuclear reaction mode following neutron absorption. Thus, in most cases, a single neutron detector cannot differentiate between high- and low-energy neutrons. However, because the neutron interaction cross-section in a material strongly depends on the incident neutron energy, different neutron detectors are sensitive to different incident neutron energies. Thus, we can crudely divide neutron detectors into two categories based on their neutron-energy-sensitivity: fast neutron detectors and thermal (slow) neutron detectors. As the neutron interaction cross-section of many materials is high for the lower energy spectrum, detectors for neutrons with energies lower than 0.5 eV (commonly known as the cadmium cutoff energy) are the most widely studied. With designs to incorporate hydrogenous materials to slow down neutrons, thermal neutron detectors can also be used to detect fast neutrons [102], [103].

1.2.3. Solid-State (Semiconductor) Neutron Detectors

The use of semiconductors in radiation detection began in 1949 with the successful detection of alpha particles by a germanium point-contact diode [104]. As advanced fabrication techniques became available, semiconductor detectors succeeded in leaving their classical counterparts (the gas-filled detectors) far behind due to their compact form factor, efficiency, portability, and adaptability to complex applications. Solid-state detectors, now, are at the base of most radiation detection applications ranging from everyday activities (photography, remote controlling) to medicine (X-ray imaging, radiation dosimetry, radiation therapy), to security (X-ray scanning, portal monitoring), to advanced material research (electron microscopy, X-ray, and electron diffraction). However, *semiconductor neutron detectors*, despite being studied for as long as other semiconductor radiation detectors [105], still remain immature due primarily to the limited availability of solid materials with significant neutron interaction probability.

Neutrons do not interact with the electrons and holes within a semiconductor directly. Thus, their detection relies on the energy released in neutron–nucleus interactions, which excites electron–hole pairs. Based on the neutron transduction process, semiconductor neutron detectors are classified into indirect-conversion and direct-conversion detectors.

1.2.3.1. Indirect-Conversion Semiconductor Neutron Detectors

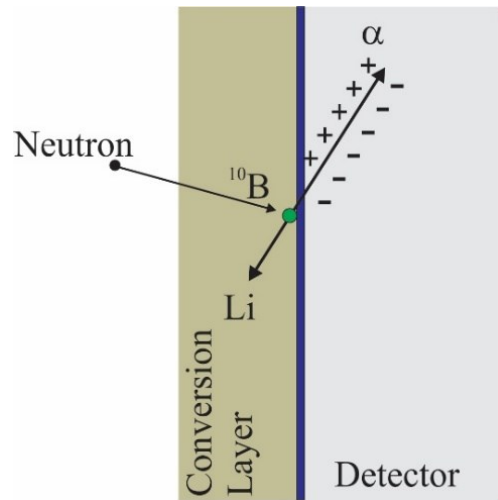


Figure 1.5. A ^{10}B -based planar indirect-conversion semiconductor neutron detector. Here, a conversion layer absorbs the incident neutron and emits primary reaction products (α particle and Li ion). Only one of the reaction products enters the semiconductor and excites electron-hole pairs.

Figure 1.5. shows a simple planar indirect-conversion semiconductor neutron detector. This can be considered the most straightforward approach to solid-state neutron detection because it utilizes an already developed high-efficiency charged particle detector, with a conversion layer composed of neutron-sensitive elements such as ^{10}B , ^6Li , and ^{157}Gd deposited on the detector surface. The conversion layer absorbs an incident neutron and emits primary reaction products. For thermal neutrons with an energy of ~ 25 meV, the linear momentum is negligibly small. The primary reaction product pairs are always emitted in random but opposite directions in all possible 4π

solid angles. One of the reaction products has a certain probability of entering the detector volume, whereas the other reaction product escapes outside the detector. The primary reaction product that enters the detector volume excites electron–hole pairs. An applied or self-established electric field in the detector then extracts the charge carriers, constituting a signal current.

As the reaction products themselves need to cross the neutron conversion layer before reaching the semiconductor detector, a significant fraction of their kinetic energy dissipates in the conversion layer. Because the primary reaction products have short mean diffusion lengths (on the order of a few microns) [97], a thick conversion layer severely affects neutron detection efficiency. Although detection efficiency as high as 22% has been reported for a-SiH detectors coated with a ^{157}Gd conversion layer [106], such devices have not been considered for widespread implementation because of their poor gamma discrimination in mixed radiation environments. Conversion layers composed of ^{10}B and ^6Li show significant gamma rejection; however, the maximum theoretical efficiency of simple planar detectors based on these isotopes is 5%, with experimentally achieved efficiency not exceeding 4% [107], [108].

Indirect-conversion neutron detectors, however, can also be designed with complex geometries and microstructures, such as narrow trenches and pillars filled with neutron conversion materials, such that both of the reaction products can be used [107], [109]–[114]. These detectors are now commonly known as microstructured semiconductor neutron detectors (MSNDs), and a detailed simulation study of different

geometries for these detectors suggests a maximum theoretical efficiency of about 90% [115]. However, the experimental detection efficiency of state-of-the-art commercially available MSNDs manufactured by Radiation Detection Technologies (RDT) is 30% [116]. Although MSNDs have shown some superiorities over gas-filled detectors, their implementation in increasing neutron detection applications is limited. Some factors that limit their widespread implementation are their complex and expensive fabrication processes [113], limited operating temperature [116], limited spatial resolution [116], higher sensitivity to radiation damage [117], [118], and poor area scalability due to their crystalline nature.

1.2.3.2. Direct-Conversion Solid-State Neutron Detectors

Figure 1.6 shows a simple schematic of a direct-conversion solid-state neutron detector. The detector consists of a neutron-sensitive semiconductor material sandwiched between two electrodes in a simple planar geometry. The detector absorbs incident neutrons within itself, resulting in the emission of primary reaction products. The probability that both primary reaction products deposit energy within the detector volume increases with detector thickness, enabling thick direct-conversion neutron detectors to have nearly 100% neutron absorption and detection efficiency [21]. The simple planar geometry of direct-conversion detectors also significantly reduces the complexities of pixelated detector fabrication. Thus, direct-conversion neutron detectors can provide all of the requirements for neutron detection applications, yet with the most straightforward and low-cost fabrication techniques.

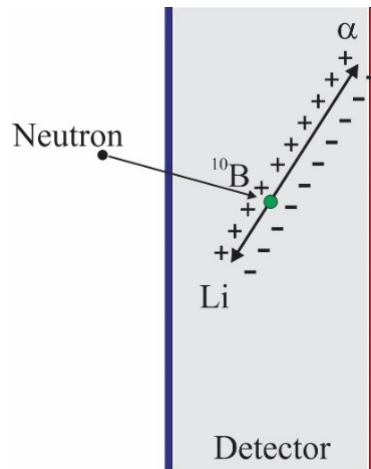


Figure 1.6. A direct-conversion semiconductor neutron detector. Here, the semiconductor material itself absorbs the incident neutron and emits primary reaction products. Both of the reaction products excite electron-hole pairs inside the detector.

Of the few semiconductor materials with neutron-sensitive isotopes (${}^6\text{Li}$, ${}^{10}\text{B}$, ${}^{28}\text{Si}$, ${}^{157}\text{Gd}$, ${}^{235}\text{U}$), only ${}^{10}\text{B}$, ${}^6\text{Li}$, and ${}^{235}\text{U}$ containing semiconductors have been considered for direct-conversion solid-state thermal neutron detectors. Interaction of thermal neutrons with ${}^{157}\text{Gd}$ results in high energy γ -photons, which are already difficult to detect and render a poor γ rejection, whereas ${}^{28}\text{Si}$ needs additional energy of 2.66 MeV for thermal neutrons to be absorbed [99]. Despite their tremendous applications and potential, direct-conversion neutron detectors, however, have not evolved beyond a few prototype detectors based on 2-D crystalline materials containing boron or lithium [50], [119], [120]. The reported neutron detection efficiencies of these prototype detectors are still lower than those of traditional ${}^3\text{He}$ -based tube detectors. However, with dedicated efforts to find suitable materials and understand their relevant properties

needed for neutron detection applications, achieving highly efficient direct conversion neutron detectors should be possible.

1.3. Amorphous Hydrogenated Boron Carbide (a-BC:H) for Direct-Conversion Thermal Neutron Detection: A Brief History

Amorphous semiconductor materials have shown tremendous success in the semiconductor industry since amorphous silicon¹ was successfully implemented in solar cells in the 1970s [121]–[123] by exploiting its greater flexibility in device fabrication. Study of amorphous boron carbide began in the late 1970s [124]–[127] for potential applications in inner wall coatings in fusion reactors and semiconductor thermoelectric generators. However, studies of amorphous hydrogenated boron carbide as a semiconductor material for diode and thin-film transistor applications appeared only after 1990 [77], [85], [128]. Lee et al. [77] demonstrated that amorphous hydrogenated boron carbide (a-BC:H) thin-films with resistivity as high as 10^{10} $\Omega\cdot\text{cm}$ and tunable optical properties could be fabricated by a PECVD process using various carborane

¹ Amorphous silicon (a-Si) thin films are generally poor for semiconducting purposes because of their high defect density. In 1969 Chittik, Alexander, and Sterling successfully fabricated hydrogenated amorphous silicon (a-Si:H) and Spear 1975 successfully demonstrated doping using phosphine and diborane respectively for n-type and p-type a-Si:H, thus opening the gate for amorphous silicon to the semiconductor world.

precursors. Their important findings were that increasing B/C ratio by increasing precursor partial pressure (B_5H_9 / CH_4) increased the optical bandgap almost linearly from 0.77 eV to 1.77 eV within a B/C ratio range of 2.4 to 50, whereas the electrical conductivity remained unaffected within a B/C ratio range of 4.7–19. Based on the high resistivity and bandgap of the deposited films, they hypothesized and demonstrated a PN heterojunction diode by depositing a-BC:H on n-type silicon. However, the absence of exponentially increasing forward current suggests that the device could be a simple metal–insulator–semiconductor diode with a-BC:H working simply as an insulating barrier. Similar diode characteristics of a-BC:H films deposited on p-type silicon have frequently been observed [129].

For nearly a decade following 1990, many studies on PECVD-grown a-BC:H were published, primarily focusing on structural characterization [82], [130]–[132], and diode (heterojunction and homojunction) and field-effect transistor fabrication [81], [83], [85], [86], [133]–[135]. Very few studies tried to study the charge transport properties in these films [133], [135]–[137]. Most of these studies agreed that the electrical conductivity in PECVD-grown a-BC:H was thermally activated, unlike the previously studied boron-doped amorphous carbon films in which the charge transport was considered to be through variable range hopping [124]–[127].

The depleting availability of ^3He after 2001 and increased demand for high-resolution neutron detectors for advanced scientific applications increased the interest in semiconductor neutron detectors. Because of its high thermal neutron absorption

cross-section and wide tunability of material properties, a-BC:H immediately received attention as one of the most promising candidate materials for solid-state neutron detection. A significant number of studies on PECVD-grown a-BC:H thin films targeted for thermal neutron detection applications were reported in the first decade of the 2000s [60], [61], [64], [65], [68], [69], [71], [88], [92], [138]–[145]. Within 2002–2006, three different types of prototype a-BC:H neutron detectors were reported: PN heterojunction diode (a-BC:H/n-Si) thermal neutron detectors [60], [65], [88], an all-boron carbide metal–insulator–metal detector [92], and an all-boron carbide PN junction detector [139]. All of the working prototype devices were fabricated using *ortho*- and/or *meta*-carborane precursors, which are believed to produce high-resistivity a-BC:H films compared to other deposition methods using individual boron and carbon precursors [146]–[148]. Although the Si/BC heterojunction detectors could detect neutrons, the results were controversial. The pulse height spectra were suggestive of an indirect-conversion detector with a-BC:H acting only as a conversion layer [60], [65], [88]. Most of the all-boron carbide devices were poor in pulse height resolution except in one report [61], which hints towards direct-conversion detection. Among these studies, those reporting working prototype detectors were mostly confined to device performance, whereas the remaining ones focused mainly on the physical and electronic structures of the material. These studies did not sufficiently investigate the charge transport properties of the detector materials. Although extraction of charge carriers is possible even with poor carrier mobility and lifetime in very thin films, such as those used in

these prototype detectors, understanding and optimizing these properties is necessary to scale the neutron detection efficiency with increasing detector thickness. However, studies on these charge transport metrics were almost non-existent.

Studies focusing on the material properties of a-BC:H, particularly motivated towards optimizing charge transport, appeared only during the last decade. Some of these studies have reported preliminary results of enhancing the carrier lifetime in these films in a controversially wide range (35 μ s –2.5 ms) [63], [70], [149]–[151] by doping the films with aromatic compounds such as benzene and pyridine. Studies of the metal-to-a-BC:H interfaces were covered by Driver, et al. [152] and James, et al. [153], the knowledge of which is crucial in forming appropriate metal contacts (Schottky, Ohmic) in device fabrication. Some publications by Nordell, et al. [93], [94], [154] and Paquette, et al. [155] present a comprehensive study of the mechanical, electrical, electronic, and optical properties of PECVD-grown amorphous hydrogenated thin films in relation to the film fabrication parameters such as substrate temperature, precursor flow rate, RF power, and process pressure. Many material properties such as bandgap, resistivity, carrier mobility, and carrier concentration were found to correlate with the hydrogen concentration and the B/C ratio. Among the significant findings of these studies, those critical for neutron detections are the ability to produce films with resistivity as high as 10^{14} $\Omega\cdot\text{cm}$, bandgap in a range of 1.6 to 4.0 eV, and carrier mobility as high as 10^{-9} $\text{cm}^2\cdot\text{V}^{-1}\cdot\text{s}^{-1}$ by varying the PECVD process parameters.

Although a significant amount of effort has been put forth to understand a-BC:H for its potential applications in neutron detection in the last three decades, the charge transport metrics, particularly the carrier mobility and carrier lifetime are not optimized enough to fabricate thicker detectors. However, recent progress on understanding a-BC:H film properties and their tunability as a function of PECVD process parameters is encouraging enough to move forward for optimizing and fabricating 5–10 μm thick films to achieve detection efficiency comparable to those obtained with contemporary techniques.

1.4. Scope of Dissertation

Understanding the charge transport properties in a-BC:H thin-films, their dependence on device fabrication conditions, and their role in charge extraction is critical towards achieving a high-efficiency neutron detector. A sufficiently thick detector is another requirement for high efficiency. In this study, we used different approaches to fabricate thin-films of a-BC:H to study and optimize their charge transport properties, fabricate stable a-BC:H thin-films with thickness exceeding 5 μm , and fabricate thick films with optimized charge transport properties, particularly the resistivity, mobility, carrier lifetime, and mobility–lifetime product.

In Chapter 2, we describe the experimental methodology for a-BC:H device fabrication including contact deposition, and their characterization using different techniques. We describe ellipsometry and UV-Visible spectrometry for optical characterization, current–voltage and capacitance–voltage measurement for electrical

characterization including resistivity and carrier mobility, steady-state and transient photoconductivity measurements for carrier lifetime and mobility–lifetime product extraction, and wafer bow method for film stress measurement.

Chapter 3 describes a numerical simulation study for the performance of a thin-film direct-conversion neutron detector, assuming single carrier transport, which is believed to be the case for a-BC:H films. Using a combination of wide ranges of charge transport metrics, such as carrier mobility, carrier lifetime, and electric field in the numerical calculation, we discuss the effect of single carrier transport in neutron detection and spectral performance of such a detector.

In Chapter 4, we present an extension to the theory of space-charge-limited current with field-dependent mobility to include negative electric field dependence, which is notably observed in disordered materials. Similarly, in Chapter 5, we discuss different approaches to extract the charge carrier mobility using the space-charge-limited current analysis when the current–voltage characteristics are potentially affected by other charge transport phenomena. We also discuss a theory to check the self-consistency of the extracted charge carrier mobility using space-charge-limited current analysis in the presence of Poole–Frenkel emission and/or field-dependent mobility.

Chapter 6 presents and discusses the results obtained from our thin-film deposition and characterization experiments. It covers a story of our efforts to optimize film thickness and charge transport properties in a-BC:H films. Chapter 7 summarizes our body of work and recommends future studies.

CHAPTER 2

DEVICE FABRICATION AND CHARACTERIZATION: THEORY AND EXPERIMENTS

2.1. Device Fabrication

Fabrication of a-BC:H devices for testing includes substrate preparation and cleaning, thin-film deposition, electrical contact deposition, and device wiring. The a-BC:H devices were grown with plasma-enhanced chemical vapor deposition (PECVD) using *ortho*-carborane ($C_2B_{10}H_{12}$) on specific substrates for different purposes. We will describe the PECVD chamber and briefly explain the steps involved in device fabrication in the following sections.

2.1.1. PECVD Chamber

A schematic of our custom-built plasma-enhanced chemical vapor deposition (PECVD) chamber with the capability of in-situ sample transfer to a magnetron sputtering system is shown in Figure 2.1. The deposition chamber consists of an SHQ400 series inverted substrate heater designed by AJA International, which houses two DC-powered halogen heating lamps controlled by a PTB SHQ-15A Precision PID controller in a water-cooled aluminum box. The cooling water line is connected to a Neslab HX300 liquid-cooled chiller outside the deposition chamber. A long vertical rotating arm, which also acts as a feed-through for an RF power supply, passes through the heating box and is connected to a stepper motor using an insulating coupler at its top

end outside the vacuum chamber. Its bottom end holds a downward-facing 12 cm diameter circular substrate holder with a lock-in mechanism below the heating box, which has a 12 cm diameter coaxial quartz window through which the heating lamps heat the substrate holder radiatively up to 600 °C.

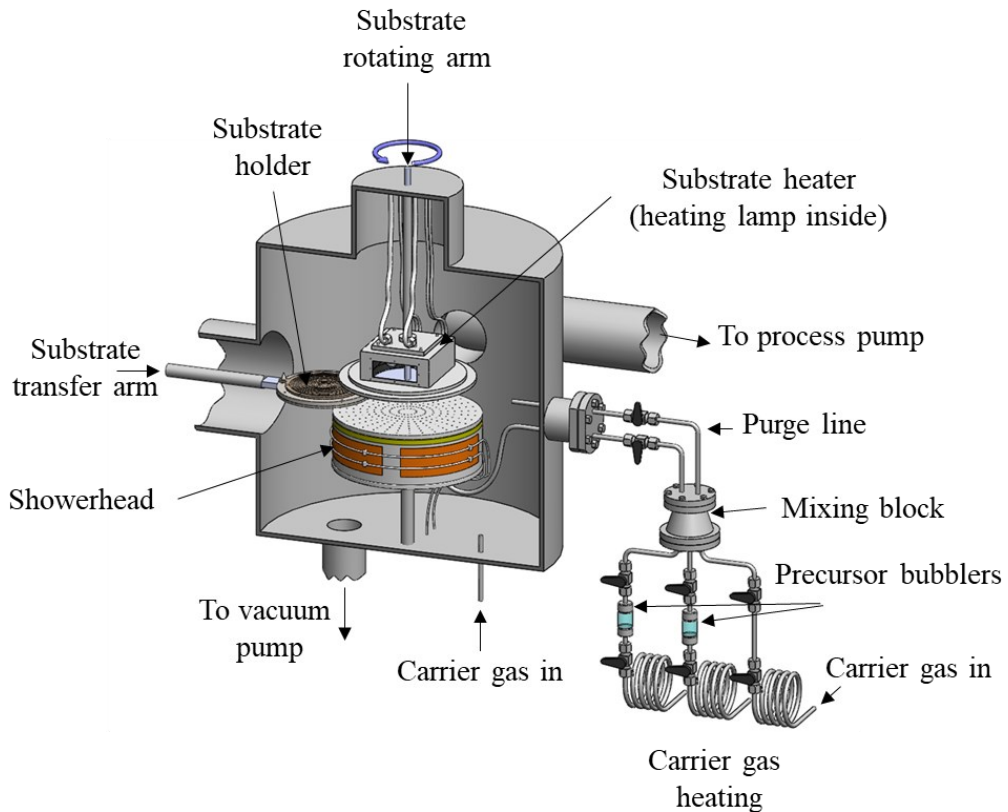


Figure 2.1 A schematic of the PECVD chamber. The substrate holder is attached under the substrate heater with a rotating arm.

The substrate holder can hold a single substrate with a diameter of up to 100 mm. It can alternatively hold eight 15 × 15 mm square substrates and one 30 × 30 mm

square substrate, using a custom designed substrate holder, as shown in Figure 2.2, so that a batch of up to nine devices can be deposited at once.

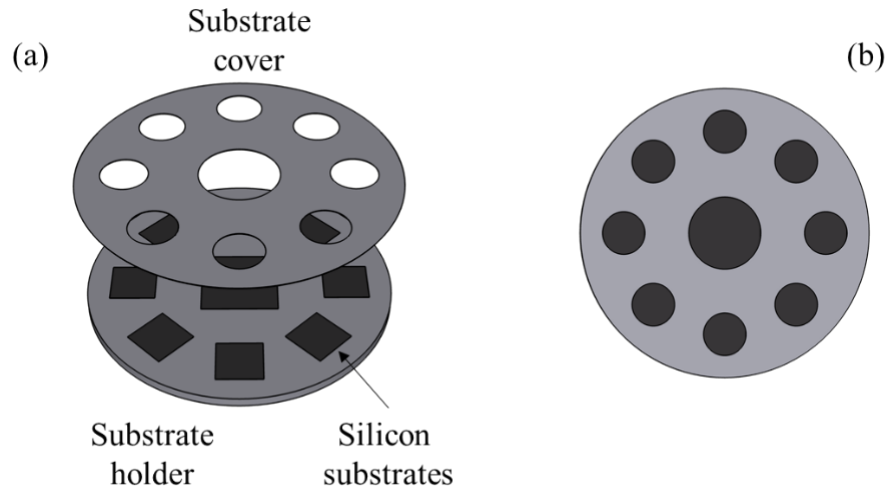


Figure 2.2 (a) A substrate holder with cleaned silicon substrates, and (b) after securing the substrates with a substrate cover.

A custom-built 10-inch diameter showerhead is located coaxially below the substrate holder. The substrate holder and the showerhead act as capacitor electrodes to which RF power of a standard frequency of 13.56 MHz is fed in through a MW-5 automatic impedance matching network. The substrate holder can be raised or lowered to change its distance from the showerhead. To inhibit precursor condensation, the showerhead is heated to 100–150 °C using a heating tape with a DC-powered source so that it does not interfere with the RF plasma. The showerhead is connected to a precursor delivery system outside the PECVD chamber.

The precursor delivery system consists of a precursor mixing block connected to two heated solid-state precursor bubblers filled with *ortho*-carborane, whose inlets are connected to an MKS mass flow controller (MFC1). The mixing block is also connected directly to another MKS mass flow controller (MFC2). The inputs of both MFC1 and MFC2 are connected to a carrier gas source through a Restek O₂ and H₂O filter. The precursor partial flow (precursor partial pressure) inside the PECVD chamber is controlled by regulating the carrier gas flow through MFC1 and MFC2 and/or changing the temperatures of the bubblers. A purge line connects the mixing block directly to the deposition chamber, and another line carries the precursor mixture to the showerhead. The mixing block, solid-state bubblers, and all carrier gas lines are heated independently using precision PID controllers, and the temperatures are maintained in increasing order from the mass flow controllers to the showerhead.

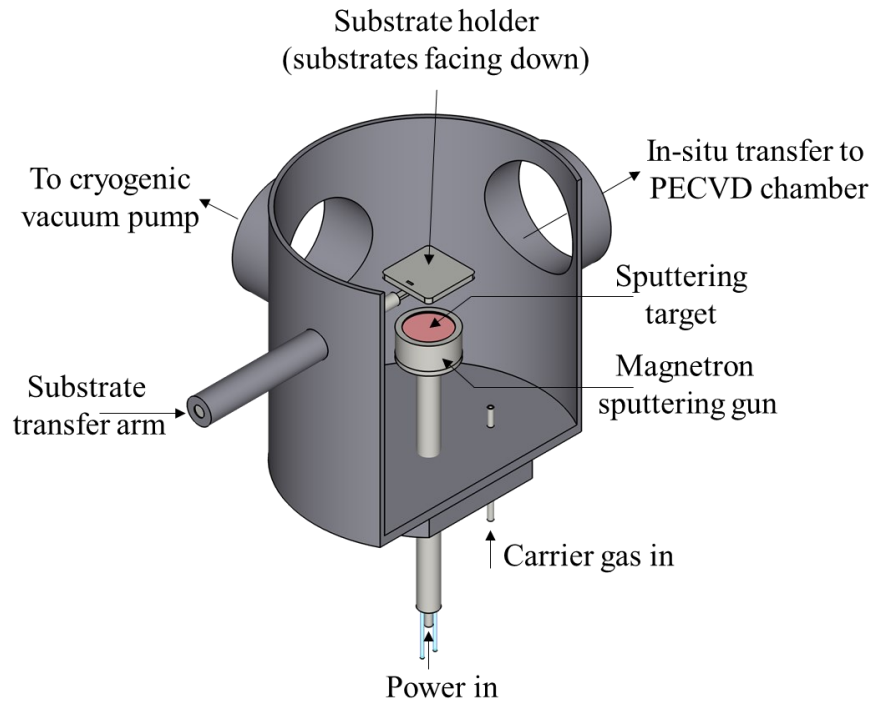


Figure 2.3. A schematic of the sputtering deposition system.

A schematic of the magnetron sputtering chamber, which also works as a load-lock chamber, is shown in Figure 2.3. The magnetron sputtering chamber is connected to the PECVD chamber through an 8-inch VAT gate valve (G1). The sputtering chamber includes two 3-inch sputtering guns, and one 2-inch sputtering gun. A variety of metal targets, including magnetic targets such as nickel, can be sputtered using both DC magnetron drive and RF power. A custom-built transfer arm is attached to the system and can transfer the substrate holder from the load-lock chamber to the deposition chamber and vice versa, for PECVD and magnetron sputtering deposition. A carrier gas line is connected to the mass flow controller MFC1 using a valve and a T connector so

that the carrier gas can be flowed to the PECVD chamber or the sputtering chamber as required.

For pumping down the PECVD and sputtering deposition chamber, a CTI CT-8F cryopump is connected to the load-lock/sputtering chamber through an 8-inch VAT gate valve (G2), which pumps down the load-lock/sputtering chamber to lower than 10^{-7} Torr, and also pumps down the PECVD chamber when the gate valve G1 is opened. The PECVD chamber is also connected to a roughing pump through a manual throttle valve and an Edwards iQDP80 dry pump through a 4-inch gate valve (G3). The dry pump works as a process pump, maintaining a process pressure of 0.1–2.0 Torr during PECVD growth with the help of an MKS type 653B throttle Valve controlled by an MKS type 127 Baratron pressure transducer.

2.1.2. Substrate Temperature Calibration

As the substrate rotates to maintain substrate temperature and film deposition uniformity, the substrate temperature is obtained indirectly by measuring the temperature of a metallic tube resting on a quartz window between the halogen lamps and the substrate holder, using a K-type thermocouple (T1) as shown in Figure 2.4.

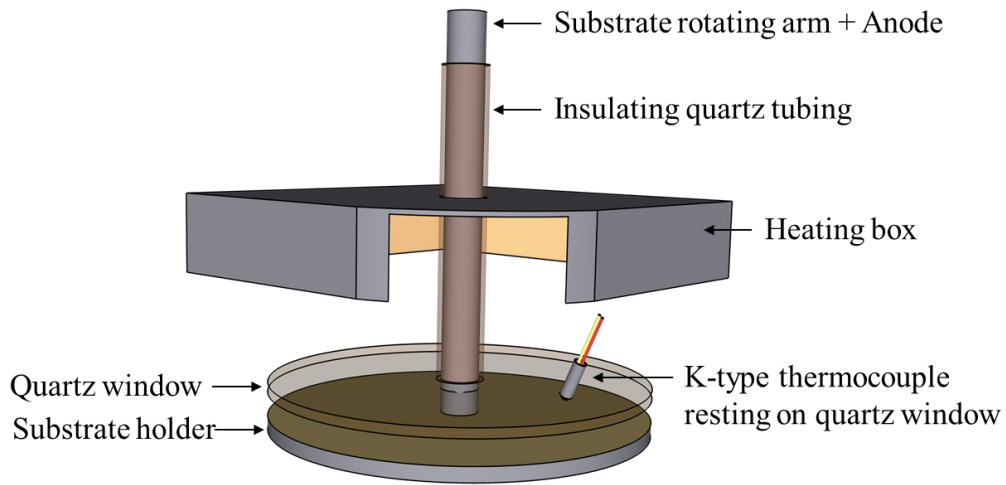


Figure 2.4. A schematic of the substrate heating system with a K-type thermocouple resting on quartz window.

Because the thermocouple does not measure the actual temperature of the substrate holder and the substrates, the actual substrate temperature must be calibrated to the temperature reading from the thermocouple. For the substrate temperature calibration, another K-type thermocouple (T2) is attached on the bottom face of the substrate holder. The PECVD chamber is then pumped down to a base pressure and the substrate heater is turned on. The substrate holder is then heated to a set temperature using the PID controller, with the feedback temperature measured by T1. During heating, the actual substrate temperature measured by T2 is recorded by a digital readout. The process is repeated for different set temperatures to cover the actual substrate temperature range from room temperature to $>500\text{ }^{\circ}\text{C}$. After recording the temperature data, a graph of actual substrate temperature against the temperature values is plotted, which is then used to find a set temperature value required for a desired

substrate temperature. It should be noted that the temperature calibration is performed without substrate rotation and plasma, which could introduce some error in the actual substrate temperature. An example of measured substrate temperature over time for different set temperature values is shown in Figure 2.5.

2.1.3. Precursor Bubbler

A schematic of a solid-state precursor bubbler is shown in Figure 2.6. The bubbler consists of a glass tube filled with glass beads in the bottom half. Precursor powder is loaded into the top half, which is separated from the bottom half by a screen. The glass beads help in dispersing the incoming carrier gas to maintain a more uniform sublimation of the precursor powder. Both ends of the bubbler are fitted with quick flange gaskets with screens so as to stop the flow of solid powder into the carrier lines. The precursor bubblers are wrapped in heating jackets and are further wrapped by aluminum foil to maintain uniform heating. The bubbler temperature is measured with a K-type thermocouple fixed on the glass surface of the bubbler.

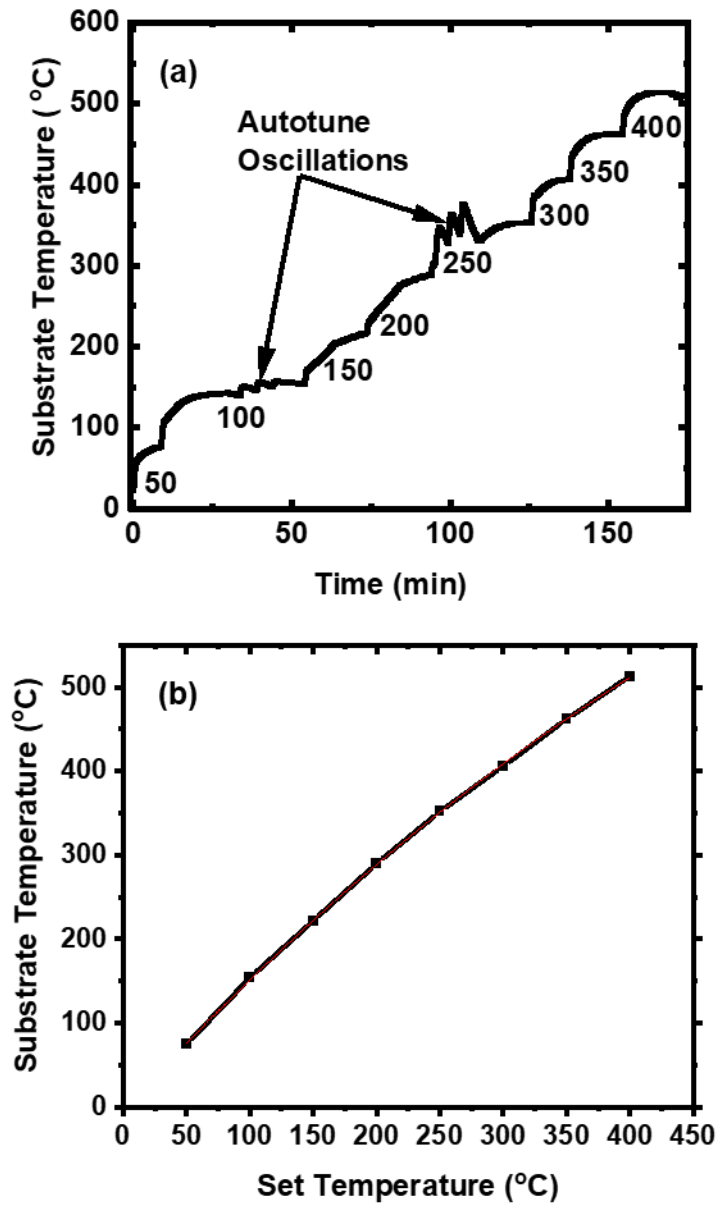


Figure 2.5. a) Actual substrate temperature recorded over time for different set temperature values (the numbers below the curve are set temperatures in °C), and b) a graph of substrate temperature as a function of set temperature values.

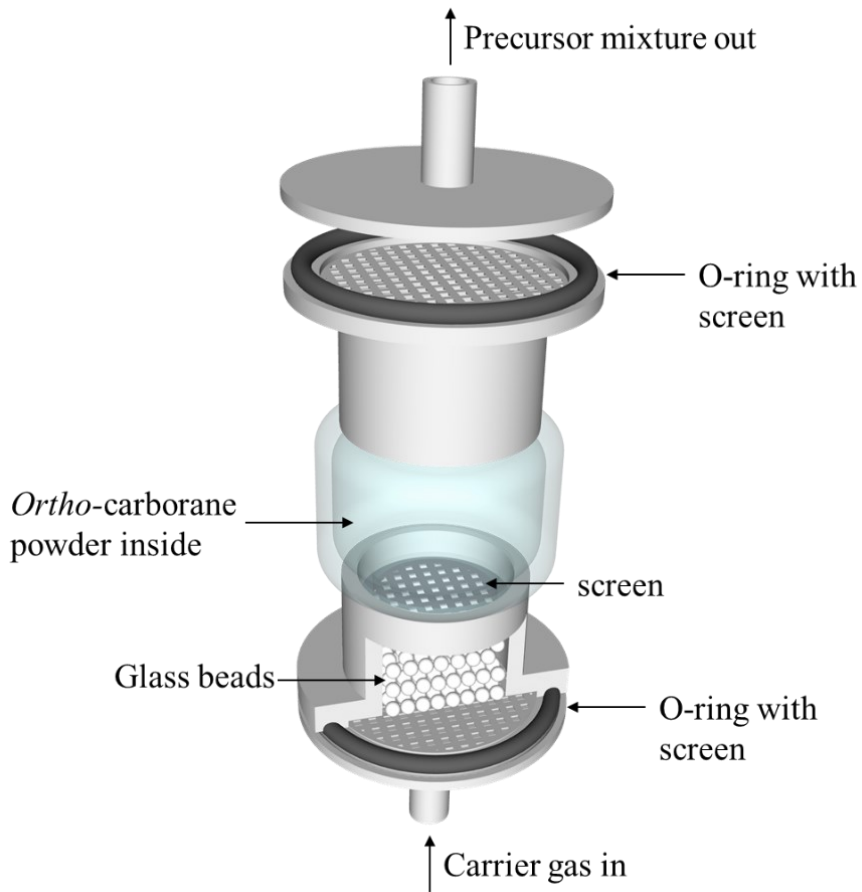


Figure 2.6. A schematic of the solid-state precursor bubbler.

2.1.4. Substrate Preparation

2.1.4.1. Substrate Materials

Low resistivity (1–15 $\Omega\cdot\text{cm}$), 30 cm diameter p-type silicon wafers were acquired from Intel corporation and were diced along the $\langle 110 \rangle$ and $\langle \bar{1}10 \rangle$ planes to make 15×15 mm and 30×30 mm square substrates. Low resistivity (1–15 $\Omega\cdot\text{cm}$), 10

cm diameter p-type silicon wafers were additionally purchased from UniversityWafer Inc. Rectangular glass slides were purchased from AmScope and cut into 15×15 mm substrates. Indium tin oxide (ITO) and fluorinated indium tin oxide (FTO) coated glass substrates of sheet resistance less than 10Ω per square were purchased from Solaronix and were cut into 15×15 mm wafers. Aluminum foil of thickness $20 \mu\text{m}$ was purchased from MTI corporation. Polycrystalline tungsten and zirconium foil with surface roughness less than 10 nm were purchased from MTI corporation and cut into 15×15 mm pieces.

2.1.4.2. Substrate Cleaning

Silicon and glass substrates were first cleaned with cleanroom-grade isopropanol and acetone in an ultrasonic bath for 10 minutes each to remove organic impurities as well as solid particles. The substrates were then dried with 99.999% pure nitrogen and transferred to a piranha solution (3:1 mixture of concentrated H_2SO_4 and 30% H_2O_2) in a beaker placed on a hot plate maintained at a temperature of $100 \text{ }^\circ\text{C}$ to remove organic as well as metallic impurities. The piranha solution was stirred continuously using a magnetic stirrer for 20 minutes during the cleaning process. After piranha cleaning, the substrates were rinsed three times with distilled water and then immersed in distilled water in a beaker. The immersed substrates were then removed and dried using the standard Marangoni drying procedure [156] in which substrates are slowly from the water while a gentle flow of nitrogen with a trace amount of isopropanol vapor is passed along the water surface to avoid the formation of water droplets. The cleaned substrates

are then transferred to the substrate holders. The transparent conducting substrates (FTO and ITO) and thick metal substrates (zirconium, tungsten, and copper) were also cleaned using the method described above, but without the piranha step. Thinner aluminum foils were used as is, and dust particles were blown off with nitrogen gas.

2.1.5. Film Growth

2.1.5.1. Precursor Preparation

Ortho-carborane ($C_2B_{10}H_{12}$) was purchased as a white powder from Sigma Aldrich, Inc. and Twelfth Vertex LLC. The precursor powder was purified in a cold-finger apparatus using vacuum sublimation under a nitrogen environment at <30 mTorr by heating the precursor at 75 °C. The sublimed *ortho*-carborane was then transferred to a nitrogen-filled glove box with oxygen levels maintained below one ppm. The purified *ortho*-carborane was crushed into powder inside the glove box in a ceramic mortar. Two solid-state precursor bubblers were then filled with purified *ortho*-carborane powder. The inlet and outlet valves of the precursor bubblers are closed upon transfer to avoid contamination with air prior to connection to the precursor delivery system.

2.1.5.2. a-BC:H Film Deposition

The substrate holder containing cleaned substrates was transferred to the PECVD chamber and was secured to the substrate rotating arm below the substrate

heater. The rotation of the substrate holder was kept low, so that it did not affect the capacitively coupled RF plasma produced between the showerhead and the substrate holder. The showerhead was kept at 25 cm from the substrate holder. After transferring the substrates to the PECVD chamber, both PECVD and sputtering chambers were pumped down to below 10^{-7} Torr using the cryopump. After the PECVD chamber reached the target base pressure, the substrate heater was turned on and allowed to reach a desired growth temperature. The showerhead heating was also turned on and allowed to reach a temperature of 110 °C. Separately, the components outside the deposition chamber—the two solid-state precursor bubblers filled with purified solid *ortho*-carborane, the mixing block, and the carrier gas line from the mixing block to the showerhead—were heated to 75, 85, and 100 °C, respectively.

After all of the components reached the required temperatures, the gate valve G1 was closed to disconnect the sputtering chamber, which also disconnects the cryopump, from the PECVD chamber. The gate valve G3 was then opened to allow the process pump to pump down the PECVD chamber. A specified flow of BIP grade (99.9999 %) argon gas obtained from Airgas Co. was then allowed to enter the precursor bubblers through the mass flow controller MFC1. The hot mixture of the sublimed precursor and argon from the bubblers were then allowed to enter the mixing block, where it mixes again with hot argon gas directly from MFC2. The final precursor mixture was then allowed to enter the PECVD chamber through a valve below the showerhead via the heated gas line. A constant process pressure was maintained using

an MKS type 653B automated throttle valve between the gate valve G3 and the process pump. The precursor partial pressure was regulated by varying the carrier gas flow rates through MFC1 and MFC2. The 13.56 MHz RF source was then turned on and was fed to the substrate holder inside the PECVD chamber through the impedance matching network to ignite the plasma, which initiates film deposition. Once the film deposition was complete, the precursor flow was stopped, and the RF power was turned off. The gate valve G3 was closed to disconnect the process pump, and the gate valve G1 was opened to pump down the PECVD chamber with the cryopump. All of the heating systems, except the substrate heater, were then turned off.

2.1.5.3. Substrate Cooling

After film deposition, the substrates were generally cooled by allowing the PECVD chamber to cool naturally by turning the heating bulbs off and continuing the flow of chilled water through the substrate heating box. As the natural cooling resulted in rapid cooling at the beginning, we implemented a protocol, referred to as a ramp-down protocol (see Section 6.3.3.1), in which we did not turn the heating lamp off abruptly. Instead, we decreased the set temperature by 50 degrees every 20 minutes and allowed a longer cooling period, potentially reducing the thermal shock on the substrates. After the substrate temperature reached a temperature below 200 °C, the heating bulbs were then turned off to allow natural cooling to room temperature. Figure 2.7 compares the temperature–time profile during the cooling step using the two methods.

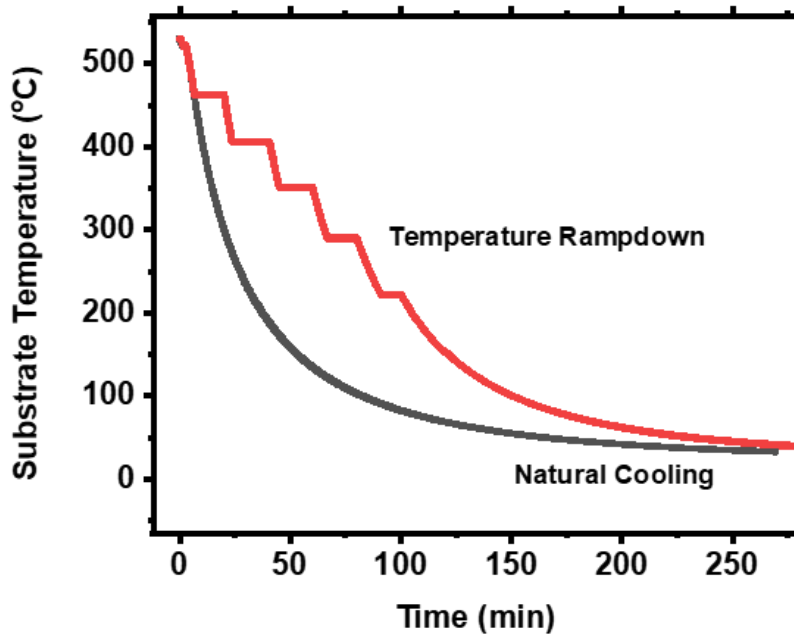


Figure 2.7. Cooling of substrates using two methods. Natural cooling resulted in a very rapid decrease in temperature at the beginning, potentially resulting in thermal shock in the films. Slow cooling was achieved using a ramp-down protocol.

2.1.6. Electrical Contact Deposition

2.1.6.1. Bottom Contact

For devices in a metal–insulator–metal geometry, the bottom contacts were deposited on the substrate before a-BC:H deposition. Two types of bottom contact were deposited, as shown in Figure 2.8. For full bottom contacts, the substrates were secured to the substrate holder with double-sided tape with the substrates facing down. For the key-hole bottom contacts, the substrates were secured to the substrate holder and covered with a key-hole mask.

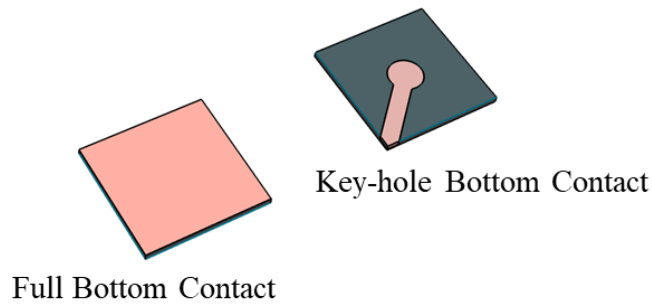


Figure 2.8. Types of bottom contact deposited on substrates.

For the sputter deposition of metal contacts, the substrate holder containing cleaned substrates was attached to the sample transfer arm and was transferred to the sputtering chamber. The PECVD and sputtering chambers were pumped down to a pressure of 10^{-7} Torr using the cryopump. After reaching the desired base pressure, the gate valve G1 was closed to disconnect the PECVD chamber from the sputtering chamber. A flow of 26 sccm of BIP grade argon gas was then allowed to enter the sputtering chamber through MFC2, and a process pressure of 25 mTorr was maintained by controlling the opening of gate valve G2. After stabilizing the process pressure, the magnetron drive power was slowly ramped up to 100 watts over 3 minutes. The sputtering was continued for at least 10 minutes to remove any surface contamination on the sputtering target. The substrate holder was then brought directly over the sputtering target and was maintained at a vertical distance of 10 cm. The sputtering deposition was then continued for a specific time to obtain the desired metal film thickness. After sputter deposition, the carrier gas flow was stopped, the magnetron

drive was turned off, and the gate valve G2 was fully opened to pump down the sputtering chamber.

2.1.6.2. Top Contact

After a-BC:H film deposition, the substrates were cooled down to room temperature. The substrate holder was then transferred to the sputtering chamber on top of a contact mask with 1/8-inch diameter circular contact holes, which could be closed with Kapton tape if required. The top contacts were then sputter deposited, as explained in Section 2.1.6.1.

2.1.7. Device Wiring

After thin-film deposition and electrical contact fabrication, the devices were immediately transferred to a nitrogen glove box. For electrical characterization, a metal-insulator-metal (MIM) device was placed on a fiber-glass board with the help of double-sided insulating tape. The top and bottom contacts were connected to copper pads on the fiber-glass board by thin gold wires using silver paint, as shown in Figure 2.9. The whole device was then placed inside a custom-designed air-tight, thick aluminum Faraday cage with a 1/8-inch circular quartz window on its backside, as shown in Figure 2.10. The quartz window was used to illuminate the device for photoconductivity experiments. The Faraday cage was either pumped down or filled with 99.999% pure nitrogen gas to maintain an inert environment inside.

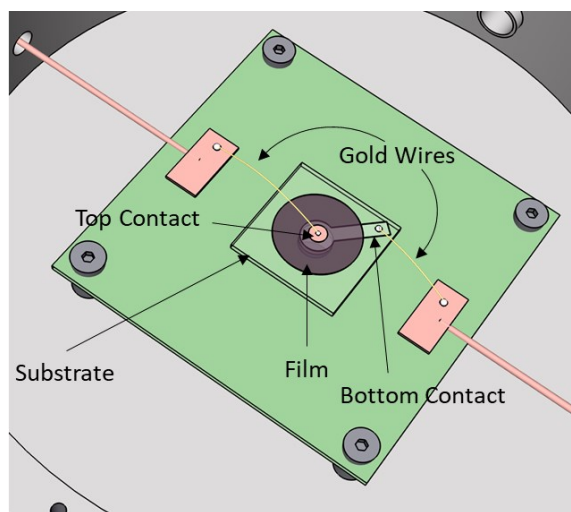


Figure 2.9. Schematic of an a-BC:H film deposited on transparent substrate connected to Faraday cage.

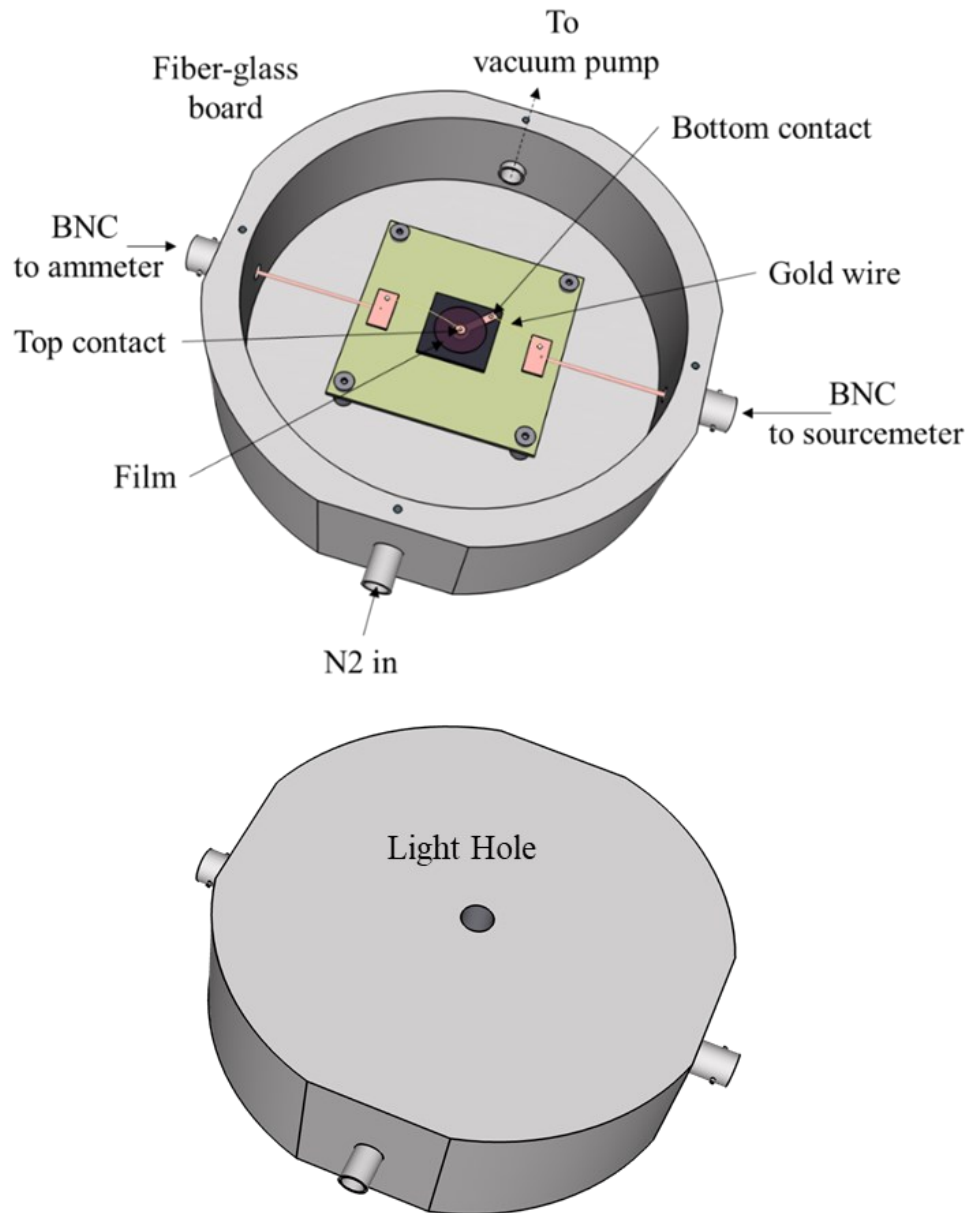


Figure 2.10. A Faraday cage designed to connect thin-film devices for electrical characterization (top) and its backside (bottom).

2.2. Basic Characterization

2.2.1. Spectroscopic Ellipsometry

Theory: In ellipsometry, an elliptically polarized light with a known phase difference (δ_1) between the p- and s-waves is incident on a thin-film-coated substrate at a particular incidence angle. The reflection from the substrate and the thin film reduces the light intensity and introduces a new phase difference (δ_2) between the two components of the light, which depends on the optical properties of the substrate and thin film, as well as the film thickness. A spectroscopic ellipsometry experiment measures two fundamental quantities, Δ and Ψ , defined as [146]

$$\Delta = \delta_1 - \delta_2 \quad (2.1)$$

and

$$\tan \Psi = \frac{|R_p|}{|R_s|} \quad (2.2)$$

for a range of wavelengths of light. Here, R_p and R_s are the complex reflection coefficients of the p- and s-waves, respectively. Once Ψ and Δ are measured for a wide range of wavelengths, the thickness and optical constants of the thin films can be measured by fitting the data with a physical model defined for the device under test.

Experiment: For ellipsometry measurements, at least one a-BC:H film was deposited on a silicon substrate in each batch of devices. All the devices in this work were studied using a J. A. Woolam Co. alpha-SE spectroscopic ellipsometer (Figure

2.11). Before each ellipsometry measurement session, the ellipsometer was calibrated for light beam alignment. A 25 nm SiO₂ standard was used for baseline measurement and ellipsometry table height adjustment. An a-BC:H film was then mounted on the ellipsometry table with vacuum suction. The ellipsometry measurements were recorded and analyzed using the CompleteEASE™ ellipsometry analysis program to extract the film thickness and refractive index.



Figure 2.11. Alpha-SE spectroscopic ellipsometer.

Most of the films grown for this study were either semi-transparent or transparent in the visible spectrum, as shown by constant amplitude oscillation in the quantity Ψ (Figure 2.12). Such films were analyzed using Cauchy's model, which relates the wavelength-dependent refractive index of a material with the three Cauchy constants, A , B , and C , by Cauchy's dispersion relation as [146]

$$n(\lambda) = A + \frac{B}{\lambda^2} + \frac{C}{\lambda^4} \quad (2.3)$$

Some transparent films resulted in high MSE (mean squared error) in the fitting process. For such films, the transparent Cauchy model with graded refractive indices for different layers was used. Most films resulted in acceptable fit quality for less than five layers. For films that showed significant absorption in the visible spectrum, an absorbing film model was used to fit the measured ellipsometry data, for which details are provided in the CompleteEASE™ manual [157].



Figure 2.12. Spectroscopic ellipsometry data fitting with CompleteEASE™ software using Cauchy model for transparent films.

2.2.2. UV-Visible Reflection and Transmission Spectroscopy

Theory: The reflectance, absorbance, and transmittance of a material depend on the wavelength of incident light. If R is the reflectance of a sample, then the intensity of the transmitted light beam Φ_T is given by the Beer–Lambert law as

$$\Phi_T = \Phi_0(1 - R) \exp(-\alpha d) \quad (2.4)$$

where Φ_0 is the intensity of the incident light beam, α is the absorption coefficient, and d is the device thickness. The absorption coefficient is obtained as

$$\alpha = \frac{\ln(1 - R) + A \ln 10}{d} \quad (2.5)$$

where $A = \Phi_0/\Phi_T$ can be measured with a UV-Vis transmission spectrometer.

Bandgap (E_g): Once the absorption coefficient of the film for a range of wavelengths of light is obtained, the optical bandgap is obtained by using a Tauc analysis [158]. In this analysis, the quantity $(\alpha h\nu)^m$ is plotted against photon energy ($h\nu$), where the exponent m is the molar extinction coefficient, which depends on whether the material has a direct or indirect bandgap. For amorphous semiconductor materials, the value of the exponent m is typically taken to be 1/2 [158]. With increasing photon energy, the quantity $(\alpha h\nu)^m$ increases sharply, consistent with the onset of a strong optical absorption due to the excitation of electrons from the valence band to the conduction band. By fitting the graph to a straight line given by

$$(\alpha h\nu)^{\frac{1}{2}} = B^{\frac{1}{2}} (h\nu - E_g), \quad (2.6)$$

the optical bandgap E_g is extracted as the energy where the fitted straight line intersects the energy axis, as shown in Figure 2.13.

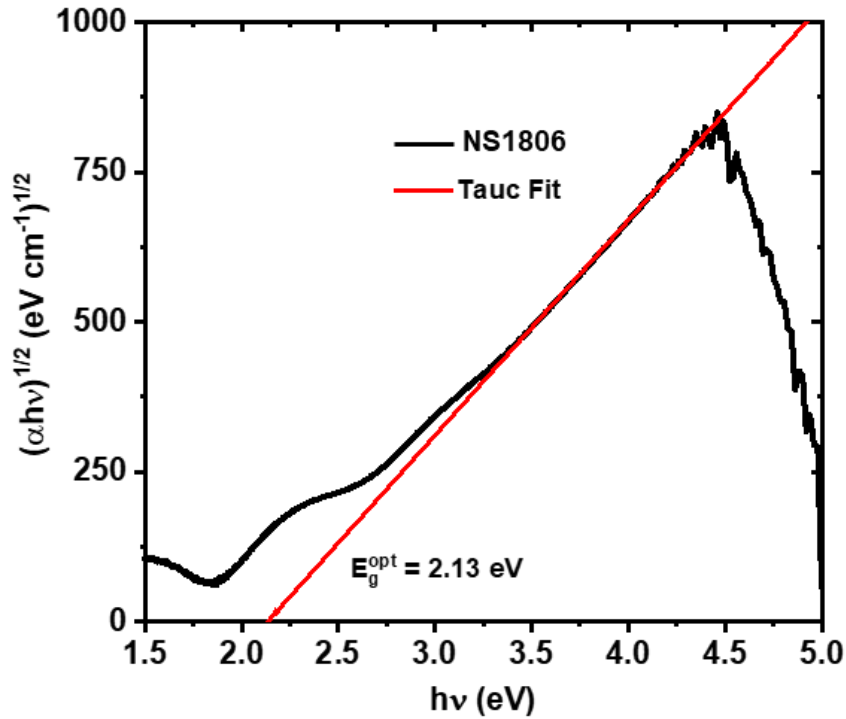


Figure 2.13. An example extraction of the optical bandgap using a Tauc analysis. The energy (2.13 eV) at which the dashed fit line (red) intersects the $h\nu$ -axis is the optical bandgap.

Iso-absorption Energy Gap (E_{04}): Sometimes, the extraction of the bandgap using a Tauc analysis is not possible due to an insufficient energy range of straight line part of the data or due to multiple reflection oscillations arising from thin-film

interferences. In such cases, the energy value corresponding to an absorption coefficient of 10^4 cm^{-1} can be considered as representative of the optical bandgap of a material.

Urbach Energy (E_U): The optical absorption in amorphous materials is characterized by an exponential absorption edge at the low energy region, given as

$$\alpha(h\nu) = \alpha_0 \exp\left(\frac{h\nu}{E_U}\right) \quad (2.7)$$

where E_U is known as the Urbach energy, which represents the width of the absorption edge. After the absorption coefficient as a function of wavelength is obtained, the Urbach energy is then obtained by fitting the data to Equation (2.7).

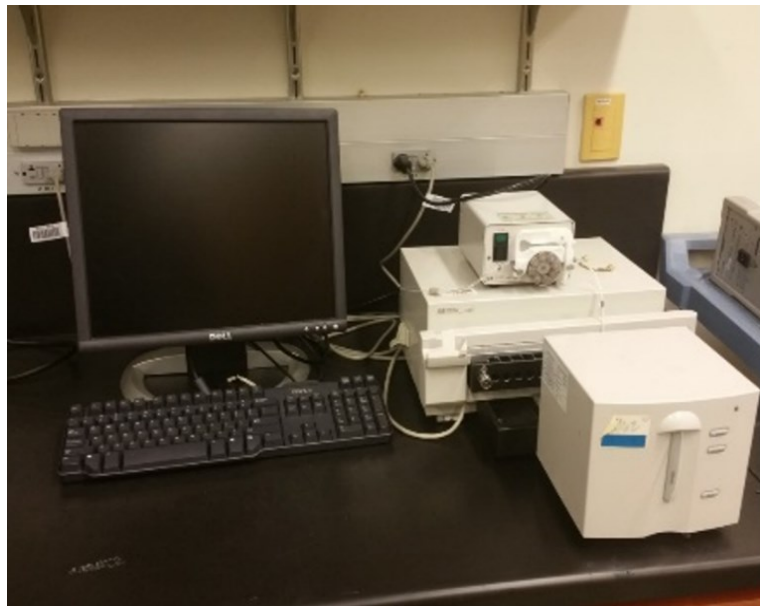


Figure 2.14. HP 8453 UV-Vis spectrometer

Experiment: For the transmission measurement, at least one a-BC:H thin-film was deposited on a transparent substrate (glass/quartz) for each batch of devices. The

transmission measurement was carried out using an HP 8453 UV-Vis spectrometer, shown in Figure 2.14. The spectrometer measures the intensity of the transmitted light as a function of wavelength. The absorbance (A) obtained from the device is defined as

$$A = \log_{10} \left(\frac{\Phi_0}{\Phi_T} \right) \quad (2.8)$$

where Φ_0 and Φ_T are the intensity of the incident and transmitted light, respectively.

In practice, the absorbance is not completely due to absorption; rather, it is a combined effect of the absorption and reflection. Because we did not have a setup to measure the reflection coefficient, the absorption coefficient obtained using Equation (2.5) assumes that the reflection coefficients were negligible. The bandgap and iso-absorption energy gap were obtained as discussed earlier. The extraction of the Urbach energy was generally difficult due to large interference oscillations in the absorption spectra at lower energies. To extract the best possible value, data points corresponding to the transmission maxima (reflection minima) were recorded as shown in Figure 2.15, and the Urbach energy was extracted by fitting the data points.

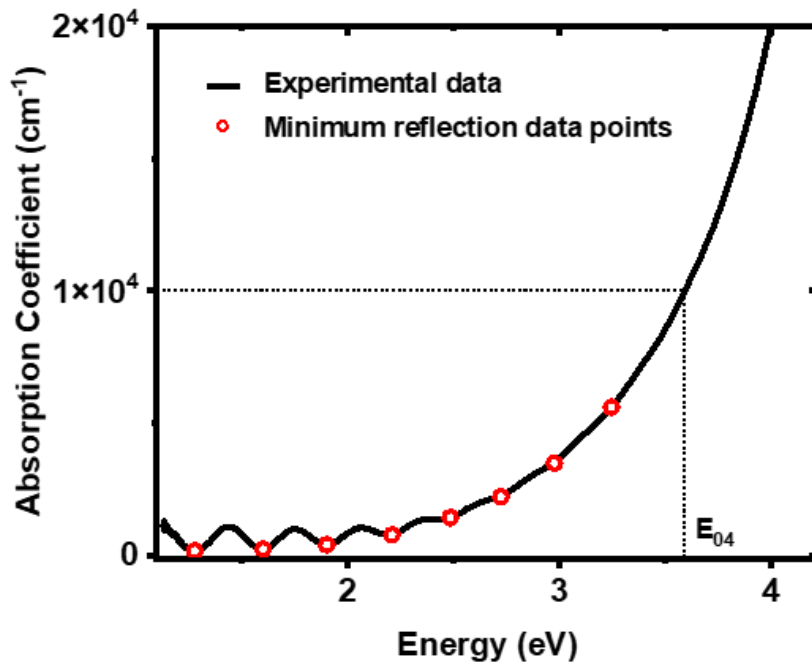


Figure 2.15. An example absorption graph with reflection oscillations in the low-energy spectrum. The circular points represent the minimum reflection data points.

2.2.3. Film Stress

Theory: A common technique for determining film stress is via the wafer curvature method using Stoney's equation [159], [160]. For a composite film–substrate system of film thickness d_f and substrate thickness d_s , the stress σ_f in the thin film is given as

$$\sigma_f = \frac{E_s d_s^2}{6(1 - \nu_s)} \frac{1}{d_f} \frac{1}{R} \quad (2.9)$$

where E_s is the Young's Modulus of the substrate, ν_s is the Poisson's ratio of the substrate, and R is the radius of curvature of the substrate. The film stress can then be determined by measuring R , assuming the other quantities are known.

Experiment: Figure 2.16 shows a custom-built profilometer that was used to measure the substrate curvature. The system was built using an MTI Microtrak II laser/detector triangulation unit that can measure height with a resolution of $\pm 0.12 \mu\text{m}$ to extract wafer curvature. The laser unit is mounted above a horizontally translating stage, onto which the sample is positioned. The stage is driven by a stepper motor coupled to a controller. The controller and laser unit are interfaced with a custom LabView program.

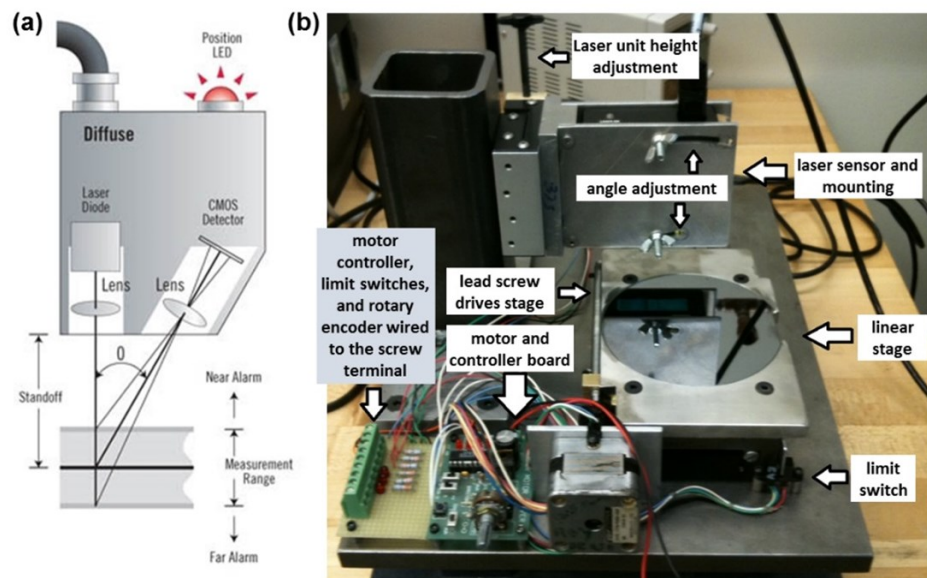


Figure 2.16. a) MTI Microtrak II laser/detector triangulation unit and b) custom-built profilometer for wafer curvature measurement.

a-BC:H thin-films for stress measurements were deposited on double side polished 100 mm full wafers. Because the silicon wafers were not ideally flat, the background curvatures of cleaned wafers were measured on one side prior to film deposition. The measurements were performed by measuring the vertical distance of the wafer from the laser source along two perpendicular lines by translating the horizontal stage. a-BC:H films were then deposited on the other side of the wafer and the measurements were repeated on the back side (the same side for which the background curvature was measured). The background readings were subtracted from the measurement point by point, and the radius of curvature was obtained by fitting the corrected data to a second-degree polynomial. The film stress was then obtained using Equation (2.9). An example of the profilometer data after background correction is shown in Figure 2.17. The film stress on some of these and a selection of other films was also measured externally using a KLA-Tencor P7 stylus profilometer, which scans the wafer surface with a physical stylus rather than using laser light.

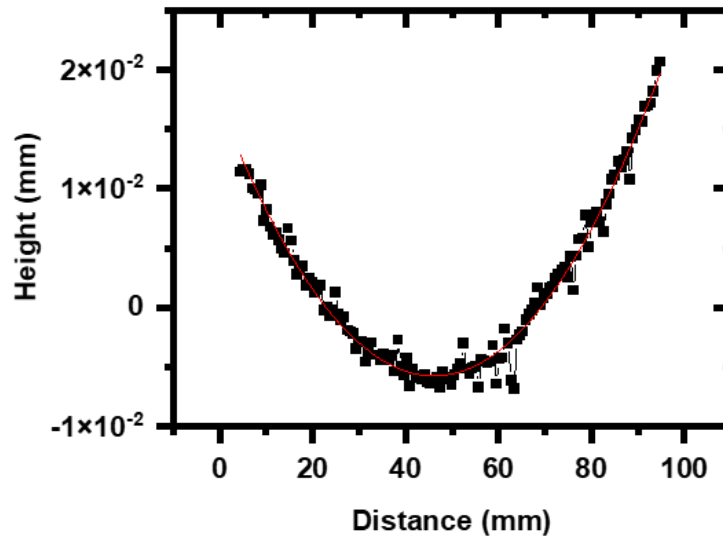


Figure 2.17. Wafer curvature data for a-BC:H sample Q32 (I), after silicon background correction.

2.3. Charge Transport Characterization

2.3.1. Dielectric Constant

Theory: The dielectric constant of a material gives information about its polarizability under an applied electric field. Capacitance–voltage (*CV*) measurements constitutes one method to measure the dielectric constant of devices fabricated in a capacitor geometry. In this experiment, a small sinusoidal AC signal is applied across a metal–insulator–metal (MIM) or metal–insulator–semiconductor (MIS) device along with a DC bias voltage. By measuring the AC impedance of the insulating device for a specified frequency of applied AC signal and comparing it to a standard parallel resistor–capacitor (*RC*) equivalent circuit, the capacitance (*C*) of the device is extracted.

Once the capacitance is known, the dielectric constant (k) of the thin-film material can then be calculated as

$$k = \frac{Cd}{\epsilon_0 A} \quad (2.10)$$

where d is film thickness, $\epsilon_0 = 8.854 \times 10^{-12} \text{ F}\cdot\text{m}^{-1}$ is the absolute permittivity of vacuum, and A is the electrical contact area of the device.

Experiment: The dielectric constants of the a-BC:H thin-films were measured on films grown directly on low-resistivity (1–15 $\Omega\cdot\text{cm}$) silicon substrates. To measure the dielectric constant, a device was placed on a mercury probe station manufactured by MDC corporation, as shown in Figure 2.18. A mercury contact spot of 0.836 mm in diameter was achieved using a vacuum system, and electrical contact to silicon was achieved via an aluminum disc. The device was then connected to a Keithley 590 CV meter, which measured the capacitance of the device at 100 kHz for a given range of DC voltages. The data was extracted with a custom program supplied by MDC corporation.

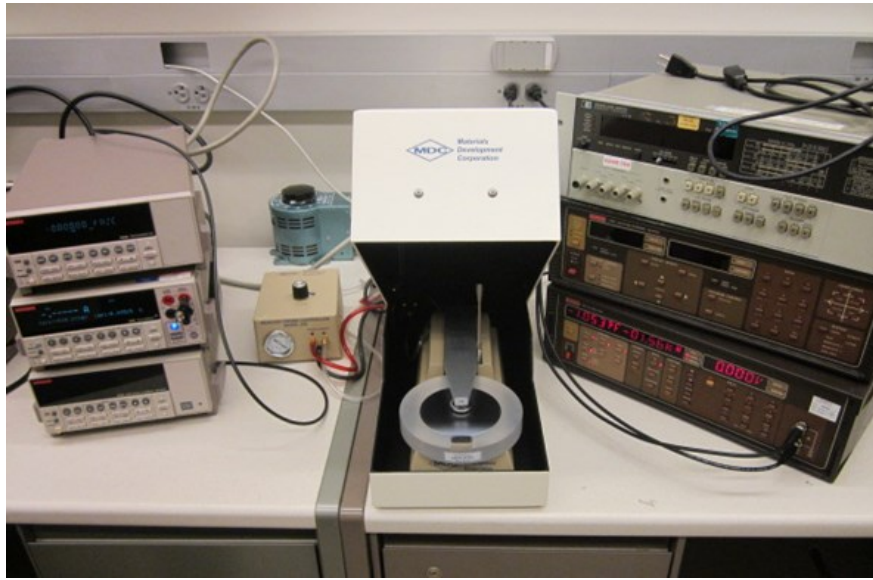


Figure 2.18. An MIS device placed on a MDC mercury probe station for capacitance–voltage and current–voltage measurements.

2.3.2. Steady-State Current–Voltage Measurements

In a current–voltage measurement, a voltage is applied across a device (MIM or MIS), and the resulting current through the device is measured. A schematic of our experimental setup for current–voltage (*IV*) measurements is shown in Figure 2.19. With an appropriate device geometry and contact electrodes, current–voltage measurements can be used to extract the resistivity (ρ) and carrier mobility (μ) using Ohm’s law and space-charge-limited current analysis, respectively. The carrier concentration in the material can then be calculated using the resistivity and carrier mobility. Current–voltage measurements in the presence of optical excitation, generally known as *photoconductivity measurements*, can be used to extract the mobility–lifetime

product ($\mu\tau$) and the quantum efficiency (η) of carrier excitation. The following sections describe current–voltage measurements to extract resistivity, carrier mobility, mobility–lifetime product, and quantum efficiency in semiconducting/semi-insulating thin-films.

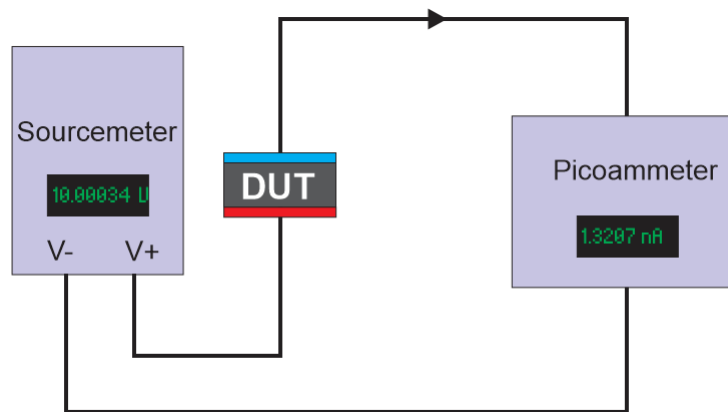


Figure 2.19. Schematic of current–voltage measurement setup. A device under test (DUT) is connected in series with a voltage sourcemeter and a picoammeter.

2.3.2.1. Contact Considerations in Electrical Measurements

Different electrical measurements require different types of electrical contacts. For example, a resistivity measurement needs Ohmic contacts so that the current–voltage data follows Ohm’s law. Charge carrier mobility estimation using the space-charge-limited current analysis requires a contact to be injecting [161], which is one type of Ohmic contact. Photoconductivity experiments are generally carried out in devices with blocking contacts [162] such that the electric current in the device is only due to the photo-excited carriers.

A metal–semiconductor interface forms different types of contacts based on the band alignment between the metal and semiconductor [161]. Here, we describe a few types of contacts in reference to a p-type semiconductor, which, we believe, is the case in a-BC:H thin-films. The band alignments presented here are based on expected a-BC:H bandgap ($E_g = 1.5$ eV), work function ($\phi_s = 4.5$ eV), and electron affinity ($\chi_s = 3.5$ eV). Band alignments based on different values are presented in Appendix A.

2.3.2.1.1. Injecting Contact

In p-type semiconductors, an injecting contact is formed if the metal work function is larger than the semiconductor work function ($\phi_m > \phi_s$), as shown in Figure 2.20. The electrons diffuse from the semiconductor to the metal due to the availability of lower energy states in the metal, forming a hole accumulation layer in the semiconductor. The accumulation layer facilitates the injection of holes into the semiconductor. Although the contact acts as an injecting contact, its efficiency—ability to supply as many free carriers as needed at high electric fields—depends on the Schottky barrier height ($\phi_b = \chi_s + E_g - \phi_m$). An efficient injecting contact is formed if the hole Schottky barrier height is negligible, or negative. A device with injecting contacts follows Ohm’s law at lower electric field. However, the current deviates significantly from Ohm’s law at high electric fields because of other dominant charge transport mechanisms such as space-charge-limited current [163] and Poole–Frenkel emission [164] of trapped charges.

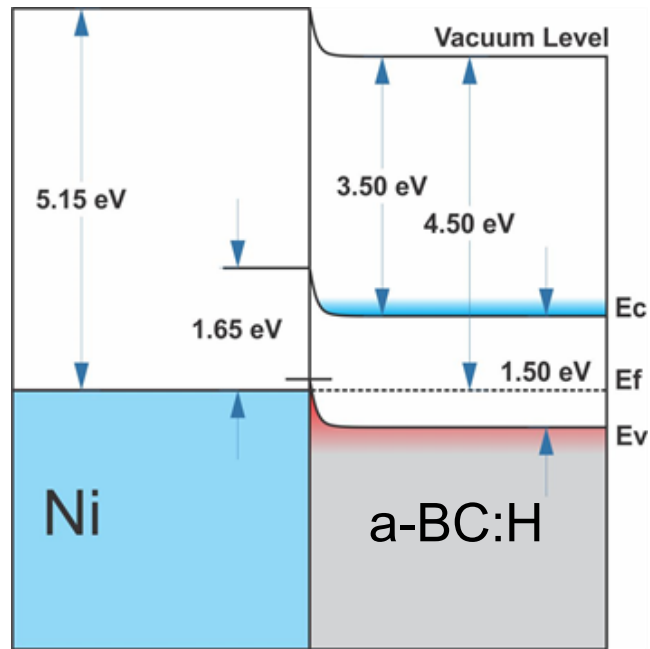


Figure 2.20. Band alignment of a-BC:H with nickel demonstrating the expected formation of a hole injecting contact.

2.3.2.1.2. Neutral Contact:

A neutral contact is formed if the metal and semiconductor work functions are equal, as shown in Figure 2.21. In such a case, the charge carriers do not diffuse from metal to semiconductor. Devices with neutral contacts follow Ohm's law at lower electric field. However, if the Schottky barrier height is large, such as in wide-bandgap materials, the contact cannot supply enough charge carriers at high electric field, leading to the depletion of carriers in the device.

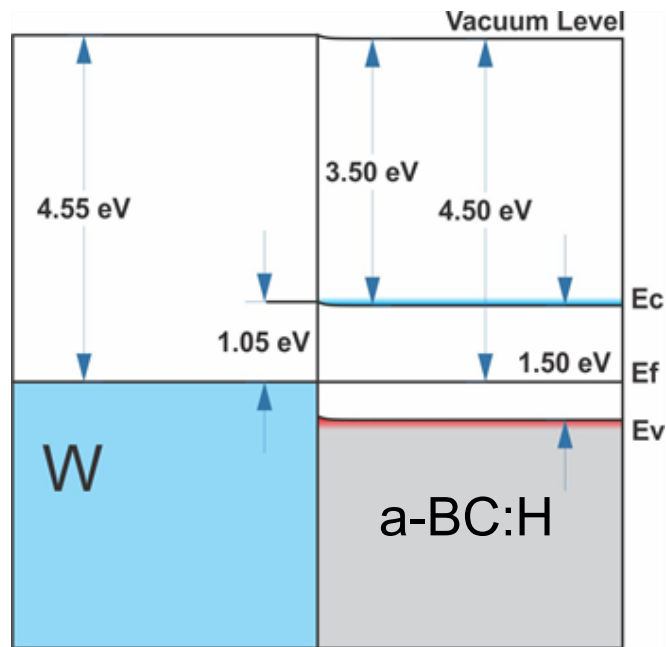


Figure 2.21. Band alignment of a-BC:H with tungsten demonstrating the expected formation of a neutral contact.

2.3.2.1.3. Blocking Contact

In a p-type semiconductor, a blocking contact is formed when the metal work function is smaller than the semiconductor work function ($\phi_m < \phi_s$), as shown in Figure 2.22. Electrons diffuse from metal to semiconductor and ionize the holes, forming a negatively charged depletion layer. When a positive potential is applied to the metal and negative potential is applied to the semiconductor, the applied field further widens the depletion layer reducing the leakage current.

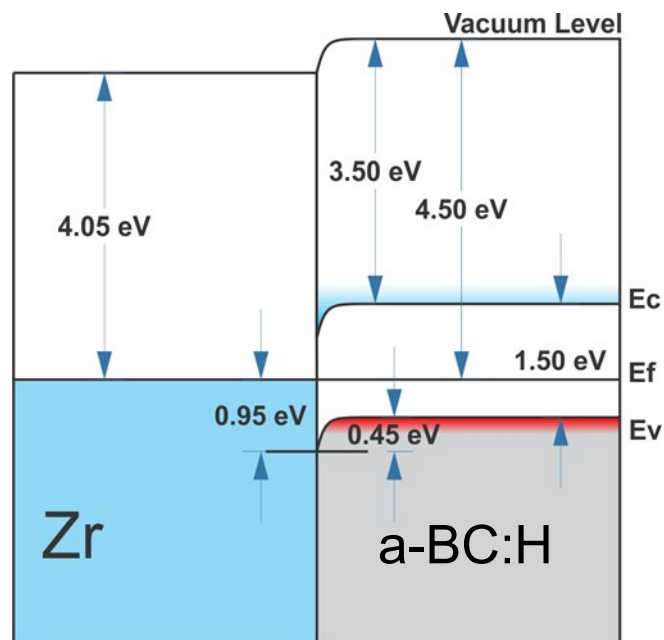


Figure 2.22. Band alignment between a-BC:H and zirconium demonstrating the expected formation of a hole-blocking contact.

Based on a previous study [152], and expected band alignment between different metals and a-BC:H films [see Appendix A], commonly available high-work-function metals, such as nickel, gold, and palladium are expected to form injecting contacts, whereas moderate-work-function metals, such as copper, titanium, and tungsten are expected to make neutral contacts. Because a-BC:H is amorphous, the distinct band edges are only approximations, and other phenomena, such as Fermi level pinning in semiconductors due to interfacial impurities [165] can change the contact behavior significantly. Further, because the charge transport in a-BC:H is believed to be due to hopping through defect states, and metal contacts can inject carriers in distributed energy states [166], we have observed during our previous studies that many metals,

such as copper, aluminum, titanium, and gold show Ohmic-injecting behavior even when they are expected to form blocking contacts, such as aluminum and titanium.

2.3.2.2. Resistivity: Ohm's Law

There are many different methods to measure the resistivity of a material, such as the 4-point van der Pauw method [167], the linear 2-point method [168], the linear 4-point method [168] and using Ohm's law in devices with a metal–insulator–metal (MIM) or metal–insulator–semiconductor (MIS) geometry. For thin films of material with a very high resistivity, such as a-BC:H, resistivity measurements using Ohm's law is superior compared to other methods as other methods require sourcing relatively large current to obtain a measurable voltage across measurement terminal. Thus, we have used Ohm's law to calculate the resistivity in a-BC:H thin-films.

Theory: The resistivity of a material can be calculated from a current–voltage measurement using Ohm's law. Ohm's law gives a linear relationship between the current (I) through a device and the voltage (V) applied across it as

$$I = \frac{V}{R} \quad (2.11)$$

where R is the resistance of the device. Once the resistance is obtained, the resistivity ρ is calculated using the relation

$$\rho = \frac{RA}{d} \quad (2.12)$$

where d is the device thickness and A is the cross-sectional area of the device. In terms of the current density, Ohm's law is written as

$$J = \frac{E}{\rho}; \quad J = \frac{I}{A}, \quad \rho = \frac{RA}{d} \quad (2.13)$$

Experiment: For the resistivity measurements, two geometries were chosen: (1) a metal–insulator–semiconductor (MIS) geometry and (2) a metal–insulator–metal (MIM) geometry. The MIS devices were mounted in the MDC mercury probe station, as described in Section 2.3.1. The aluminum terminal of the mercury probe station (connected to the p-type silicon substrate) was connected to a Keithley 2400 source meter, and the mercury contact was connected to a Keithley 6485 picoammeter through two BNC cables. The MIM devices were mounted inside Faraday cages, as described in Section 2.1.7. A voltage was applied across the device using a Keithley 2400 source meter, and the current through it was measured using a Keithley 6485 picoammeter, as shown in Figure 2.18.

The current–voltage (IV) data were extracted by using a set of LabView programs. For all devices tested in this study, the current–voltage measurements were performed at a low voltage range for at least two runs of complete hysteresis cycling: increasing the voltage from zero to a maximum positive defined value, then lowering down to zero, increasing to the maximum negative value, and returning to zero, as shown in Figure 2.23. This approach helped to understand the electrical stability of the devices and choose the most representative data set from the measurements. If the

device was stable electrically for the applied voltage range, then the measurement sequence was repeated for a higher voltage range.

Most of the devices showed some hysteresis effect: the current not returning to zero when the applied voltage was decreased to zero from both positive and negative maximum values. So, for the current–voltage data analysis, the current was reduced by an offset amount to bring the current to zero at zero applied voltage. The corrected current was then plotted against the voltage applied, yielding a straight line representing Ohm’s law at lower electric fields. In a log–log scale, the current–voltage data also produced a straight line, as shown in Figure 2.24, representing the following equation:

$$\log J = \log \left(\frac{1}{\rho} \right) + \log E \quad (2.14)$$

with the slope of the straight line being equal to 1.0. The resistivity of the device is then obtained as

$$\rho = 10^{-a} \quad (2.15)$$

Where $a = \log (1/\rho)$ is the intercept made by the straight line with the $\log J$ axis.

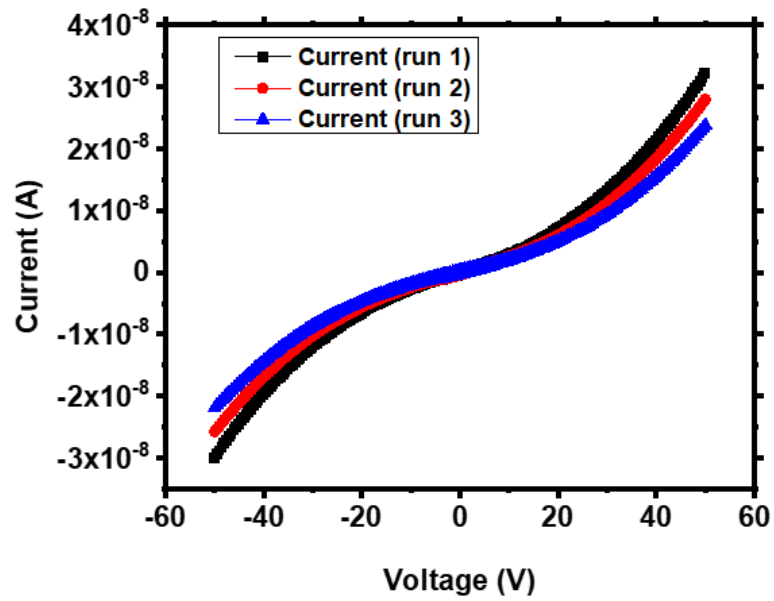


Figure 2.23. An example of current–voltage data obtained from an a-BC:H film.

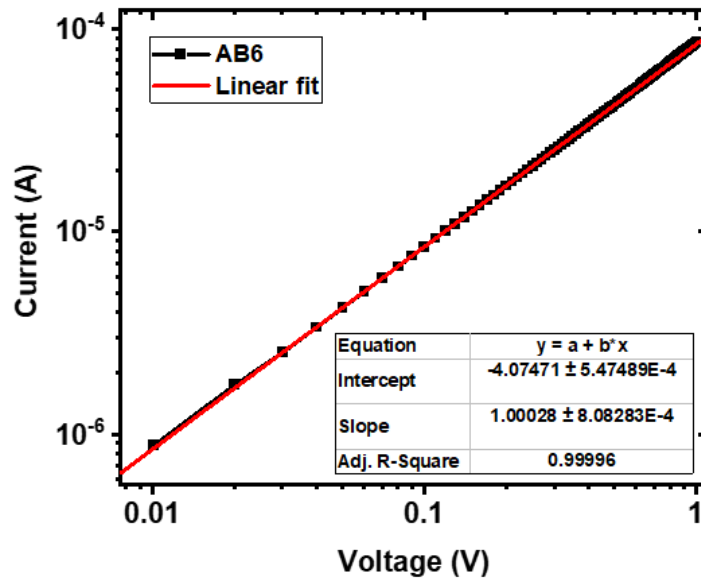


Figure 2.24. Extraction of resistivity of device AB6 using Ohm’s law. The red line represents the fit to Equation (2.14).

2.3.2.3. Carrier Mobility: Steady-State Space-Charge-Limited Current

Theory: Charge carrier mobility can be extracted from current–voltage data using a steady-state space-charge-limited current analysis [163], [169], [170]. When an electric field is applied to an insulator or semiconductor sandwiched between injecting contacts, the current typically follows Ohmic behavior ($I \propto V$) at low electric field. In this regime, the contact supplies an amount of charge, which is only sufficient to replace the charge carriers leaving the device. The injected charge carriers slowly drift through the device to get neutralized/screened by the available mobile charge carriers inside the device (a phenomenon known as *dielectric relaxation*) before they exit at the other electrode. This phenomenon ensures that the device remains electrically neutral in the Ohmic transport regime.

As the electric field increases, the injected charge carriers acquire higher drift velocity, and at a certain point, their *transit time* ($t_t = d/\mu E$)—the time required to travel the device thickness d —becomes equal to the *dielectric relaxation time* ($t_d = \rho\epsilon$) [161] of the material (where $\epsilon = \epsilon_0\epsilon_r$ is the absolute permittivity of the device with ϵ_0 representing the absolute permittivity of free space and ϵ_r the relative dielectric constant of the material). With further increase in the applied electric, the injected charge carriers do not get sufficient time to be neutralized by the free carriers, and they accumulate within the device, causing a buildup of space-charge. The space-charge modifies the internal electric field in the device, and the charge transport deviates from

the Ohmic regime to the space-charge-limited regime where the current follows the Mott–Gurney law [163]

$$J_{SCLC} = \frac{9}{8} \epsilon \mu A \frac{E^2}{d} \quad (2.16)$$

where A is the cross-sectional area of the device. Equation (2.16) shows that the space-charge-limited current (SCLC) is independent of the charge carrier density, n , and depends only on one unknown parameter: μ , the charge carrier mobility. Because the absolute permittivity, ϵ , can be measured independently using the capacitance–voltage (CV) measurement, as explained in Section 2.3.1, the charge carrier mobility can be extracted by fitting the current–voltage data to equation (2.16) within the space-charge-limited current regime.

Experiment: Current–voltage measurements for carrier mobility extraction were performed as described in Section 2.3.2.2. The current–voltage data were then plotted in a log–log scale to find a linear region with a slope of 2, corresponding to the SCLC regime, as shown in Figure 2.25, representing the equation

$$\log J_{SCLC} = \log \left(\frac{9 \epsilon \mu}{8 d} \right) + 2 \log E \quad (2.17)$$

The charge carrier mobility was then obtained from the intercept of the straight line as

$$\mu = \frac{8 d}{9 \epsilon} \cdot 10^a \quad (2.18)$$

where $a = \log(9\epsilon\mu/8d)$ is the intercept made by the straight line with the $\log J_{\text{SCLC}}$ axis. Some a-BC:H devices required a more complex analysis to extract the carrier mobility, which will be further described in Chapters 5 and 6.

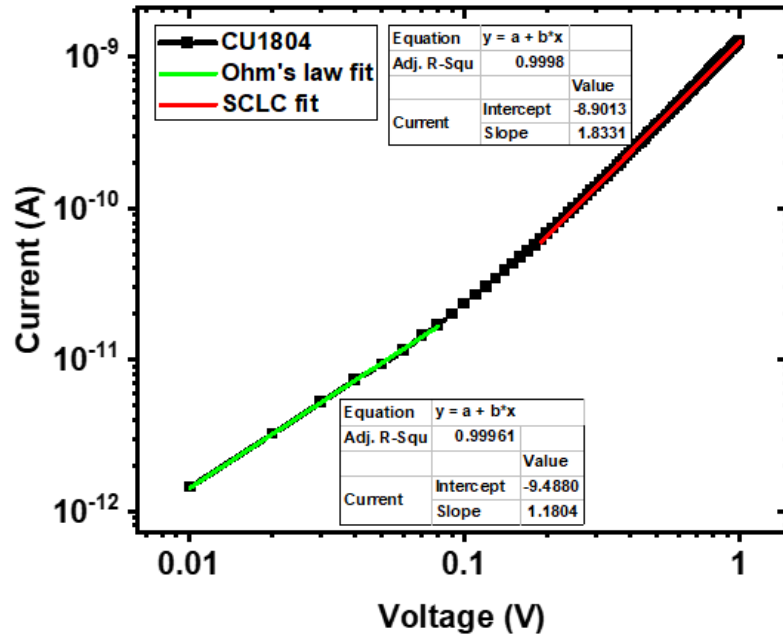


Figure 2.25. Extraction of resistivity and carrier mobility from I–V measurements in the Ohmic and SCLC current regimes.

2.3.2.4. Mobility–Lifetime Product ($\mu\tau$): Steady-State Photoconductivity

Theory: When light of suitable wavelength illuminates semiconductors/semi-insulators, electron–hole pairs are excited, which can move under the influence of an externally applied electric field, increasing the electrical conductivity of a solid. The current–voltage measurements of a solid material under optical illumination can be used

to obtain the material's photoconductivity. Under steady-state conditions, the photoconductivity, σ_{ph} , is defined as

$$\sigma_{\text{ph}} = \sigma_{\text{ill}} - \sigma_{\text{dark}} \quad (2.19)$$

where σ_{ill} and σ_{dark} are the conductivity of the insulator/semiconductor when it is illuminated and in the dark, respectively. Steady-state photoconductivity analysis is generally performed to obtain the charge carrier mobility–lifetime product ($\mu\tau$), a key figure of merit in radiation detection.

Because the photoconductivity response of a device depends on device geometry and experimental conditions, different approaches are used to extract the mobility–lifetime product. We will describe these approaches in the following sections.

2.3.2.4.1. Devices with Injecting Contacts

In devices with injecting contacts, if the absorption of light is uniform across the device, the photoconductivity at low electric field in the Ohmic charge transport regime is related to the mobility–lifetime ($\mu\tau$) product as [171]

$$\sigma_{\text{ph}} = qG\mu\tau \quad (2.20)$$

where G is the photo-carrier generation rate and q is the charge of the photo-carrier. The recombination/trapping kinetics of the carriers are approximated with a single lifetime (τ). The photo-carrier generation rate in the case of uniform light absorption is given as

$$G = \eta(1 - R) \frac{\alpha I_0}{h\nu} \quad (2.21)$$

where η is the quantum efficiency, the ratio of generated e–h pairs to the total number of photons absorbed by the device, and α is the absorption coefficient at the photon frequency ν . Since the quantum efficiency (η) cannot be obtained with this experiment, Equations (2.20) can be used to extract $\eta\mu\tau$, the effective mobility–lifetime product. Depending on whether the photocurrent is due to a single type of carrier or both types of carriers, Equation (2.20) can be used to extract carrier dependent or average mobility–lifetime value.

Equation (2.20), however, cannot be applied if the device is very thick compared to the optical absorption depth or the electric field is high so that both conditions can lead independently to space-charge-limited current in the device. Under space-charge-limited current conditions, the photogenerated carriers do not contribute to any appreciable increase in current.

2.3.2.4.2. Devices with Neutral or Blocking Contacts

In devices with neutral or blocking transparent contacts, assuming a uniform absorption of light, the photocurrent due to a single type of charge carrier moving along the electric field is given by the Hecht relation [172] as

$$J_{ph} = 2J_0 \frac{\mu\tau E}{d} \left[1 - \frac{\mu\tau E}{d} \left(1 - \exp\left(-\frac{d}{\mu\tau E}\right) \right) \right] \quad (2.22)$$

where $J_0 = qGd$ is the saturation photocurrent achieved when $\mu\tau E/d \gg 1$ so that the carrier extraction rate exceeds the carrier generation rate. A similar expression can be

used for the current due to the charge carriers moving opposite to the electric field. If the current is only due to a single type of charge carrier, it is possible to extract both the mobility–lifetime product ($\mu\tau$) and quantum efficiency (η) independently by fitting photocurrent–voltage data to Equation (2.22).

When the device is very thick compared to the optical absorption depth, the carriers are generated very close to the incident surface. In such a case, only one type of charge carrier moving towards the other contact contributes to the photocurrent. This offers an added benefit that the mobility–lifetime products for both types of charge carriers (electrons and holes) can be independently extracted just by changing the direction of the electric field. The photocurrent under surface excitation is given as [173]

$$J_{ph} = \frac{J_0 \frac{\mu\tau E}{d} \left[1 - \exp\left(-\frac{d}{\mu\tau E}\right) \right]}{1 + \frac{s}{\mu E}} \quad (2.23)$$

where s is a parameter, called the *surface recombination velocity*, which represents the surface recombination of the charge carriers on the illuminated surface/interface.

Experiment: Figure 2.26 shows the experimental setup for steady-state photoconductivity measurements. The a-BC:H devices were grown on transparent conducting substrates (ITO and FTO coated glass substrates) and were mounted inside a Faraday cage so that the bottom contact (ITO/FTO) faces towards the 1/8-inch diameter optical window, as described in Section 2.1.7. The devices were illuminated through the optical window with light of a particular wavelength using a Horiba HR 640 monochromator coupled with the light output from an OBB PowerArc 75W Xe

broadband arc lamp light source. For photocurrent measurements, current–voltage data with and without illumination were taken following the procedure explained in Section 2.3.2.2. The photocurrent–voltage data is then fitted to the appropriate Hecht equations from which the mobility–lifetime product ($\mu\tau$) can be obtained as a parameter. Comparing the saturation photocurrent (J_0) to the absorbed photon flux, the quantum efficiency (η) can also be obtained.

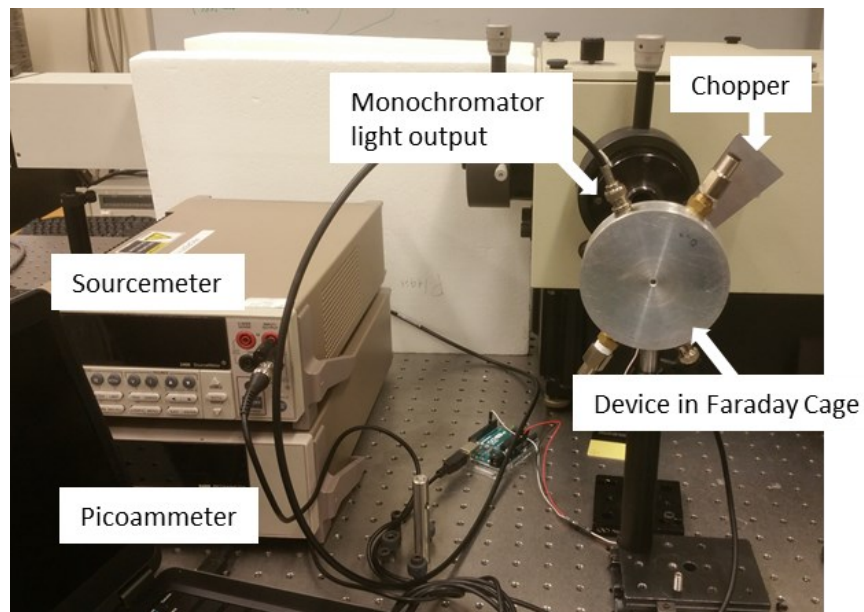


Figure 2.26. Experimental setup for steady-state photoconductivity experiments.

2.3.3. Transient Photoconductivity

Transient photoconductivity is an experiment in which a short pulse of light illuminates a device, and the resulting photocurrent is recorded as a function of time. From transient photocurrent experiments, charge carrier mobility, charge carrier

lifetime, and mobility–lifetime product can be extracted, as explained in the following sections.

2.3.3.1. Carrier Lifetime

Theory: The transient photocurrent decay can be used to estimate the lifetime of generated carriers. Under the simplest assumption that carrier trapping (note that in the case of surface generation, the current is dominated by trapping, not recombination) is described by a single lifetime, photocurrent decay at a low electric field is approximated by an exponential decay as

$$I = I_0 \exp\left(-\frac{t}{\tau}\right) \quad (2.24)$$

Because this exponential decay may not represent the photocurrent decay in amorphous films in general (*vide infra*), an approximation of the lifetime can be made from the slope of the initial decay consistent with Equation (2.24) as

$$\frac{1}{\tau} = -\frac{1}{I_0} \left(\frac{dI}{dt}\right)_{t=0} \quad (2.25)$$

Although this may not give the true carrier lifetime, it will give the effective lifetime, which is an important metric in a detector’s performance. Lifetime can also be indirectly extracted from a combination of the carrier mobility (μ) and mobility–lifetime ($\mu\tau$) values obtained from transient photoconductivity experiments, as described in the following sections.

2.3.3.2. Carrier Mobility: Time of Flight Experiment

Theory: The time of flight (TOF) experiment is one of the most common methods to extract drift mobility in semiconductors [174]–[178], and has been successfully used to study amorphous semiconductors [179]–[183]. In this experiment, the device under test is connected to an external biasing source via transparent blocking contacts so that the contacts do not inject additional charge carriers and modify the electric field. A short pulse of strongly absorbed light excites a thin sheet of e–h pairs on the illuminated surface. To ensure that e–h pair generation is constrained to the surface, the device should be thick relative to the optical absorption depth. Under the applied electric field, one type of carrier (electrons/holes) moves toward the opposite electrode and induces a current in the external circuit as [184], [185]

$$I = \frac{Q\mu E}{d} \quad (2.26)$$

where Q , E , and d are respectively the photo-generated charge, applied electric field, and the device thickness.

For perfect crystalline materials, in the absence of traps, the photocurrent remains constant until the moving carriers reach the collecting electrode, and the current quickly decays to zero. The time at which the current drops to zero from the constant value is the carrier transit time t_t , which is given as

$$t_t = \frac{d}{\mu E} \quad (2.27)$$

Hence, by identifying the transit time from the transient photocurrent data, it is possible to calculate the drift mobility.

In practice, however, many other mechanisms reduce the current, making the identification of transit time difficult. Two commonly experienced difficulties are current decay due to carrier trapping and dielectric relaxation. If the transit time is longer than both the carrier trapping time (τ) and the dielectric relaxation time (RC), where R and C are respectively the device resistance and capacitance, the transit time cannot be seen. So, for the time of flight experiment, the transit time should be made shorter than both the trapping and dielectric relaxation time by increasing the applied electric field. Further, to observe the transit time, the generated charge, Q , should be small relative to CV , the charge stored due to the device capacitance, so that the photo-generated carriers do not distort the electric field.

There are variations of this method to account for the trapping of charge carriers during their transit, which changes the photocurrent transient significantly from the ideal response and increases the complexity of determining transit time. For amorphous materials with an exponential distribution of localized states, the commonly used expression for the photocurrent transient is [181]

$$\begin{aligned}
 I &\propto t^{-(1-\alpha_1)}; t < t_t \\
 I &\propto t^{-(1+\alpha_2)}; t > t_t
 \end{aligned}
 \tag{2.28}$$

where α_1 and α_2 are fitting parameters related to the distribution of localized states in the bandgap. Because of the continuous decay of the current with time and the presence

of the post-transit current caused by the release of trapped carriers, the transit time cannot be observed on a linear scale. However, plotting the current transient on a log–log plot yields two photocurrent decay regions with two straight lines with negative slopes, as shown in Figure 2.27. The intersection of the two lines represents the transit time, which can then be used to extract the drift mobility.

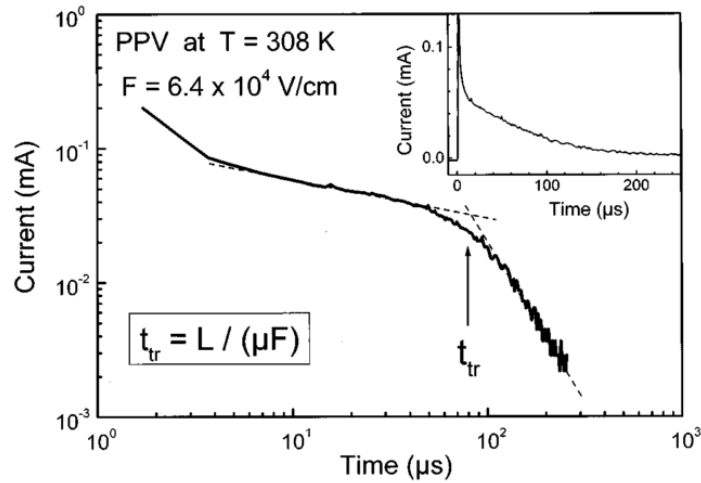


Figure 2.27. Example TOF signal with dispersive transport of carriers. The figure is taken from reference [176].

3.1.1.1. Mobility–Lifetime ($\mu\tau$) Product

Theory: The TOF transient signal can be used to perform a Hecht analysis [172] of the collected charge. For this, the transient current is measured at different applied electric field values, and the charge collected by the external circuit is obtained from the area under the $I-t$ curve as

$$Q_{\text{coll}} = \int Idt \quad (2.29)$$

The collected charge increases with applied electric field, eventually saturating at a sufficiently high field. Assuming surface absorption of light, the collected charge is related to the generated charge, Q , by Many's expression [186] as

$$Q_{\text{coll}} = \frac{Q \frac{\mu\tau E}{d} \left[1 - \exp\left(-\frac{d}{\mu\tau E}\right) \right]}{1 + \frac{s}{\mu E}} \quad (2.30)$$

where s is the surface recombination velocity. In the case of uniform absorption (small absorption coefficient/thin film), the collected charge is given as [172]

$$Q_{\text{coll}} = 2Q \frac{\mu\tau E}{d} \left[1 - \frac{\mu\tau E}{d} \left(1 - \exp\left(-\frac{d}{\mu\tau E}\right) \right) \right] \quad (2.31)$$

By fitting the experimental data to Equation (2.30) or (2.31) depending on the absorption conditions used, the generated charge (Q), mobility–lifetime product ($\mu\tau$), and the quantum efficiency (η) can be estimated. From the estimated value of $\mu\tau$ and the direct measurement of drift mobility, lifetime can be calculated.

Experiment: A schematic and an experimental setup for the transient photoconductivity experiment are shown in Figure 2.28 and Figure 2.29, respectively. For the experiment, a-BC:H devices were mounted inside a custom-built Faraday cage with a light hole, as described in Section 2.1.7. A Coherent CompexPro laser that produces 20 ns pulses at a wavelength of 350 nm at a variable repetition rate of 1 to 10 Hz was used as the optical excitation source. The wavelength was in the correct range

relative to the optical gap of a-BC:H and the optical properties of transparent ITO and FTO substrates. A transient laser beam from the source was split using a beam splitter with one beam hitting a fast-rise-time photodiode, whose output signal was used to trigger an oscilloscope. Another beam was used to illuminate the a-BC:H device. The output photocurrent signal obtained from the device was connected to a wideband current sensitive DHPCA-100 amplifier, having a variable transimpedance gain from 10^3 – 10^8 Ohms. The amplified current signal was then fed into the input terminal of an oscilloscope to record the photocurrent transient. The available memory of 1 Gpts of the oscilloscope helped record a transient signal for up to 0.05 seconds with a resolution of 20 points per ns. The recording length and resolution were optimal for the a-BC:H device, for which we expected the transient photocurrent to remain for microseconds to milliseconds.

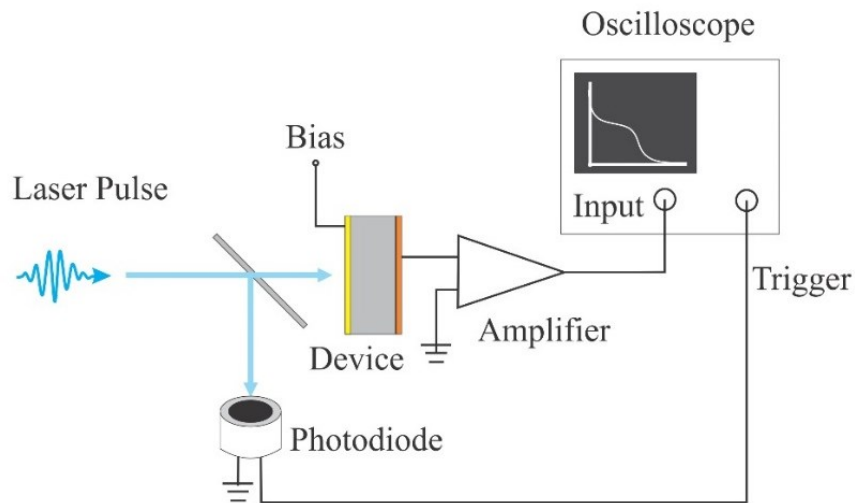


Figure 2.28. A schematic of transient photocurrent measurement setup.

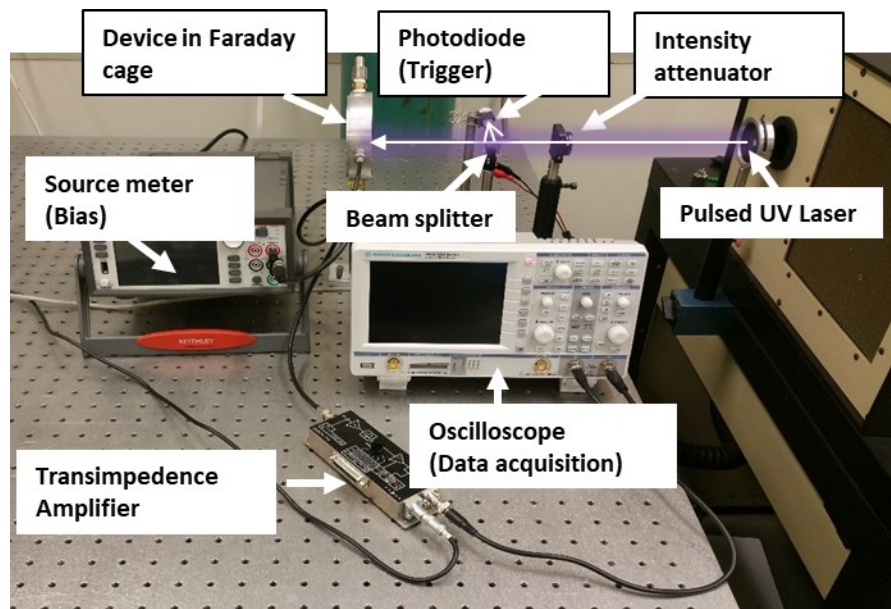


Figure 2.29. Experimental setup for the transient photoconductivity experiment.

CHAPTER 3

SINGLE-CARRIER CHARGE COLLECTION IN THIN DIRECT-CONVERSION SEMICONDUCTOR NEUTRON DETECTOR: A NUMERICAL SIMULATION

(This chapter is reproduced in part from reference [187] with the permission of AIP Publishing)

3.1. Introduction

Since the first successful detection of alpha particles by a germanium point-contact diode in 1949 [104], solid-state semiconductor detectors have revolutionized the field of radiation detection, particularly in the case of charged particles and high-energy photons. These types of radiation interact readily with various mature semiconductor materials, facilitating efficient and reliable detection. However, the solid-state detection of neutral particles such as neutrons is more challenging because these particles do not interact with any currently well-established semiconductor materials. In the case of thermal (~ 25 meV) neutrons in particular, only a limited number of isotopes (^3He , ^6Li , ^{10}B , ^{157}Gd , ^{235}U , and ^{238}U) demonstrate a significant neutron capture probability [97], which leaves very few material options.

Solid materials composed of neutron-sensitive isotopes can be used for neutron detection in two ways: direct-conversion and indirect conversion (see Section 1.2.3), both exploiting the detection of ionizing charged particles produced upon neutron capture. Compared to indirect-conversion detectors, which are the state-of-the-art

semiconductor neutron detectors at present with neutron detection efficiencies as high as 30% [116], direct-conversion detectors are simple in terms of fabrication and can theoretically achieve neutron detection efficiencies as high as 100% [21], [89]. However, no neutron-sensitive semiconductor material has reached sufficient maturity to enable this technology beyond the basic research stage.

A number of solid materials comprised of neutron-sensitive elements have been considered for direct-conversion solid-state neutron detection [21]. The most researched among these include the ^{10}B materials such as boron phosphide [47], [48], boron carbide [60]–[71], boron nitride [49]–[54], boron arsenide [55]–[57] and boron selenide [58], [59], with some reports of lithium-containing chalcogenides [120], [188]. The main challenges in the development of these materials include establishing suitable fabrication methods and achieving adequate charge transport properties. To be considered for radiation detection, a semiconductor material should possess high charge carrier mobilities (μ_e, μ_h), long carrier lifetimes (τ_e, τ_h), and low leakage current. Low carrier mobilities and/or short lifetimes result in lower charge collection efficiency as a result of rapid carrier trapping. Low carrier mobilities also increase charge collection time, leading to slower detector response. The problems associated with suboptimal charge transport properties, however, can be improved by using thin films such that charge carriers are collected within a shorter timeframe with higher efficiency, even at relatively low applied electric fields. While this approach may lead to tradeoffs in neutron absorption efficiency and therefore, detection efficiency, pursuing such thin-

film detectors may be the best path forward given currently available material options. Additionally, thin-film technology presents more flexible fabrication options, integrates with thin-film based processing, and can enable the development of wide-area and flexible detectors, important for applications such as neutron imaging [20], [189], and neutron spectroscopy [190].

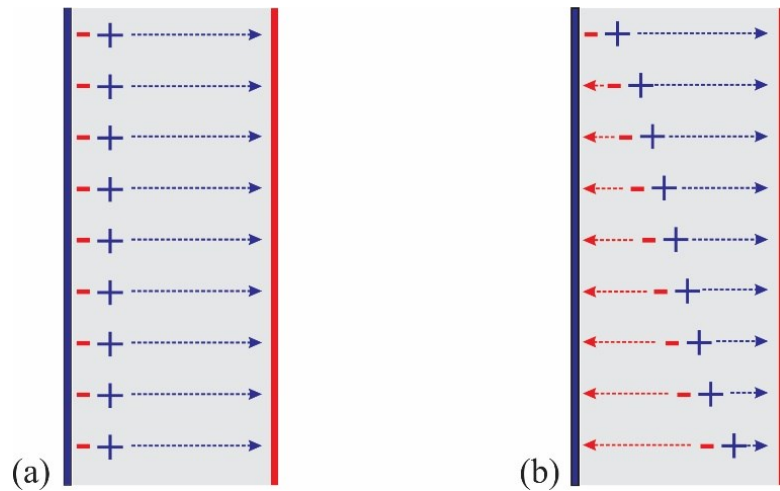


Figure 3.1 (a) Surface excitation by short-penetration-depth radiation: only one type of carrier contributes to total charge collection. (b) Excitation within the detector volume: both carriers contribute to total charge collection.

In developing thin-film neutron detectors, it is important to consider the unique physics associated with this configuration. The thickness of a direct-conversion semiconductor affects not only the absorption of incident radiation but also the charge collection process. In detectors where incoming radiation has a very short penetration depth relative to detector thickness (Figure 3.1a), charge carriers are generated very

close to the incident surface, and the detector essentially works in single-carrier mode. The induced current signal is predominantly due to charge carriers drifting from the incident surface toward the collecting electrode. However, in thin-film detectors where radiation has a high penetration depth relative to detector thickness (Figure 3.1b), charge carriers are generated throughout the detector volume. Here, the ideal requirement for maximum detection efficiency would be the collection of both types of charge carriers (electrons and holes). However, because existing neutron-sensitive materials are not optimized as semiconductors, and their charge transport properties are unknown or controversial [21], we cannot assume that both types of charge carriers are mobile. It is more likely that there is an order of magnitude or greater difference in mobility between charge carriers, as is the case for many semiconductors (for example, SiC, GaAs, CdZnTe, and CdS). If one of the charge carrier types is much slower than the other, only the faster carrier contributes to the actual charge collection. Further, because the collected charge depends on the actual distance traveled by the drifting carriers, the faster carriers induce only a fraction of the total deposited charge depending on their initial distance from the collecting electrode and the integration/shaping time of the detector electronics. This results in incomplete charge collection that depends on the position of the incident radiation interaction in the detector, which in general leads to decreased energy resolution as well as challenges in interpreting the resulting signal.

Although a few detector designs [191]–[195] have been specifically developed to exploit single-carrier transport (for example, Frisch detectors, coplanar grid

detectors) to increase energy resolution at the expense of overall detection efficiency, the vast majority of radiation detectors are based on dual-carrier transport, and single-carrier devices are rarely discussed. Additionally, most detectors are based on well-developed semiconductors with optimized charge carrier transport properties (including the above-mentioned single-carrier devices). In the case of direct-conversion solid-state thermal neutron detection, with fewer available materials to work with, a detailed understanding of the performance of such detectors with only one type of mobile carrier and/or with low carrier mobility is necessary for the screening of potential materials. To our knowledge, such work has not yet been published. For thermal neutron detectors specifically, theoretical studies of both indirect-conversion detectors (including microstructured neutron detectors) and direct-conversion detectors have been published [61], [64], [71], [89], [107], [114], [196], however without rigorous treatment of charge transport properties. In these reports, either complete charge collection is assumed, or the charge collection process is simplified, and studies using advanced simulation toolkits tend to focus on tracking the primary reaction products inside the detector. For direct-conversion detectors in particular, however, the effects of the charge transport properties on detection efficiency far outweigh those of the small deviations in the tracks followed by the reaction products.

Herein we investigate the performance of thin (relative to neutron penetration depth) direct-conversion solid-state neutron detectors with a wide range of charge carrier mobilities, carrier lifetimes, and detector thicknesses using Monte Carlo

simulation techniques, assuming only one type of charge carrier is mobile. The simulations are focused on boron-based materials, specifically using ^{10}B -enriched boron carbide (B_4C) as a representative neutron absorber/semiconductor, as this material class has been the most heavily studied in the context of direct-conversion neutron detection [60]–[71], [92]. However, the results should apply to B_xC stoichiometric variations or other boron-based solids in general. Unlike in most other simulations, we do not track the primary reaction products in the detector but rather apply a simplified energy deposition scheme with the charged particles traveling along a straight path within the detector medium based on the Stopping and Range of Ions in Matter (SRIM) package [197]. We provide a detailed analysis of the effects of charge transport properties on theoretical detection efficiency and pulse height spectra and describe how charge transport properties and detector operation can be optimized. This work will be helpful to researchers working in neutron or other radiation detection fields where available detector materials exhibit immature fabrication processes or semiconducting properties.

3.2. Interaction of Thermal Neutrons with B_4C

Neutrons interact with nuclei in many different ways, as we discussed in Section 1.2. Specifically for thermal neutrons, the most dominant interaction mechanisms in B_4C is their absorption by ^{10}B , resulting in the emission of an α particle and a Li ion, as described by Equation (3.1).

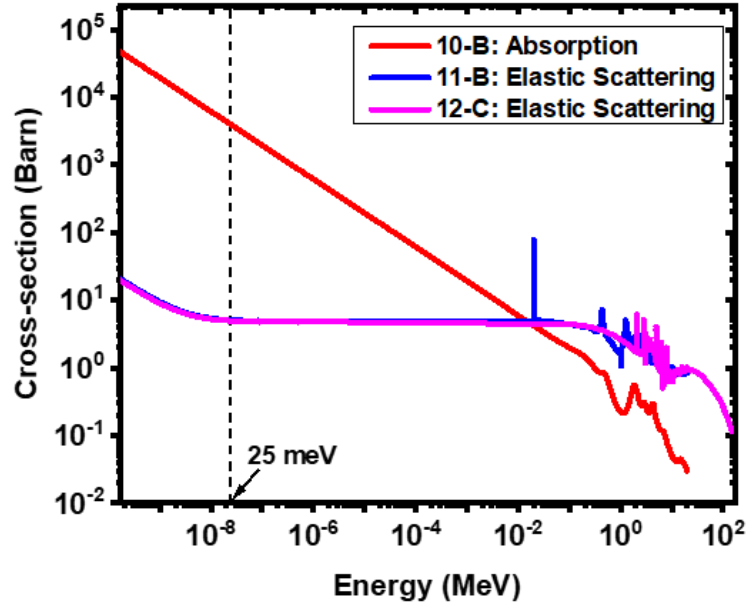
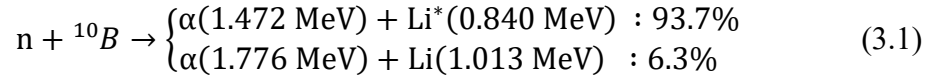


Figure 3.2. Microscopic neutron cross-sections for the constituent nuclei of B₄C for dominant thermal neutron interaction processes. The absorption of neutrons by ¹⁰B is significantly higher than any other interaction process.

The neutron interaction probability in a material compound is determined by the total macroscopic cross-section (Σ), which is defined as

$$\Sigma = \sum_i \frac{N_a \rho}{M} \sigma_i n_i \quad (3.2)$$

where N_a , ρ , and M are Avogadro's constant, density, and molar mass of the compound, respectively, and n_i and σ_i are respectively the number and microscopic cross-sections

of the i^{th} type nuclei in a molecule of the compound. Figure 3.2. shows the microscopic cross-sections for the most dominant interaction mechanism for neutrons in B_4C . As we can see in the figure, the most dominant interaction mechanism for thermal neutrons is by far their absorption by ^{10}B , and the other types of interaction cross-sections can be neglected for calculation purposes.

The absorption cross-section of ^{10}B for thermal neutrons (26 meV) is 3850 barns (1 barn = 10^{-24} cm^2). Taking the density of B_4C as $2.52 \text{ g}\cdot\text{cm}^{-3}$ [198], the macroscopic cross-section for neutron absorption in the detector material can be shown to be 423.02 cm^{-1} , which corresponds to a thermal neutron mean free path (i.e., neutron absorption depth) of $23.6 \text{ }\mu\text{m}$. As the macroscopic absorption cross-section is equivalent to the absorption coefficient for penetrating radiation, the thermal neutron intensity decays exponentially as a function of depth of the absorbing medium, and the probability of neutrons absorbed by a thin sheet of thickness dz at a depth z is given as

$$P(z) dz = \Sigma \exp(-\Sigma z) dz; \quad 0 \leq z \leq d \quad (3.3)$$

The total neutron absorption probability of a detector as a function of its thickness d is then given as

$$P(d) = 1 - \exp(-\Sigma d) \quad (3.4)$$

Figure 3.3 shows the neutron absorption probability of a ^{10}B -enriched B_4C detector as a function of detector thickness. The figure shows that a $20 \text{ }\mu\text{m}$ thick detector absorbs >50% of incident neutrons.

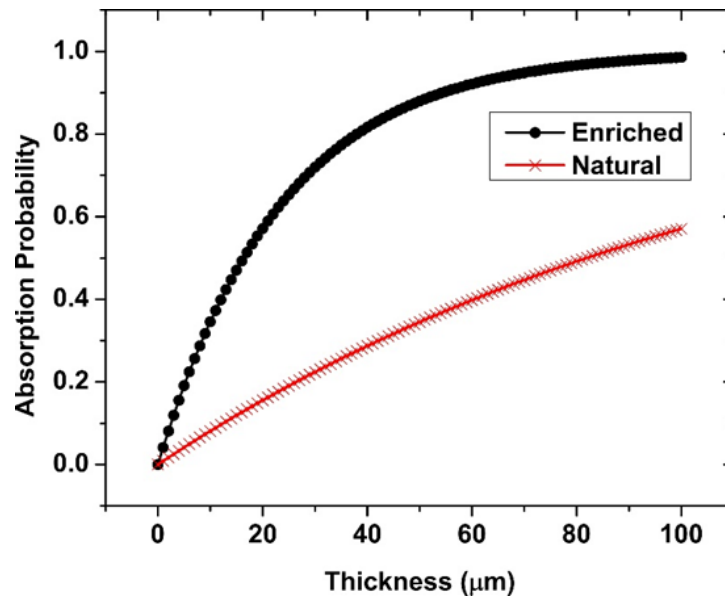


Figure 3.3 Thermal neutron absorption probability of natural B_4C and ^{10}B -enriched B_4C thin film as a function of detector thickness.

3.3. Theory: Direct-Conversion Neutron Detection

As a neutron-sensitive nucleus captures a thermal neutron, two ionizing primary reaction products are emitted, as shown in Figure 3.4. Because of the negligible momentum of the incident neutron, the reaction products are emitted in opposite directions following the conservation of linear momentum. Since the emission process is random, the primary reaction products are emitted in any direction within a 4π solid angle. If a reaction product makes an angle θ with the direction of the incident neutron, the probability that the reaction products are emitted within a small range $d\theta$ about θ is given by

$$P(\theta) d\theta = \frac{1}{2} \sin \theta d\theta; \quad 0 \leq \theta \leq \pi \quad (3.5)$$

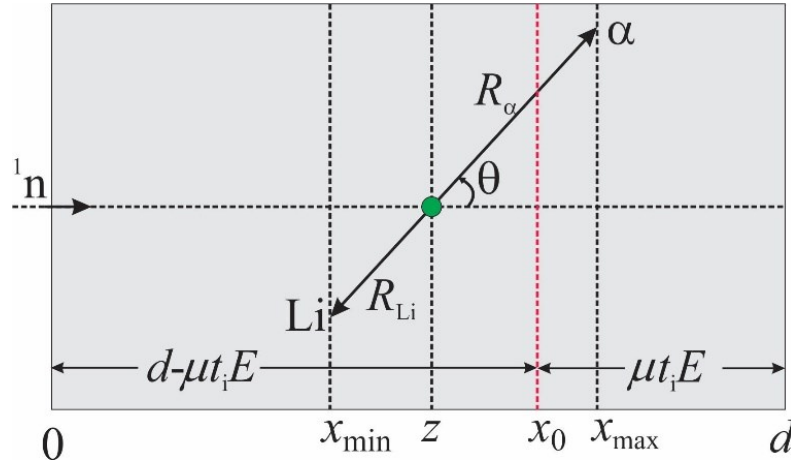


Figure 3.4 Schematic of neutron absorption and energy deposition in a direct-conversion neutron detector.

As the reaction products travel within the detector material, they excite electron–hole pairs along their tracks within a few picoseconds. As soon as the charge carriers are generated, they move under the applied electric field within the detector and induce a signal current, which is described by the Shockley–Ramo theorem as[184]

$$I_0 = \frac{q\mu E}{d} = \frac{q}{t_{tr}} \quad (3.6)$$

where q is the charge generated in the device by the ionizing radiation, μ is the charge carrier mobility, E is the applied electric field, d is the device thickness, and $t_{tr} = d/\mu E$ is the carrier transit time, the time required for a charge carrier to travel the total device thickness d . In all semiconductor materials, charge carriers have a finite lifetime

because of carrier trapping and recombination. If τ is the carrier lifetime, under the simplest assumption, the induced current decays exponentially as

$$I = I_0 \exp\left(-\frac{t}{\tau}\right) \quad (3.7)$$

In the case of energy deposition by neutrons in boron-10 compounds, the track length of the primary reaction products is generally 5–10 μm [97], which can be comparable to detector thickness. As the charge carriers are distributed along the track lengths, the signal current not only decreases due to carrier trapping/recombination, but also due to charge carriers being extracted from the device continuously by the applied electric field.

Single-particle detectors generally do not amplify the current signal directly to a voltage signal (e.g., by using a transimpedance amplifier). For detectors with optimized charge carrier mobilities, the rise time of the current signal can be very short (\sim picoseconds), and accurately measuring the peak current I_0 is difficult with the limited bandwidth of the amplifiers. Instead, these detectors integrate the current signal and convert the collected charge to a voltage signal that remains across a capacitor long enough for the detector electronics to process it.

The total charge collected in an ideal integrator circuit for a specific integration time (t_i) is obtained as

$$Q_{\text{coll}} = \int_0^{t_i} I dt \quad (3.8)$$

We note that here, the integration time (t_i) does not necessarily refer to the commonly used RC integration time, but rather the time at which the collection of charge is effectively stopped.

With sufficiently high mobility and under sufficiently high electric fields, integration time can be set longer than carrier transit time ($d/\mu E$), which is the general approach used for mature semiconductor detectors. In such cases, if $q(x)$ is the linear charge carrier density excited by the incident radiation, the charge induced by the charge carriers in a small thickness dx at a distance x from the incident surface moving along the x -axis is then given by

$$dQ_{\text{coll}} = \frac{\mu E}{d} q(x) dx \int_0^{\frac{d-x}{\mu E}} \exp\left(-\frac{t}{\tau}\right) dt \quad (3.9)$$

where $(d-x)/\mu E$ is the transit time of the carriers generated at x . With this assumption, the total charge collected due to the motion of all of the carriers excited between x_{min} and x_{max} (see Figure 3.4) is obtained by integrating Equation (3.9) as

$$Q_{\text{coll}} = \frac{\mu \tau E}{d} \left[Q_{\text{deposited}} - \exp\left(-\frac{d}{\mu \tau E}\right) \int_{x_{\text{min}}}^{x_{\text{max}}} q(x) dx \exp\left(\frac{x}{\mu \tau E}\right) \right] \quad (3.10)$$

Similarly, for the charge carriers moving along the negative x -axis, the total charge collected is given as

$$Q_{\text{coll}} = \frac{\mu \tau E}{d} \left[Q_{\text{deposited}} - \int_{x_{\text{min}}}^{x_{\text{max}}} q(x) dx \exp\left(-\frac{x}{\mu \tau E}\right) \right] \quad (3.11)$$

If both types of charge carriers are mobile, the total charge collected is given by the sum of Equations (3.10) and (3.11). These equations also show that the collected charge in a detection event can be described by the mobility–lifetime product ($\mu\tau$). However, the role of the initial charge carrier distribution $q(x)$ within a small region of the detector volume becomes very important when a single type of charge carrier contributes to charge collection.

For semiconductors with low carrier mobility, it is not always possible to achieve a transit time shorter than the integration or pulse shaping time. There are limits to increasing mobility via increasing electric field owing to challenges with leakage current or device breakdown, and/or possible instrumentation constraints. Further, extending the integration time can lead to charge saturation of the capacitor within the integration circuit or problems with signal overlap due to successive incident radiation events. In such cases, it may be necessary or desirable to cut off the charge collection at a shorter integration time. In practice, this can be done by actually setting a shorter RC time or by setting the pulse shaping time shorter than the carrier transit time.

In the case where integration time (t_i) is shorter than carrier transit time ($d/\mu E$), the charge collection due to a single type of carrier moving along the x -axis is given as

$$Q_{\text{coll}} = Q_{\text{deposited}} - \frac{\mu\tau E}{d} \exp\left(-\frac{t_i}{\tau}\right) \int_{x_{\min}}^{x_0} q(x) dx - \frac{\mu\tau E}{d} \exp\left(-\frac{d}{\mu\tau E}\right) \int_{x_0}^{x_{\max}} q(x) \exp\left(\frac{x}{\mu\tau E}\right) dx \quad (3.12)$$

where $x_0 = d - \mu t_i E$ separates two regions of the detector such that all of the carriers generated in the region $x < x_0$ cannot make it to the collecting electrodes within the integration time (t_i), resulting in partial charge collection. Here, we assume that the carriers moving toward the positive x -axis are mobile (faster) such that they can travel a longer distance in the detector for the majority of the neutron absorption events and contribute to higher charge collection. In Equation (3.10), the parameters x_{\min} , x_0 , x_{\max} , and the charge density $q(x)$ depend on the random nature of the neutron absorption position and the emission angle of the primary reaction products. Thus, an analytical expression of charge collection for a single event does not exist, and a numerical approach must be used to evaluate the charge collection in each event, the pulse height spectrum obtained from such detectors, and the overall detection efficiency.

3.4. Simulation Setup

3.4.1. Detector Geometry, and Contacts

The thermal neutron detector chosen for this simulation is a direct-conversion-type metal–insulator–metal device of thickness d with ideal Schottky contacts, such as that shown in Figure 1.6 so that the leakage current in the device is negligible. The detector area is very large compared to detector thickness, such that the fraction of neutron absorption events resulting in the escape of primary reaction products from the edge of the detector can be considered negligible.

3.4.2. Energy Deposition by Primary Reaction Products

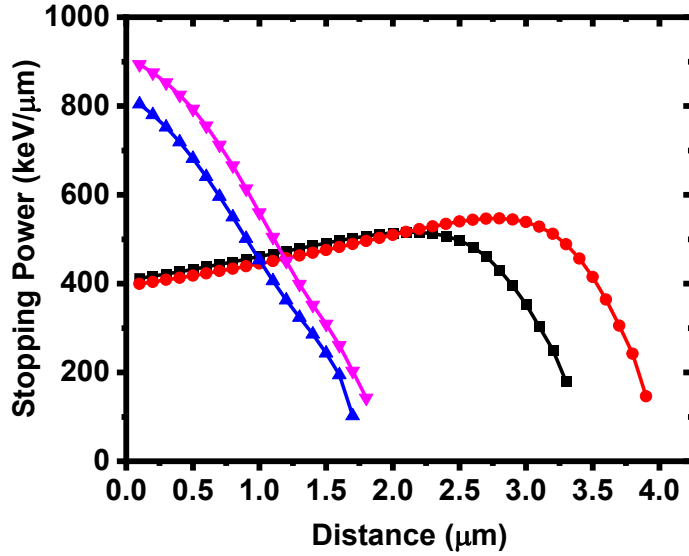


Figure 3.5 Stopping powers of 1.47 MeV α particle (\blacksquare), 1.78 MeV α particle (\bullet), 0.84 MeV Li ion (\blacktriangle), and 1.02 MeV Li ion (\blacktriangledown) emitted from neutron- ^{10}B interaction in B_4C .

The primary reaction products (α particle and Li ion) travel along straight lines and deposit energy primarily via the Coulomb interaction with the electrons in the detector medium. The stopping power of the detector medium (B_4C) for the primary reaction products is calculated using the Stopping and Range of Ions in Matter (SRIM) package [199], as shown in Figure 3.5. For simulation purposes, the stopping power for each reaction product is approximated by polynomials. The total energy deposited is then obtained by integrating the stopping power over the reaction product track lengths within the detector volume.

3.4.3. Charge Carrier Excitation and Collection (Signal Generation)

The stopping power obtained from SRIM calculations represents the stopping power along the track length of a primary reaction product. However, to calculate the charge collection using Equation (3.10), we need the charge density $q(x)$ as a function of coordinates along the detector thickness. Thus, the stopping power along the primary reaction product tracks is transformed to the stopping power along the detector thickness based on the emission angle of the primary reaction product. If $u(x)$ is the stopping power along the detector thickness, the linear charge density is then obtained as

$$q(x) = \frac{u(x)e}{E_p} \quad (3.13)$$

where e is the electronic charge, and E_p is the energy cost per electron–hole pair excitation given as [200]

$$E_p = \frac{14}{5} E_g + \langle r \rangle \quad (3.14)$$

where E_g is the bandgap of the detector material, and $\langle r \rangle$ is a material-dependent constant that lies between 0.5 and 1 eV. For simulation purposes, to represent a broad class of materials for neutron detection, we assume a bandgap of 3–4 eV, which corresponds to an energy cost of about 10 eV per pair. However, the inclusion of a specific value of bandgap in the calculation is straightforward, and the value chosen only changes the total charge deposited in the device. Taking an energy cost of 10 eV per pair, the total charge deposited in a single neutron absorption event is about 37 or

45 fC based on the selected branch of the neutron–boron interaction given in Equation (3.1).

With a simple rearrangement of Equation (3.10), we obtain that the collected charge depends on three parameters: $\mu\tau E/d$, $\mu t_i E/d$, and the device thickness d . Here, $\mu\tau E/d$ is the ratio of charge carrier drift length to device thickness and $\mu t_i E/d = t_i/t_{tr}$ is the ratio of integration time to carrier transit time. Both of these quantities represent the average distance that charge carriers can travel within the device before they get trapped/recombined or the integration is stopped for signal processing purposes. To understand the effect of these parameters on charge collection and detection efficiency, numerical calculations are performed within the following ranges of parameters that represent a broad combination of material properties and experiment configurations: carrier mobility (μ), carrier lifetime (τ), device thickness (d), and integration time (t_i).

- A detection threshold (lower level discrimination) of 10 fC. In an ideal case when both carriers are mobile, a total of 10 fC of charge is about 25% of the total charge deposited in a B₄C device. Because we are considering a single-carrier device, the maximum possible charge collection efficiency in thin devices ($d \ll 1/\Sigma$) is 50%, resulting in the detection threshold being 50% of the maximum possible charge collection. Thus, we believe a threshold of 10 fC is appropriate based on the total charge available as well as the device limits of currently available charge sensitive amplifiers.

- $0.1 \leq \mu\tau E/d \leq 1000$ with 20 data points per decade. The lower bound of $\mu\tau E/d = 0.1$ is chosen because this represents a charge collection efficiency of 10%, which corresponds to a collected charge of about 5 fC and falls below the detection threshold of 10 fC. (We note that for detector materials in which the deposited charge can be very high such as in uranium oxides, where an incident neutron results in the fission of uranium and a large amount of deposited energy, even 1% charge collection can constitute a detectable signal, which can be easily incorporated in the calculation.) The upper bound of 1000 represents a value above which charge collection does not increase significantly. Thus, the selected range can represent any combination of detector thickness, carrier mobility, and carrier lifetime that can be appropriate for signal generation and detection.
- $0.1 \leq \mu t_i E/d \leq 1.0$ in steps of 0.1. The lower bound is chosen again based on the fact that the charge collection for $\mu t_i E/d < 0.1$ is less than 10% and does not contribute to a detectable signal for a B₄C device. The maximum value of 1.0 represents an integration time equal to the transit time of the carriers. Although charge-sensitive preamplifiers can use integration times longer than carrier transit time, this does not increase charge collection. A longer integration time is used only to maintain the voltage signal for a longer time if the current signal decays very fast. We recall that $\mu t_i E/d$ is the ratio of integration time to charge carrier transit time (t_i/t_{tr}), and a lower

value of $\mu t_i E/d$ does not merely represent a shorter integration time, but additionally the case of low charge carrier mobility where transit time is inherently longer than integration time.

- Detector thickness (d) 1–25 μm in steps of 1 μm . Very thin devices suffer from partial energy deposition as the primary reaction products escape from the detector volume. To represent these thin detectors, a lower limit of 1 μm is chosen. The upper bound of 25 μm is chosen because the neutron absorption depth of the example material (B_4C), is 23.6 μm , and a 25 μm thick device absorbs nearly 65% of the total incident neutron. This range therefore clearly captures the trends in thickness increase, while limiting total simulation time.

3.4.4. Simulation Process

For each of the material or detector parameters listed above, one million neutrons are simulated. It is assumed that the neutron beam is collimated and perpendicular to the detector surface. For the interaction position of an incident neutron inside the detector, a random number z is generated with the probability distribution given by Equation (3.3). All of the numbers that fall within $z > d$ are labeled not absorbed and discarded from further calculations. For all other z , the emission angle of the primary reaction product is obtained by generating a random number θ with a probability distribution given by Equation (3.5). To select the appropriate branch of the

neutron–boron interaction given by Equation (3.1), random numbers between 0 and 1 are generated with a uniform probability distribution. All resulting numbers below 0.937 are assigned to the first branch, and the remaining numbers are assigned to the second branch. Based on the interaction position z , emission angle θ , selected interaction branch, and detector thickness d , the linear energy density $u(x)$ and the linear charge density $q(x)$ are calculated. The total energy deposited within the detector volume is obtained by integrating the energy density $u(x)$ over the range of the primary reaction products, and the total charge collected is calculated using Equation (3.10).

To analyze the data obtained, the deposited energy and the collected energy/charge are recorded for every incident neutron. The distribution of the energy deposited/collected is then converted to a histogram with an energy width of 20 keV. Although a neutron is labeled “detected” when the collected charge is above the set detection threshold, it is impractical to define the charge collection efficiency (CCE) for all one million individual incident neutrons. Thus, CCE is evaluated by averaging the total charge collected for all absorbed neutrons (either detected or not detected). The charge collection efficiency defined in this way is identical to the charge collection efficiency defined in the case of photoconductivity experiments [172], [186], [201], which is a standard form of characterization for many detector materials.

3.5. Results and Discussion

3.5.1. Total Energy Deposition: The Case of 100% Charge Collection of Both Types of Charge Carriers

For most mature radiation detector technologies, the charge collection efficiency is assumed to be 100% such that the spectroscopic information from the incident radiation is accurately obtained. Although this work primarily focuses on the case of incomplete charge collection due to both single-carrier transport as well as potentially low carrier mobility (leading to transit times longer than integration times), we first present the case of complete charge collection assuming both carrier types are mobile and contribute to detection. This result also allows us to confirm the validity of our simulations through comparison with previously reported results obtained using different simulation schemes.

Figure 3.6 shows the deposited energy spectra obtained by averaging multiple runs of the simulation, each having one million incident neutrons, for different detector thicknesses. The energy resolution is set at 20 keV.

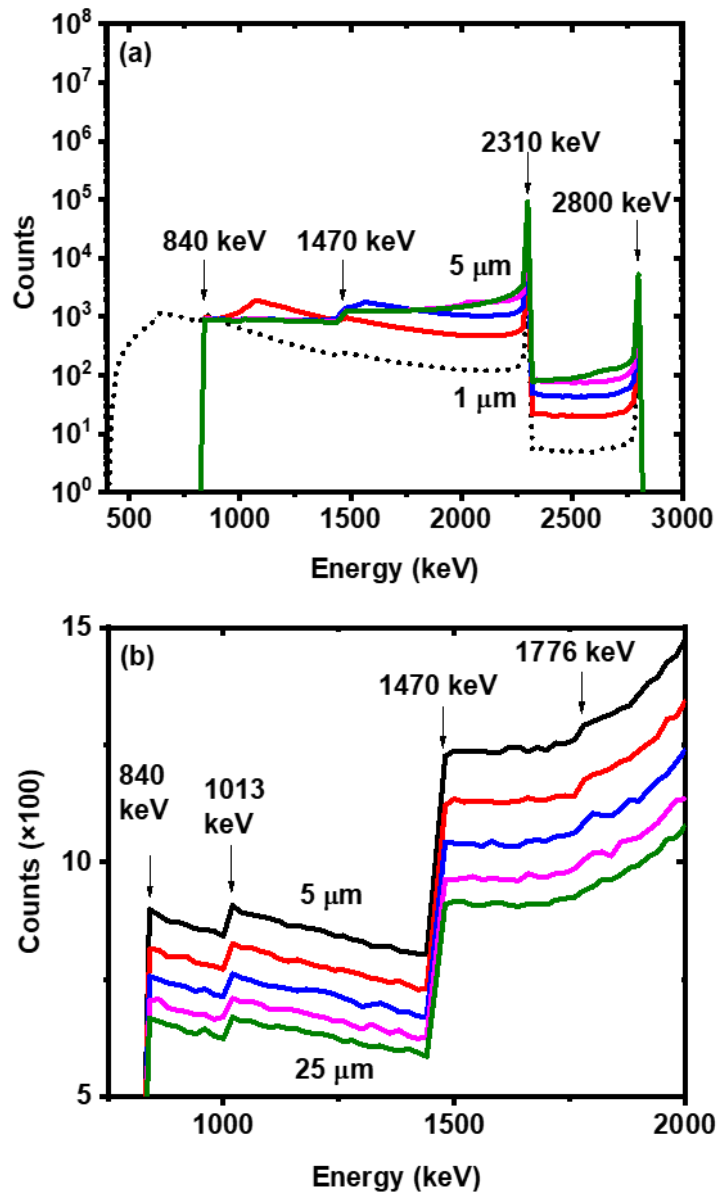


Figure 3.6 (a) Energy deposition pulse height spectra for B_4C devices with thicknesses of 1–5 μm and (b) 750–2000 keV region of the pulse height spectra for devices with thicknesses of 5–25 μm .

Figure 3.6a shows the energy deposition pulse height spectra for 1–5 μm thick devices. The spectrum obtained for a 1 μm thick device shows features similar to those

obtained by other studies [61], [71], [89], including some using the GEANT simulation package, and theoretical calculations based on the so-called simple physical model [71]. The first spectral peak seen at ~ 650 keV is due to partial energy deposited by the primary reaction products. Because the shortest range of the primary reaction product is $1.74 \mu\text{m}$ for Li (840 keV), as soon as the detector thickness exceeds this number, a minimum energy of 840 keV is deposited in the detector. Thus, the pulse height spectra for detectors thicker than $1.74 \mu\text{m}$ start from 840 keV. For these devices, two individual peaks corresponding to the Li (840 keV) and α (1470 keV) particles are seen as small steps, whereas the individual peaks corresponding to the Li (1013 keV) and α (1776 keV) particles are very weak and are visible only when zoomed in with a linear scale, likely due to the small probability of the second branch of interaction given in Equation (3.1). Although the individual peaks are weak, because they correspond to only those neutrons which are absorbed very close to the detector surfaces, the sum peaks at 2310 and 2800 keV, which correspond to the total energy deposited according to the first and second branches of Equation (3.1), are clearly visible, and the intensities of the sum peaks increase with device thickness. Figure 3.6b shows the 750–2000 keV region of the pulse height spectra for detectors with thicknesses of 5, 10, 15, 20, and 25 μm with a linear scale. It can be seen that the intensities of the individual peaks decrease with increasing device thickness, commensurate with the increase in the sum peaks. Other than small changes in peak intensities, devices thicker than 5 μm show similar spectral features.

Although our simulations do not consider scattering and straggling of the primary reaction products that the commonly used simulation packages incorporate, the pulse height spectra calculated in this study are similar to those obtained with the standard packages. Our conclusion is that, although scattering and straggling have significant implications in designing microstructured indirect-conversion neutron detectors (MSNDs) [109]–[114], [202], they do not affect the performance of direct-conversion detectors.

3.5.2. Charge Collection Efficiency: Effect of Charge Transport Properties and Device Thickness

Our motivation in this work is to understand the effect of incomplete charge collection in neutron detection, which can occur for two reasons: (1) single-carrier transport, and/or (2) low carrier mobility, such that carrier transit time ($d/\mu E$) becomes longer than integration time. However, to start our discussion, we first assume single-carrier transport with charge carrier mobility high enough to achieve a transit time shorter than the integration time so that the quantity $\mu t_i E/d$ does not affect the charge collection efficiency. Figure 3.7a summarizes the charge collection efficiency calculated for devices with thicknesses of 1–25 μm as a function of $\mu\tau E/d$ under such conditions. The figure shows that the charge collection efficiency for thin devices ($\Sigma d \ll 1$) is limited to 50%. This is because when the detector is very thin relative to the absorption depth of the incident radiation ($d \ll 1/\Sigma$), the charge carriers can be assumed to be generated uniformly throughout the detector volume, and on average

travel across only half of the detector thickness (i.e., carriers generated at the incident surface travel across the entire detector thickness whereas carriers generated on the collecting surface do not travel at all), leading to 50% CCE. In such a case, the charge collection efficiency can be described by Hecht relation [172], [186] for the uniform absorption, used to describe charge collection in photoconductivity experiments as

$$CCE = \frac{\mu\tau E}{d} \left[1 - \frac{\mu\tau E}{d} \left(1 - \exp\left(-\frac{d}{\mu\tau E}\right) \right) \right] \quad (3.15)$$

For the general case, where radiation attenuates exponentially with device thickness, the expression for charge collection efficiency for a single type of carrier can be shown to be

$$CCE = \frac{\mu\tau E}{d} \left[1 - \frac{\Sigma d \frac{\mu\tau E}{d}}{\Sigma d \frac{\mu\tau E}{d} - 1} \left[\frac{\exp\left(-\frac{d}{\mu\tau E}\right) - \exp(-\Sigma d)}{1 - \exp(-\Sigma d)} \right] \right] \quad (3.16)$$

where Σ is the macroscopic neutron absorption cross-section (or absorption coefficient in the case of light) and explains the increasing CCE for increasing device thickness in Figure 3.7a. However, because the macroscopic neutron absorption coefficient of B₄C used in this simulation is 423.02 cm⁻¹, devices with thicknesses up to 25 μ m still generally adhere to the uniform radiation absorption approximation, and the charge collection efficiencies of a 1 μ m and a 25 μ m device are therefore similar. Equation (3.16) can be used to obtain the mobility–lifetime product ($\mu\tau$) from steady-state irradiation experiments (neutron or other) without requiring either surface or uniform absorption conditions (i.e., not requiring very specific device thicknesses).

For very thick devices ($d \gg 1/\Sigma$), the absorption gradually shifts toward surface absorption, and the charge collection efficiency is given as [172], [186]

$$CCE = \frac{\mu\tau E}{d} \left[1 - \exp\left(-\frac{d}{\mu\tau E}\right) \right] \quad (3.17)$$

Although a high charge collection efficiency is expected when $\mu\tau E/d$ (or more generally, $\mu\tau$, the mobility–lifetime product) is sufficiently large, it is possible that these large values might represent long carrier lifetimes rather than high charge carrier mobilities. If the carrier mobility is too low, the transit time can be longer than the integration time, and we must consider the individual effects of carrier mobility and carrier lifetime, as well as the choice of integration time, and not just the $\mu\tau$ product. We, therefore, consider the second case of a large value of $\mu\tau E/d$, however with low charge carrier mobility (and therefore a relatively long carrier lifetime) such that the charge collection efficiency depends on the integration time (or the parameter $\mu t_i E/d = t_i/t_{tr}$). Figure 3.7b shows the variation of charge collection efficiency as a function of $\mu t_i E/d$ for a sufficiently large value of $\mu\tau E/d$ ($\mu\tau E/d > 10$). For thin detectors, the maximum charge collection efficiency, considering only one type of charge carrier, as a function of $\mu t_i E/d$ can be written as

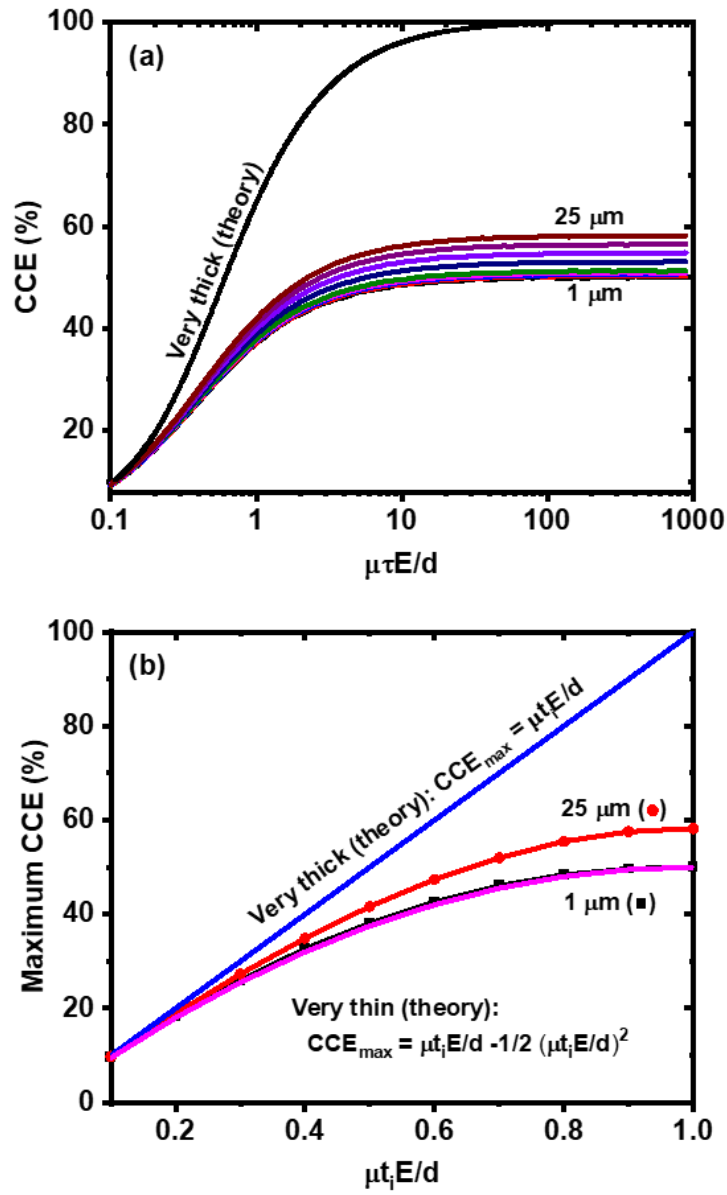


Figure 3.7. (a) Charge collection efficiency for B₄C detectors 1–25 μm thick as a function of $\mu\tau E/d$ assuming a single type of charge carrier for $t_i \geq d/\mu E$. (b) Maximum charge collection efficiency possible as a function of $\mu t_i E/d$ with high enough $\mu\tau$ product.

$$CCE_{\max} = \frac{\mu t_i E}{d} - \frac{1}{2} \left(\frac{\mu t_i E}{d} \right)^2; \quad \frac{\mu t_i E}{d} \leq 1, \quad \frac{\mu \tau E}{d} > 10 \quad (3.18)$$

When the device becomes very thick, the maximum CCE is then given as

$$CCE_{\max} = \frac{\mu t_i E}{d}; \quad \frac{\mu t_i E}{d} \leq 1, \quad \frac{\mu \tau E}{d} > 10 \quad (3.19)$$

In both of these cases, the increase in charge collection efficiency with increasing integration time is a result of charge carriers traveling a further distance inside the detector.

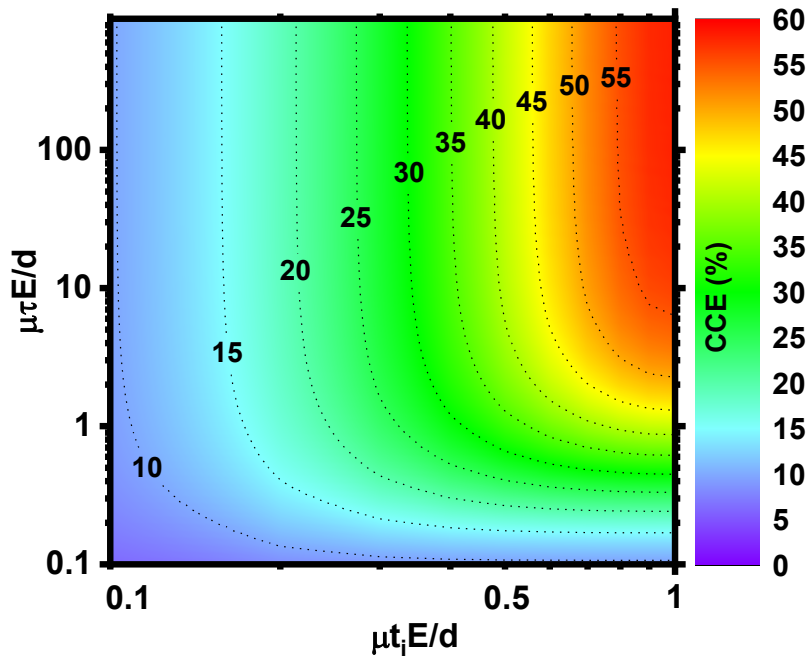


Figure 3.8. The variation of charge collection efficiency (CCE) as a function of $\mu \tau E/d$ and $\mu t_i E/d$ for a 25 μm thick device.

Figure 3.8 illustrates how charge collection efficiency depends on both $\mu\tau E/d$ and $\mu t_i E/d$ for the case of a 25 μm detector. If we recall that a lower value of $\mu t_i E/d$ represents the case of low charge carrier mobility, we can say that the figure demonstrates the effect of carrier lifetime along the vertical axis and of carrier mobility along the horizontal axis on charge collection efficiency. For low values of $\mu\tau E/d$ (e.g., <1), the charge collection efficiency is low in general, which can be either due to a low carrier mobility or low carrier lifetime. However, when $\mu\tau E/d$ exceeds ~ 10 , which represents a longer carrier lifetime, the charge collection efficiency saturates at a value which depends on $\mu t_i E/d$, which can be considered as a proxy for carrier mobility. Thus, for maximal CCE, a high $\mu\tau$ value is not sufficient, but rather a high $\mu\tau$ and μ value is required.

3.5.3. Detection Efficiency: Effect of Charge Transport Properties and Device Thickness

As we have defined the charge collection efficiency (CCE) as a collective measure of a large number of simulated neutrons, it is reasonable to expect this charge collection efficiency to show behavior similar to that of the CCE defined for photoconductivity experiments as we discussed in the previous sections. The detection of an individual neutron cannot be simply related to the thus defined CCE because the charge collection for a single event depends on many factors (neutron interaction position, emission angle, and nuclear reaction branch). However, if we define a

detection threshold and corresponding minimum charge collection efficiency (CCE_{\min} = detection threshold / total charge), then we can determine the minimum carrier mobility required to achieve neutron detection.

In neutron detection, there is a finite probability that the primary reaction products are emitted perpendicular to the detector thickness ($\theta = \pi/2$ in Equation (3.5)) even in a very thin detector. In fact, the probability density for $\theta = \pi/2$ is maximum. In such cases, the collected charge is independent of the initial spatial distribution of charge carriers and increases linearly with integration time, similar to the case of very thick detectors (see Figure 3.7b and Equation (3.19)), provided that the charge carriers have a long enough lifetime to remain free during this period. The absolute minimum mobility required for detection in such cases is then obtained by solving

$$\frac{\mu t_i E}{d} \geq CCE_{\min} \quad (3.20)$$

As it is relatively straightforward to obtain the maximum safe electric field that can be applied, and to select an integration time that depends on the detection application (e.g., radiation flux in a given detection environment) and/or available detector electronics, the expression can also be used to obtain the maximum possible thickness of a device that can effectively work as a detector for a given value of carrier mobility, and ultimately the maximum detection efficiency it can achieve, which then scales with carrier lifetime (or $\mu\tau E/d$).

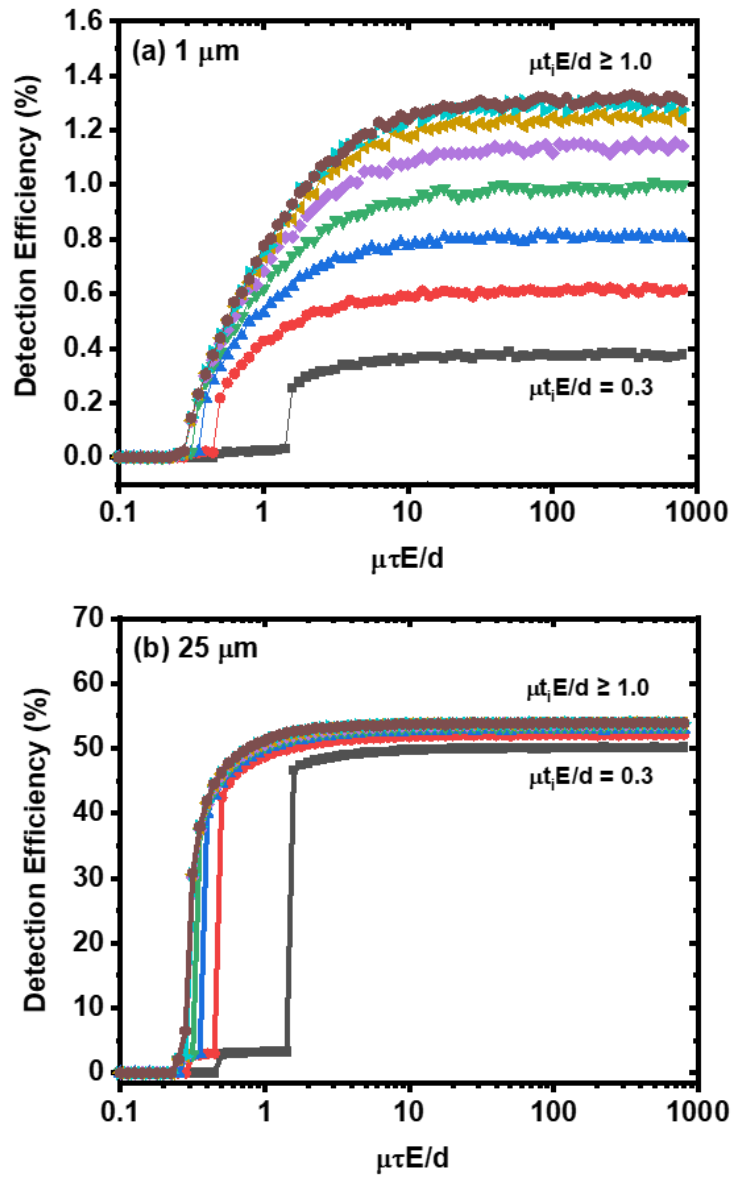


Figure 3.9. Neutron detection efficiency as a function of $\mu\tau E/d$ at different values of $\mu t_i E/d$ for (a) a 1 μm device and (b) a 25 μm thick device. The detection threshold is set at 10 fC.

Figure 3.9 presents the neutron detection efficiency for 1 and 25 μm thick devices as a function of $\mu\tau E/d$ at different values of integration time ($\mu t_i E/d$). The

data for $\mu t_i E/d = 0.1$ and 0.2 have been discarded because these values result in charge collection lower than the set detection threshold (10 fC) even for very large $\mu\tau E/d$. We can see from Figure 3.9 that detection is possible when $\mu t_i E/d$ exceeds 0.3, which satisfies the detection condition given in Equation (3.20). We can also see that for lower values of $\mu t_i E/d$, detection starts at a higher value of $\mu\tau E/d$, which is expected because of the dependence of charge collection efficiency on integration time, given as

$$CCE = \frac{\mu\tau E}{d} \left(1 - \exp\left(-\frac{\frac{\mu t_i E}{d}}{\frac{\mu\tau E}{d}}\right) \right) \quad (3.21)$$

We can see that the detection efficiency of thinner devices increases slowly with increasing $\mu\tau E/d$. However, for thicker devices, the detection efficiency quickly rises and saturates to a maximum value as soon as $\mu\tau E/d$ exceeds the detection threshold. Figure 3.9 also shows that the maximum detection efficiency of a detector is limited not only by its thickness but also by the chosen integration time ($\mu t_i E/d$). However, as can be seen more clearly in Figure 3.10, with increasing detector thickness, the effect of choosing a shorter integration time decreases for very thick devices as long as the collected charge is above the detection threshold. For example, the loss of ~6% detection efficiency from a maximum detection efficiency of 14% for a 5 μm thick detector is more significant than the loss of ~4% from the maximum detection efficiency of 54% for a 25 μm thick detector.

When the detector is very thick relative to the range of the primary reaction products so that the excited charged particles are confined at a point, the detection efficiency as a function of $\mu\tau E/d$ with a sufficiently long integration time can be shown to be

$$\eta = 1 - \exp\left[-\Sigma d \left(1 + \frac{\mu\tau E}{d} \ln\left(1 - CCE_{\min} \frac{d}{\mu\tau E}\right)\right)\right] \quad (3.22)$$

where CCE_{\min} is the detection threshold. The maximum detection efficiency is then obtained by setting $\mu\tau E/d \rightarrow \infty$ as

$$\eta_{\max} = 1 - \exp[-\Sigma d(1 - CCE_{\min})] \quad (3.23)$$

which also applies to using a shorter integration time. Thus, as long as we have a high enough mobility–lifetime product ($\mu\tau$) to achieve the detection threshold, the use of a shorter integration time does not affect the detection efficiency. In fact, this improves the spectral resolution of the detector, as we describe in the next section.

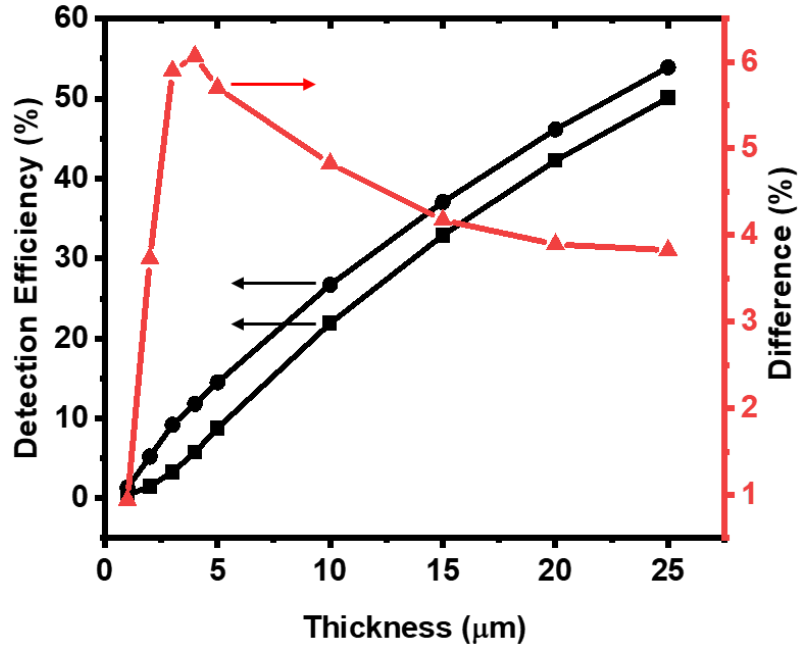


Figure 3.10. Maximum detection efficiency as a function of detector thickness for $\mu t_i E/d = 0.3$ (■), $\mu t_i E/d = 1.0$ (●), and their percentage difference (▲).

3.5.4. Pulse Height Spectra: Effect of Charge Transport Properties, Integration Time, and Device Thickness

When both types of charge carriers are mobile and contribute to complete charge collection, the pulse height spectrum of a device becomes identical to that for the charge/energy deposited, as demonstrated for the ideal case in Figure 3.6. In this simulation, however, we have assumed that only one type of charge carrier is mobile, which results in position-dependent charge collection. For devices with lower charge carrier mobility, using an integration time shorter than the carrier transit time ($t_i < d/\mu E$) further decreases charge collection efficiency. Here, we discuss the effect of

incomplete charge collection due to both single-carrier transport and the use of integration time shorter than transit time.

We first start with the case of integration time (or charge collection time) long enough ($\mu t_i E/d \geq 1.0$) to collect all of the free carriers reaching the collecting electrodes. Figure 3.11 shows the pulse height spectra of devices 1, 5, 10, and 25 μm thick as a function of $\mu\tau E/d$. To more easily compare spectral features, the pulse height spectra are normalized to intensity.

We can see from Figure 3.11a that, for a 1 μm thick device with $\mu\tau E/d = 0.1$, the only visible peaks are the two sum peaks (2310 keV and 2800 keV) and a low-energy peak, p-2. Because devices thinner than 4 μm are subject to significant escape of the primary reaction products, the probability of total energy deposition is low, which results in a tall low-energy peak (p-2) and relatively small sum peaks. Because of the low probability of the second branch of Equation (3.1), the sum peak at 2800 keV is particularly small. As $\mu\tau E/d$ increases (particularly for $\mu\tau E/d \geq 0.3$), the sum peaks disappear and only the lower energy peak (p-2) remains visible.

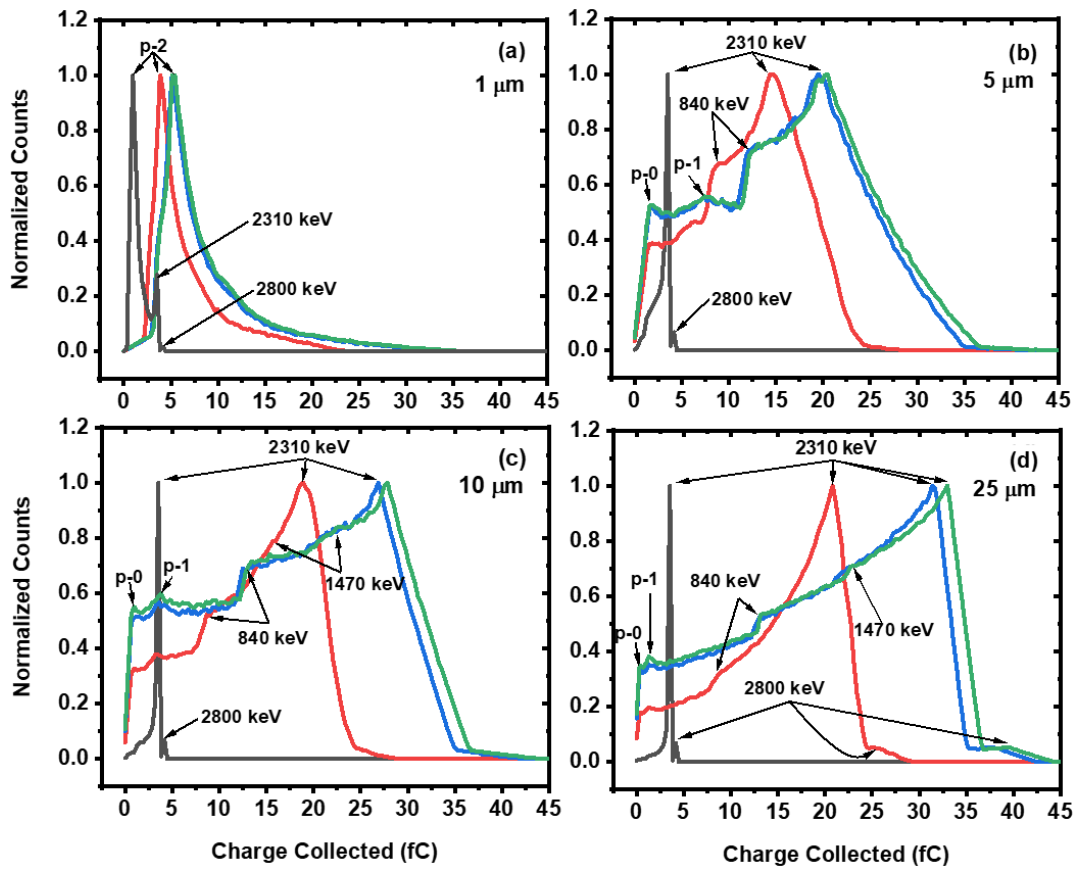


Figure 3.11. Intensity-normalized pulse height spectra of B_4C detectors with thicknesses of 1, 5, 10, and 25 μm for long integration time ($\mu\tau_i E/d \geq 1.0$) for $\mu\tau E/d = 0.1$ (—), $\mu\tau E/d = 1$ (—), $\mu\tau E/d = 10$ (—), and $\mu\tau E/d = 100$ (—). The p-0 and p-1 peaks are assigned to incomplete charge collection of the 840 keV Li ions and 1470 keV α particles arising from neutrons absorbed close to the collecting electrode of the device. Peak p-2 arises from partial energy deposition in very thin devices, which can be seen even if both types of charge carriers are mobile, as shown in Figure 3.6a. The peaks at 2310 keV and 2800 keV are the sum peaks from Equation (3.1).

As seen in Figure 3.11b–d, for thicker devices, only the two sum peaks (2310 and 2800 keV) are visible for small values of $\mu\tau E/d$. With increasing $\mu\tau E/d$, the individual peaks (840 and 1470 keV) start to appear as steps in the pulse height spectrum, along with two satellite peaks, p-0 and p-1, which correspond to incomplete charge collection from the 840 keV Li ions and 1470 keV α particles resulting from neutrons absorbed close to the collecting electrode (*vide infra*). The low-energy peak p-2 observed in thinner devices ($d \leq 3 \mu\text{m}$) is replaced by a tall sum peak (2310 keV) in thicker devices ($d > 4 \mu\text{m}$) because the majority of the neutrons absorbed result in complete energy deposition. Because of the incomplete charge collection due to single-carrier transport, however, the sum peak at 2310 keV is significantly broadened, and the sum peak at 2800 keV is entirely absent in these devices until the device thickness exceeds 20 μm . It can be inferred from these observations that with increasing thickness and for $\mu\tau E/d > 10$, both of the sum peaks (2310 and 2800 keV) shift toward the limiting case of complete charge collection (37 and 45 fC, respectively) as the device transitions to a surface absorption mode where only one type of carrier effectively contributes to detection regardless of whether one or both types of carriers is/are mobile.

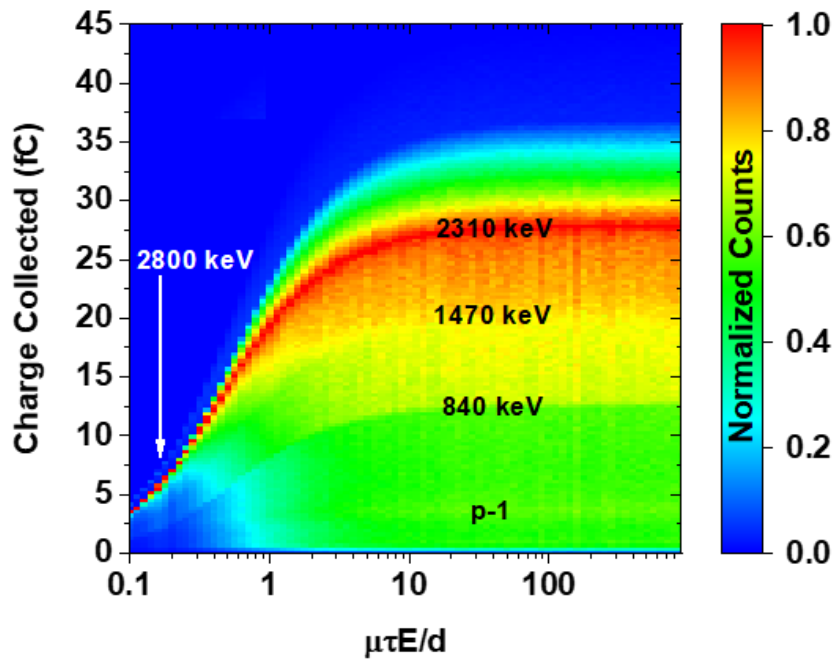


Figure 3.12. Intensity map of normalized pulse height spectra of a 10 μm thick B_4C device as a function of $\mu\tau E/d$ for long integration time ($\mu t_i E/d \geq 1.0$). The discrete shifts in color represent the steps in the pulse height spectra corresponding to the individual peaks, with the red representing the sum peak at 2310 keV.

Figure 3.12 shows the pulse height spectra of a 10 μm thick B_4C device as a function of $\mu\tau E/d$ as an intensity map. We can see from the figure that the individual peaks are observed as distinct shifts in color, with the 2310 keV sum peak appearing as a red band, and the 2800 keV sum peak as very faint blue dots above the red dots for $\mu\tau E/d < 0.3$. With increasing $\mu\tau E/d$, the visible peaks (p-1, 840, 1470, and 2310 keV) become more distinct and shift toward higher charge collection values until approximately $\mu\tau E/d > 10$, at which point a plateau is observed.

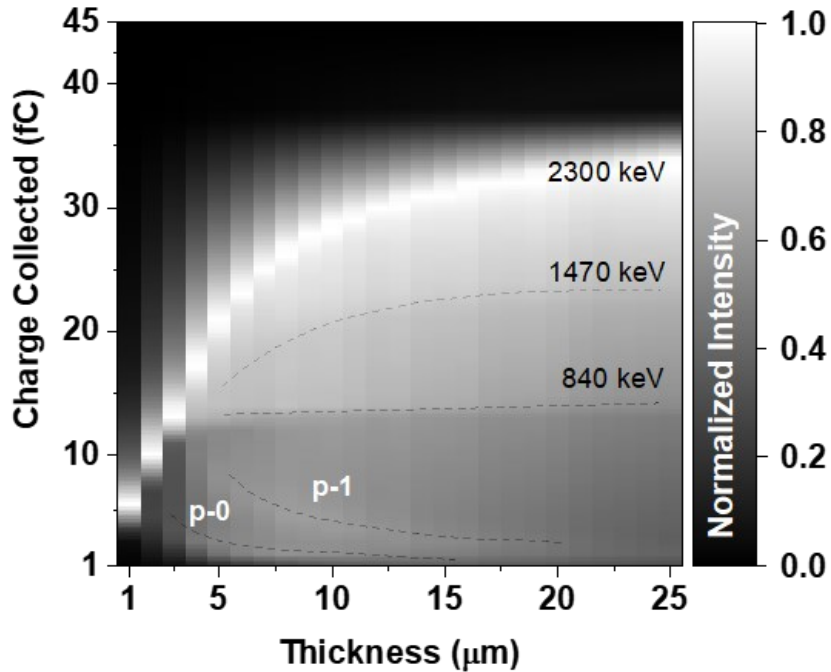


Figure 3.13. The evolution of the pulse height spectra of a B₄C detector as a function of detector thickness for $\mu\tau E/d \gg 10$, and integration time longer than transit time ($\mu t_i E/d \geq 1.0$). The pulse height spectra are normalized to intensity. The dashed lines are visual guidelines for the shift of the individual peaks.

Figure 3.13 shows the evolution of the pulse height spectra of an ideal single-carrier detector ($\mu\tau E/d \gg 10$ and $\mu t_i E/d \geq 1.0$) with detector thickness. We can see that for thinner devices ($d \leq 3 \mu\text{m}$), the low-energy peaks exhibit maximum intensities (counts). As the device thickness increases, the individual peaks (840 and 1470 keV) and their satellite peaks (p-0 and p-1) start to appear along with the broadened sum peak at 2310 keV. The 1470 keV individual peak and the 2310 keV sum peak both shift toward a higher charge collection value with increasing device thickness. The 840 keV

individual peak, however, remains fairly stationary because only those neutrons that are absorbed in the first 1.74 μm (the range of the 840 keV Li ion) of the detector contribute to the peak, and for detectors thicker than 10 μm , these events effectively follow surface absorption behavior, resulting in more than 80% charge collection. It is interesting to note that the p-0 and p-1 peaks shift toward lower charge collection values and disappear for very thick devices. As we are considering the case of $\mu\tau E/d \gg 10$, any charge collection below the 840 keV peak should be related to the position-dependent incomplete charge collection corresponding to the neutrons absorbed deeper within the detector further from the incident surface. As a majority of such events result in the sum peak at 2310 keV, only those neutrons absorbed very close to the collecting electrode contribute to the p-0 and p-1 peaks. Because the charge carriers generated in these regions can only travel a limited distance (up to the ranges of the primary reaction products), the increase in device thickness decreases the range-to-device thickness ratio (R_α/d and R_{Li}/d), resulting in lower charge collection.

We have seen from Figure 3.6b that, for ideal neutron detectors with both carriers mobile, the sum peak at 2310 keV is the most prominent spectral feature. Similarly, for single-carrier devices, we have shown in Figure 3.11b–d that despite the differences in spectral features, the 2310 keV sum peak is still the tallest peak, even for very low $\mu\tau E/d$. However, none of the boron-based direct-conversion detectors reported with experimental pulse height spectra [119], [120] show this feature, which suggests that additional analysis and interpretation is necessary in evaluating these

prototype detectors. Further, having a clear theoretical understanding of these differences in spectral features can potentially be used to distinguish between single- and dual-carrier transport in relatively thin real devices.

Next, we investigate the effect of using shorter integration times ($\mu t_i E/d \leq 1.0$), which represents the case of low carrier mobility such that carrier transit time becomes longer than integration time. Figure 3.14a–f show the pulse height spectra of devices with thicknesses of 1, 5, and 25 μm for different values of $\mu\tau E/d$ and $\mu t_i E/d$. We can see from the figures that the use of integration/shaping time shorter than carrier transit time ($\mu t_i E/d < 1.0$) renders the two sum peaks at 2310 keV* and 2800 keV* as sharp spectral features even with lower values of $\mu\tau E/d$ in all detector thicknesses simulated. Here, the asterisk notation is used to distinguish the recovered sum peaks as a result of using shorter integration time from the original broadened 2310 keV and 2800 keV sum peaks. Because a shorter integration time results in a majority of the charge carriers traveling the same distance (i.e., they do not have the opportunity to reach the electrodes within the integration time), the charge collected becomes proportional to the charge deposited, which allows for recovery of the spectral shape of the ideal pulse height spectrum (Figure 3.6), however with the energy axis compressed by the factor $\mu t_i E/d$ (*vide infra*). It is interesting to note, however, that the broadened sum peak at 2310 keV that is visible with integration time longer than transit time still exists even with the recovery of the true sum peaks. This is because, for a certain value of $\mu t_i E/d$, only those carriers generated in the region $d - \mu t_i E$ adjacent to the incident

surface can travel the distance $\mu t_i E$ and contribute to the recovered 2310 keV* and 2800 keV* sum peaks, and the carriers generated in the remaining region of the detector contribute to the original broadened 2310 keV and 2800 keV sum peaks. If longer integration times ($\mu t_i E/d \geq 1.0$) are used, the charge carriers travel different distances based on their original position, which results in a continuum of charge collection, yielding a broader smeared out 2310 keV sum peak. In such cases, however, the sum peak at 2800 keV appears only for devices thicker than 20 μm , as discussed previously.

We can also see from Figure 3.14 that the use of shorter integration time results in higher sum peak counts. However, because of the very tall 2310 keV* sum peak, the individual peaks are barely visible, particularly for thinner devices. With increasing integration time ($\mu t_i E/d$), the relative intensity (counts) of the sum peak decreases and the individual peaks start to appear. Further, with increasing integration time, all of the individual and sum peaks shift toward the right (higher energy collection values) due to the charge carriers being able to travel greater distances. However, as the integration time approaches the carrier transit time, the recovered sum peaks (2310 keV* and 2800 keV*) disappear.

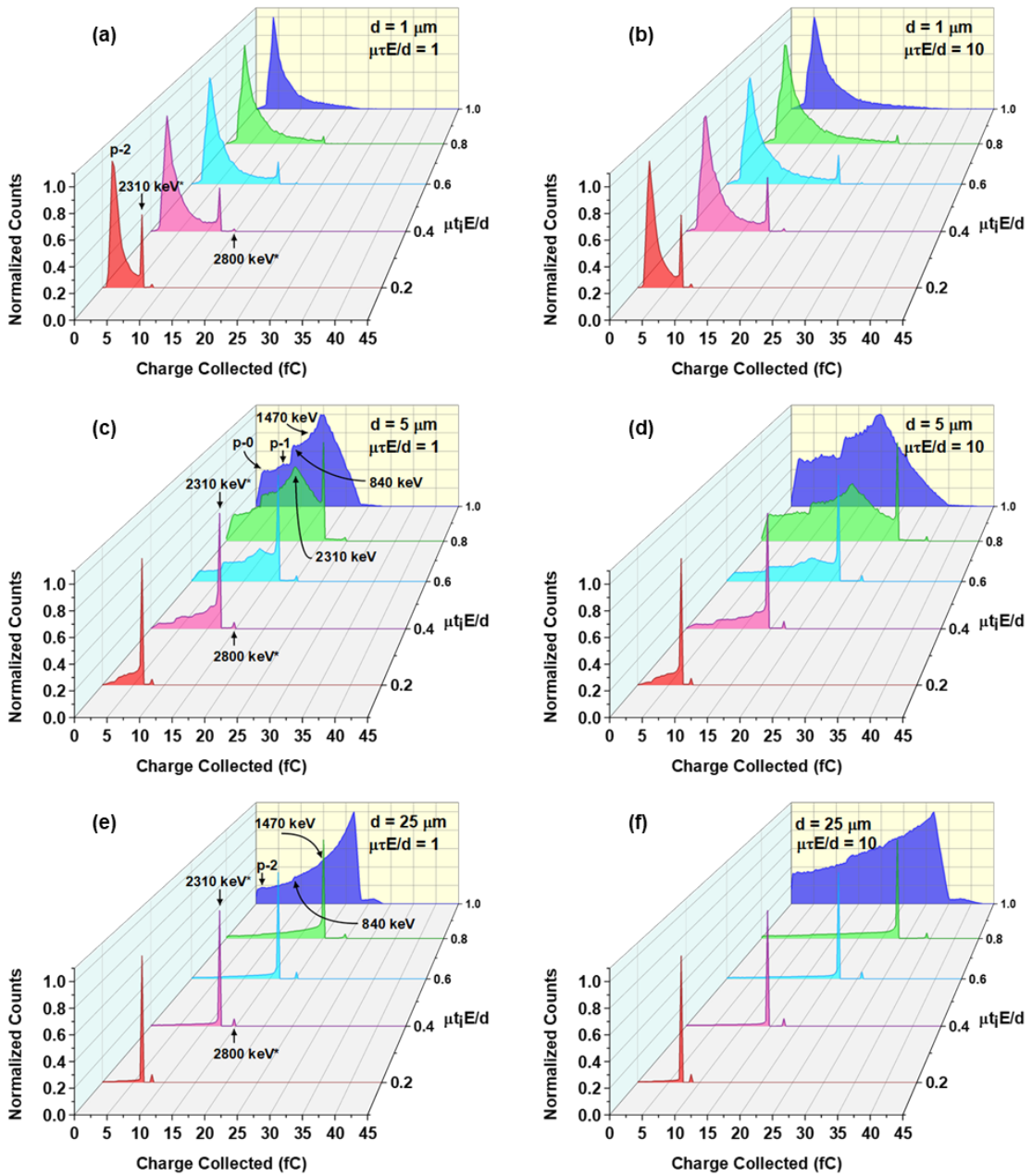


Figure 3.14. Normalized pulse height spectra of devices with thicknesses of 1, 5, and 25 μm for $\mu t E/d = 1$ and 10 as a function of $\mu t_i E/$.

Although the majority of thermal neutron detectors are not able to resolve incident neutron energies, the pulse height spectrum obtained from such a detector can still be used in applications requiring neutron identification, and/or gamma discrimination in mixed radiation environments, such as in radiation portal monitoring systems. We can see from Figure 3.14 that the spectral features are recovered with the use of integration time shorter than transit time, as long as the charge collected is above the detection threshold. However, using a shorter integration time also reduces the signal level, which could render features difficult or impossible to resolve. In cases where collected charge is sufficiently large relative to detection threshold, a shorter integration time can be used without significantly decreasing detection efficiency, and can in principle provide a “dial” for resolving spectral features.

3.5.5. Energy Scaling of the Pulse Height Spectra

In Part a of this section, we described the charge collection efficiency as the ratio of total charge collected to total charge deposited by all of the neutrons absorbed within the detector, which is equivalent to the charge collection efficiency commonly defined in photoconductivity experiments. In the case of single-carrier transport, such charge collection efficiency saturates to 50% for thin detectors, eventually reaching unity as the device becomes very thick relative to the neutron absorption depth ($\Sigma d \gg 1$). This also applies to the case of steady-state neutron detection where individual neutrons are not counted but rather a continuous flux is measured. However, in the case of individual neutron detection with single-carrier transport, such a definition of the charge collection

efficiency cannot describe the pulse height spectrum obtained because the distinct spectral peaks (both individual and sum peaks) arise only from a certain fraction of neutrons absorbed that satisfy specific conditions. For example, the individual peak at 840 keV arises only from neutrons absorbed very close to the incident surface, which emit 840 keV Li ions within the detector (represented by the small shaded semicircle on the surface A in Figure 3.15). Thus, in practice, the charge collection efficiency in the case of single-particle detection is defined as the ratio of the charge collected for a spectral peak to the total charge deposited by the corresponding radiation event, i.e.,

$$CCE = \frac{\text{Charge collected corresponding to a spectral peak}}{\text{Charge deposited corresponding to that peak}} \quad (3.24)$$

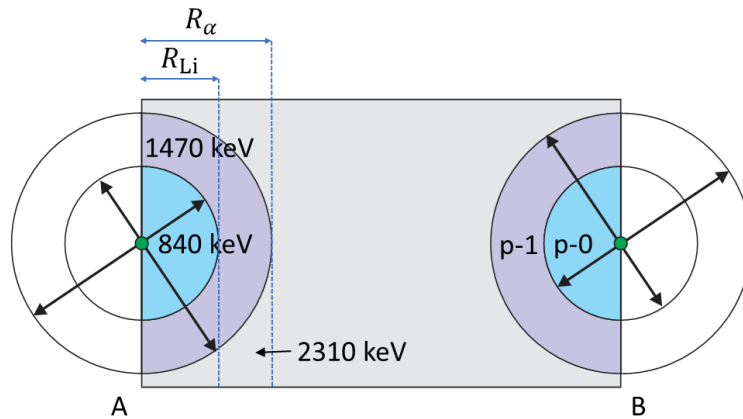


Figure 3.15. Schematic of neutron absorption in a ^{10}B -based direct conversion detector showing the regions that correspond to the specific spectral peaks obtained, considering only the first branch of the ^{10}B nuclear reaction (Equation (3.1)).

To discuss the energy scaling of the spectral peaks as a function of the charge transport properties of a detector, we first start with the case of integration time longer than carrier transit time ($\mu t_i E/d \geq 1.0$). Figure 3.16 shows the intensity map of the pulse height spectra (in the form of charge collected as a function of $\mu\tau E/d$) obtained for a 10 μm device overlaid with the curve fits for the corresponding spectral peaks. To explain the curves fits, we can assume that the absorbed neutrons resulting in a specific spectral peak are averaged at a point inside the detector and deposit an average charge packet. For example, the average position of the neutrons absorbed that result in the 840 keV individual peak lies somewhere inside the small semicircle labeled 840 keV in Figure 3.15. If C is the distance of the average charge packet from the incident surface, the charge collected corresponding to the motion of the charge packet can be obtained as

$$Q = Q_0 \frac{\mu\tau E}{d} \left[1 - \exp\left(-m \frac{d}{\mu\tau E}\right) \right] \quad (3.25)$$

where Q_0 is the total charge corresponding to the spectral peak, and $m = 1 - C/d$ can be used as a fitting parameter.

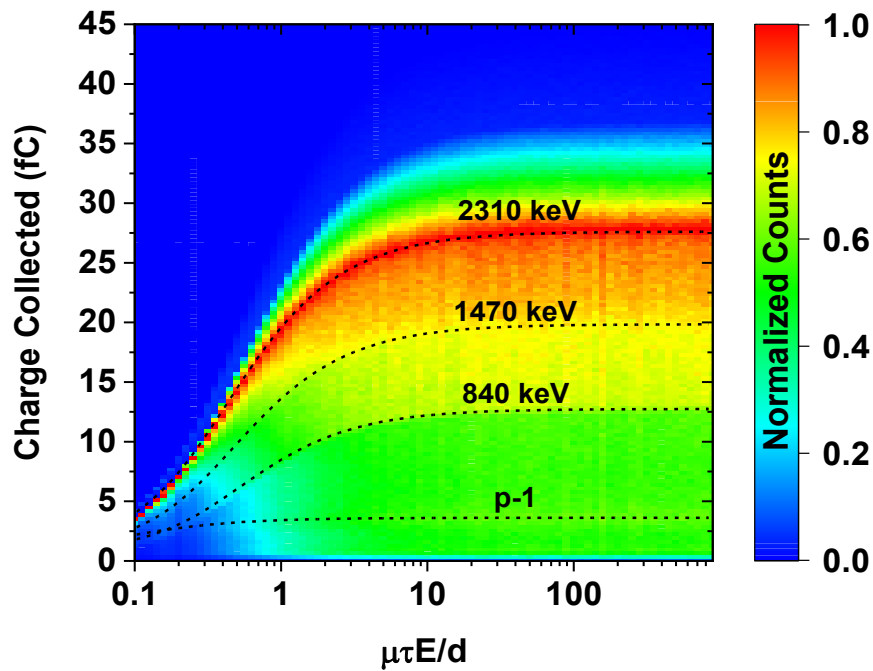


Figure 3.16. Intensity map of normalized pulse height spectra of a 10 μm thick detector overlapped with fit curves for charge collection.

Table 3.1. Position of the deposited charge packets that contribute to their associated spectral peaks in single-carrier B_4C neutron detector.

Spectral Peak	Distance of charge packet from incident surface (C)	
	(μm)	
840 keV	0.75	
1470 keV	1.65	
2310 keV	2.52	
p-1	1.35*	
p-0	0.52*	

*Distance from the collecting surface

Table 3.1 gives the fit values of the average charge packet positions corresponding to their associated spectral peaks. From the results, we observe that the

charge packet distances from the incident surface for the 840, 1470, and 2310 keV peaks are nearly half of the corresponding ranges of the primary reaction products: 1.7 μm (Li 840 keV), 3.3 μm (α 1470 keV), and 5.0 μm (the sum of the ranges of Li ion and α particle), respectively. The distances of the charge packets corresponding to the satellite peaks p-0 and p-1 relative to the collecting surface are slightly lower than those for the corresponding individual peaks. These distance values are related to the neutron absorption distance at which full energy deposition occurs based on the range of the primary reaction products (Li, α , or Li + α), taking into consideration that for single-carrier transport, the percent charge collection drops continuously from 100% as one moves further away from the incident surface, resulting in broadening of the spectral features. Because neutron absorption also decreases exponentially moving away from the surface, the “peak” can be mapped to the average distance from the incident surface representing the initial onset of full charge deposition, with spectral intensity tailing off moving further away.

One important result of this analysis is that the fit parameter C (or m) is independent of device thickness. (Note that the validity of this result could not be checked for the 2310 keV sum peak for devices thinner than 5 μm as it is not resolved in this case). Although we may not know the value of C *a priori*, we can use Equation (3.25) to obtain the mobility–lifetime product ($\mu\tau$) and the parameter m by tracking the shift of any discernable spectral peak as a function of applied electric field (E). For $m = 1$, Equation (3.25) reduces to Equation (3.17), the Hecht equation[172] for surface

absorption, which is routinely used to obtain the $\mu\tau$ value of a detector by analyzing the pulse height spectra as a function of electric field [203]. The use of Equation (3.17), however, is only suitable if the radiation is absorbed on the surface, or if both types of charge carriers have comparable $\mu\tau$ values. For the case of non surface absorption and single-carrier transport, which could apply to many types of radiation (e.g., high-energy electrons, X-rays, γ -rays, and neutrons) and a wide class of emerging semiconductor materials, Equation (3.25) provides an alternative means for estimating $\mu\tau$ product.

Now we describe the energy scaling of the pulse height spectra obtained with integration time shorter than transit time. As stated in the previous section, this scenario can allow for the recovery of spectral features. However, it also results in proportionally lower charge collection, while compressing the energy axis of the pulse height spectra.

Figure 3.17 shows the charge collection efficiency corresponding to both of the sum peaks (2310 keV* and 2800 keV*) as a function of $\mu\tau E/d$ and $\mu t_i E/d$. We can see from the figure that the saturation charge collection efficiency corresponding to the sum peaks increases proportionally with $\mu t_i E/d$, the ratio of integration time to transit time. As the integration time approaches the transit time ($\mu t_i E/d \rightarrow 1$), the recovered sum peaks disappear, and the proportionality can no longer be applied. One interesting result obtained from this analysis is that the charge collection efficiency defined in this way does not depend on the thickness of the device (relative to radiation penetration depth). This is because for a particular value of integration time, t_i , the distance traveled by any given fraction of the charge carriers is $\mu t_i E$, which is similar to the case of

surface absorption wherein the charge carriers all travel the same distance, leading to thickness-independent charge collection efficiency. We additionally find that the charge collection efficiency in the case of integration time less than carrier transit time ($\mu t_1 E/d < 1.0$) also fits to Equation (3.25) with $m = \mu t_1 E/d$.

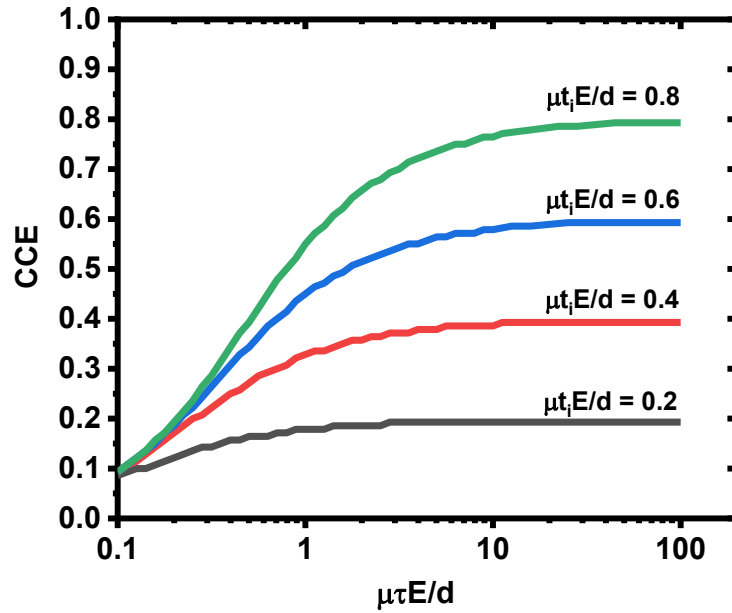


Figure 3.17. Charge collection efficiency (CCE) defined by Equation (3.24) obtained for the sum peaks (2310 keV* and 2800 keV*) as a function of $\mu\tau E/d$ for different values of $\mu t_1 E/d$. Graphs corresponding to $\mu t_1 E/d = 0.9$ and 1.0 are not included as distinct sum peaks were not observed for thinner devices with larger values of $\mu\tau E/d$. The charge collection efficiencies are independent of device thickness.

3.5.6. Boron Carbide Detector: An Example

Among boron-based materials, boron carbide has been the most studied [60]–[71], [92] for thermal neutron detection. For the last two decades, there have been many attempts to fabricate direct-conversion thermal neutron detectors using amorphous boron carbide, primarily because of its very high resistivity (low leakage current), and its toughness under harsh (thermal, mechanical, radiation) environmental conditions. For a boron-based solid-state neutron detector, which results in an energy release of 2310 keV in most cases, a detection threshold of 25% is a reasonable choice. Assuming a detector material that can withstand an electric field of 1 MV/cm, which is generally achieved in a-BC thin films [93], [154], the minimum required carrier mobility can be obtained using Equation (3.20). Figure 3.18 shows the minimum carrier mobility required as a function of device thickness for different integration times. As can be seen, the choice of integration time has a dramatic effect on mobility requirement, which ranges from $10^{-4} \text{ cm}^2 \cdot \text{V}^{-1} \cdot \text{s}^{-1}$ for $t_i = 1 \text{ } \mu\text{s}$ to $10^{-7} \text{ cm}^2 \cdot \text{V}^{-1} \cdot \text{s}^{-1}$ for $t_i = 1 \text{ ms}$.

Neutron detectors in field applications such as portal monitoring systems and hand-held monitoring scenarios, in contrast to those in very high neutron flux environments such as nuclear reactors and nuclear laboratories, are not expected to operate at a very high count rate. In such applications, we assume an integration time of about 10 μs should be sufficient, which provides a neutron count rate of $\sim 10^5 \text{ n/s}$. Thus, for this example, we use an integration time of 10 μs , which also results in a detectable

signal current of 1 nA for a charge collection of 10 fC given that the leakage current can be sufficiently minimized (e.g., by using blocking contacts).

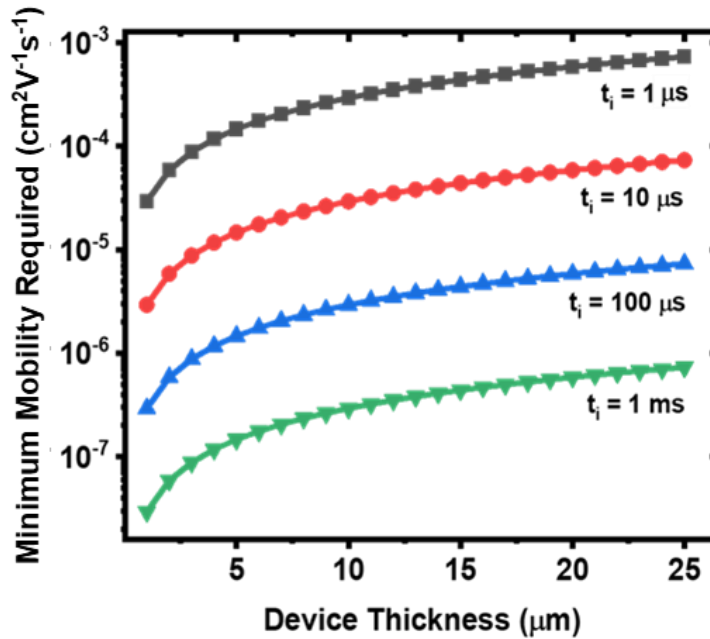


Figure 3.18. Minimum charge carrier mobility required to achieve neutron detection in a planar B_4C detector as a function of device thickness for different integration times when carrier lifetime is sufficiently long. For an order of magnitude decrease in integration time, the required minimum carrier mobility increases by an order of magnitude.

As discussed previously, devices thinner than $5 \mu\text{m}$ suffer from partial charge deposition because of the escape of primary reaction products. Balancing this issue with the difficulties associated with fabricating thicker films, we thus take a $5 \mu\text{m}$ thick B_4C detector as a representative target for a direct-conversion detector, which should be able

to achieve reasonable spectral performance. With these assumptions, and considering the case of single-carrier transport, Figure 3.19 shows the simulated detection efficiency of such a detector as a function of $\mu\tau$ for different values of charge carrier mobility higher than the minimum required value.

We can see from Figure 3.19 that for a 5 μm thick boron carbide device with an integration time of 10 μs (and a lower level discriminator set at 25% of the maximum deposited energy), detection starts as soon as charge carrier mobility exceeds $1.5 \times 10^{-5} \text{ cm}^2 \cdot \text{V}^{-1} \cdot \text{s}^{-1}$ with a $\mu\tau$ value $> \sim 10^{-9} \text{ cm}^2 \cdot \text{V}^{-1}$ (and therefore carrier lifetime $> 10^{-4} \text{ s}$). For boron carbide thin films, carrier lifetimes longer than milliseconds have been reported [151]. At this mobility value, the maximum detection efficiency is $\sim 9\%$. The maximum detection efficiency we can obtain with an integration time of 10 μs or longer is $\sim 14\%$ for charge carrier mobility of $5 \times 10^{-5} \text{ cm}^2 \cdot \text{V}^{-1} \cdot \text{s}^{-1}$ and higher.

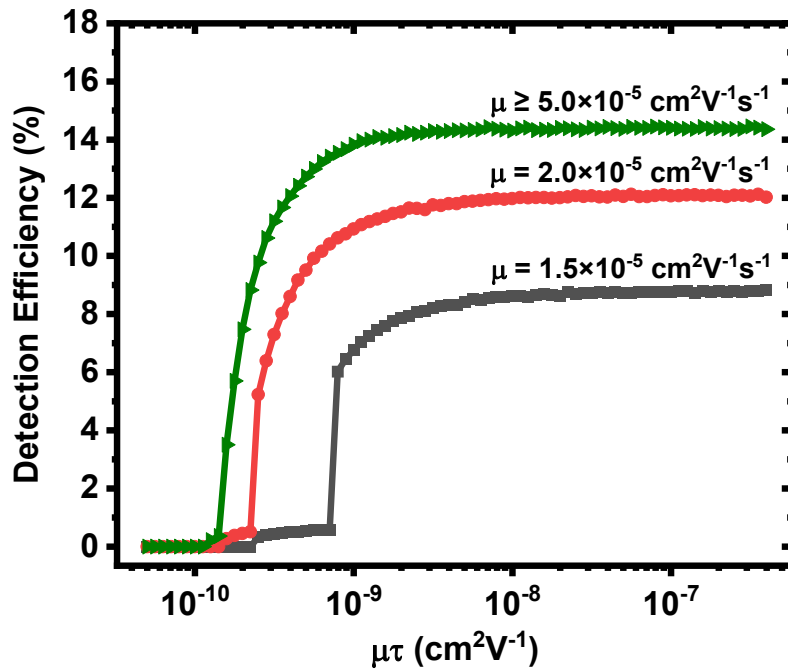


Figure 3.19. Theoretical detection efficiency as a function of mobility–lifetime product ($\mu\tau$) for different charge carrier mobilities of a 5 μm thick B_4C neutron detector taking 10 fC of charge ($\sim 25\%$ of total energy deposition) as the lower level discriminator and 10 μs as the integration time.

3.6. Conclusions

We have investigated the case of thin (relative to neutron penetration depth) direct-conversion neutron detectors with partial charge collection due to single-carrier transport and/or suboptimal charge transport properties. Using a Monte Carlo simulation approach, and $^{10}\text{B}_4\text{C}$ as a prototypical detector material, we have modeled the performance of neutron detectors with a range of thicknesses (d), charge carrier mobilities (μ), charge carrier lifetimes (τ), and integration times (t_i), specifically considering the cases of integration time both longer and shorter than carrier transit time.

Through simulations of a large number of incident neutrons, we have shown how the average charge collection efficiency varies as a function of μ , τ , d , and t_i . We have defined a general expression that can be used to extract the $\mu\tau$ product of a single-carrier device using field-dependent steady-state irradiation experiments (neutron or other). We have demonstrated that a higher $\mu\tau$ product does not in itself guarantee satisfactory device performance, but that both the carrier mobility and carrier lifetime must also be sufficiently high, unlike in the case of mature semiconductor detectors wherein the $\mu\tau$ product can be considered as a standalone figure of merit. Specifically,

in cases with constraints on integration/pulse processing time (e.g., high radiation flux environments) and poor mobility, the ratio of integration time to carrier transit time must be considered.

Additionally, by analyzing the current and charge collected for individual neutron detection events, we have investigated the detection efficiency and pulse height spectra of single-carrier boron-based neutron detectors for different material and experimental conditions. We have defined an expression for determining detection efficiency based on a given charge collection threshold, as well as the minimum mobility required to achieve detection. For example, we demonstrate that boron-containing materials with poor charge transport properties can still be effective as neutron counters if the devices are thin enough to reduce carrier transit time to tens of microseconds, and the carrier lifetimes remain on the order of the transit times. Specifically for boron carbide (B_4C) detectors, a 1 μm thick detector can detect neutrons with carrier mobility $>10^{-8} \text{ cm}^2 \cdot \text{V}^{-1} \cdot \text{s}^{-1}$ when carrier transit time and carrier lifetime are in the order of 1 ms, which corresponds to mobility–lifetime product $>10^{-11} \text{ cm}^2 \cdot \text{V}^{-1}$. With shorter lifetimes, the mobility requirement increases significantly, and a carrier mobility value of $>10^{-5} \text{ cm}^2 \cdot \text{V}^{-1} \cdot \text{s}^{-1}$ is required when carrier lifetime and transit time are in the order of 1 μs . With increasing detector thickness, the mobility requirement further increases proportionally to the inverse of the thickness. Assuming carrier lifetime on the order of 1 ms [151], a 5 μm B_4C detector, for example, can achieve a detection efficiency in the range of $\sim 10\text{--}15\%$ with carrier mobility on the order of $10^{-5} \text{ cm}^2 \cdot \text{V}^{-1} \cdot \text{s}^{-1}$.

As regards the pulse height spectra, we have shown that for the case of integration time longer than carrier transit time, due to partial charge collection, it is impossible to recover the features of the incident radiation; spectra are distorted and a broadened sum peak at 2310 keV dominates. However, for the case of integration time shorter than carrier transit time, for which detection is still possible, the ideal peaks can be recovered, and thus integration/shaping time can be used as a “dial” to resolve spectral features, even for unknown $\mu\tau$, as long as the charge collected remains above the detection threshold. Such a strategy could therefore be used for positive neutron discrimination. Knowledge of the behavior of the pulse height spectra under various conditions will help to more accurately characterize previously reported and future ^{10}B -based detectors (e.g., determination of $\mu\tau$ product, distinction of single- vs dual-carrier transport, confirmation of direct-conversion behavior, etc.). Further, we have obtained a modified Hecht equation that can be used to estimate the $\mu\tau$ product in a single-carrier device by analyzing the shift of spectral peaks with increasing electric field. This $\mu\tau$ analysis can be applied to any penetrating radiation (neutron or other) and is not confined to the requirements of surface or uniform absorption.

Our results expand the theoretical understanding of direct-conversion neutron detectors with single-carrier and or suboptimal charge transport properties, which currently represent the majority of candidates for this technology. It is clear that charge transport, combined with signal processing methods, have a significant effect on detection efficiency and pulse height spectra and should be accounted for in detector

modeling efforts and analysis of real devices. The theory, simulation code, and results presented here will help to move the field of direct-conversion detector development forward more rigorously. It is our further hope that this work invites continued research into materials that may not have been prioritized due to poor charge transport properties, but as we show here still have clear potential in radiation detection applications.

CHAPTER 4

SPACE-CHARGE-LIMITED CURRENT IN DISORDERED MATERIALS: NEGATIVE FIELD DEPENDENCE IN MOBILITY

(This chapter is reproduced in part from reference [204] with the permission of AIP Publishing)

4.1. Introduction

The surge in popularity of thin-film organic electronics [205]–[207] has spurred challenges in applying traditional analysis techniques to the measurement of charge transport properties in these materials. One charge transport parameter essential to performance in many devices is charge carrier mobility. Of the methods available for measuring mobility in low-mobility thin-film semiconductors, the steady-state space-charge-limited current (SS-SCLC) experiment stands out as arguably the most simple yet generally effective technique [208]. This technique is based on the analysis of a current density vs. voltage (J - V) curve of a sandwich thin-film structure and is amenable to screening a wide range of samples. Alternative transient, drift-mobility-based techniques, while potentially more appealing from a theory and accuracy standpoint, entail more elaborate experimental setups and maintain very specific requirements in terms of test heterostructure configuration (e.g., film thickness, contact type) and applicable charge transport property range [209], rendering them less versatile

as a general measurement tool. Time-of-flight measurements, for example, require relatively thick (>1 μm) films and transparent blocking contacts [209], [210]. Other techniques, including transient or dark-injection space-charge-limited current [211], charge extraction by linearly increasing voltage [212], and admittance spectroscopy [212], possess similarly exacting requirements to achieve successful measurements. Despite the relative simplicity and utility of the SS-SCLC technique, however, it is not without its challenges [208], including the appropriate treatment of samples exhibiting field-dependent mobility, specifically for negative field dependence, as will be the focus of this work.

The theoretical treatment of SS-SCLC enhanced by the Poole-Frenkel emission of trapped charge carriers has been reviewed by Murgatroyd [213], Hartke [214], and Barbe [215]. Because of the similar form of field dependence, these treatments are also applicable for the case of SS-SCLC enhanced by positive-field-dependent mobility. A more complicated and controversial case is that of negative-field-dependent mobility, which has been demonstrated in a number of different disordered materials using various transient mobility measurement techniques [216]–[220]. However, there are not reports of negative-field-dependent mobility based on SS-SCLC analysis. This lies in contrast to the case of positive-field-dependent mobility, which has been shown using both transient and steady-state measurements [221]. In principle, however, since all of the transient experiments used to determine carrier mobility require that the device under test be well into the space-charge-limited-current regime, the steady-state SCLC

analysis should yield a negative field dependence for samples that present this behavior in the transient experiment. One reason for the lack of experimental SS-SCLC evidence for negative-field-dependent mobility may be a lack of theoretical framework. Although the numerical solution given by Murgatroyd (Equation (4.4)) describes SS-SCLC with positive field dependence, to our knowledge, a solution for negative field dependence has not been reported, and one cannot simply apply Murgatroyd's treatment to this case. Here, we revisit a solution for the space-charge-limited current incorporating the Poole–Frenkel or Poole–Frenkel-like effect for *both* positive and negative electric field dependence. In contrast to Murgatroyd's original solution, which uses numerical integration, this solution uses analytical integration. We compare our exact solution for the positive case to Murgatroyd's original solution as well as to Barbe's analytical solution for high field and discuss best practices for and implications of the SS-SCLC analysis for materials exhibiting negative-field-dependent mobility.

4.2. Space-Charge-Limited Current

When an electric field is applied across an insulator (or insulating semiconductor) with injecting electrodes, space-charge-limited conduction occurs when the injected carrier concentration exceeds the thermal equilibrium concentration, leading to an excess of charge and non-uniform electric field profile across the film [161]. For a perfect crystalline trap-free insulator, the theory of space-charge-limited current (SCLC) was developed by Mott and Gurney [163], and the current density, J , through a single-carrier parallel-plate device is given as

$$J = \frac{9}{8} \epsilon \mu \frac{V^2}{d^3} \quad (4.1)$$

where V is applied voltage across the insulator, and d , ϵ , and μ are its thickness, permittivity, and charge carrier mobility, respectively. The SCLC theory has been revised by many authors [161], [222] for different cases and different kinds of trap distributions in solids.

Carrier mobility is typically extracted by fitting the experimental J - V data to Equation (4.1). However, complications in data analysis arise when the carrier concentration and/or mobility exhibit an electric field dependence. One cause for such a dependence is the Poole–Frenkel effect [164], wherein an increase in the electric field lowers the effective trap depth, leading to an increase in free charge carrier concentration given as:

$$n = n_0 \exp(\beta\sqrt{E}) \quad (4.2)$$

and thus deviation from strict SCLC behavior. Here n_0 represents the limiting free carrier concentration at zero electric field, and

$$\beta = \frac{1}{kT} \left(\frac{e^3}{\pi\epsilon} \right)^{\frac{1}{2}} \quad (4.3)$$

A well-known and often applied numerical solution for the space-charge-limited current density enhanced by Frenkel emission was reported by Murgatroyd [213] as:

$$J = \frac{9}{8} \epsilon \mu \frac{V^2}{d^3} \exp\left(0.891\beta \sqrt{\frac{V}{d}}\right) \quad (4.4)$$

Although a complete analytical solution for the problem has not been obtained, analytical solutions with low-field ($\beta\sqrt{V/d} \ll 1$) and high-field ($\beta\sqrt{V/d} \gg 1$) approximations have been given by Barbe [215], and an exact but parametric solution has been reported by Bisquert et al. [223]

4.3. Field Dependence of Carrier Mobility

Exponential electric field dependence in space-charge-limited current can also arise from the field dependence of the mobility related to the hopping transport of carriers in disordered materials [224], which takes on the same functional form as in the case of Frenkel emission:

$$\mu(E) = \mu_0 \exp(\gamma\sqrt{E}) \quad (4.5)$$

Here, μ_0 is the low-field carrier mobility and γ is a fitting factor related to the material disorder. Although the factor γ is not necessarily equivalent to the Poole–Frenkel coefficient, β , this behavior is commonly referred to as Poole–Frenkel-like and the two treatments are often used interchangeably. An interesting experimental result [216]–[220], [225], [226] obtained for a number of disordered organic semiconductors is a negative value of γ at low electric field, which cannot be explained on the basis of Frenkel emission. Although controversial [166], [219], [225], many have proposed,

mostly based on numerical simulations, that under the Gaussian disorder model of hopping transport this negative field dependence can result from the superposition of positional and energetic disorder in organic semiconductors [224], [227], [228]. The functional form of the field-dependent mobility in this model is given as:

$$\mu(T, E) = \mu_0 \exp\left(-\frac{2}{3}\hat{\sigma}^2\right) \exp[C(\hat{\sigma}^2 - \Sigma^2)\sqrt{E}] \quad (4.6)$$

where $\hat{\sigma} = \sigma/k_B T$ is a measure of energetic disorder, with σ being the width of the Gaussian density of states, Σ is a measure of positional disorder, and C is a fitting parameter. This equation implies that when the positional disorder, Σ , exceeds the energetic disorder, $\hat{\sigma}$, particularly at high temperatures, the mobility exhibits negative field dependence. The usual phenomenological explanation [224] is that in three-dimensionally disordered systems with a high positional disorder, the most energetically favorable path for percolative hopping transport will proceed via randomly oriented jumps; however, with increasing electric field, charge carriers are forced to make less energetically favorable jumps in the direction of the field, thus reducing mobility.

4.4. Results and Discussion

For a single type of mobile carrier flowing through an insulator with field-dependent mobility given by Equation (4.5), the total current through the insulator can be written as:

$$J = \epsilon\mu_0 \exp\left(\gamma\sqrt{E(x)}\right) E(x) \frac{\partial E(x)}{\partial x} \quad (4.7)$$

with the charge density replaced by Poisson's equation:

$$\nabla \cdot E = \frac{\rho(x)}{\epsilon} \quad (4.8)$$

Here, the current due to the thermal equilibrium carrier concentration has been neglected. Equation (4.7) can also represent the case of space-charge-limited current enhanced by Frenkel emission. However, in this case, μ_0 represents $\mu\theta_0$ where θ_0 is the ratio of free carrier concentration to the total carrier concentration (free+trapped)

The solution of the continuity equation under steady-state conditions requires boundary conditions on the electric field. The usual consideration in the space-charge-limited current analysis is that the electric field at the injecting electrode ($x = 0$) is negligibly small because the electric field set up by the injected carriers opposes the applied electric field [163]. Since the current density should remain constant spatially in the steady-state case, it is reasonable to solve the problem by direct integration of Equation (4.7) with the boundary condition $E(0) = 0$, which gives:

$$\frac{\gamma^4 J}{2\epsilon\mu_0} x = \exp\left(\gamma\sqrt{E(x)}\right) \times \left(\left(\gamma\sqrt{E(x)}\right)^3 - 3\gamma^2 E(x) + 6\gamma\sqrt{E(x)} - 6 \right) + 6 \quad (4.9)$$

It should be noted that for a real physical system, only the solution to Equation (4.9) yielding positive $\sqrt{E(x)}$ should be chosen so that the field dependence in the carrier concentration (Equation (4.2)) and the carrier mobility (Equation (4.5)) remain

physically meaningful. For the case of negative field dependence (negative γ), the right-hand-side of Equation (4.9) saturates at 6 at high field, which in turn causes the current to saturate. However, in real devices, other high-field effects increase the current significantly, and the high field saturation is not actually observed.

Because an analytical solution to Equation (4.9) for $E(x)$ is not possible, we will proceed to a parametric solution following the method used by Murgatroyd. For this, we reduce Equation (4.9) to a dimensionless format by defining some variables as:

$$\text{Normalized current density: } \eta = \frac{2dJ\gamma^4}{\epsilon\mu_0} \quad (4.10)$$

$$\text{Normalized electric field: } z = \gamma^2 E \quad (4.11)$$

$$\text{Normalized thickness: } y = \frac{x}{d} \quad (4.12)$$

$$\text{Normalized voltage: } \xi = \frac{3V}{2d}\gamma^2 \quad (4.13)$$

where V and d are the applied voltage and thickness of the device, respectively. With these variables defined, Equation (4.9) takes the following form for positive field dependence:

$$\eta y = 24 + 4 \exp(\sqrt{z}) \left(z^{\frac{3}{2}} - 3z + 6\sqrt{z} - 6 \right) \quad (4.14)$$

And for negative field dependence:

$$\eta y = 24 - 4 \exp(-\sqrt{z}) \left(z^{\frac{3}{2}} + 3z + 6\sqrt{z} + 6 \right) \quad (4.15)$$

In both equations, the variable \sqrt{z} is positive and ηy is a monotonically increasing function of \sqrt{z}

The applied voltage across an insulator of thickness d is obtained by integrating the electric field over the entire thickness as:

$$V = \int_0^d E(x) dx \quad (4.16)$$

which can easily be translated to the normalized form as:

$$\xi = \frac{3}{2} \int_0^1 z dy \quad (4.17)$$

The analytical solutions to Equations (4.14) and (4.15) give z as a function of ηy . Thus, it is reasonable to change the integral variable (y) in Equation (4.17) to ηy . Since the normalized current (η) is a function of the normalized voltage (ξ), it is possible to write Equation (4.17) as:

$$\xi(\eta) = \frac{3}{2\eta} \int_0^\eta z(\eta y) d(\eta y) \quad (4.18)$$

As the closed-form solutions of Equations (4.14) and (4.15) are not possible, the integral in Equation (4.18) can be obtained as:

$$\xi(\eta) = \frac{3}{2\eta} I \quad (4.19)$$

with:

$$I = z_0\eta - \int_0^{z_0} \eta y(z) dz \quad (4.20)$$

where z_0 is the normalized electric field at the collecting electrode of the device ($y = 1$) where $\eta y = \eta$.

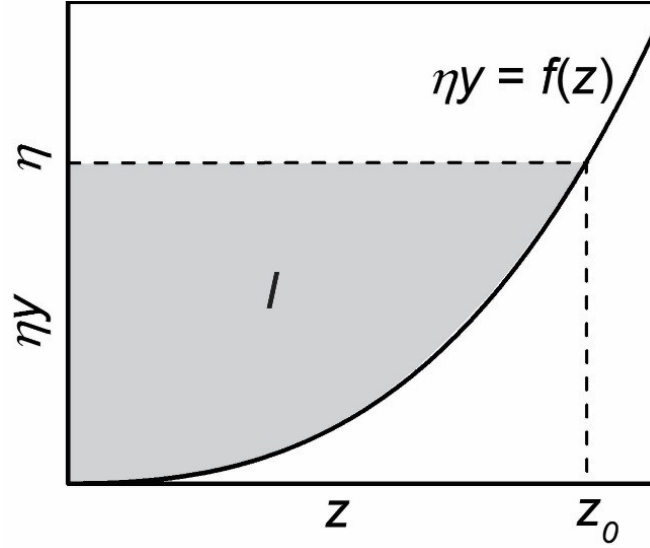


Figure 4.1. Variation of ηy against the normalized electric field z for positive field dependence. The integral I (shaded portion) is obtained by subtracting the area of the unshaded portion from the rectangle of area ηz_0 .

For positive field dependence, using Equation (4.14) for the expression of $\eta y(z)$, the integral I can be easily calculated to obtain

$$I = 4 \exp(\sqrt{z_0}) \left(z_0^{\frac{5}{2}} - 5z_0^2 \right) + 20\eta \quad (4.21)$$

Hence, the normalized voltage $\xi(\eta)$ from Equation (4.19) can be written as:

$$\xi(\eta) = 30 + \frac{6 \exp(\sqrt{z_0}) \left(z_0^{\frac{5}{2}} - 5z_0^2 \right)}{\eta} \quad (4.22)$$

Proceeding similarly to the above, we get the normalized voltage in the case of negative field dependence as:

$$\xi(\eta) = 30 - \frac{6 \exp(-\sqrt{z_0}) \left(z_0^{\frac{5}{2}} + 5z_0^2 \right)}{\eta} \quad (4.23)$$

Although z_0 cannot be solved for η analytically, it is possible to obtain the relation between the normalized current (η) and the normalized voltage (ξ) numerically. Since $\sqrt{z_0}$ is always positive as required for the field dependence, we can start with $z_0 = 0$ and calculate the normalized current (η) using Equations (4.14) and (4.15). Using Equations (4.22) and (4.23), the normalized voltage (ξ) can then be calculated. Although the process is numerical, the variation of the normalized current η as a function of normalized voltage ξ is exact. Thus, Equations (4.22) and (4.23), along with Equations (4.14) and (4.15), provide an exact solution for the space-charge-limited current for both positive as well as negative field dependence. For the positive field dependence case, the solution is equivalent to the parametric solution given by Bisquert et al [223].

Figure 4.2 shows the variation of the normalized current η against the normalized voltage ξ for both positive and negative field dependence obtained using Equations (4.22) and (4.23) compared to data obtained using Murgatroyd's expression

and Barbe's high-field approximation. As can be seen at a low electric field ($\xi < 1$, corresponding to ~ 4 kV/cm for a material with $\epsilon_r = 5$), the log-log plot of η against ξ yields a straight line with slope 2, consistent with the pure square-law dependence of the SCLC given by Mott and Gurney. Above $\xi \approx 1$ however, the current deviates significantly from the Mott-Gurney law. In comparing the exact values calculated here to Murgatroyd's and Barbe's treatments, we see that Murgatroyd's expression gives current-voltage data close to the exact values (within 11%) up to moderate electric field ($\xi < 100$, corresponding to < 0.4 MV/cm for a material with $\epsilon_r = 5$) (Figure 4.2a) and remains the better choice as compared to Barbe's expression up to $\xi \approx 1000$ (corresponding to ~ 4 MV/cm for a materials with $\epsilon_r = 5$). It is only above this field, which is sufficiently high to cause dielectric breakdown in most materials, that Barbe's expression becomes closer to the exact one (Figure 4.2b).

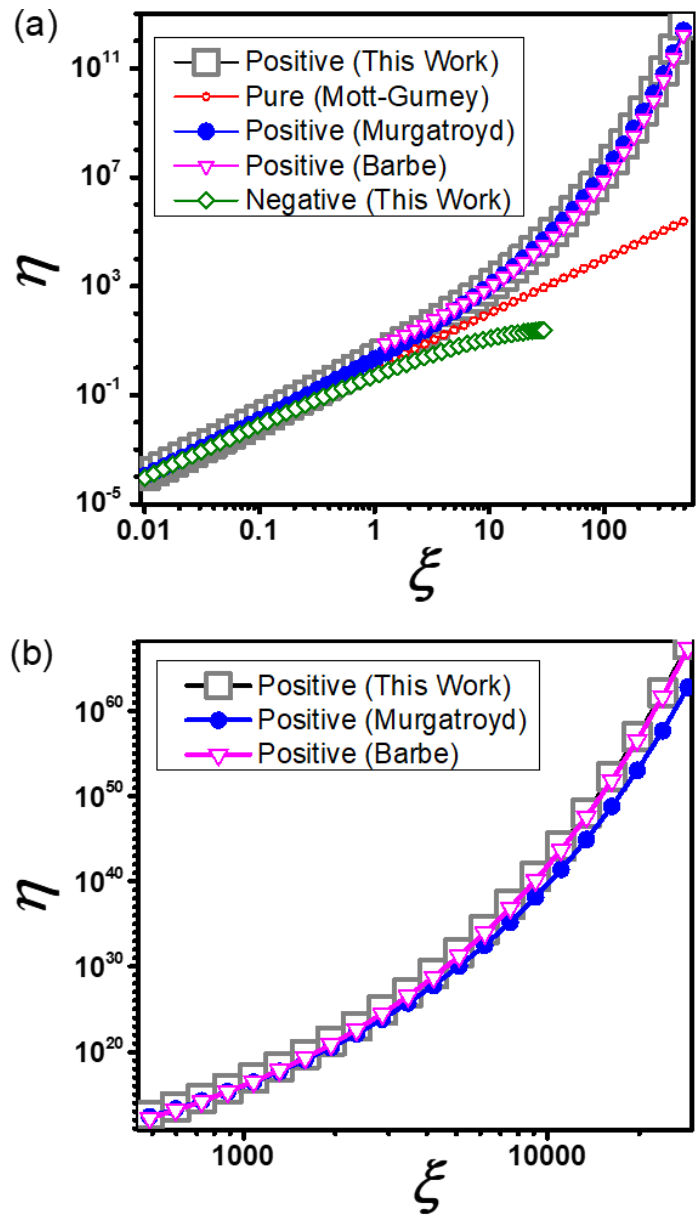


Figure 4.2. Variation of normalized current density (η) against normalized applied voltage (ξ) obtained from the exact solution derived here in comparison to pure SCLC (Mott and Gurney), Murgatroyd's original solution, and Barbe's analytical solution for (a) $\xi < 500$ and (b) $\xi > 500$.

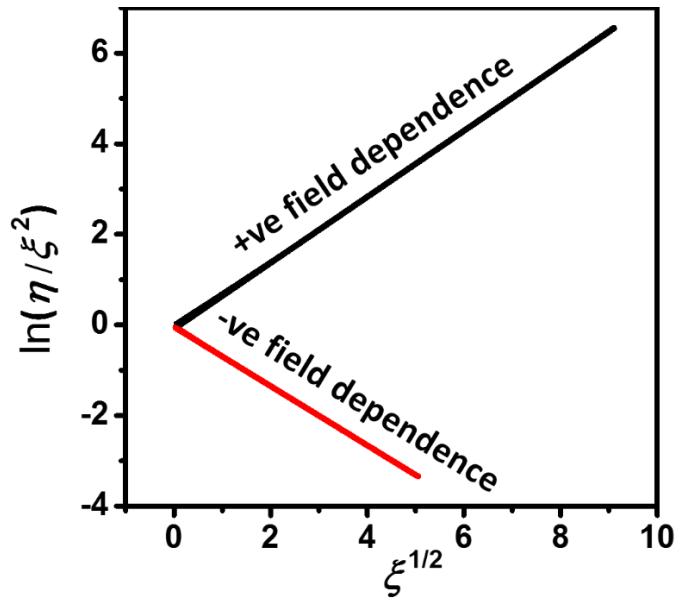


Figure 4.3. Plotting the variation of $\ln \eta / \xi^2$ against $\sqrt{\xi}$ yields a straight line, which supports the exponential dependence of the normalized current (η) on the square root of the normalized voltage $\sqrt{\xi}$.

Because the carrier mobility/carrier concentration has an exponential relation with the square root of the electric field, it is reasonable to check whether the same exponential relation holds for the normalized current and the square root of the normalized voltage applied. Figure 4.3 shows the variation of $\ln(\eta/\xi^2)$ versus $\sqrt{\xi}$. For both positive as well as negative field dependence, the data fit very closely to straight lines. However, at very high field, the data for the positive field dependence begins to deviate from linearity. Neglecting the small intercepts in the fit, the relation between η and ξ can be approximated closely as:

$$\eta = \xi^2 \exp(0.727\sqrt{\xi}); \quad \text{for positive field dependence} \quad (4.24)$$

$$\eta = \xi^2 \exp(-0.654\sqrt{\xi}); \quad \text{for negative field dependence} \quad (4.25)$$

Equations (4.24) and (4.25) can now be converted to the relation between the current density and the applied voltage as:

$$J = \frac{9}{8} \epsilon \mu_0 \frac{V^2}{d^3} \exp\left(0.891\gamma \sqrt{\frac{V}{d}}\right); \quad \text{for positive field dependence} \quad (4.26)$$

$$J = \frac{9}{8} \epsilon \mu_0 \frac{V^2}{d^3} \exp\left(-0.801\gamma \sqrt{\frac{V}{d}}\right); \quad \text{for negative field dependence} \quad (4.27)$$

The expression for positive field agrees with that reported by Murgatroyd and very closely represents the exact J - V data for a moderately high electric field. In the case of negative field dependence, the solution takes the same functional form as for positive field dependence but with a different exponential factor of -0.801 .

When using Murgatroyd's SCLC expression to probe the charge carrier mobility in disordered materials, one typically does not *a priori* know the nature (zero, positive, negative) of its electric field dependence. However, in the case of negative field dependence, the use of Murgatroyd's original expression would be incorrect, and the expression derived here specifically for this case (Equation (4.27)) should instead be used. In order to accurately fit the data using SS-SCLC analysis, one must therefore first both identify the correct SCLC region to fit *and* the nature of the electric field

dependence. If the test material exhibits field-dependent mobility, a traditional log–log analysis of the J – V data [208] will not produce a straight line with slope 2. In particular, a material exhibiting negative field dependence would yield a region with slope less than 2, which can easily be overlooked without careful analysis. On the other hand, the natural transition between Ohmic and space-charge-limited regimes in a log–log plot could possibly be mistaken as a region of negative field dependence. A better approach is arguably, therefore, to begin by plotting a graph of $\ln(\eta/\xi^2)$ against \sqrt{E} , which will yield a straight line with a negative slope in the case of SCLC with negative field dependence and a straight line with a positive slope in the case of SCLC with positive field dependence. A region of zero slope corresponds to SCLC with no field dependence. Independently, an investigation of the thickness dependence of the current–voltage behavior can confirm the existence of space-charge-limited current based on the expected inverse proportionality between current and thickness at constant V/d (Equations (4.26) and (4.27)) [208]. With this information in hand, one can then proceed to fit the appropriate region of the data with Equation (4.26) or (4.27) to obtain the desired charge transport parameters.

4.5. Conclusions

We have extended the theory of space-charge-limited current with an exponential electric field dependence of mobility/carrier concentration, originally reported by Murgatroyd, for the case of negative field dependence. Although the obtained current–voltage relations are based on fitting of the normalized current–

normalized voltage (η - ξ) data similarly to Murgatroyd's original work, here, an exact integration procedure has been used in lieu of the inherently inexact numerical integration procedure originally applied by Murgatroyd. For the case of positive field dependence, the correct solution is compared with Murgatroyd's numerical solution as well as with the analytical solution given by Barbe at high field. At low to the moderately high field, Murgatroyd's result is very close to the exact solution, and only at a very high field does Barbe's result begin to converge with the exact solution. In the case of negative field dependence, the current-voltage relation can be described by a function identical to that originally given by Murgatroyd, but with a different negative exponential factor of -0.801 . This newly derived equation can and should be applied to the steady-state current-voltage analysis of materials exhibiting negative-field-dependent mobility. Importantly, this development of steady-state space-charge-limited current analysis extends the utility of this technique to a greater range of challenging materials, and may provide an important tool for verifying transient results.

CHAPTER 5

MOBILITY EXTRACTION USING SPACE-CHARGE-LIMITED CURRENT ANALYSIS: EFFECT OF COMPETING CHARGE TRANSPORT PHENOMENA

5.1. Introduction

One of the objectives of this study is to estimate the charge carrier mobility in PECVD-grown a-BC:H thin films. Charge carrier mobility is one of the key metrics in a semiconductor detector material. It determines the magnitude of the signal current in a detector and the speed with which it can detect a large number of incident particles/radiation. In combination with charge carrier lifetime, carrier mobility determines the maximum possible thickness of a detector within a safe electric field and maximum detection efficiency the detector can achieve. However, the charge transport metrics in a-BC:H films, including the charge carrier mobility, are not well understood. In this chapter, we will describe the extraction of charge carrier mobility using steady-state space-charge-limited current (SS-SCLC) analysis and associated challenges.

We chose SS-SCLC analysis to extract the charge carrier mobility in a-BC:H films, as described in Section 2.3.2.3, because of its simplicity and applicability in high-resistivity and low-mobility films as compared to other methods discussed in CHAPTER 2. However, even with an ideal device geometry and contact requirements (*vide supra*), carrier mobility extraction using SCLC current analysis sometimes becomes difficult or impossible when other competing charge transport processes interfere with the SCLC mechanism. Two such processes: the Poole–Frenkel emission

[164] of trapped charge carriers at high electric fields and the exponential field dependence of charge carrier mobility [224], [227], [228], including negative field dependence [216]–[220], [225], [226] have been described in Chapter 4. In addition to these two processes, there are specific cases of SCLC, such as the trap-limited SCLC in the presence of a continuous distribution of defect states/traps in disordered materials, in which the extraction of carrier mobility becomes challenging. In such cases, the space-charge-limited current deviates significantly from the ideal Mott–Gurney law and may mimic other charge transport phenomena. The following sections describe these competing charge transport phenomena and the approaches we used to extract charge carrier mobility, if possible, and other properties in the PECVD-grown a-BC:H films under such conditions.

5.2. Ohmic Charge Transport with Poole–Frenkel Emission or Field-Dependent Mobility

5.2.1. Poole–Frenkel Emission

In the presence of Poole–Frenkel emission—the emission of trapped charge carriers as the applied electric field lowers the trap depth—the equilibrium thermal carrier concentration in an insulator/semiconductor is related to the applied electric field as [164]

$$n = n_0 \exp(\beta\sqrt{E}); \quad \beta = \frac{1}{kT} \left(\frac{e^3}{\pi\epsilon} \right)^{\frac{1}{2}} \quad (5.1)$$

where n_0 is the thermal equilibrium carrier concentration in the absence of electric field and β is the Poole–Frenkel coefficient, which depends on the high-frequency dielectric constant ϵ and the absolute temperature T . Poole–Frenkel emission, however, saturates at very high electric field when the trapping centers are completely ionized and further enhancement in the carrier concentration is not possible. Here, we assume that the electric field is within this saturation limit. The current–voltage relation for a device in the Ohmic regime, then, can be written as

$$J = \sigma_0 E \exp(\beta\sqrt{E}) \quad (5.2)$$

where $\sigma_0 = n_0 e \mu$ is the low-field conductivity.

In a device with efficient injecting contacts, it is generally expected that space-charge-limited current dominates the charge transport beyond a particular electric field, known as the cross-over field. Phenomenologically, the cross-over field can be understood as the electric field beyond which the carrier transit time ($d/\mu E$) in a device becomes shorter than the dielectric relaxation time ($\rho\epsilon$) so that the injected carriers are not neutralized/relaxed by thermal carriers [161], leading to an accumulation of space-charge in the device. In the absence of Poole–Frenkel emission, it can be approximated as

$$\frac{d}{\mu E_0} \approx \rho \epsilon \Rightarrow E_0 \approx \frac{ned}{\epsilon} \quad (5.3)$$

The exact value of the cross-over field is obtained by equating the Ohmic current to the ideal SCL current as

$$ne\mu E_0 = \frac{9}{8} \epsilon \mu \frac{E_0^2}{d} \Rightarrow E_0 = \frac{8ned}{9\epsilon} \quad (5.4)$$

However, in the presence of the Poole–Frenkel emission, the increased carrier concentration increases the minimum electric field required for the SCLC charge transport to dominate, as explained below.

The SCL current in the presence of Poole–Frenkel emission is given by the Murgatroyd's equation [229] as

$$J = \frac{9}{8} \epsilon \mu \frac{E^2}{d} \exp(0.891\beta\sqrt{E}) \quad (5.5)$$

Thus, for SCL current to dominate over Ohmic current with Poole–Frenkel emission, we need

$$\frac{9}{8} \epsilon \mu \frac{E^2}{d} \exp(0.891\beta\sqrt{E}) > n_0 E \mu E \exp(\beta\sqrt{E})$$

which can be rearranged to obtain

$$E > E_0 \exp(0.109 \beta\sqrt{E}) \quad (5.6)$$

where the right hand side represents the cross-over field in presence of Poole–Frenkel emission, and it shows that the cross-over field itself changes with the applied field. The SCL current is dominant only for electric field higher than the cross-over field. For

particular values of β and E_0 , both of which depend on material properties and device thickness, we can define a constant, referred to as the device constant C as

$$C = 0.109 \beta \sqrt{E_0} = 0.109 \frac{2e^2}{3\epsilon_0 kT} \left(\frac{2n_0 d}{\pi \epsilon_r \kappa} \right)^{\frac{1}{2}} \quad (5.7)$$

where e , ϵ_0 , k , T , n_0 , d , ϵ_r , and κ are respectively the electronic charge, vacuum permittivity, Boltzmann constant, absolute temperature, thermal equilibrium carrier concentration, device thickness, high-frequency dielectric constant, and low-frequency dielectric constant. Then, Equation (5.6) can be written as

$$\frac{E}{E_0} > \exp \left(C \sqrt{\frac{E}{E_0}} \right) \quad (5.8)$$

Equation (5.8) can be solved for E only if $C < 2/e = 0.736$, i.e., Murgatroyd's equation (Equation (5.5)) represents the device current only if the device constant is less than 0.736. Otherwise, Ohmic current enhanced by Poole–Frenkel emission always dominates the charge transport, and SCLC analysis cannot be used for the carrier mobility extraction. This can also be understood as Poole–Frenkel emission and SCLC can co-exist only within a certain region of the applied electric field, and only within that allowed electric field region, Murgatroyd's equation represents the current–voltage characteristics.

The allowed electric field region for the co-existence Poole–Frenkel emission and SCL charge transport is shown by the shaded part in Figure 5.1. Since the device constant C increases with device thickness, the above result also suggests that Poole–

Frenkel emission and SCL charge transport cannot co-exist if the device becomes thicker than the limiting thickness at which the device constant exceeds 0.736. The limiting (maximum) film thickness can be obtained by solving Equation (5.7) as

$$d \leq 23.865 \frac{\epsilon_r \kappa}{n_0} \left(\frac{\epsilon_0 k T}{e^2} \right)^2 \quad (5.9)$$

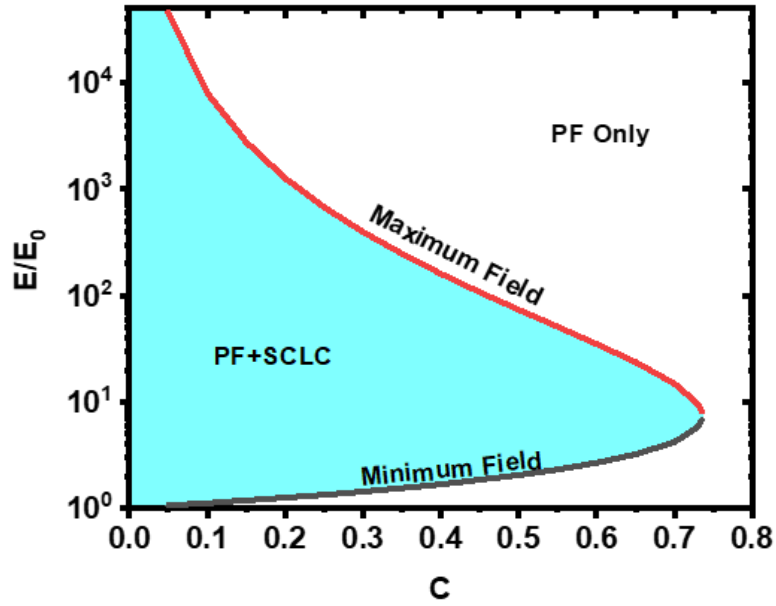


Figure 5.1. Minimum and maximum electric field as a function of the device constant C (Equation (5.7)) for Poole–Frenkel emission and SCLC to co-exist. E_0 is the cross-over field between Ohmic and SCLC charge transport in the absence of Poole–Frenkel emission. The colored region represents the allowed electric field region.

Equation (5.9) shows that the limiting thickness increases with increasing dielectric constant (both low- and high-frequency) but decreases inversely with

increasing thermal equilibrium carrier concentration. For a material with $\kappa = 5$ and $\epsilon_r = 4$, which, on average, represents the PECVD-grown a-BC:H films in this study, the device constant as a function of device thickness for different thermal equilibrium carrier concentrations, is shown in Figure 5.2.

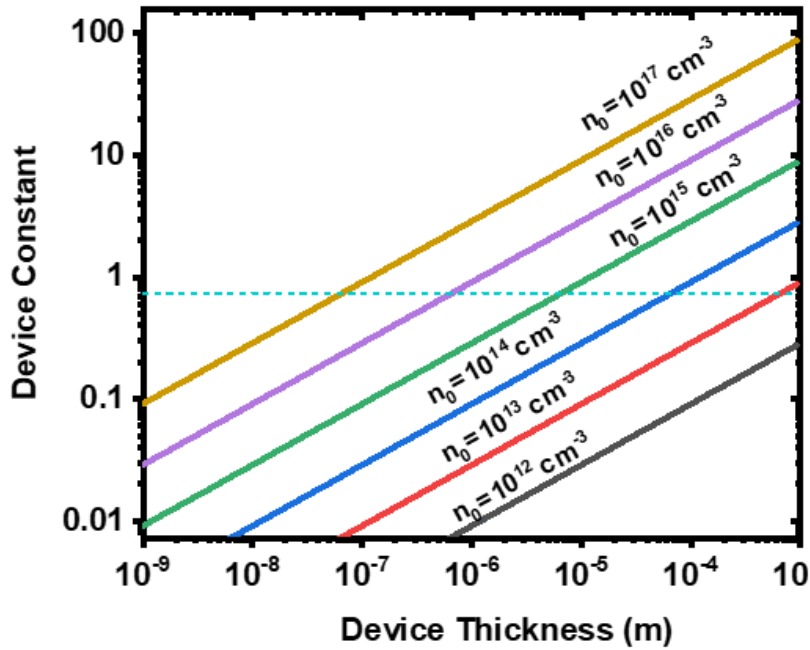


Figure 5.2. Device constant as a function of device thickness for different values of thermal equilibrium concentration. The low- and high-frequency dielectric constants assumed are 5 and 4, respectively. The dotted line in a is the limiting device constant (0.736) beyond which SCLC with Poole–Frenkel is not possible.

We can see from Figure 5.2 that the device constant increases with the carrier concentration as well as the device thickness. For example, for a carrier concentration of 10^{15} cm^{-3} , the device constant exceeds the limiting value when the device thickness

exceeds 9 μm . Thus, it is critical to identify whether a device can exhibit SCLC with Poole–Frenkel effect given the range of the carrier concentration and device thickness.

As discussed earlier, Poole–Frenkel emission saturates at very high electric fields [230], [231]. In such cases, in the absence of any other high-field effects, the ideal space-charge-limited current is theoretically possible. However, we can safely assume that the exponential dependence, $n = n_0 \exp(\beta\sqrt{E})$, holds true for $E \leq 100E_0$ so that for devices with $C < 0.736$, the carrier concentration does not increase by more than three orders of magnitude. If the device thickness and thermal equilibrium carrier concentration are large, the device constant becomes large (Figure 5.2), and the Poole–Frenkel emission may saturate. However, saturation of Poole–Frenkel emission generally needs an electric field in the range of MV/cm, which can be practically challenging to achieve in thicker devices. Thus, Poole–Frenkel emission can mask the onset of the expected SCLC charge transport at higher electric fields, as reported by some researchers [232], [233], and it should be considered while analyzing the current–voltage characteristics of materials with expected high defect densities.

5.2.2. Field-Dependent Mobility

In disordered materials, the exponential field dependence of charge carrier mobility is considered to be due to the hopping transport of the carriers, which can be written as

$$\mu(E) = \mu_0 \exp(\gamma\sqrt{E}) \quad (5.10)$$

Here, μ_0 is the low-field carrier mobility and γ is a fitting factor, as defined in Equation (4.6), which relates to the spatial and energetic disorder in material. Although the phenomenon is different, the current–voltage characteristics of devices in the injection-limited regime takes an identical form as for Poole–Frenkel emission as

$$J = \sigma_0 E \exp(\gamma\sqrt{E}) \quad (5.11)$$

However, because the current enhancement in this case is due to the increased carrier mobility, rather than carrier concentration, the minimum electric field required for SCL current to be observed does not change from the ideal cross-over field (E_0). Thus, at electric fields $E \geq E_0$, the current–voltage characteristic is again given by Murgatroyd’s equation with the Poole–Frenkel coefficient β replaced by the field-dependence factor γ as

$$J = \frac{9}{8} \epsilon\mu_0 \frac{E^2}{d} \exp(0.891 \gamma\sqrt{E}) \quad (5.12)$$

In the case where the field-dependent factor is negative, the current–voltage characteristic is given as (see CHAPTER 4)

$$J = \frac{9}{8} \epsilon\mu_0 \frac{E^2}{d} \exp(-0.801 \gamma\sqrt{E}) \quad (5.13)$$

However, the condition of the minimum electric field does not apply in this case.

In the case of positive field dependence, although the SCLC may be observed at $E \geq E_0$, carrier mobility extraction using SCLC analysis is possible only if the SCLC dominates over the Ohmic current enhanced by field-dependent mobility. i.e.,

$$\frac{9}{8} \epsilon \mu_0 \frac{E^2}{d} \exp(0.891 \gamma \sqrt{E}) > n e \mu_0 E \exp(\gamma \sqrt{E})$$

which can be simplified to

$$\frac{E}{E_0} > \exp\left(C \sqrt{\frac{E}{E_0}}\right); \quad C = 0.109 \gamma \sqrt{E_0} \quad (5.14)$$

which is identical to Equation (5.8), and can be solved only if $C < 0.736$. However, unlike the Poole–Frenkel coefficient β , which is related to the independently obtained resistivity and high-frequency dielectric constant of the material, the field-dependence factor γ is not known *a priori*. Thus, the device constant in this case should be calculated from the fit value of γ .

5.2.3. Experimental Considerations

In this section, we now discuss the practical implications of the charge transport process discussed in the previous sections and describe how the information can be used to analyze experimentally obtained current–voltage data to extract charge carrier mobility. When extracting charge carrier mobility using SCLC analysis, we generally look for a region where the current–voltage data produces a slope ≥ 2 on a log–log scale. However, with increasing electric field, particularly when $\beta \sqrt{E}$ or $\gamma \sqrt{E}$ exceeds 2, the

current–voltage data in the Ohmic regime with Poole–Frenkel emission or field-dependent mobility also produce a curve with slope >2 , giving a false impression of SCLC with positive field dependence, as shown in Figure 5.3. Fitting the current–voltage data to Murgatroyd’s equation then results in an incorrect estimation of charge carrier mobility and its associated field dependence factor. Thus, to avoid reporting incorrect charge transport metrics, the current–voltage data should also be fitted to the standard Poole–Frenkel format (Equation (5.2) or (5.11)) in addition to fitting to the Murgatroyd’s equation.

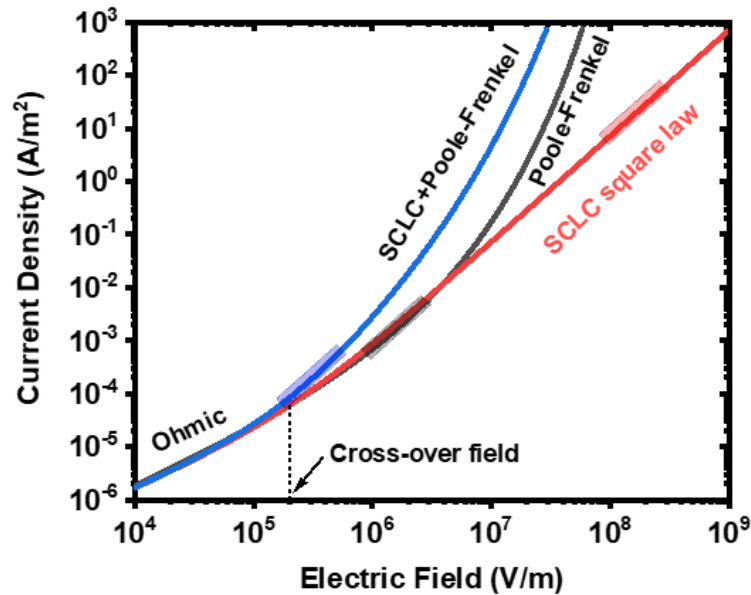


Figure 5.3. Theoretical current-voltage data of a 700 nm device with carrier concentration $n_0 = 10^{14} \text{ cm}^{-3}$, carrier mobility $\mu = 10^{-7} \text{ cm}^2 \cdot \text{V}^{-1} \cdot \text{s}^{-1}$, low-frequency dielectric constant $\kappa = 5$, and high-frequency dielectric constant $\epsilon = 4$ under different

charge transport phenomena. The slope of the current–voltage data is 2 in the shaded regions of corresponding curves.

If the charge transport is dominated by Ohmic transport enhanced by Poole–Frenkel emission or field-dependent mobility, in the standard Poole–Frenkel format, plotting $\ln(J/E)$ against \sqrt{E} produces a straight line

$$\ln\left(\frac{J}{E}\right) = \ln(\sigma_0) + m\sqrt{E}; \quad m = \beta \text{ or } \gamma \quad (5.15)$$

whereas, if the charge transport is dominated by SCLC enhanced by the Poole–Frenkel emission or by the field-dependent mobility, plotting $\ln(J/E^2)$ against \sqrt{E} produces a straight line as

$$\ln\left(\frac{J}{E^2}\right) = \ln\left(\frac{9}{8} \frac{\epsilon\mu_0}{d}\right) + 0.891m\sqrt{E}; \quad m = \beta \text{ or } \gamma \quad (5.16)$$

Figure 5.4 shows the current–voltage data of Figure 5.3 plotted in the format of Equations (5.15) and (5.16) to demonstrate the straight-line regions corresponding to the dominant charge transport phenomena. We can see from the figure that only Ohmic charge transport with Poole–Frenkel emission or field-dependent mobility produce straight line when plotted in the format of Poole–Frenkel Equation (5.15) (Right axis), whereas, only SCL charge transport with Poole–Frenkel emission or field-dependent mobility produce straight line when plotted in the format of Murgatroyd Equation (5.16) (Left axis).

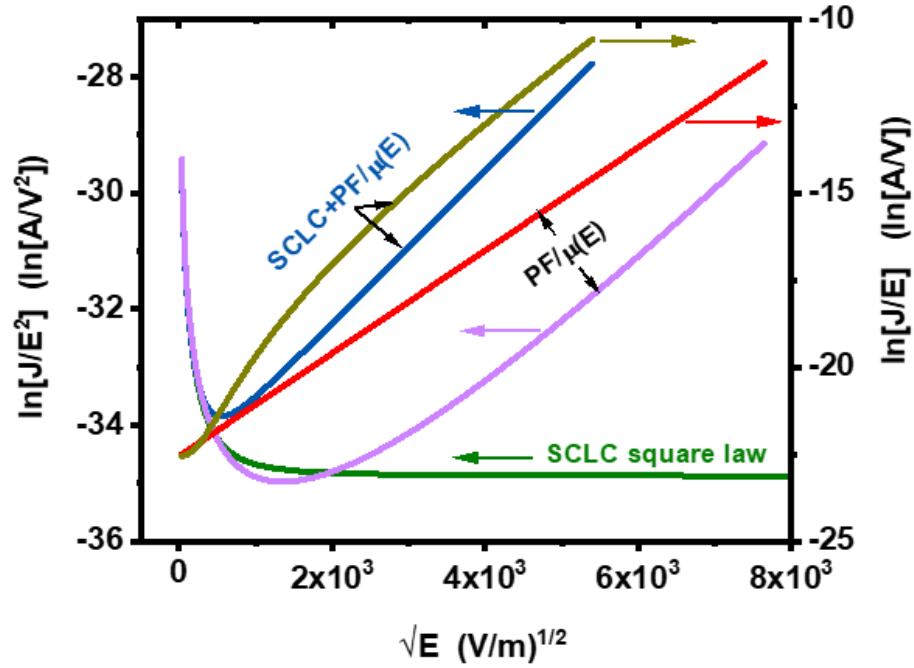


Figure 5.4. Current–voltage data of Figure 5.3 plotted in the format of Equations (5.15) and (5.16). Only Ohmic charge transport with Poole–Frenkel emission or field-dependent mobility produces straight line in the format of Equation (5.15), and only the SCLC enhanced by Poole–Frenkel emission or field-dependent mobility produces straight line in the format of Equation (5.16), which, along with the device constant calculated from the fit parameters, helps in determining whether SCLC is present or not.

In the case of Poole–Frenkel emission, the low-field conductivity (σ_0) can be obtained from the intercept, and the field-dependence factor (β or γ) can be extracted from the slope of straight line (Equation (5.15)). The high-frequency dielectric constant can be estimated from β using Equation (4.3). By comparing the values of the high-frequency dielectric constants obtained from this fitting to the values obtained from

other independent experiments, such as ellipsometry, and looking at the goodness of the fits, the likelihood of the behavior being attributed to Poole–Frenkel emission can be attributed. However, even if Poole–Frenkel emission is not possible, field-dependent mobility could still be used to explain the charge transport as long as the fit quality is appropriate to choose field-dependence as a dominating charge transport mechanism. If Poole–Frenkel emission or field-dependent mobility does not appropriately explain the charge transport, then we proceed to test for SCL charge transport.

In the case of SCLC enhanced by Poole–Frenkel emission or field-dependent mobility, the Poole–Frenkel coefficient β or the field-dependence factor γ can be obtained from the slope of straight line (Equation (5.16)) and can be checked for their consistency as described previously. From the intercept of the straight line, the carrier mobility can be obtained as

$$\mu_0 = \frac{8d}{9\epsilon} \exp(\text{Intercept}) \quad (5.17)$$

Once the carrier mobility is obtained, the carrier concentration can be calculated using the resistivity calculated from the low-field Ohmic regime. For the self-consistency of the calculated carrier mobility and carrier concentration, the device constants for Poole–Frenkel emission and field-dependent mobility are calculated using Equations (5.7) and (5.14), respectively, and should be checked whether the values are within the limiting value of 0.736. In the case of SCLC enhanced by Poole–Frenkel emission, the extracted high-frequency dielectric constant from the coefficient β should be checked against the experimental value even if the device constant is below the

limiting value. In the case of field-dependent mobility, however, the field-dependence factor cannot be checked against an experimental value and the decision should be made based on the comparison of fit quality relative to other charge transport processes, which we will describe in the following sections.

5.3. Space-Charge-Limited Current with Continuous Distribution of Traps

The ideal Mott–Gurney square law of space-charge-limited current (Equation (2.16)) generally applies to ideal crystalline solids or solids with discrete sets of empty shallow traps which trap the injected carriers and reduce device current. In the case of a single set of shallow traps, the Mott–Gurney law takes a form identical to the original form as [161]

$$J = \frac{9}{8} \epsilon \mu \theta \frac{V^2}{d^3} \quad (5.18)$$

where θ is the ratio of the free carrier concentration to the trapped carrier concentration. With the increased injected charge carriers, when the traps are filled completely, the current again follows the ideal Mott–Gurney law after displaying a nearly vertical section in a current–voltage plot, generally known as the *trap-filled limit* (TFL) [161]. In materials with discrete set of traps with well separated energy levels, the current–voltage plot displays multiple TFL sections from which the trap densities of corresponding energy levels can be obtained [161].

In disordered semiconductors, however, traps are distributed continuously in energy [161], and the ideal Mott–Gurney law may not describe the SCLC charge transport in such materials. If traps are distributed exponentially in energy, given as

$$N_t(\varepsilon) = \frac{N_t}{kT_c} \exp\left(-\frac{|\Delta\varepsilon|}{kT_c}\right) \quad (5.19)$$

where N_t/kT_c is the trap density at the conduction or valence band edge, T_c is a characteristic temperature of the trap distribution, and $\Delta\varepsilon$ is the depth of the trap energy from the corresponding band edge, the trap-limited SCLC current is given as [161]

$$J_{T \text{ SCLC}} = \sigma_0 E \left(\frac{E}{E_x}\right)^l; \quad l = \frac{T_c}{T} \quad (5.20)$$

Here, σ_0 is the low-field conductivity and E_x is the cross-over voltage between the Ohmic and SCLC regime. The cross-over voltage is given as

$$E_x = \frac{eN_t d}{\epsilon} \left(\frac{n_0}{N_c}\right)^{\frac{1}{l}} \left(\frac{l+1}{2l+1}\right)^{\frac{l+1}{l}} \frac{l+1}{l} \quad (5.21)$$

where N_c is the density of states at the band edge related to the thermal equilibrium carrier concentration, n_0 , as

$$n_0 = N_c \exp\left(-\frac{|\Delta\varepsilon_f|}{kT}\right) \quad (5.22)$$

with $\Delta\varepsilon_f$ being the depth of the Fermi energy from the corresponding band edge. In some cases, where the transition from Ohmic to space-charge-limited current is very slow,

i.e., a distinct change in the slope of the current–voltage curve is not observed, a modified expression has also been used, which is given as [161]

$$J = \sigma_0 E \left(1 + \frac{E}{E_x} \right)^l \quad (5.23)$$

In experiments, if $\log (J_{\text{T SCLC}}/E)$ is plotted against $\log (E)$, we obtain a straight line

$$\log \left(\frac{J_{\text{T SCLC}}}{E} \right) = \log \sigma_0 - l \log E_x + l \log E \quad (5.24)$$

with slope l . Because the transition field E_x is related to the unknown parameters N_t , N_c , and n_0 , the carrier mobility cannot be extracted using SCLC analysis in this case. Although the characteristic temperature T_c can be extracted from the slope l , its physical significance is not yet clear, except Lampert [161] has suggested that it might represent the temperature at which the annealing of material during the cooling phase is ceased. However, in practical cases, sometimes, the characteristic temperature obtained from such an analysis becomes very high compared to the fabrication temperature of the device and the characteristic temperature does not represent the annealing temperature. In such cases, the experimental current–voltage data is better represented with a uniform distribution of traps, as an approximation of the exponential distribution with large T_c . If the traps are distributed uniformly in energy, given as

$$N_t(\varepsilon) = N_n$$

then, the trap-limited SCLC current is given as [161]

$$J_{T \text{ SCLC}} = 2\sigma_0 E \exp\left(\frac{2\epsilon E}{N_n e d kT}\right) \quad (5.25)$$

If $\ln(J_{T \text{ SCLC}}/E)$ is plotted against E , a straight line is obtained as

$$\ln\left(\frac{J_{T \text{ SCLC}}}{E}\right) = \ln(2\sigma_0) + \frac{2\epsilon}{N_n e d kT} E \quad (5.26)$$

from which, the low-field conductivity can be extracted from the intercept, and the trap density can be extracted from the slope as

$$N_n = \frac{2\epsilon}{e d kT} \frac{1}{(\text{slope})} \quad (5.27)$$

Again, due to the unknown thermal equilibrium carrier concentration n_0 , which determines the low-field conductivity σ_0 , carrier mobility cannot be extracted from the SCLC analysis if the traps are distributed uniformly. In both the exponential and uniform distribution, however, the carrier mobility extraction is possible if the electric field is sufficient to fill all the empty traps so that the charge transport enters the trap-filled square law regime, and the SCLC follows ideal Mott–Gurney law.

If the observed current–voltage data shows evidence for a continuous distribution of traps, either uniform or exponential, but the trap-filled region is not achieved within the maximum applied electric field, a minimum limit for charge carrier mobility can be estimated as follows. If $\ln(J/E^2)$ is plotted against \sqrt{E} , the current–voltage data produce a curve similar to that of the SCLC enhanced by Poole–Frenkel emission, as shown in Figure 5.4, however without the straight-line part after the minima predicted by Murgatroyd’s expression. If we further increase the electric field,

theoretically, we should reach to the trap-filled limit above which the current follows the Mott-Gurney square law, producing a horizontal straight line. The intercept made by the horizontal line at this condition should give the trap free carrier mobility as

$$\mu_0 = \frac{8d}{9\epsilon} \exp(\text{Intercept}) \quad (5.28)$$

Although we do not know at which field the trap-filled limit is achieved, we know for sure that the field will be higher than the field at which the current–voltage data have produced the minima. Thus, if we extract the carrier mobility corresponding to the intercept made by a horizontal line passing through the minima using Equation (5.28), it will be the minimum carrier mobility in the device.

5.4. Mobility Extraction of Selected Films

For the charge carrier mobility determination in the a-BC:H films, the space-charge-limited current analysis was routinely used for previously grown films [95], [234], [235]. Specifically, a protocol published by the National Physics Laboratory by Blakseley et al. [170] was used to analyze the current–voltage data as the PECVD-grown a-BC:H films are believed to fulfil the requirements outlined in the protocol for extracting carrier mobility using the space-charge-limited current analysis [208]. The carrier mobility values were extracted by fitting the current–voltage data to Murgatroyd’s equation (Equation (5.12)), if possible, and for other cases, the values were calculated as described in previous section. In the case of the films obeying the ideal square law, the carrier mobility values were extracted using the Mott–Gurney law,

which also corresponds to Murgatroyd's equation with the field-dependence factors (β or γ) equal to zero. Since a single method to extract the carrier mobility was not consistent with all a-BC:H films, the following sections explain the mobility extraction in some selected films grown for this study using different methods explained in previous section.

5.4.1. PCITO Series Films: Films Grown at Low Temperature and Low RF Power

The PCITO series films were grown at lower substrate temperature and lower RF power, and generally resulted in high resistivity ($\sim 10^{12} \Omega\cdot\text{cm}$). We will discuss the detailed growth conditions and film properties later in CHAPTER 6. Figure 5.5 shows the current–voltage data of the PCITO series films in the format of Murgatroyd's Equation (5.16). We can see from the figure that, except for the PCITO11c and PCITO10a films, the current–voltage data fit to the equation, and demonstrate clear straight lines corresponding to the SCLC charge transport regime. Thus, the carrier mobility values were extracted using the field-dependent SCLC analysis. Since PCITO10a exhibited a wide range of electric field for which the slope is nearly zero (corresponding to ideal SCLC), the carrier mobility was calculated using the Mott–Gurney law.

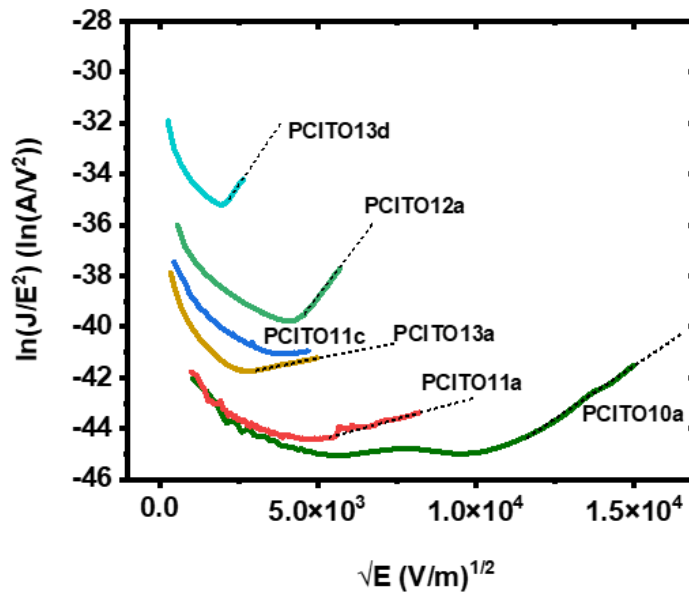


Figure 5.5. Current–voltage data of the PCITO series films plotted in the format of Murgatroyd's equation. The dashed lines at the end of data are the trend lines of the fit.

5.4.2. V and AA Series Films: Films Grown at High Temperature and High RF Power

The V and AA series films were grown at high substrate temperature and high RF power with a combination of low and high precursor flow rate, which we will describe in detail in Chapter 6. The films in the V series were also characterized after additional annealing for 4 hours at $>500^{\circ}\text{C}$. The plot of $\ln(J/E^2)$ against \sqrt{E} for the V series films before and after annealing are shown in Figure 5.6.

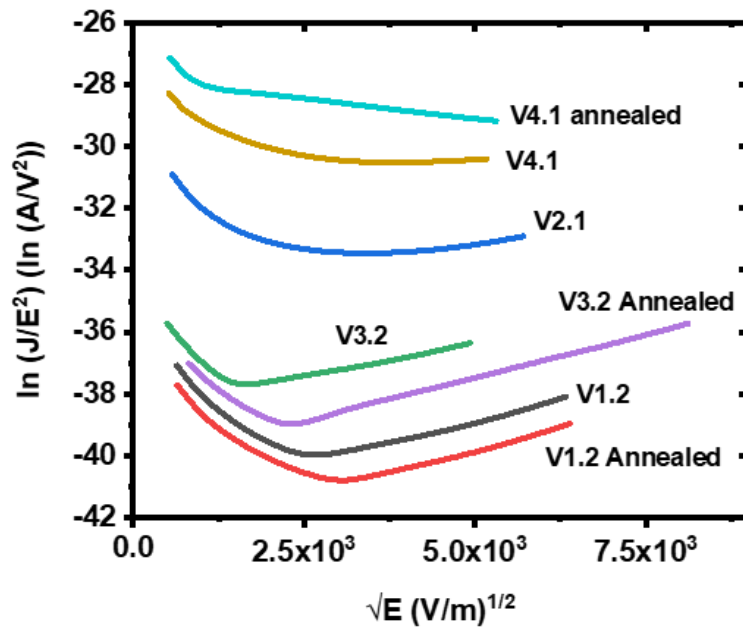


Figure 5.6. Current–voltage data of the V series films plotted in the format of Murgatroyd's equation.

We can see from Figure 5.6 that the V1.2 and V3.2 films produced straight lines after reaching the minima with increasing electric field, showing that the current–voltage data of these films fit well with the Murgatroyd's equation, whereas the films V2.1 and V4.1 show a gradual increase in slope, for which the Murgatroyd fit could give an incorrect carrier mobility. The V4.1 film after annealing, however, produced a straight line with a negative slope, suggesting negative field-dependence in carrier mobility. Table 5.1 summarizes the parameters extracted from the Murgatroyd fit for the V series films that are consistent with the theory.

From Table 5.1, we can see that, except for the V1.2 and V4.1 films, the calculated device constants ($C(\beta)$) corresponding to the Poole–Frenkel emission are

below the limiting value (0.736), consistent with the SCLC with Poole–Frenkel emission. However, the higher fit values of the high-frequency dielectric constants do not agree with this mechanism. Since the device constants $C(\gamma)$ for all of the films corresponding to the field-dependent mobility are below the limiting value, the IV data are more consistent with the SCLC charge transport with field-dependent mobility.

Figure 5.7 shows the current–voltage data of the AA series films plotted in the format of the Murgatroyd’s Equation (5.16). Except for the four films in Figure 5.7(b), all of the other films showed characteristics similar to those obtained for the V2.1 and V4.1 films in that the slope of the curves increases slowly after attaining the minimum. Also, the minima in the plots are within a small range of electric field at ~ 0.1 MV/m, which is not expected based on their varying film thickness, indicating that the films grown at higher temperatures and higher total flow rates could have a different dominating charge transport process. However, because the data produced nearly straight lines for a wide range of electric field after reaching the minima, the carrier mobility values were extracted using Murgatroyd fit as a first order approximation. The carrier mobility values and parameters extracted from the Murgatroyd fit are summarized in Table 5.2.

Table 5.1. Parameters extracted from the Murgatroyd fit for the V series films. Symbols μ_0 , n , and ϵ_r represent respectively the carrier mobility, carrier concentration, and the high-frequency dielectric constant.

Film	μ_0 (cm ² /V·s)	n (cm ⁻³)	ϵ_r (exp)	β, γ (m/V) ^{1/2}	ϵ_r (fit)	$C(\beta)$	$C(\gamma)$
V1.2	8.9×10^{-11}	2.3×10^{16}	4.67	5.1×10^{-04}	33.3	0.78	0.29
V1.2 Annealed	2.8×10^{-11}	6.7×10^{16}	4.67	5.6×10^{-04}	27.5	1.32	0.54
V3.2	1.4×10^{-09}	3.1×10^{15}	4.67	4.2×10^{-04}	48.5	0.27	0.08
V3.2 Annealed	4.6×10^{-10}	4.6×10^{15}	4.75	6.1×10^{-04}	23.1	0.47	0.21
V4.1 Annealed	7.1×10^{-05}	3.8×10^{14}	5.66	-2.9×10^{-04}	–	–	–

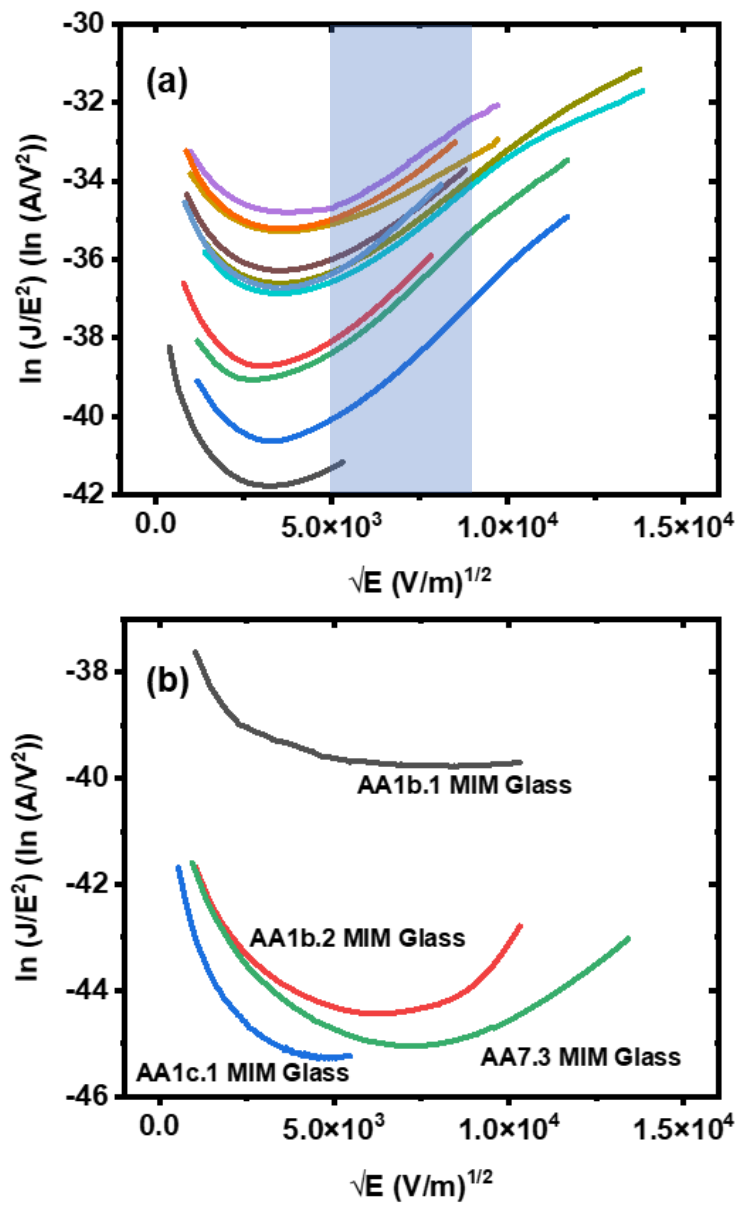


Figure 5.7. Current–voltage data of the AA series films a) films that potentially fit to Murgatroyd's Equation (5.16) in the shaded region and b) films that do not fit to Murgatroyd's equation.

Table 5.2. Parameters extracted from the Murgatroyd fit of current–voltage data of the selected V and AA series films. Symbols μ_0 , n , and ϵ_r represent respectively the carrier mobility, carrier concentration, and the high-frequency dielectric constant.

Film Name	μ_0 (cm ² /V·s)	n (cm ⁻³)	ϵ_r (exp)	β, γ (m/V) ^{1/2}	ϵ_r (fit)	$C(\beta)$	$C(\gamma)$
V2.1	5.9×10 ⁻⁰⁸	1.4×10 ¹⁶	5.29	4.5×10 ⁻⁰⁴	42.8	0.70	0.25
V4.1	2.1×10 ⁻⁰⁶	1.8×10 ¹⁵	5.11	1.4×10 ⁻⁰⁴	430.5	0.19	0.02
AA1.1	1.5×10 ⁻¹¹	1.0×10 ¹⁶	3.96	5.3×10 ⁻⁰⁴	31.1	0.76	0.27
AA1b.1 MIM Glass	2.9×10 ⁻⁰⁹	2.2×10 ¹⁴	3.80	–	–	–	–
AA1b.2 MIM Si	1.1×10 ⁻¹¹	2.8×10 ¹⁵	3.80	1.2×10 ⁻⁰⁴	568.5	0.75	0.06
AA1c.1 MIM Glass	7.4×10 ⁻¹²	2.8×10 ¹⁵	4.12	–	–	–	–
AA2c.1	7.5×10 ⁻¹¹	2.8×10 ¹⁶	3.88	9.6×10 ⁻⁰⁴	9.5	1.67	1.07
AA7.3 MIM Glass	8.1×10 ⁻¹⁴	3.8×10 ¹⁷	3.72	5.0×10 ⁻⁰⁴	35.1	5.27	1.72
AA13b.1	3.0×10 ⁻¹²	1.0×10 ¹⁷	4.58	9.9×10 ⁻⁰⁴	8.9	1.96	1.41
AA13b.3	1.8×10 ⁻¹¹	8.7×10 ¹⁵	4.58	9.4×10 ⁻⁰⁴	9.8	0.48	0.33
AA14.1	3.6×10 ⁻⁰⁹	1.9×10 ¹⁶	4.88	6.8×10 ⁻⁰⁴	18.8	0.82	0.42
AA14.2	3.7×10 ⁻⁰⁹	1.7×10 ¹⁶	4.88	5.5×10 ⁻⁰⁴	28.4	0.75	0.31
AA15.1	1.5×10 ⁻¹⁰	2.0×10 ¹⁷	4.62	8.0×10 ⁻⁰⁴	13.7	2.08	1.21
AA15.2	2.7×10 ⁻¹⁰	2.3×10 ¹⁷	4.54	7.8×10 ⁻⁰⁴	14.2	2.17	1.23
AA15.3	2.5×10 ⁻¹⁰	1.2×10 ¹⁷	4.67	7.6×10 ⁻⁰⁴	15.1	1.61	0.90
AA17.1	2.3×10 ⁻⁰⁹	5.5×10 ¹⁶	4.58	7.3×10 ⁻⁰⁴	16.2	1.62	0.86
AA17.2	2.8×10 ⁻¹⁰	1.1×10 ¹⁷	4.62	9.2×10 ⁻⁰⁴	10.3	2.36	1.58

We can see from Table 5.2 that the calculated device constants ($C(\beta)$) of most of the films are above the limiting value 0.736, which indicates that the charge transport in these devices is not consistent with SCLC enhanced by Poole–Frenkel emission. Although the films V2.1, V4.1, and AA13b.3 have device constants below the limiting value, the fit values of the high-frequency dielectric constants of the films are much higher than the experimentally obtained values, which is inconsistent with SCLC enhanced by Poole–Frenkel emission. Similarly, half of the films listed in Table 5.2 have device constants ($C(\gamma)$) are below the limiting value while the other half of the films have device constants above the limiting value, suggesting that some of the films can be considered to be consistent with the SCLC enhanced by the field-dependent mobility. However, the similarity of their current–voltage characteristics, irrespective to their device constants differing, suggests that a different charge transport process could be dominating in these films, and that the Murgatroyd fit could result in incorrect mobility values.

5.4.2.1. Test for Ohmic Charge Transport with Poole–Frenkel Emission or Field-Dependent Mobility

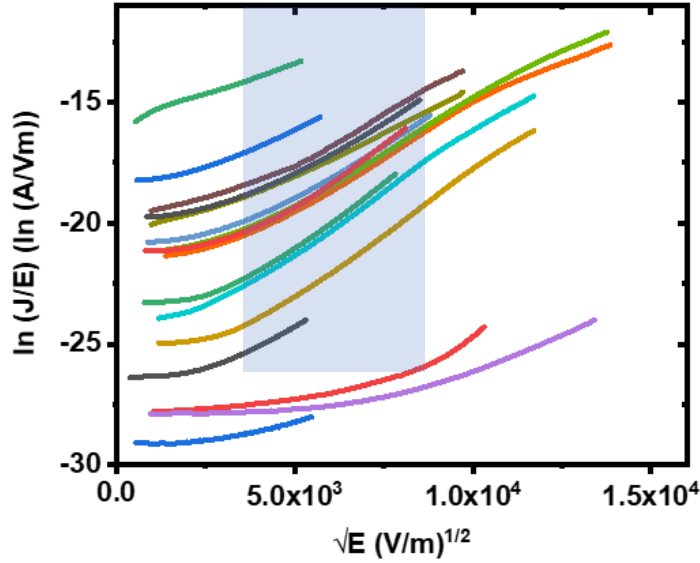


Figure 5.8. Current–voltage data of the V and AA series plotted in the standard Poole–Frenkel format (Equation (5.15)). The shaded portion represents the electric field region where the data produces nearly straight lines.

Figure 5.8 shows the current–voltage data for the AA and V series films in the standard Poole–Frenkel format (Equation (5.15)). We can see that most of the plots produce straight lines in a wider field region at >9 MV/m ($\sqrt{E} = 3 \times 10^3$ ($V^{1/2}m^{1/2}$)) compared to the Murgatroyd fits. Thus, we extracted the field-dependence factor (β or γ) and the high-frequency dielectric constant from the Poole–Frenkel fit, which are tabulated in Table 5.3.

Table 5.3. Field-dependence factor and high-frequency dielectric constant extracted from the Poole–Frenkel fit of the AA and V series films.

Film Name	β, γ (m/V)^{1/2}	ϵ_r (fit)	ϵ_r (exp.)
V2.1	6.5×10^{-04}	20.72	5.29
V4.1	5.2×10^{-04}	31.80	5.11
AA1.1	8.2×10^{-04}	12.96	3.96
AA1b.2 MIM Si	1.0×10^{-03}	8.22	3.80
AA1c.1 MIM Glass	4.4×10^{-04}	45.02	4.12
AA2c.1	1.1×10^{-03}	7.47	3.88
AA7.3 MIM Glass	6.1×10^{-04}	23.40	3.72
AA13b.1	1.0×10^{-03}	8.06	4.58
AA13b.3	1.1×10^{-03}	7.76	4.58
AA14.1	8.9×10^{-04}	11.02	4.88
AA14.2	7.4×10^{-04}	15.90	4.88
AA15.1	9.3×10^{-04}	10.06	4.62
AA15.2	9.1×10^{-04}	10.47	4.54
AA15.3	9.0×10^{-04}	10.75	4.67
AA17.1	8.9×10^{-04}	11.07	4.58
AA17.2	1.1×10^{-03}	7.61	4.62

As we can see from the table, the high-frequency dielectric constants obtained from the Poole–Frenkel plot are generally more than double the corresponding experimental values obtained with ellipsometry. This suggests that Poole–Frenkel emission alone cannot describe the charge transport in these films. However, Ohmic charge transport enhanced by field-dependent mobility also results in identical current–voltage characteristics. Thus, the charge transport in these films could be dominated by a combined effect of Poole–Frenkel emission and field-dependent mobility.

5.4.2.2. Test for SCLC with Exponential Distribution of Traps

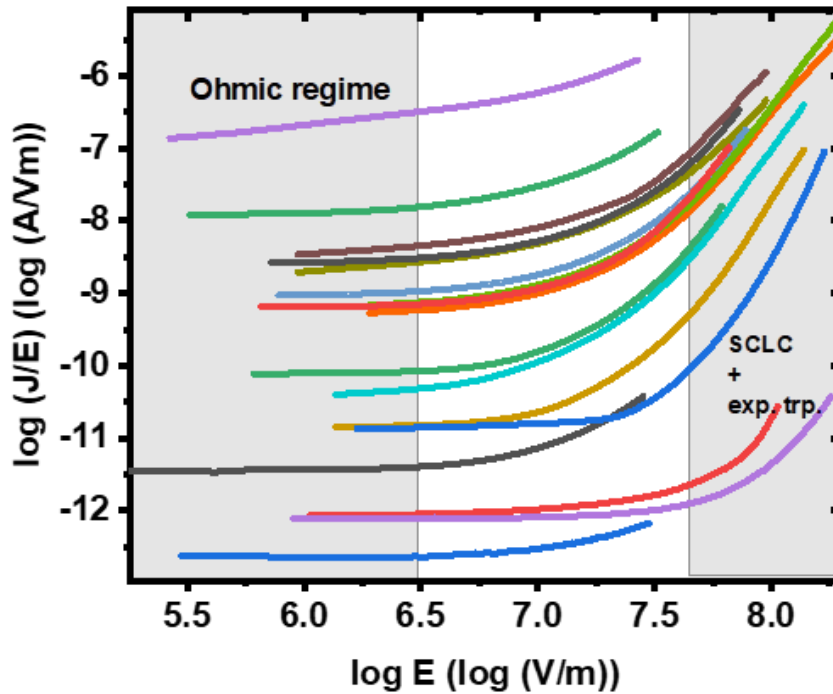


Figure 5.9. Current–voltage data of the AA and V series films plotted in the format of Equation (5.24), describing SCLC with exponential distribution of traps.

Figure 5.9 shows the current–voltage data of the AA and V series films plotted in the format of Equation (5.24). Although some of the graphs produce straight lines at >30 MV/m (0.3 MV/cm), the characteristic temperatures obtained from the fit values of the exponent (l) for all of the films are higher than their deposition temperatures. Because these higher characteristic temperature values cannot be interpreted as the temperature at which the annealing stops [161], and such higher characteristic

temperature are often interpreted as evidence for the uniform distribution of traps, we further analyzed the data for this case.

5.4.2.3. Test for SCLC with Uniform Distribution of Traps

Figure 5.10 shows the current–voltage data of the AA and V series films in the format of Equation (5.26), representing the SCLC charge transport with the uniform distribution of traps. The figure shows that the plots of most of the films produce nearly straight lines for a fairly large electric field range (0–0.6 MV/cm) compared to the field range of fit for the Poole–Frenkel emission and SCLC with the exponential distribution of traps. Further, unlike in other cases, here, the straight lines start from low-field region, which is expected if the charge transport is dominated by traps. Thus, the uniform distribution of traps better described the charge transport in the AA series films grown at high temperature and RF power compared to other charge transport processes described before. Further, the slow saturation of the current at >1 MV/cm may suggest that the current is approaching the trap-filled limit (TFL). Because carrier mobility extraction using the SCLC analysis in this case is not possible unless we can achieve the trap-field limit, the minimum carrier mobility values were extracted using the procedure described in Section 5.3. The minimum carrier mobility and the extracted trap density for the AA and V series films are tabulated in Table 5.4.

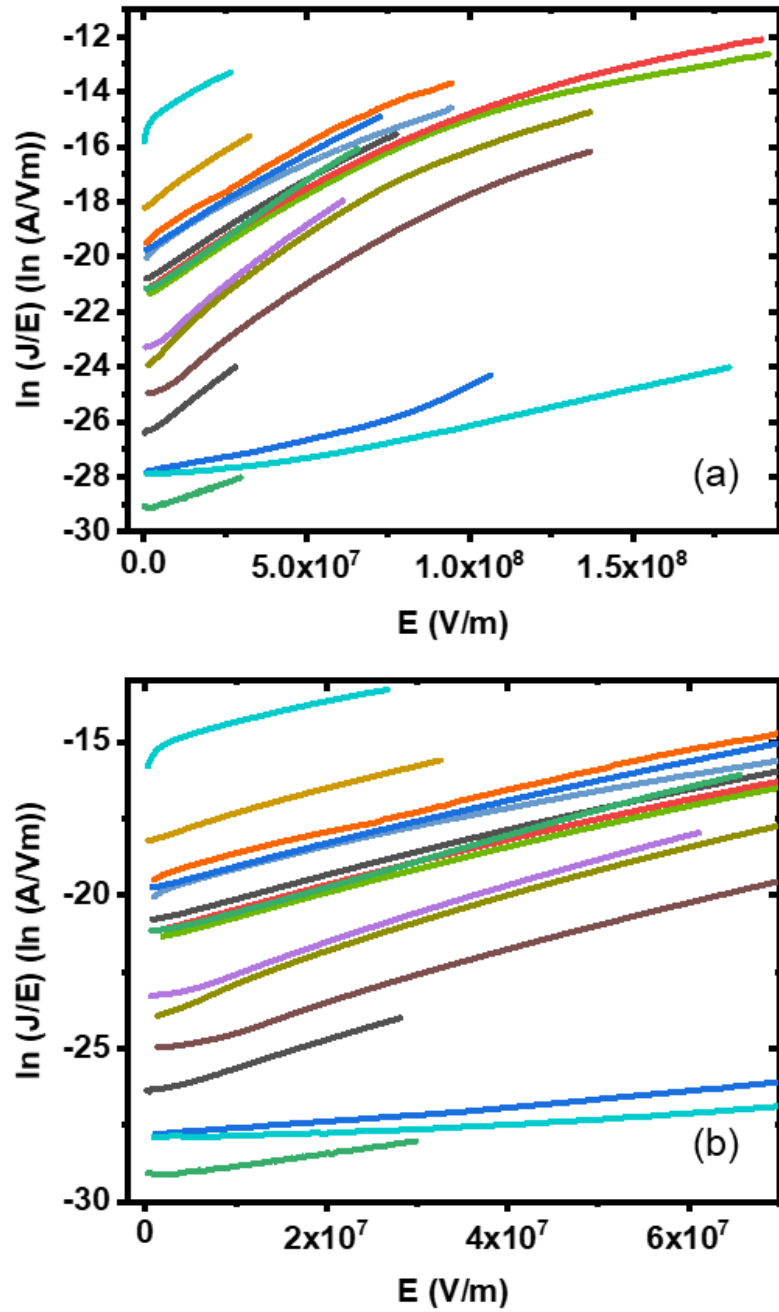


Figure 5.10. Current–voltage data for the AA and V series films (a) plotted in the format of Equation (5.26) and (b) a zoomed section where data fit to straight lines.

Table 5.4. Minimum carrier mobility and the trap density extracted from the SCLC analysis of the AA and V series films. Symbols μ_{\min} and N_t represent the minimum carrier mobility and trap density, respectively.

Film Name	μ_{\min} ($\text{cm}^2 \cdot \text{V}^{-1} \cdot \text{s}^{-1}$)	N_t ($\text{cm}^{-3} \text{eV}^{-1}$)
V2.1	3.4×10^{-07}	5.07×10^{17}
V4.1	3.7×10^{-06}	9.13×10^{17}
AA1.1	9.9×10^{-10}	3.71×10^{17}
AA1b.2 MIM Si	2.2×10^{-11}	4.01×10^{17}
AA1c.1 MIM Glass	6.2×10^{-12}	3.20×10^{17}
AA2c.1	3.7×10^{-09}	2.17×10^{17}
AA7.3 MIM Glass	4.5×10^{-12}	1.03×10^{18}
AA13b.1	2.3×10^{-10}	5.64×10^{17}
AA13b.3	7.9×10^{-10}	7.16×10^{17}
AA14.1	8.0×10^{-08}	6.21×10^{17}
AA14.2	4.6×10^{-08}	7.35×10^{17}
AA15.1	5.8×10^{-09}	1.04×10^{18}
AA15.2	1.0×10^{-08}	1.03×10^{18}
AA15.3	7.5×10^{-09}	1.07×10^{18}
AA17.1	6.8×10^{-08}	4.56×10^{17}
AA17.2	1.6×10^{-08}	3.73×10^{17}

5.4.3. Thickness Dependence Test for Space-Charge-Limited Current

A common way to confirm space-charge-limited conduction is to conduct a thickness-dependent current measurement at a constant electric field. In this experiment, the current–voltage data is extracted from identical devices of different thicknesses. Based on Equations (2.15), (5.5), and (5.12), the current in the space-charge-limited regime should be proportional to the inverse of the device thickness at a constant electric field, and based on Equation (5.4), the transition from the Ohmic regime to the space-

charge-limited regime should occur at an electric field proportional to the device thickness.

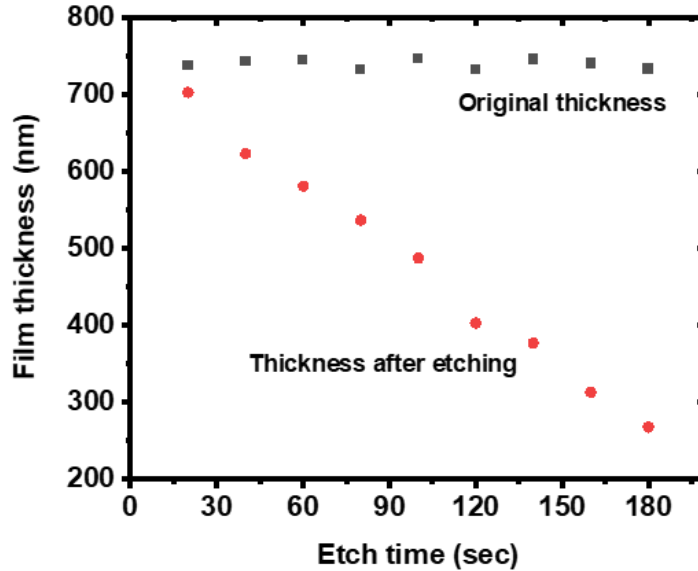


Figure 5.11. Thickness of the TD1703 films determined by spectroscopic ellipsometry before and after $C_2F_6 + O_2$ plasma etching.

For the thickness dependence test, we needed identical devices with different thicknesses. However, because the properties of a-BC:H films are known to be sensitive to growth time, and films tend to not be perfectly reproducible batch-to-batch, growing identical films with different thicknesses was not straightforward. Thus, instead of growing different films, one a-BC:H film, referred to as TD1703, was grown on a full 4-inch wafer using the AA series growth conditions, and nine samples were cleaved out of it. The films were then etched in a $C_2F_6+O_2$ plasma for different etch times to obtain films of varying thicknesses. To reduce possible systematic error, the sample etching

was randomized. Based on the thicknesses measured with spectroscopic ellipsometry, a uniform etch rate of 2.6 nm/s was obtained. The film thickness before and after etching as a function of etch time is shown in Figure 5.11.

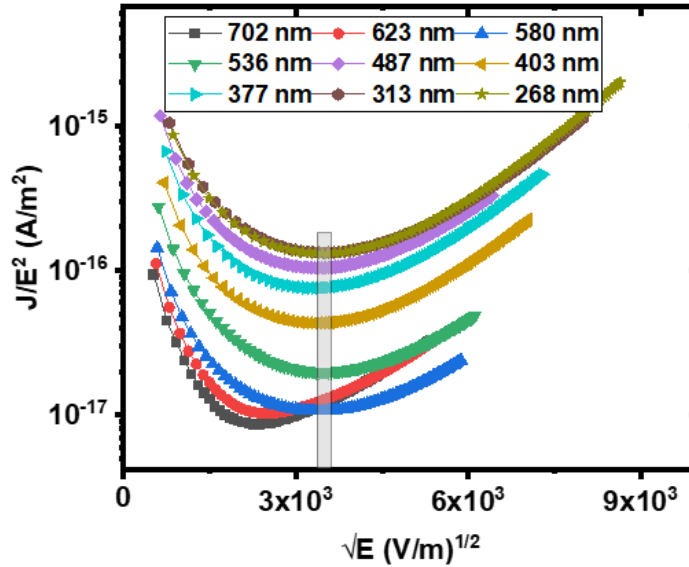


Figure 5.12. Graph of J/E^2 against \sqrt{E} of the film TD1703 with different thicknesses achieved after C_2F_6 etching. The vertical bar at $\sim 10^7$ V/m (0.1 MV/cm) represents the field region at which the curves attain the minima.

Figure 5.12 shows the current–voltage data of the films with different thicknesses plotted in the format of the Murgatroyd’s equation. Except for the two films with thicknesses of 702 and 623 nm, all the films displayed a narrow range of transition field around 10^7 V/m (0.1 MV/cm), irrespective to their thicknesses, which also matches with the field at which $\ln(J/E^2)$ was found to attain minima in the AA series films.

Thus, the analysis could not verify whether these samples exhibited the SCLC charge transport or not.

Table 5.5 summarizes the resistivity (extracted using Ohm's law at low electric field, and the carrier mobility, carrier concentration, and device constants extracted using the Murgatroyd fit for the TD1703 films. We can see that the resistivity of the films decreased as the films became thinner after etching, which is also shown in Figure 5.13. This result was unexpected considering that the films were supposed to be identical. Based on the linear fit of the resistivity data, the average resistivity as a function of film thickness can be written as

$$\langle \rho(d) \rangle = \rho_0 \exp\left(\frac{d}{d_0}\right) \quad (5.29)$$

where $\rho_0 = 1.4 \times 10^{10} \Omega \cdot \text{cm}$ and $d_0 = 107 \text{ nm}$ are the fit values for TD1703 films. Thus, the spatial resistivity profile (resistivity of the film as a function of distance from the substrate) can be written as

$$\rho(x) = \rho_0 \exp\left(\frac{x}{d_0}\right) \left(1 + \frac{x}{d_0}\right); \quad (5.30)$$

Table 5.5. Parameters extracted from the Murgatroyd fit of current–voltage data for the TD1703 films. Symbols μ_0 , n , and ϵ_r represent respectively the carrier mobility, carrier concentration, and the high-frequency dielectric constant.

Film Thickness (nm)	Resistivity* ($\Omega\cdot\text{cm}$)	μ_0 ($\text{cm}^2/\text{V}\cdot\text{s}$)	n (cm^{-3})	β, γ (m/V)^{1/2}	ϵ_r (fit)	$C(\beta)$	$C(\gamma)$
702	1.18×10^{13}	1.8×10^{-10}	2.9×10^{15}	6.6×10^{-04}	19.8	0.39	0.18
623	4.93×10^{12}	1.6×10^{-10}	7.9×10^{15}	6.6×10^{-04}	20.0	0.60	0.28
580	3.14×10^{12}	1.4×10^{-10}	1.4×10^{16}	5.5×10^{-04}	28.4	0.77	0.30
536	1.31×10^{12}	2.0×10^{-10}	2.4×10^{16}	5.9×10^{-04}	25.3	0.96	0.40
487	2.92×10^{11}	7.2×10^{-10}	3.0×10^{16}	6.5×10^{-04}	20.5	1.03	0.47
403	7.91×10^{11}	1.9×10^{-10}	4.2×10^{16}	7.2×10^{-04}	17.0	1.11	0.56
377	4.00×10^{11}	2.0×10^{-10}	7.9×10^{16}	7.9×10^{-04}	14.1	1.46	0.81
313	1.91×10^{11}	2.2×10^{-10}	1.5×10^{17}	8.0×10^{-04}	13.7	1.78	1.02
268	2.41×10^{11}	1.5×10^{-10}	1.8×10^{17}	8.5×10^{-04}	12.1	1.83	1.11

*resistivity is independently extracted from the Ohmic regime of IV data.

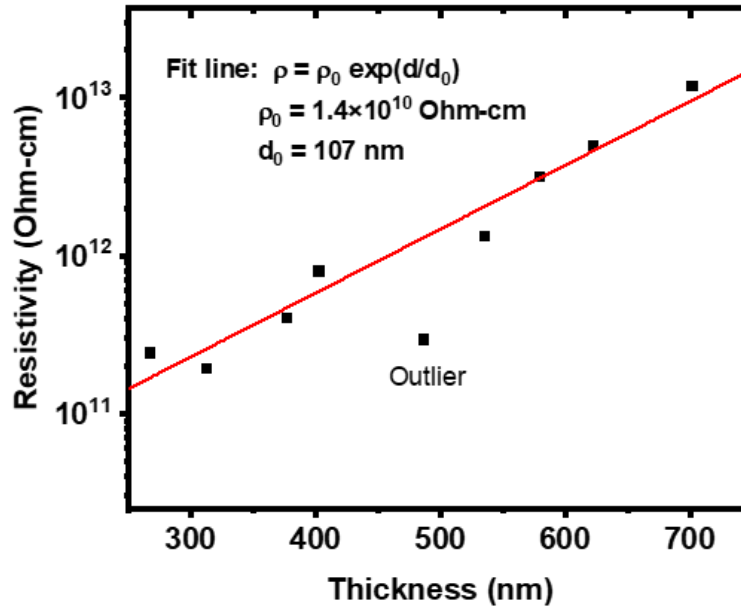


Figure 5.13. Resistivity of TD1703 films as a function of their film thickness.

Although we don't have a clear understanding of the change in resistivity as a function of film depth, it might be potentially due to a longer effective annealing time spent by the bottom layers during the growth, which resulted in higher conductivity. Because of this change in resistivity, we could not test for the inverse relationship of the SCLC current with the device thickness as the current was already affected by the conductivity in the Ohmic regime.

Based on the extracted values of the high-frequency dielectric constant and the device constants ($C(\beta)$) (Table 5.5), we discarded the possibility of the SCLC charge transport enhanced by the Poole-Frenkel emission alone. However, the device constants ($C(\gamma)$) corresponding to the field-dependent mobility for the first six thicker films are

within the limiting value (0.736), suggesting that the charge transport in these films could still be SCLC enhanced by field-dependent mobility. But, because all of the films showed identical current–voltage characteristics despite their device constants being below or above the limiting value, it was not convincing to confirm the mobility values extracted as the true values. Further, despite the increasing conductivity with the decreasing film thickness, the carrier mobility values extracted remained nearly constant, which is counterintuitive in that a longer annealing time increased the conductivity but not the carrier mobility.

For the possibility of alternative charge transport, we performed current–voltage analysis for Ohmic charge transport with Poole–Frenkel, SCLC with exponential trap distribution, and SCLC with uniform trap distribution. Figure 5.14 shows the current–voltage data of the TD1703 films plotted in the format of these mechanisms.

Figure 5.14 shows that the current–voltage data of the TD1703 films fit the best to the SCLC with uniform distribution of traps. Thus the minimum carrier mobility, maximum carrier concentration, and the trap density were calculated using the procedures described in Section 5.3. Table 5.6 summarizes the parameters extracted based on the SCLC with the uniform distribution of traps model.

Table 5.6. Minimum carrier mobility, maximum carrier concentration, and trap density in the TD1703 films extracted using SCLC with the uniform distribution of traps model.

Film Thickness (nm)	Resistivity ($\Omega\cdot\text{cm}$)	μ_{min} ($\text{cm}^2/\text{V}\cdot\text{s}$)	n_{max} (cm^{-3})	N_t $\text{cm}^{-3}\text{eV}^{-1}$
580	3.14×10^{12}	1.2×10^{-09}	1.7×10^{15}	4.70×10^{17}
536	1.31×10^{12}	2.0×10^{-09}	2.4×10^{15}	5.27×10^{17}
487	2.92×10^{11}	9.6×10^{-09}	2.2×10^{15}	5.55×10^{17}
403	7.91×10^{11}	3.3×10^{-09}	2.4×10^{15}	6.49×10^{17}
377	4.00×10^{11}	5.4×10^{-09}	2.9×10^{15}	7.05×10^{17}
313	1.91×10^{11}	7.7×10^{-09}	4.2×10^{15}	9.12×10^{17}
268	2.41×10^{11}	6.8×10^{-09}	3.8×10^{15}	1.04×10^{18}

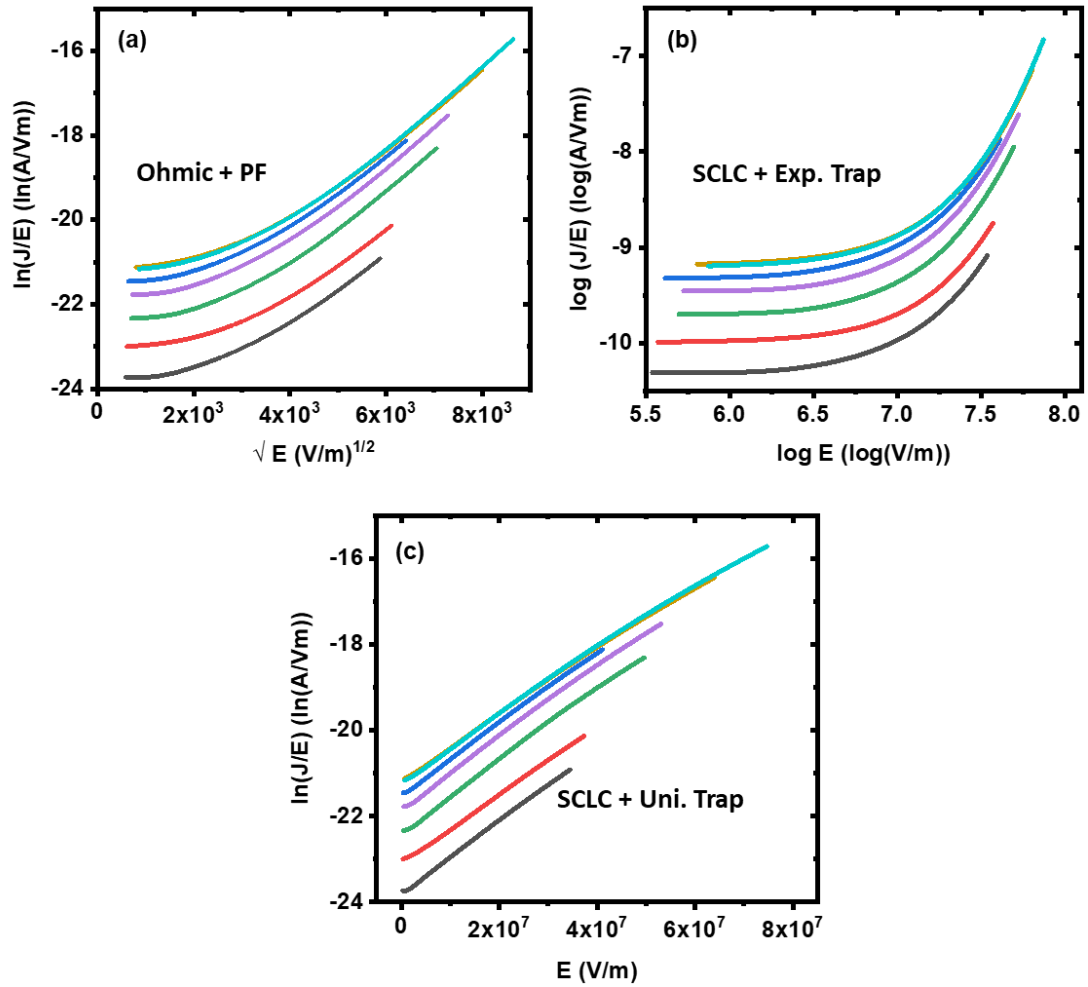


Figure 5.14. Current–voltage data of the TD1703 films plotted in the format of a) Ohmic current enhanced by Poole–Frenkel emission, b) SCLC with exponential distribution of traps, and c) SCLC with uniform distribution of traps.

Table 5.6 shows that the carrier mobility increases as the device becomes thinner, which is more convincing than the previous result obtained with the Murgatroyd fit, in which the carrier mobility remained constant, but the carrier concentration increased with etching. As we can see from the table, the trap density increased slightly

with the decreasing film thickness, which may also explain the slightly higher carrier concentration for the thinner films.

5.5. Conclusions

In this chapter, we discussed the effect of different charge transport mechanisms in the analysis of current–voltage data and discussed the methods we followed to extract charge carrier mobility values in a-BC:H films using the most consistent method. From the analysis of the PCITO series films, we concluded that the films grown at lower temperature and RF power are generally consistent with space-charge-limited current enhanced by the field-dependent mobility. The space-charge limited current enhanced by Poole–Frenkel emission, however, was not consistent with the current–voltage data of any of the low temperature films. The current–voltage data for the V and AA series films grown at high temperatures and RF power, however, were described better with the trap-limited space-charge-limited current mechanism with uniform distribution of traps. To check for the presence of the space-charge-limited conduction in the high-temperature films, the TD1703 films were etched to obtain films of different thicknesses, and current–voltage data were obtained for the thickness dependence test for SCLC charge transport. The study, however, could not provide sufficient evidence for the presence of SCLC with Poole–Frenkel emission or field-dependent mobility. Similarly to the V and AA series films, the films were better described by SCLC mechanism with a uniform distribution of traps. The study of the TD1703 films also revealed that the resistivity of a-BC:H films decreased as the films became thinner with

etching, suggesting that the resistivity profile is not uniform along the device thickness. Along with the minimum charge carrier mobility, the trap concentrations were also extracted for the AA and TD1703 films, which suggested that the trap concentration decreases as the film becomes thicker during film deposition.

CHAPTER 6

CHARGE TRANSPORT OPTIMIZATION OF AMORPHOUS HYDROGENATED BORON CARBIDE FILMS

6.1. Mobility Measurement and Optimization

The specific goals of this study were to optimize charge transport metrics, including charge carrier mobility, in PECVD-grown amorphous hydrogenated boron carbide (a-BC:H) thin films and then grow high mobility-films of greater thickness, which are required for neutron detection applications. Previous studies [93], [95] on the charge transport and mechanical properties of a-BC:H thin films had identified ranges of PECVD process parameters (*vide supra*) that yielded higher charge carrier mobility films as well as ranges that produced thicker films—combining these two is critical to obtain high-mobility thick films for detector fabrication. For higher charge carrier mobility in particular, two growth regimes were identified: “gentle” growth conditions, which used lower substrate temperatures and lower RF powers, and “harsh” growth conditions, which used higher substrate temperatures and higher RF powers as shown in Figure 6.1. The gentle growth conditions yielded low-density films containing higher hydrogen concentration, and the harsh growth conditions yielded hard, high-density films with lower hydrogen concentration. Thus, we first focused on further exploring these two growth regimes to optimize carrier mobility in thin films, however, experimenting with different PECVD process parameters to potentially yield higher growth rates to produce high-mobility thick films. Further, we also experimented with

post-growth thermal treatments in an effort to improve the charge transfer and mechanical stability of these films.

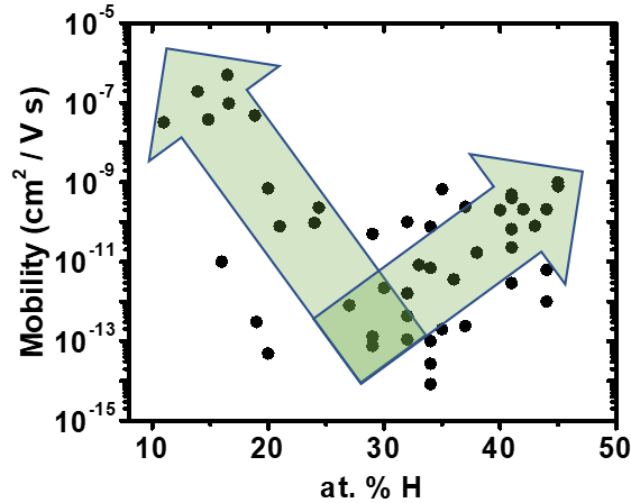


Figure 6.1. Charge carrier mobility of a-BC:H thin-films as a function of hydrogen concentration observed in previous studies within the group. Lower/higher hydrogen concentration correspond to harsh/gentle growth conditions.

6.1.1. Gentle Growth Conditions: Low RF Power and Low Substrate Temperature

6.1.1.1. The PCITO series Films

Besides relatively high mobility, the “gentle” growth conditions had also exhibited the highest growth rate in previously grown and studied thin films [93], [95]. Thus, we chose to further explore the effect of temperature (in a relatively low temperature range) and partial precursor pressure because these were identified to affect the carrier mobility and film growth rate, respectively. Thus, a 2² factorial experiment

was designed as outlined in Table 6.1, in which we used a total of 4 combinations of substrate temperature and partial precursor pressure. Additionally, we included the growth condition of film N25 grown in the previous study [95], which had resulted in the highest growth rate highest carrier mobility. Table 6.2 summarizes the growth conditions of this series of films, referred to as the PCITO series, based on the factorial design Table 6.1, and Table 6.3 summarizes their properties.

Table 6.1. 2^2 factorial experiment design for a-BC:H film growth in the low-power/low-temperature regime. Other process conditions were held constant at a power of 15 W, pressure of 0.2 Torr, and total carrier gas flow rate of 200 sccm.

Variables	Low	High
Temperature (°C)	125	225
Partial flow rate	0.2	1*

* indicates that two precursor bubblers were used with 100 sccm flowed through each.

Table 6.2. Growth conditions for the PCITO series films. The films PCITO 10, 11, 13, and 14 were grown for the 2^2 factorial experiments, as given in Table 6.1, and the film PCITO12 was grown using the growth conditions of a previously grown film N25.

Film Name	Temperature (°C)	Power (W)	Pressure (Torr)	Total Flow (sccm)	Partial o-carborane flow	Growth Time (min)
PCITO10	225	15	0.2	200	1*	20
PCITO11	225	15	0.2	200	0.2	20
PCITO13	125	15	0.2	200	1*	20
PCITO14	125	15	0.2	200	0.2	20
PCITO12	100	10	0.2	100	0.5	20

*indicates that two precursor bubblers were used.

Table 6.3. Properties of the PCITO series films. Symbols RI, κ , ρ , μ_0 , E_g , and E_U are respectively the refractive index, low-frequency dielectric constant, resistivity, low-field mobility, bandgap, and Urbach energy.

Film Name	Thickness (nm)	Growth rate (nm/min)	RI	κ	ρ ($\Omega\cdot\text{cm}$)	μ_0 ($\text{cm}^2/\text{V}\cdot\text{s}$)	γ (cm/V) ^{1/2}	E_g (eV)	E_U (meV)
N25	1302	109	1.7	3.7	2.7×10^{13}	8.0×10^{-10}	1.8×10^{-3}	2.7	240
PCITO12a	154	8	1.6	3.7	1.5×10^{12}	5.7×10^{-13}	1.8×10^{-4}	3.5	476
PCITO12b	1366	68	2.5	7.1	–	–	–	3.6	235
PCITO10a	89	4	1.8	3.5	2.4×10^{14}	7.7×10^{-13}	–	3.6	323
PCITO10b*	905	45	1.8	–	–	–	–	–	–
PCITO10c	407	20	1.9	4.3	–	–	–	3.6	332
PCITO11a*	300	15	2.2	4.2	1.2×10^{14}	5.7×10^{-13}	4.0×10^{-3}	–	–
PCITO11c	453	23	1.8	4.5	7.8×10^{13}	1.6×10^{-09}	–	3.8	917
PCITO13a	806	40	1.7	5.7	1.5×10^{12}	8.3×10^{-10}	2.6×10^{-3}	3.6	370
PCITO13d	1433	72	1.7	8.0	4.4×10^{11}	2.9×10^{-09}	2.1×10^{-3}	4.1	641
PCITO14*	311	16	1.8	4.2	–	–	–	4.1	794

Labels ‘a’, ‘b’, etc. represent repeat growths using the same conditions. *denotes the films delaminated or tended to delaminate prior to testing.

Many a-BC:H films in the PCITO series were grown multiple times because of frequent film delamination and observed variation in the growth rate. Films grown immediately after refilling the precursor bubbler (films with labels ‘a’ in Table 6.3) were much thinner, and film thickness gradually increased with repeated growths. However, we could not achieve growth rates higher than 100 nm/min, as expected from the growth conditions of the film N25. Since the growth rate is strongly correlated to the precursor partial flow rate [95], its variation suggested possible inconsistency in the *ortho*-carborane sublimation from the bubbler. The suggested varying sublimation rate did not allow us to accurately study the effect of measured precursor flow rate on the film properties. However, it did allow us to study the charge transport properties of films as a function of the growth rate itself, which could better represent the actual precursor flow rate than the measured carrier gas flow rate. Figure 6.3 and Figure 6.3 show the variation of optical, electronic, and electrical properties of the PCITO series films as a function of film growth rate.

We can see from Figure 6.3 that the refractive index ($n = \sqrt{\epsilon_r}$) decreased with the growth rate, while the low-frequency dielectric constant (κ) increased. Figure 6.3 shows that the electrical resistivity decreased with increasing growth rate while the carrier mobility increased. Specifically, across a narrow range of growth rates (0–40 nm/min), the charge carrier mobility in a-BC:H films increased by more than three orders of magnitude, while the electrical resistivity decreased by nearly two and a half orders of magnitude, indicating a small decrease in carrier concentration with the

increase in growth rate. Because all of the potentially thicker films delaminated, we could not expand the study for higher growth rates.

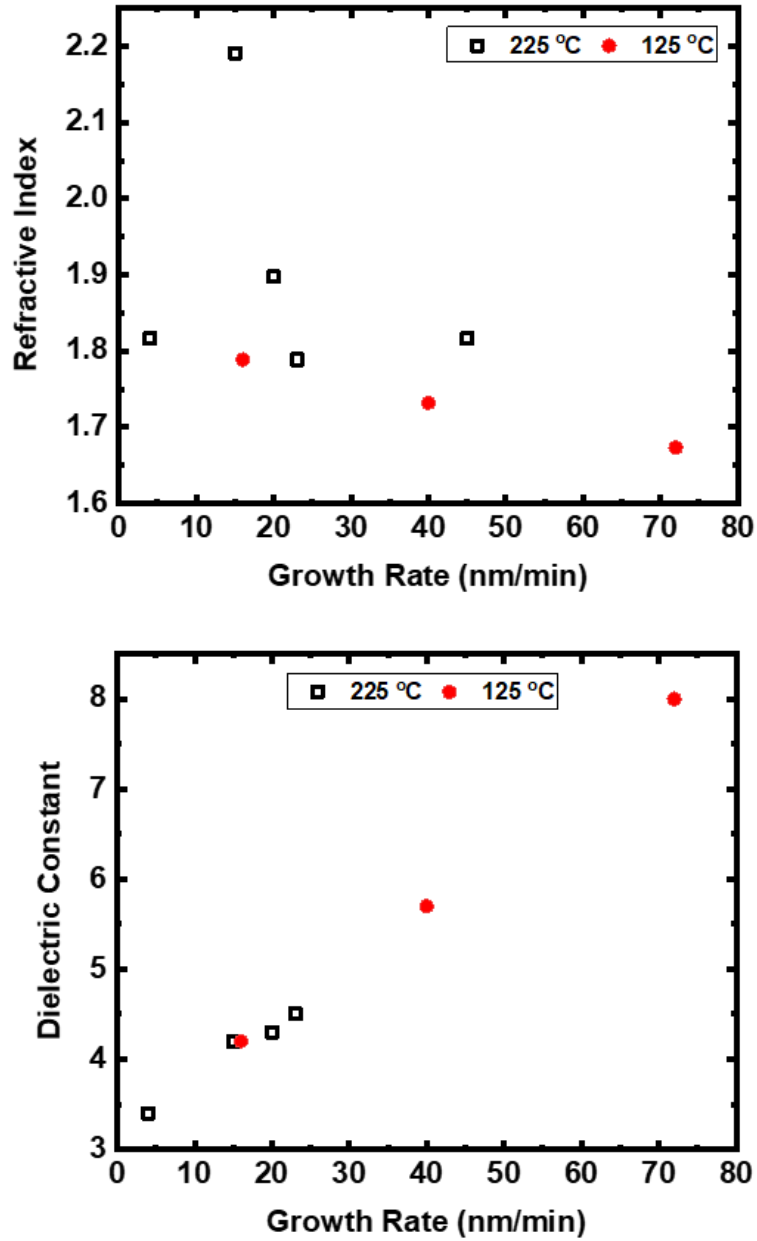


Figure 6.2. Refractive index and low-frequency dielectric constant of the PCITO series films as a function of growth rate for substrate temperature of 125 °C and 225 °C.

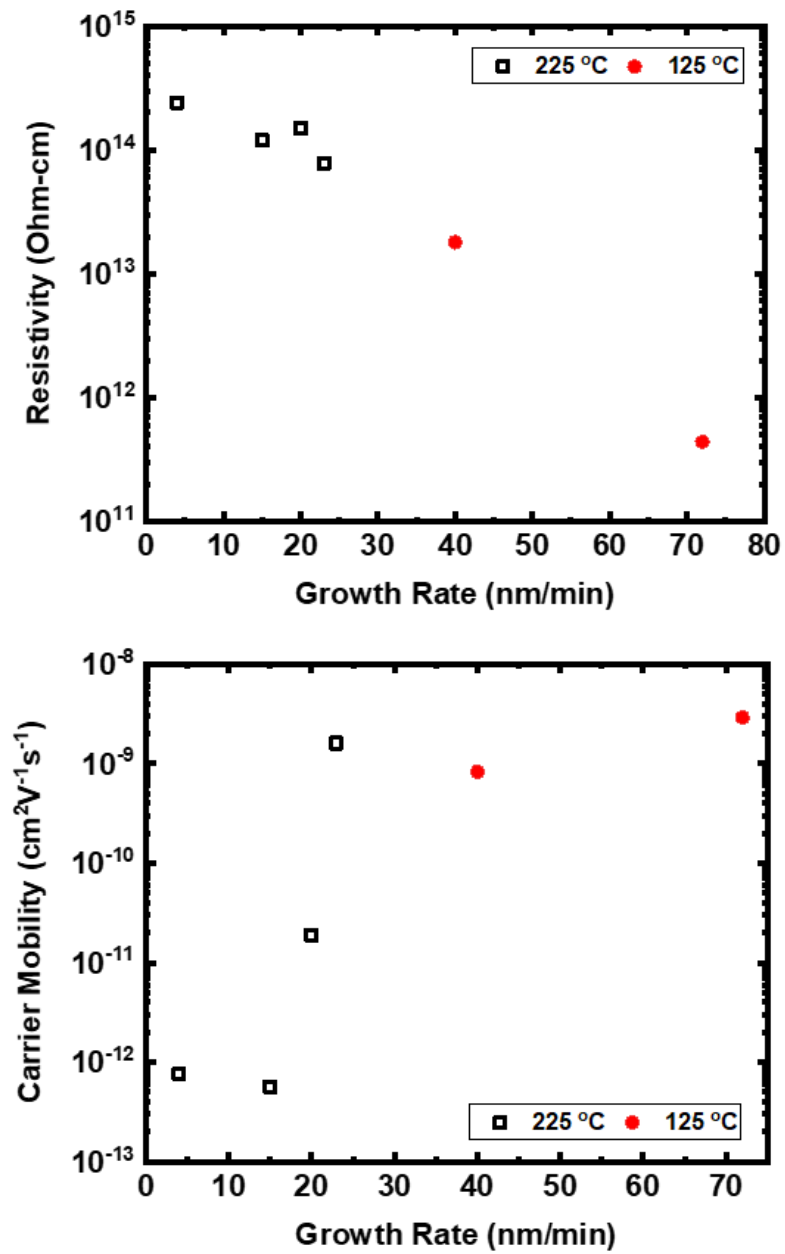


Figure 6.3. Resistivity and carrier mobility of the PCITO series films as a function of growth rate for substrate temperature of 125 °C and 225 °C.

We expected the PCITO series films grown with the “gentle” growth conditions to extend the range of carrier mobility to higher than $10^{-9} \text{ cm}^2 \cdot \text{V}^{-1} \cdot \text{s}^{-1}$, as expected for the growth conditions of the film N25. However, we found that this is the higher limit of carrier mobility obtainable with these growth conditions. However, this study provided new insight into the fact that the growth rates could play an important role in optimizing the electronic and charge transport properties in PECVD-grown a-BC:H films.

6.1.2. Harsh Growth Conditions: High RF Power and Substrate Temperature

6.1.2.1. The V series films

Harsher growth conditions (high temperature and high RF power), which produced films with lower hydrogen concentration, as shown in Figure 6.1, were also identified as conducive to producing thin films with higher carrier mobility [93], [95]. However, the films were grown using lower precursor partial flow, and the growth conditions were not optimized for high growth rates. Thus, we chose to explore the effect of total flow rate and precursor partial flow rate at higher substrate temperature and higher RF power as a means to potentially increase carrier mobility beyond the range obtainable with the gentle growth conditions and obtain higher growth rates simultaneously. We designed a 2^2 factorial experiment to produce films using the “harsh” growth conditions based on a matrix of total flow rate and partial flow rate

parameters as given in Table 6.4. The growth conditions of the films, referred to as the V series, are summarized in Table 6.5.

Table 6.4. 2² factorial experiment design for film growth at high temperature and high power.

Process Parameters	Low	High
Total Flow Rate (sccm)	50	200
Partial Flow Rate	0.2	1*

*indicates two solid-state bubblers were used.

Table 6.5. Growth conditions for V series films grown according to the 2² factorial experiment design outlined in Table 6.4. The films were grown at 500 °C and 40 W at a pressure of 0.2 Torr for 20 minutes.

Film Name	Total Flow Rate (sccm)	Partial <i>o</i>-carborane Flow
V1	50	0.2
V2	200	0.2
V3	50	1*
V4	200	1*

*indicates two solid-state bubblers were used.

Table 6.6. Properties of V series thin films grown with the growth conditions given in Table 6.5. Symbols RI, κ , ρ , μ_0 , E_{04} , and E_U are respectively the refractive index, low-frequency dielectric constant, resistivity, low-field mobility, iso-absorption gap, and Urbach energy.

Film Name	Thickness (nm)	Growth Rate (nm/min)	RI	κ	ρ ($\Omega\cdot\text{cm}$)	μ_0 ($\text{cm}^2/\text{V}\cdot\text{s}$)	γ ($\text{cm}^2/\text{V}\cdot\text{s}$)	E_{04} (eV)	E_U (meV)
V1.2	498	25	2.16	6.7	3.1×10^{12}	8.9×10^{-11}	5.1×10^{-3}	2.25	530
V1.2^a	490	–	2.16	6.7	3.3×10^{12}	2.8×10^{-11}	5.6×10^{-3}	1.22	1060
V2.1	922	46	2.30	8.1	7.8×10^{09}	3.4×10^{-07}	–	2.01	490
V2.1^a	Delaminated	–	–	–	–	–	–	–	–
V3.2	412	21	2.16	6.4	1.4×10^{12}	1.4×10^{-09}	4.2×10^{-3}	2.13	670
V3.2^a	403	–	2.18	3.0	2.9×10^{12}	4.6×10^{-10}	6.1×10^{-3}	0.66	1280
V4.1	375	19	2.26	5.7	1.6×10^{09}	3.7×10^{-06}	–	1.86	810
V4.1^a	355	–	2.38	4.2	2.3×10^{08}	7.1×10^{-05}	-2.9×10^{-3}	0.56	1100

^a refers to the films after annealing for 4 hours.

The charge transport and electronic properties of the V series films are summarized in Table 6.6. We found that the higher total flow rate improved carrier mobility in these films. However, the effect of precursor partial flow rate was ambiguous. The V series films were also annealed at 500°C for >4 hours to investigate the effect of post-growth thermal treatment on charge carrier mobility. Although we could not characterize the film V2.1 after annealing as the film delaminated, the annealing increased the mobility for the films grown with high total flow rate (200 sccm) and decreased that for the films grown with low total flow rate (50 sccm). Overall, the V series growth conditions produced high-mobility films, and the films grown with higher total flow rates (200 sccm) yielded carrier mobility in the range of 10^{-7} – 10^{-6} $\text{cm}^2 \cdot \text{V}^{-1} \cdot \text{s}^{-1}$

6.1.2.2. The AA and AB Series Films

The electrical characterization of most of the V series and prior films, including the PCITO series, was performed on the films deposited directly on low resistivity (<15 $\Omega\text{-cm}$) p-type silicon substrates. The current–voltage measurements were carried out using a Hg probe. Films in the PCITO series were also grown on ITO/glass substrates in a metal–insulator–metal (MIM) geometry. However, most of these devices did not perform well in terms of electrical measurement, possibly due to the RF plasma etching of the ITO layer. A major problem with the films deposited directly on silicon substrates was that they could not be characterized by other advanced techniques such as steady-state and transient photoconductivity, which require at least one transparent electrode.

Also, a film grown directly on a silicon substrate cannot work as a direct-conversion neutron detector unless the film thickness is far greater than the neutron penetration depth. Thus, it was essential to growing mechanically stable films with front and back contacts in a MIM geometry, which could support high electric fields.

As the V series films exhibited the highest carrier mobility among a-BC:H films deposited to date, we sought to build off the V series growth conditions with two goals: (1) to grow films using similar but slightly varied growth conditions to test their reproducibility and potentially further optimize conditions, and (2) to grow films in a MIM geometry to perform advanced characterization. The films, referred to as the AA series, were grown directly on silicon and also in Cu/a-BC:H/Cu sandwich structures on silicon and glass substrates. The growth time was decreased from 20 minutes to 9 minutes (compared to the V series) to reduce the film thickness, which would enable the use of transient space-charge-limited current analysis (dark-injection) to extract carrier mobility. However, these films were annealed for an extra 11 minutes to compensate for the loss of anneal time. Towards the end of the AA series film growth, we implemented a ramp-down protocol for sample cooling (see Section 6.3.3.1), which provided better mechanical stability to the films. Thus, another series of films, referred to as the AB series, was grown using similar growth conditions as that of the AA series, however, for longer growth times with the goal of producing thicker films ($>1 \mu\text{m}$) to study their reproducibility. The films were also deposited in the MIM geometry for advanced charge transport characterizations. The growth conditions for the AA and AB

series films are given in Table 6.7, and their properties are tabulated in Table 6.8 and 6.9, respectively.

Table 6.7. Growth conditions of the AA series films. The process pressure was set at 0.2 Torr.

Film	Temp (°C)	RF Power (W)	Total Flow Rate (sccm)	Partial Flow	Growth Time (min)	Post Growth Anneal Time (min)
AA1	500	40	200	0.2	6	11
AA2 ^a	500	40	200	0.2	9	11
AA3 ^a	400	40	200	1*	9	11
AA4 ^a	450	40	200	1*	9	11
AA5 ^{a,b}	300+500	40	200	1*	1+8	11
AA6 ^a	400	40	200	1*	9	2 h
AA7	400	40	200	1*	9	11
AA8 ^a	450	30	200	1*	9	11
AA9 ^a	400	40	200	1*	9	18 h
AA10 ^a	500	40	50	1*	9	11
AA11 ^a	400	40	200	1*	9	11
AA12	500	40	200	1*	9	11
AA13	400	40	200	1*	9	1 h
AA14	500	40	200	1*	9	RD
AA15	500	30	200	1*	9	RD
AA16	500	40	100	1*	9	RD
AA17	500	40	400	1*	9	RD
AA18	400	40	400	1*	9	1h+RD
AB1-AB2	500	40	200	1*	45	RD
AB3-AB14	500	40	200	1*	20	RD
AB15-AB16	500	40	200	1*	9	11 min +RD

^afilms tended to delaminate; ^bgrown for 1 min at lower temperature (300 °C) followed by higher temperature growth; RD indicates the temperature was ramped down at a rate of 50 °C/20 min.; *indicates two bubblers were used.

Table 6.8. Properties of the AA series a-BC:H films.

Film Name	Device Geometry/Substrate	Thickness (nm)	Growth Rate (nm/min)	RI	κ (1 MHz)	ρ ($\Omega\cdot\text{cm}$)	μ ($\text{cm}^2/\text{V}\cdot\text{s}$)	E_{04} (eV)	E_U (meV)
AA1.1	MIS/Si	711	119	1.99	5.3	4×10^{13}	9.9×10^{-10}	2.55	500
AA1b.1	MIM/Glass	1880	209	1.95	3.6	1×10^{13}	2.9×10^{-09}	3.13	430
AA1b.2	MIM/Si	1880	209	1.95	4.2	2×10^{14}	2.2×10^{-11}	3.13	430
AA1c.1	MIM/Glass	1569	174	1.96	5.0	3×10^{14}	6.2×10^{-12}	2.80	420
AA1d	MIS/Si	1267	140	1.97	–	–	–	–	–
AA2b	MIS/Si	1686	187	2.08	–	–	–	–	–
AA2c	MIS/Si	1637	182	1.97	7.0	3×10^{12}	3.7×10^{-09}	–	–
AA3.1	MIS/Si	861	96	1.80	5.4	3×10^{11}	2.0×10^{-09}	3.63	530
AA4	MIS/Si	934	103	2.00	–	–	–	–	–
AA4c.1	MIS/Si	2230	248	1.91	7.6	2×10^{12}	7.0×10^{-10}	3.08	410
AA7.3	MIM/Glass	1113	124	1.93	6.9	2×10^{14}	4.5×10^{-12}	3.59	550
AA7.1	MIS/Si	1113	124	1.93	6.9	1×10^{12}	7.0×10^{-09}	3.59	550
AA7.2	MIS/Si	1113	124	1.93	6.9	6×10^{12}	7.0×10^{-10}	3.59	550
AA8	MIS/Si	1983	220	1.87	4.3	–	–	3.39	440
AA12	MIS/Si	427	47	2.00	–	–	–	2.88	620
AA13	MIS/Si	701	78	1.99	–	–	–	3.49	570
AA13b.1	MIS/Si	365	41	2.14	3.6	2×10^{13}	2.3×10^{-10}	2.40	680
AA13b.3	MIS/Si	365	41	2.14	5.1	4×10^{13}	7.9×10^{-10}	2.40	680
AA14.1	MIS/Si	530	59	2.21	5.2	9×10^{10}	8.0×10^{-08}	2.15	600
AA14.2	MIS/Si	530	59	2.21	5.5	1×10^{11}	4.6×10^{-08}	2.15	600
AA15.1	MIS/Si	261	29	2.15	4.4	2×10^{11}	5.8×10^{-09}	–	–
AA15.2	MIS/Si	258	29	2.15	4.6	1×10^{11}	1.0×10^{-08}	–	–
AA15.3	MIS/Si	264	29	2.15	4.5	2×10^{11}	7.5×10^{-09}	–	–
AA16	MIS/Si	359	40	2.25	–	–	–	–	–
AA17.1	MIS/Si	691	77	2.14	5.2	5×10^{10}	6.8×10^{-08}	–	–
AA17.2	MIS/Si	762	85	2.15	5.5	2×10^{11}	1.6×10^{-08}	–	–

‘a’, ‘b’, ‘c’ etc. represent that the films were grown multiple times with the same conditions because the films tended to delaminate or delaminated prior to characterization.

Table 6.9. Properties of AB series films. The symbols RI, κ , ρ , μ , and N_t are respectively the refractive index, dielectric constant, resistivity, minimum mobility, and trap density.

Film Name	Device Geometry /Substrate	Thickness (nm)	Growth Rate (nm/min)	RI	κ (1 MHz)	ρ ($\Omega\cdot\text{cm}$)	μ ($\text{cm}^2/\text{V}\cdot\text{s}$)	N_t ($\text{eV}^{-1}\text{cm}^{-3}$)
AB1.1	MIM/Glass	1100	24	2.23	6.7	5.6×10^{10}	6.3×10^{-8}	3.16×10^{17}
AB1.3	MIS/Si	1100	24	2.23	6.0	6.4×10^{10}	9.7×10^{-8}	2.61×10^{17}
AB2.1	MIS/Si	354	18	2.32	–	–	–	–
AB3.1	MIS/Si	338	17	2.25	7.1	5.4×10^{10}	7.4×10^{-8}	–
AB4.1	MIM/Glass	748	37	2.32	6.5	5.2×10^8	4.2×10^{-6}	4.52×10^{17}
AB4.2	MIS/Si	748	37	2.32	6.8	2.1×10^9	6.2×10^{-6}	4.96×10^{17}
AB4.3	MIM/Glass	748	37	2.32	8.1	3.9×10^8	5.0×10^{-6}	5.20×10^{17}
AB5.1	MIM/Glass	678	34	2.29	7.8	1.2×10^9	1.9×10^{-6}	4.55×10^{17}
AB5.2	MIM/Glass	678	34	2.29	7.8	1.2×10^9	–	–
AB5.3	MIS/Si	678	34	2.29	6.9	8.9×10^9	4.5×10^{-7}	4.39×10^{17}
AB6.1	MIS/Si	431	22	2.53	6.4	4.2×10^{10}	–	–
AB6.2	MIM/Glass	431	22	2.53	10.8	2.1×10^7	2.0×10^{-5}	2.40×10^{18}
AB6.3	MIM/Glass	431	22	2.53	9.5	2.4×10^7	–	–
AB7.1	MIS/Si	687	34	2.26	8.1	1.0×10^{10}	5.0×10^{-7}	7.20×10^{17}
AB10.1	MIS/Si	1005	50	2.03	4.4	1.4×10^{12}	6.2×10^{-10}	–
AB11.1	MIM/Glass	717	36	1.97	8.3	2.2×10^{12}	9.9×10^{-11}	–
AB15.3	MIM/Si	590	66	2.29	–	2.8×10^9	–	–
AB16.1	MIS/Si	547	61	2.23	5.7	2.7×10^9	8.6×10^{-8}	7.59×10^{17}
AB16.2	MIM/Si	547	61	2.23	7.0	7.3×10^8	1.6×10^{-6}	8.40×10^{17}
AB16.3	MIM Si	547	61	2.23	7.0	8.7×10^8	1.3×10^{-6}	8.90×10^{17}

Many of the films grown at higher substrate temperature (500 °C) prior to AA13 either delaminated during growth or were unstable during electrical characterization, so these films were regrown multiple times (the letters a, b, c represent first, second, and third growths). Films AA6, AA7, AA9, and AA13 were grown at lower temperatures in the hopes of producing more stable films, and then annealed for different times to investigate any change in mobility with annealing. Films AA6 and AA9, annealed for 2 and 18 h, respectively, were completely delaminated before electrical testing, whereas AA7 and AA13, annealed for 11 min and 1 h, respectively, were relatively stable.

One notable and consistently observed trend in the film growths was the large variability in film growth rate. As an example, the growth rate of 208 nm/min for the AA1b batch was almost double the growth rate for the AA1 batch (118 nm/min) for the same growth conditions. Further, the decreased growth rates of the AB series films with increased growth times compared to the AA series films certainly indicated an inconsistency in the precursor flow rate. This high inconsistency in growth rate made it difficult to study film properties as a function of other important growth parameters, such as substrate temperature and precursor partial pressure. Nonetheless, as explained previously in the context of the PCITO series films, the growth rate itself provided a proxy for actual precursor flow rate and allowed us to investigate correlations.

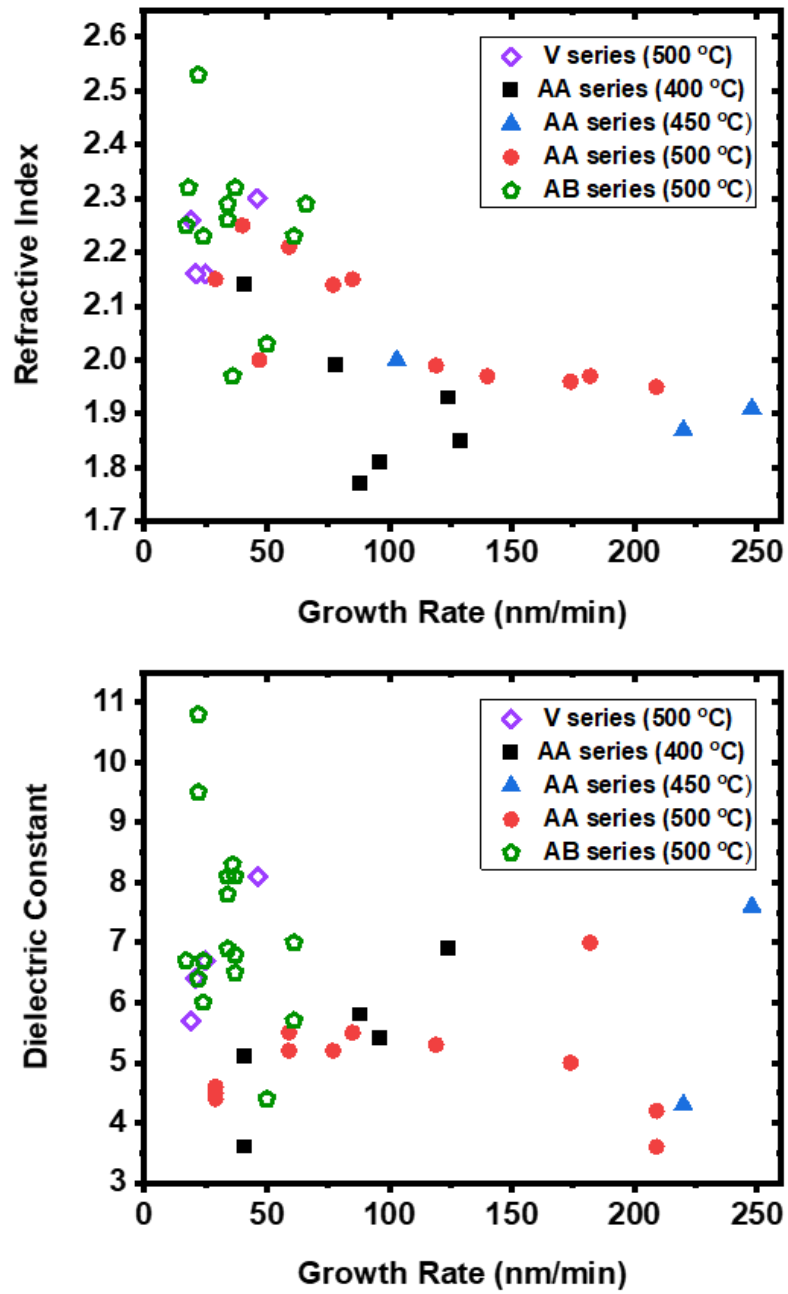


Figure 6.4. Refractive index and dielectric constant of the AA, AB and V series films as a function of growth rate.

Figure 6.4 shows the refractive index and dielectric constant of the V, AA, and AB series films as a function of growth rates. We can see from the figure that the refractive indices of the films showed a decreasing trend with increasing growth rate in general, similar to the results obtained for the PCITO series. However, for the AB series films alone, it did not show a definite trend, possibly due to small growth rate range. The dielectric constant of the AA series films increased with increasing growth rates up to ~ 60 nm/min, and then decreased for increasing growth rate. However, the dielectric constants of the V and AB series films did not show a definite trend.

The iso-absorption energy gap (E_{04}) and the Urbach energy of the films in the V and AA series films as a function of growth rates are shown in Figure 6.5. As we can see, the bandgap of the films grown at higher temperatures (450–500 °C) followed an increasing trend with growth rate, whereas the Urbach energy, showed a decreasing trend, suggesting their inverse relationship, as observed in previous studies [234].

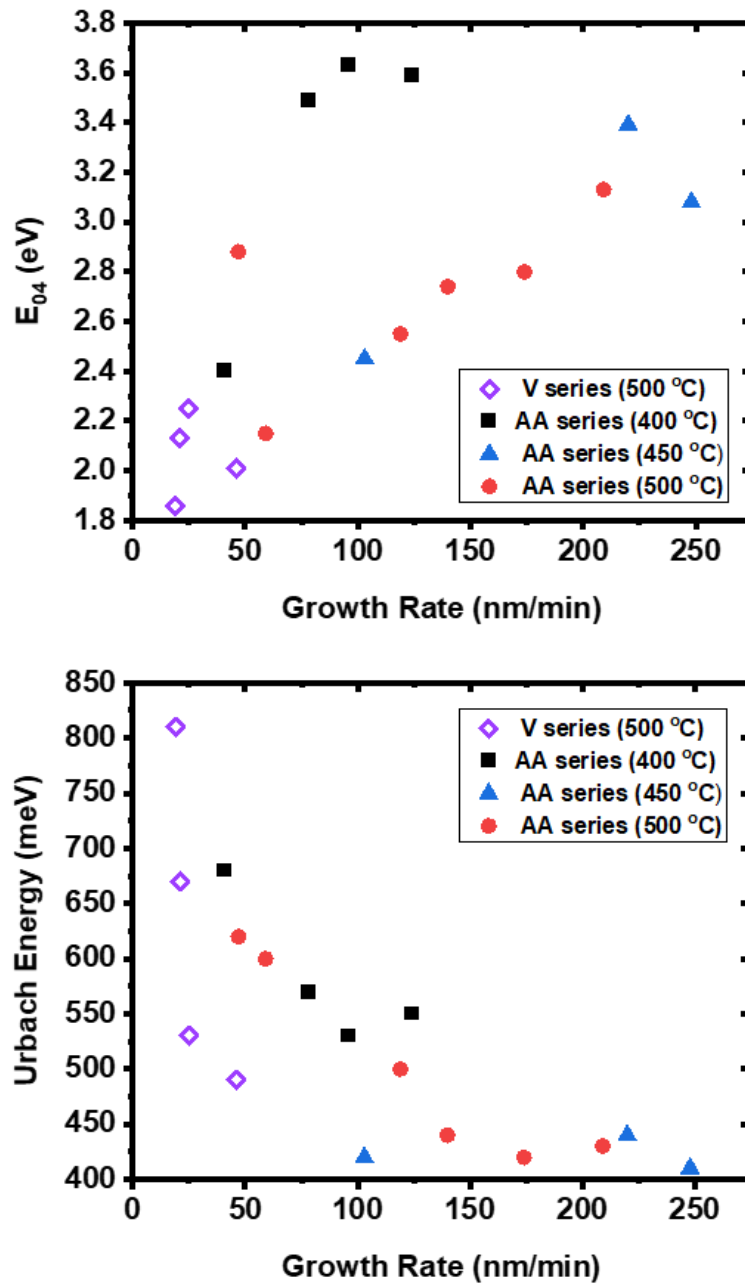


Figure 6.5. Iso-absorption energy gap (E_{04}) and Urbach energy of AA and V series films as a function of growth rate.

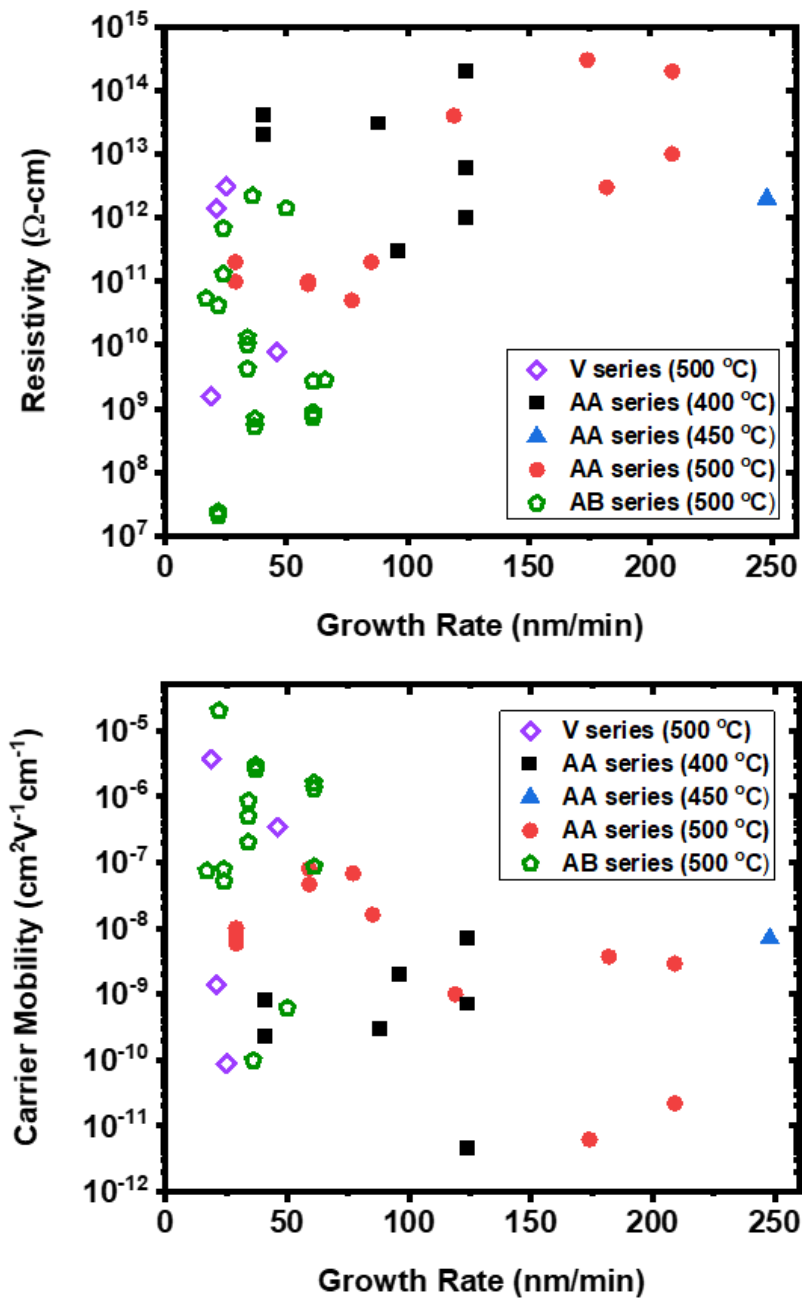


Figure 6.6. Resistivity and carrier mobility values of a-BC:H films in the AA, AB and V series films as a function of growth rate.

The electrical resistivity and the carrier mobility of the films in the AA, AB, and V series films are shown in Figure 6.6. Prior to the V series films, charge carrier mobility values were extracted using the space-charge-limited current analysis with field-dependent mobility approximation [213]. However, this analysis was incompatible with the current–voltage characteristics of some of the V series and most of the AA and AB films. Thus, for these films, only the minimum limiting mobility values were extracted using the analysis of trap-limited SS-SCLC, as explained in Section 5.3. Although we had planned to extract the carrier mobility with transient DI-SCLC experiment, the expected mobility values and film thicknesses were incompatible for the experiment, and none of the films produced any discernible transient signal.

Figure 6.6 shows that the resistivity of the films showed an increasing trend with growth rate initially up to ~ 150 nm/min before saturating at higher value for increasing growth rates in general. However, looking at the individual series, only the films in the AA series grown at 500 °C showed an increasing trend with growth rate. The figure further shows that the carrier mobility achieved higher values ($\sim 10^{-6}$ cm²·V⁻¹·s⁻¹) at a growth rate of ~ 25 – 60 nm/min and decreasing values for increasing growth rates.

6.2. Photoconductivity Measurements

6.2.1. Mobility-Lifetime Product Measurement: Steady-State Photoconductivity

The mobility–lifetime ($\mu\tau$) product is an important figure of merit in detector materials as it determines how much charge can be collected before the carriers recombine or are trapped. Although individual characterization of carrier mobility and carrier lifetime can also provide information about the $\mu\tau$ product, it can be extracted directly using steady-state photoconductivity, as described in Section 2.3.2.4. For this experiment, a-BC:H films were grown with different transparent conducting substrates (ITO and FTO) with the same growth conditions as the AB series, however, at different temperatures because high-temperature films tended to delaminate. The growth conditions and film status of the PC17 series films are summarized in Table 6.10.

Steady-state photocurrent measurements on the a-BC:H films were initially carried out by performing current–voltage measurements both in the dark and during illumination. The photocurrent was then calculated by subtracting the two, as described in Section 2.3.2.4. However, as seen in Figure 2.23, many a-BC:H films tended to exhibit continuously changing current–voltage responses over time. Because the magnitude of the photocurrent obtained was generally very small and on the order of the variations in the dark current, identifying the true photocurrent from the variations in the dark current was difficult. Therefore, we used an alternative approach to extract the photocurrent by sequentially measuring the dark current and the photocurrent at a constant voltage over a specific period of time before repeating the experiment at the

next voltage. Although this method also introduced a time effect in the measurement, such as device charging over time, this method helped us confirm the observed difference between the dark and light response as the photocurrent. Figure 6.7 shows the scheme used to measure the photocurrent as an example.

Table 6.10. PC17 series films grown for photoconductivity measurements and their status. Films were grown with RF power of 40 W, process pressure of 0.2 Torr, total flow rate of 200 sccm, and precursor partial flow of 100%.

Film Name	Growth Temperature (°C)	Growth Time (min)	Substrate	Thickness (nm)	Film Status
PC1701	500	9	FTO		Delaminated
PC1702	400	20	ITO	2963	Stable, but not noticeable photocurrent
PC1703	400	20	FTO	1777	Stable
PC1704	400	20	ITO	1721	Stable
PC1705	400	20	FTO	1465	Stable
PC1706	500	20	FTO	–	Delaminated
PC1707*	500	20	TiW	484	Thinner films and stable
PC1708	500	20	FTO/ITO	1224	Stable on Si, delaminated on FTO/ITO
PC1709	300	20	FTO	1630	Stable
PC1710	400	20	FTO	1113	Stable
PC1711	400	20	FTO/SiO ₂	1312	Unstable IV
PC1712	350	20	FTO	1904	Stable
PC1713	450	20	FTO	1746	Stable

*Film was grown with 1% hydrogen partial flow

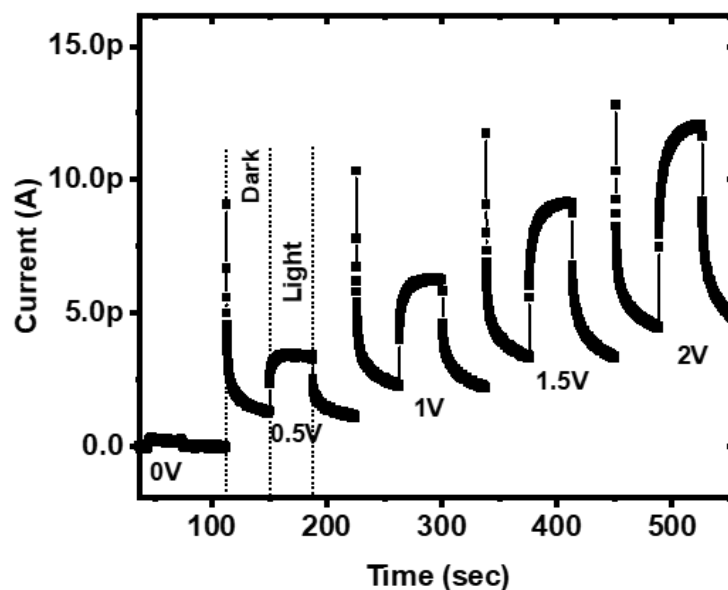


Figure 6.7. Photocurrent measurements of film PC1703 using a new approach where the current values in the dark and light were measured successively at each voltage interval. The high current spikes in the dark are the capacitive charging current spikes observed when the bias voltage was increased to the next value.

We can see in Figure 6.7 that the photocurrent attained a steady-state value earlier at lower electric fields. In contrast, it continued to increase over time at higher electric fields, and we could not achieve a true steady-state response. However, because the rate of increase was not very high, the measurement for a single voltage either in the dark or with illumination was performed for 30 seconds to obtain a quasi-steady-state data point. The photocurrent was then extracted by subtracting the lowest value of the dark current from the maximum value of the total current with illumination.

We can see from Table 6.10 that all of the films grown at 500 °C delaminated during their growth or during device wiring. Thus, we could not perform photoconductivity measurements on high-temperature films. All of the remaining films were tested across a wide wavelength range of light. For all of the films, we observed maximum photocurrent values at 470 nm, except for the PC1709 film, which exhibited maximum photocurrent at 400 nm. The PC1707 film, which was grown on a glass/TiW semitransparent substrate, did not exhibit any photocurrent, probably due to the TiW layer lacking transparency in the appropriate wavelength range.

Figure 6.8 and Figure 6.9 show the photocurrent data obtained for some of the films in the PC17 series. Figure 6.8 and Figure 6.9 further show that the photocurrent values measured for most of the films are nearly equal for both positive and negative bias applied. In the case of single carrier transport, which we believe is the case in a-BC:H films, the photocurrent in devices illuminated through transparent contacts depends on the direction of the applied bias and the nature of the optical absorption. In the case of surface absorption, the photocurrent can be seen only if the applied bias pushes the mobile carriers across the device. However, if the bias is applied such that the mobile carriers are extracted out through the same contact, photocurrent is not observed. If light is absorbed uniformly, the photocurrent can be observed in both directions of applied bias and its magnitude will be equal. Thus, the observed equal photocurrent in both bias directions is likely due to the uniform absorption of light at

the appropriate wavelength, which is also suggested by the optical absorption measurement.

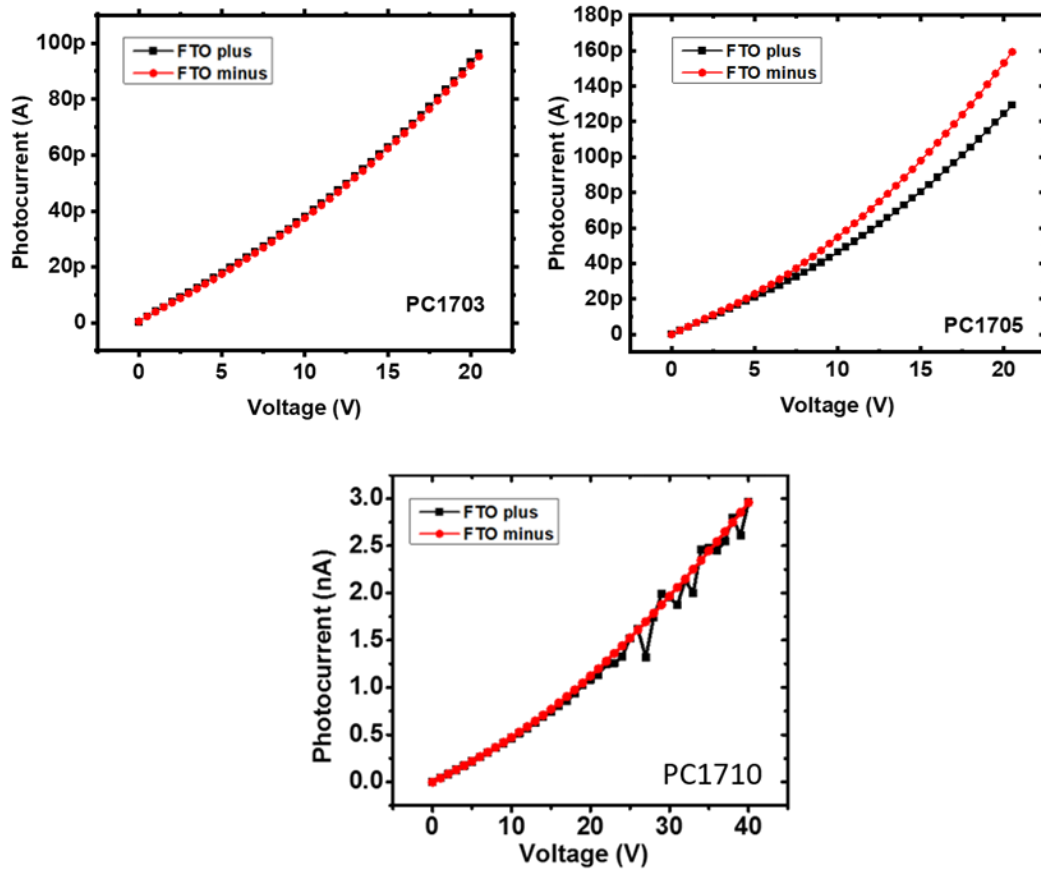


Figure 6.8. Photocurrent–voltage data for films PC1703, PC1705, and PC1710. The terms “plus” and “minus” represent the polarity of the voltage applied to the transparent ITO/FTO contacts.

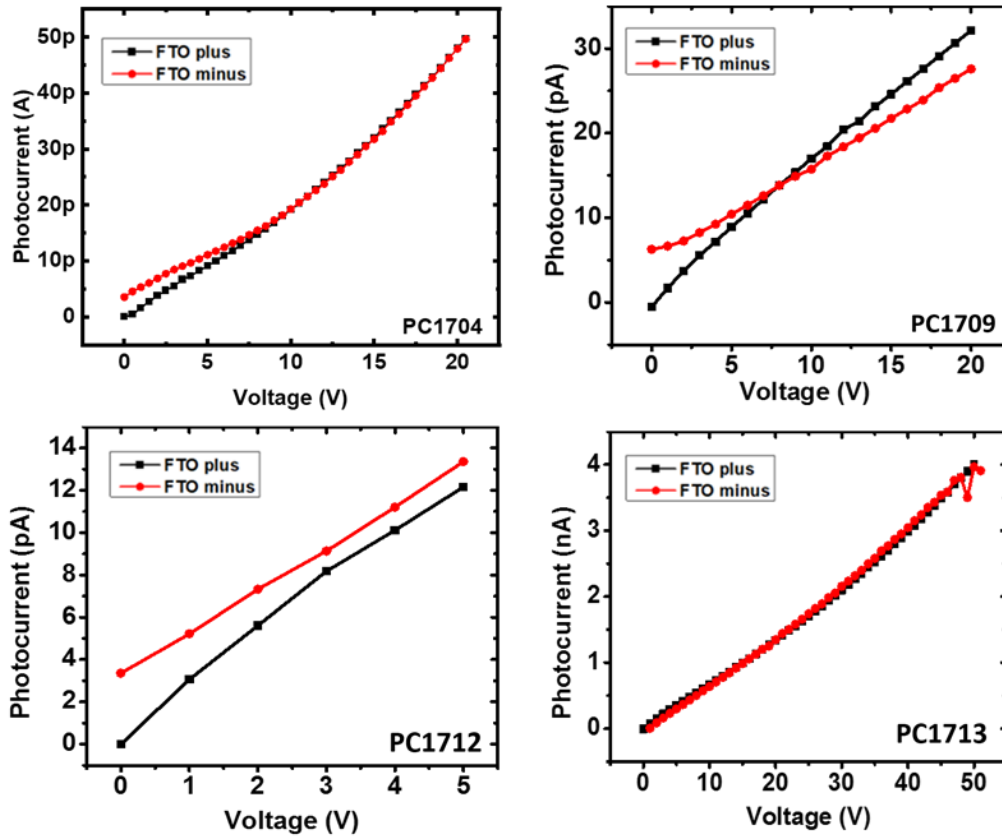


Figure 6.9. Photocurrent–voltage data for films PC1704, PC1709, PC1712, and PC1713. The terms “plus” and “minus” represent the polarity of the voltage applied to the transparent FTO contacts. Only the photocurrents with “FTO plus” show saturation in limited electric field regimes.

Among the films for which we could measure photocurrent, the mobility–lifetime extraction using a Hecht analysis was not appropriate for the PC1703, PC1705, and PC1710 films (Figure 6.8) because of the absence of photocurrent saturation at higher voltages. Hecht analysis is applicable only when the photocurrent saturates at high electric field when the carrier drift length ($\mu\tau E$) exceeds the device thickness. Thus,

only the effective mobility–lifetime product ($\eta\mu\tau$), which we have defined as the product of the mobility–lifetime product and the quantum efficiency, was calculated using the low field approximation, as described in Section 2.3.2.4. The extracted values of $\eta\mu\tau$ along with other properties are tabulated in Table 6.11

Table 6.11. Effective mobility lifetime products and other properties of some PC17 series films. A uniform absorption of light is considered for mobility–lifetime estimation.

Film	Growth rate (nm/min)	RI	E_g (eV)	E_U (eV)	ρ ($\Omega\cdot\text{cm}$)	$\eta\mu\tau$ (cm^2/V)
PC1703	89	1.97	2.00	0.40	1.6×10^{14}	8.3×10^{-14}
PC1705	73	1.91	2.18	0.41	1.6×10^{14}	5.4×10^{-13}
PC1710	56	2.01	2.02	0.48	1.4×10^{13}	4.6×10^{-13}

For all other PC17 series films, we only observed the photocurrent saturates within some applied field region before it increases again at higher fields. This was observed only when the transparent contacts (ITO/FTO) were positively biased. Thus, the mobility–lifetime products were extracted for positive charge carriers using the Hecht analysis. Figure 6.10 shows an example of a Hecht fit for the photocurrent of the PC1704 film, for which the IV curve appeared to saturate before once again increasing. The increasing current at higher fields, which we observed for the PC1704 and PC1713 films, might be because of high-field effects, such as carrier injection from the contacts [186], field-dependent mobility and/or Poole–Frenkel emission. The mobility–lifetime

products and the quantum efficiencies calculated for some of the PC17 series are summarized in Table 6.12.

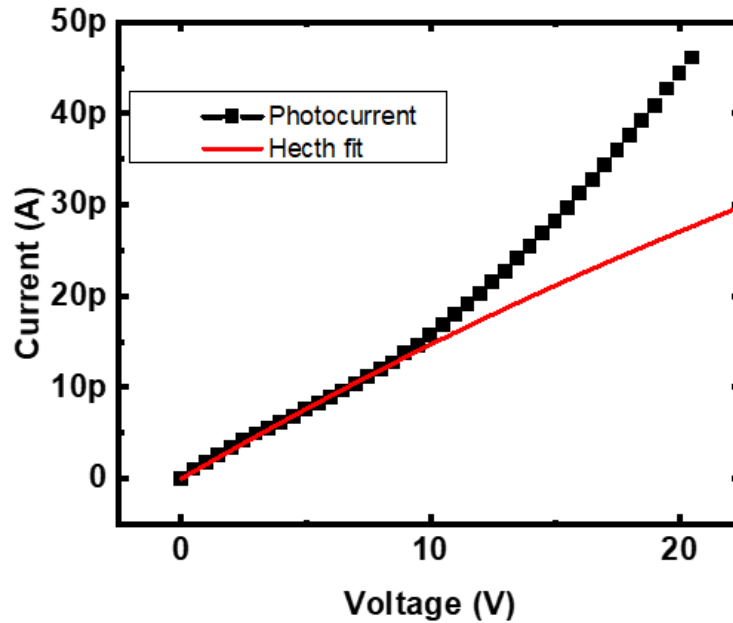


Figure 6.10. Hecht photocurrent fit of film PC1704.

Table 6.12. Mobility–lifetime product and other properties of some of the PC17 series films. A uniform absorption of light is considered for mobility–lifetime estimation.

Film	Growth Rate nm/min	RI	E_g (eV)	E_U (eV)	ρ ($\Omega \cdot \text{cm}$)	$\mu\tau$ (cm^2/V)	η
PC1704	90	2.04	2.15	0.44	–	2.1×10^{-10}	1.6×10^{-4}
PC1707	24	2.43	–	–	3.0×10^9	–	–
PC1709	82	2.00	2.33	0.66	2.0×10^{14}	1.5×10^{-10}	1.5×10^{-3}
PC1712	95	1.97	2.35	0.44	2.4×10^{14}	1.6×10^{-9}	8.9×10^{-5}
PC1713	87	1.97	1.98	0.43	1.5×10^{12}	1.8×10^{-10}	6.8×10^{-3}

We can see from Table 6.11 and Table 6.12 that the extracted $\mu\tau$ products for the PC17 series films are on the order of 10^{-10} $\text{cm}^2\cdot\text{V}^{-1}$. Comparing the effective mobility–lifetime product ($\eta\mu\tau$) obtained for the PC1703, PC1705, and PC1710 films with the product of the quantum efficiency (η) and mobility–lifetime product ($\mu\tau$) obtained for the remaining films in the PC17 series, it is expected that all of the films in the PC17 series have mobility–lifetime product values on the order of 10^{-10} – 10^{-9} $\text{cm}^2\cdot\text{V}^{-1}$. Since all of these films were grown at lower temperatures and expected to have lower charge carrier mobility values, the films grown at higher substrate temperature may likely exhibit higher values of mobility–lifetime products.

6.2.2. Carrier Lifetime Measurements: Transient Photoconductivity

Carrier lifetime in a device is measured by analyzing the photocurrent decay with time after photoexcitation. Transient photocurrent measurements were performed on the PC17 series films using the experimental setup described in Section 2.3.3. We were able to obtain a discernable photocurrent signal only on the PC1713 film using the in-built bias source of the signal amplifier at biasing voltage ≤ 8 V. Measurements of the transient photocurrent at higher voltages were not possible because of higher noise due to large device capacitance and poor voltage regulation of the external biasing sources available.

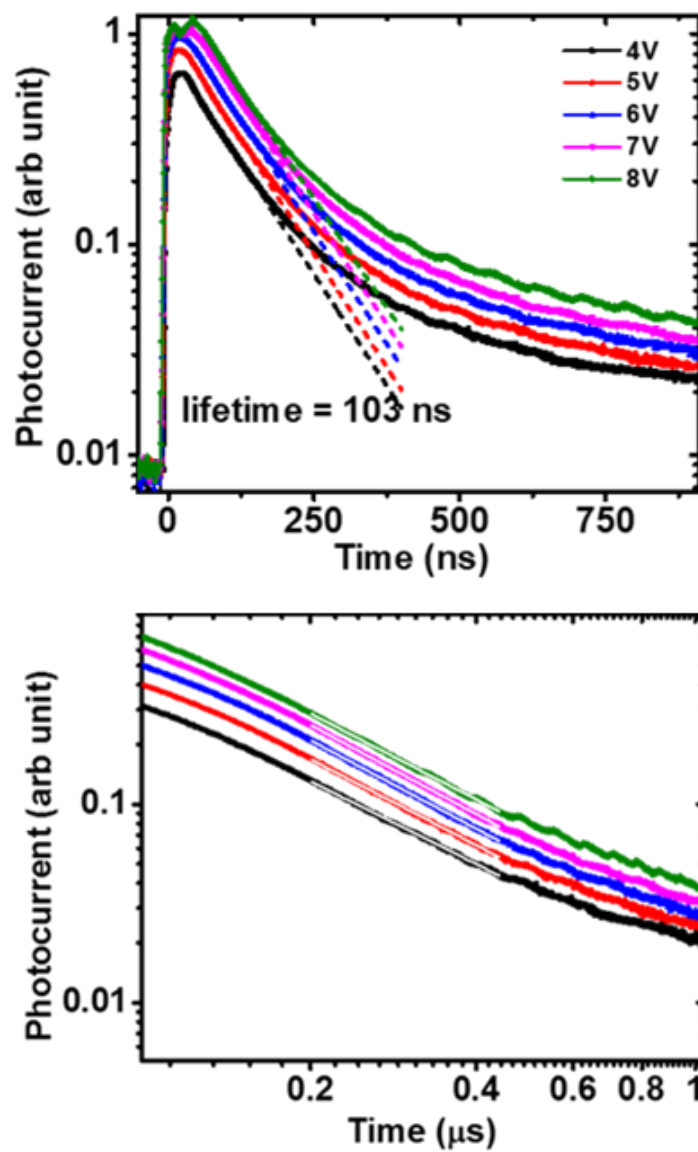


Figure 6.11. Photocurrent transient of PC1713 with 20 ns laser pulse at 351 nm for different applied biasing voltages. The dashed lines of corresponding color (top) indicate exponential fits to obtain carrier lifetime.

Figure 6.11 shows photocurrent transients obtained for film PC1713 with a 20 ns laser pulse at 351 nm. It is seen that the current initially decays exponentially with

time, with a decay time of approximately 100 ns, before decaying more slowly. The initial decay may describe the deep trapping/recombination of the carriers after their excitation, which gives a deep trapping/recombination time of ~ 100 ns, and the later slower photocurrent decay may describe the slower de-trapping of trapped carriers, which defines the mobility–lifetime product estimated using the steady-state photoconductivity experiment, but with a very small number of free excited carriers remaining, which may explain the very small quantum efficiency observed.

Because of the amorphous nature of the material, we might expect the photocurrent transient to exhibit dispersive nature, characterized typically by a power law for the photocurrent decay, given as [236]

$$I = I_0 t^{-(1-\alpha_1)} ; t < t_t \quad (6.1)$$

and

$$I = I_0 t^{-(1+\alpha_2)} ; t > t_t \quad (6.2)$$

where α_1 and α_2 are material-dependent fitting constants and t_t is the transit time that the carriers take to reach the collecting electrode. When current is plotted against time in a log–log scale, the photocurrent transient should produce straight lines, as we observe in Figure 6.11 (b) after 200 ns, which is consistent with the dispersive nature of the photocurrent transient in a-BC:H films. Even with the maximum charge carrier mobility extracted in a-BC:H films so far, the transit time with an applied voltage of 8 V is longer than 1 ms. Thus, the power law of the current seen here represents the case of $t < t_t$.

In summary, we were able to perform steady-state photoconductivity on a limited number of the PC17 series films grown at lower temperatures (350–400 °C) to extract the mobility–lifetime product values, and transient photoconductivity on one film to extract the carrier lifetime. Photoconductivity measurements on the films grown at high temperatures (450–500 °C) were not possible primarily due to issues related to the delamination of expected thicker films and transparent ITO/FTO contacts.

6.3. Thick Films and Film Stability

6.3.1. Growth Rate Inconsistency of Previous Films

6.3.1.1. Gentle Growth Conditions

We knew from a previous full factorial experiment [95] that the film growth rate was mostly affected by total process pressure and partial precursor flow rate/pressure. The effect of RF power on growth rate was minimal but still statistically significant. Higher growth rates were observed for lower process pressures and higher partial precursor flow rate, which can be explained in terms of the increased mean free path of reactive species at lower pressure and their increased density at higher partial precursor flow rates. Among the previous films grown with “gentle” growth conditions, the N25 film [95], which was grown with the same conditions as PCITO12, had the highest measured growth rate of 109 nm/min. Thus, we chose PCITO12 growth conditions as a base for obtaining thicker films, and three additional batches of the PCITO series films

were grown with increasing growth times, keeping all other growth parameters constant.

The results are summarized in Table 6.13.

We expected the thickness of the PCITO12 series films to increase with increasing deposition time. However, the films exhibited highly inconsistent growth rates, and we could not reproduce the expected growth rate equal to that of N25. The film grown for 60 minutes, which was expected to be thicker than 5 μm , delaminated. The highest growth rate obtained in the PCITO12 series was 68 nm/min for the PCITO12-20 film, which was grown for 20 minutes.

Table 6.13. Growth rates for PCITO12 series films with longer growth times. The films were grown at substrate temperature of 100 °C, RF power of 10 W, total pressure of 0.2 Torr, total flow of 200 sccm and partial precursor pressure of 1.

Film Name	Growth Time (min)	Film Thickness (nm)	Growth Rate (nm/min)
PCITO12-7.5	7.5	170	23
PCITO12-20	20	1366	68
PCITO12-30	30	977	34
PCITO12-60	60	Delaminated	—

6.3.1.2. Harsh Growth Conditions

The films grown with the “harsh” growth conditions, discussed in Section 6.1.2, also showed a high growth rate inconsistency. In the V series films, we obtained films with growth rates in the range of 19–46 nm/min. In the AA series films prior to the AA14 film, after which we implemented the ramp-down protocol for substrate cooling,

we observed a very wide growth rate range of 41–248 nm/min with films as thick as 2230 μm (see Table 6.8). It may or may not be a coincidence that the thickest films in the AA series: AA4c and AA8, were both grown at 450 $^{\circ}\text{C}$.

6.3.2. Delamination of Thicker Films

A frequently observed problem with a-BC:H film deposition was the frequent delamination of expected thicker ($>1 \mu\text{m}$) films. As we have seen from the PCITO, V, and AA series films that many films were regrown using the same conditions due to the original films being delaminated. The delamination of a-BC:H films grown at moderate substrate temperature was also reported in previous study [237], and the delamination patterns (Figure 6.12) were identical to the buckling-based delamination [238]–[240] in a high compressive-stress generally accelerated by high-humidity conditions. However, as we started exploring the “harsh” growth conditions (the V and AA series films), we observed a different pattern of delamination of films grown on silicon. The films tore apart along the crystal planes of silicon and peeled off from the substrates, suggesting that the lattice mismatch and poor adhesion of the films to the substrates may have been the primary cause of delamination. The majority of the AA series films were thicker than 1 μm and suffered such delamination either during growth, during substrate cooling, or shortly after taking out from growth chamber. However, the films grown on glass substrates (both directly on glass and glass/Cu) in the same batch were relatively stable, both mechanically and electrically. Although it is not explicitly clear why the films grown on Si/Cu substrates were unstable compared to the films grown on glass/Cu,

the diffusion between copper and silicon to form copper silicide at temperatures as low as 225 °C [237] might be the reason behind it as the interfacial copper silicide may lead to a change in electrical properties of the contacts or lattice expansion [237] that could cause residual stress in the a-BC:H films.

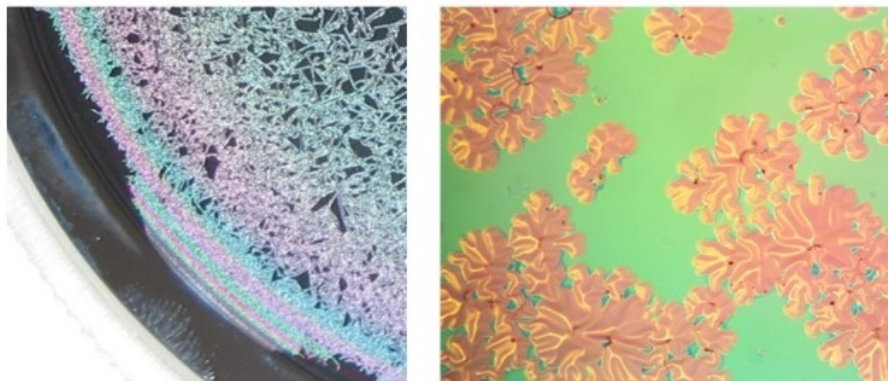


Figure 6.12. Buckling-based delamination observed in a-BC:H films grown at 350 °C, typically accelerated by higher humidity conditions.

Although we obtained some relatively thick films with very high growth rates using the “harsh” growth conditions, for a majority of film growths, obtaining thick films was more luck than design due to substantial fluctuations in growth rates for the same conditions and frequent delamination of expected thicker films grown at high substrate temperature. As we observed that the growth rate has a significant effect on the properties of films grown with both the “gentle” and “harsh” growth conditions, an identical growth condition would result in entirely different set of properties. Thus, to mitigate such issues, different experiments to study film stability and consistency were designed, which are described in the following sections.

6.3.3. Film Stress Measurement

When a system of two materials having different thermal expansion coefficients is heated or cooled, it experiences stress because of differential expansion between the two materials. A large residual stress in a substrate–thin-film system may cause the film to tear apart and/or delaminate. Thus, to measure and better understand the film stress on the PECVD-grown a-BC:H films, two different growth conditions were chosen to produce relatively thicker films, as shown in Table 6.14, and four films for each growth condition were deposited on 4-inch silicon wafers for film stress measurements. The film stress values were measured using the wafer curvature method, using a custom-built profilometer, as explained in Section 2.2.3. The measured thickness and stress values of the films are tabulated in Table 6.15.

Table 6.14. Growth conditions of the B4 and Q32 films grown for stress measurements.

Film Name	Temp (°C)	Power (W)	Pressure (Torr)	Total Flow Rate (sccm)	Precursor Partial Flow	Growth Time (min)
B4	450	30	0.2	50	0.2	30
Q32	270	40	2	200	1*	40

Table 6.15. Measured thickness and stress values in the B4 and Q32 films. A positive/negative stress value represents tensile/compressive stress.

Film Name	Thickness (nm)	Stress (MPa)
B4-I	837	772
B4-II	888	308
B4-III	551	-103
B4-IV*	657	-261
Q32-I	439	-368
Q32-II	421	-291
Q32-III	443	-387
Q32-IV	648	-582

*Film stress measured on this film using a KLA Tencor P-7 stylus profilometer was -139 MPa.

We can see from Table 6.15 that a majority of the films exhibited compressive stress with moderate values of hundreds of MPa, which may explain the observed buckling-based delamination, as shown in Figure 6.12. While the Q32 films were somewhat consistent, the B4 films ranged substantially and also resulted in both types (compressive and tensile) of stress. The tensile stress observed in the films B4-I and B4-II could be due to fluctuations in atmospheric humidity and/or the difference in their thickness compared to the other films. Because these films were grown at 400 °C and were thicker than the other films studied for stress measurement, they represented relatively thicker films obtained in the AA series, and are consistent with their delamination patterns. Among the films, B4-IV was sent for external stress measurements. The stress value of -139 MPa measured with the KLA Tencor profilometer was within the range of the stress measured with the custom-built

profilometer, suggesting the measured values were representative of the actual stress on those films.

6.3.3.1. Effect of Slow Substrate Cooling

We hypothesized that, in addition to the residual stress, rapid cooling of substrates from a high temperature introduces thermal shock in the films, leading to film delamination, as observed in some of the thick films in the AA series grown at 500 °C. Those films were cooled down from 500 °C to room temperature by turning off the substrate heater and circulating cold water through the heating lamp compartment. Such a method resulted in a very rapid drop in temperature by more than 200 °C in less than 30 minutes (see Figure 2.7). Thus, to slow down the substrate cooling, beginning with the AA14 growth, we implemented a ramp-down protocol to cool the substrates by lowering the substrate temperature manually at a rate of 50 °C per 20 minutes. Although this still resulted in rapid cooling by ~50 °C within the first five minutes (see Figure 2.7), the substrate remained at the next lower temperature level for about 15 minutes, which provided additional time to reach thermal equilibrium.

The films in the AA series beginning with the AA14 film as well as the films in the AB series were grown utilizing the ramp-down protocol. Compared to the previous films, they exhibited better stability. However, it was not immediately clear whether the improved stability was actually due to the ramp-down protocol because these films were also relatively thinner (growth rates less than 100 nm/min), and such films were generally more stable even with regular cooling. Although some of the films in the AB

series grown on silicon substrates delaminated, most of the films grown on glass substrates in MIM geometry did not. However, some of these films shorted during electrical characterization. To further investigate the effect of the ramp-down protocol on film stability and film stress, a series of films, referred to as the ST17 series, was grown for longer growth times at different substrate temperatures in an attempt to produce thicker films. The RF power, total flow rate, partial precursor flow, and process pressure were fixed at 40 W, 200 sccm, 0.2, and 0.2 Torr, respectively. The film stress values in these films were measured using a KLA Tencor P-7 profilometer using the wafer curvature method along two perpendicular diametrical axes. The growth conditions and the film stress values of the ST17 series films are summarized in Table 6.16.

We can see from the table that the film deposited at 500 °C delaminated, and the films deposited at lower temperatures (300–400 °C) were as thick as 3867 nm, which was the thickest a-BC:H film obtained so far. Although the ST1701 and ST1704 films had growth rates of ~100 nm/min, the ST1705 film had a growth rate of 57/nm and was thinner than expected.

Table 6.16. Growth conditions and film stress values of the ST series films.

Film Name	Growth Temperature (°C)	Growth Time (min)	Thickness (nm)	Growth Rate (nm/min)	Orientation (degrees)	Stress (MPa)		
						Side1	Center	Side 2
ST1701	300	20	2251	112	0 90		216 221	
ST1702	500	20	Delaminated	–	–	–	–	–
ST1703	400	20	2000*	100*	0 90	69 104	–113 –80	63 106
ST1704	400	40	3867	97	0 90		–59 –24	
ST1705	400	60	3420**	57	–			

*The thickness could not be measured. The estimated growth rate of 100 nm/minute was used to estimate the thickness.

**Thickness measured with KLA Tencor P-7 profilometer was 3029 nm.

Table 6.16 further shows that the ST1701 and ST1704 films respectively showed compressive and tensile stress, while the ST1703 film showed an average tensile stress with an unusual stress pattern of compressive stress at the center and tensile stress on the sides, as indicated by a double-well feature on the wafer curvature map in Figure 6.14. However, the stress values were in the range of 10's to 100's of MPa, which is in the range of moderate stress. It should be noted that the ST1701 film was grown at 300 °C whereas the ST1703 and ST1704 films were grown at 400 °C. Furthermore, the ST1704 film was grown for 40 min and was a thick film. Although we could not measure the film stress in the ST1702 film, the delamination of the film and other thicker films grown at higher temperatures suggested that these films had higher stress in general. If we compare the film stress from the B4 and Q32 films with the ST series film results, we can make a preliminary hypothesis that there might be a transition from compressive to tensile stress as the growth temperature increases, as indicated by the tear and peel delamination pattern of the thicker high-temperature films. This could possibly be due to a change in the thermal expansion coefficient of the a-BC:H films as Q32 films were deposited at lower substrate temperature (270 °C). However, the frequent delamination of films grown at higher temperatures (>450 °C) made it impossible to make a conclusive determination about the nature of film stress as a function of growth temperature.

In summary, our investigation of the AA, AB, and ST series films concluded that the ramp-down cooling protocol after film growth was a major contributing factor

to film stability and was much more efficient than regular annealing. The thickness of ST1705 measured with the profilometer (Figure 6.16) confirmed that stable films as thick as 4 μm could be deposited on silicon substrates at moderate temperatures (up to 400 $^{\circ}\text{C}$). The Stability of thicker films grown on higher temperature, however, was always poor, and we proceeded for more investigation on other issues such as the choice of substrate material.

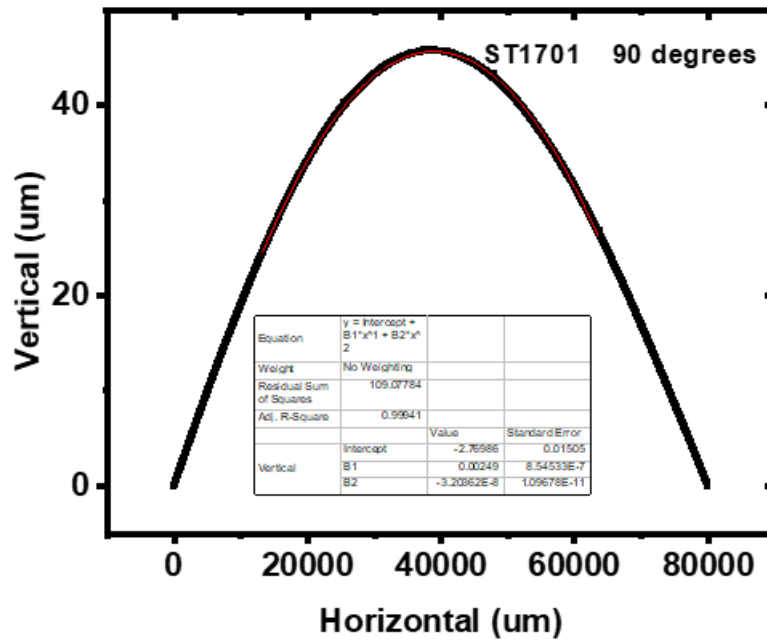
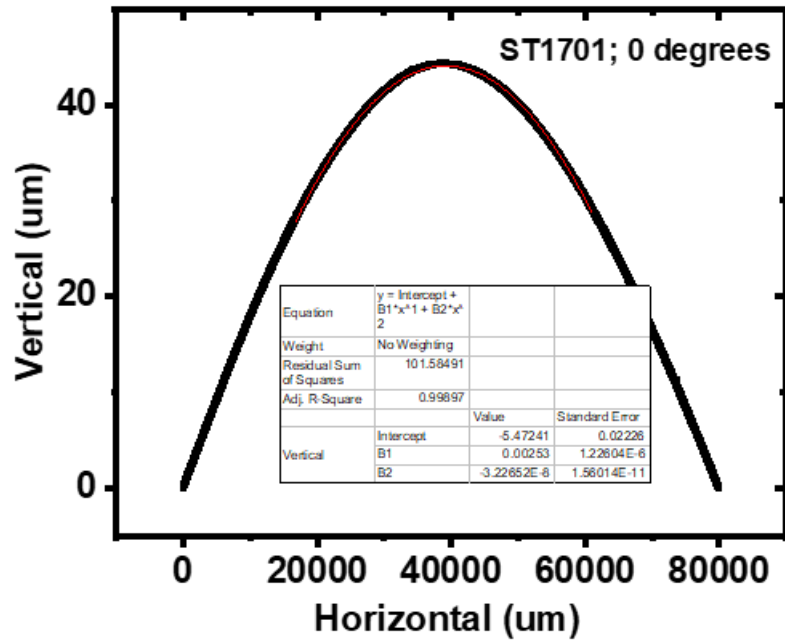


Figure 6.13. Wafer curvature measurement of the ST1701 film grown on a 4-inch silicon wafer.

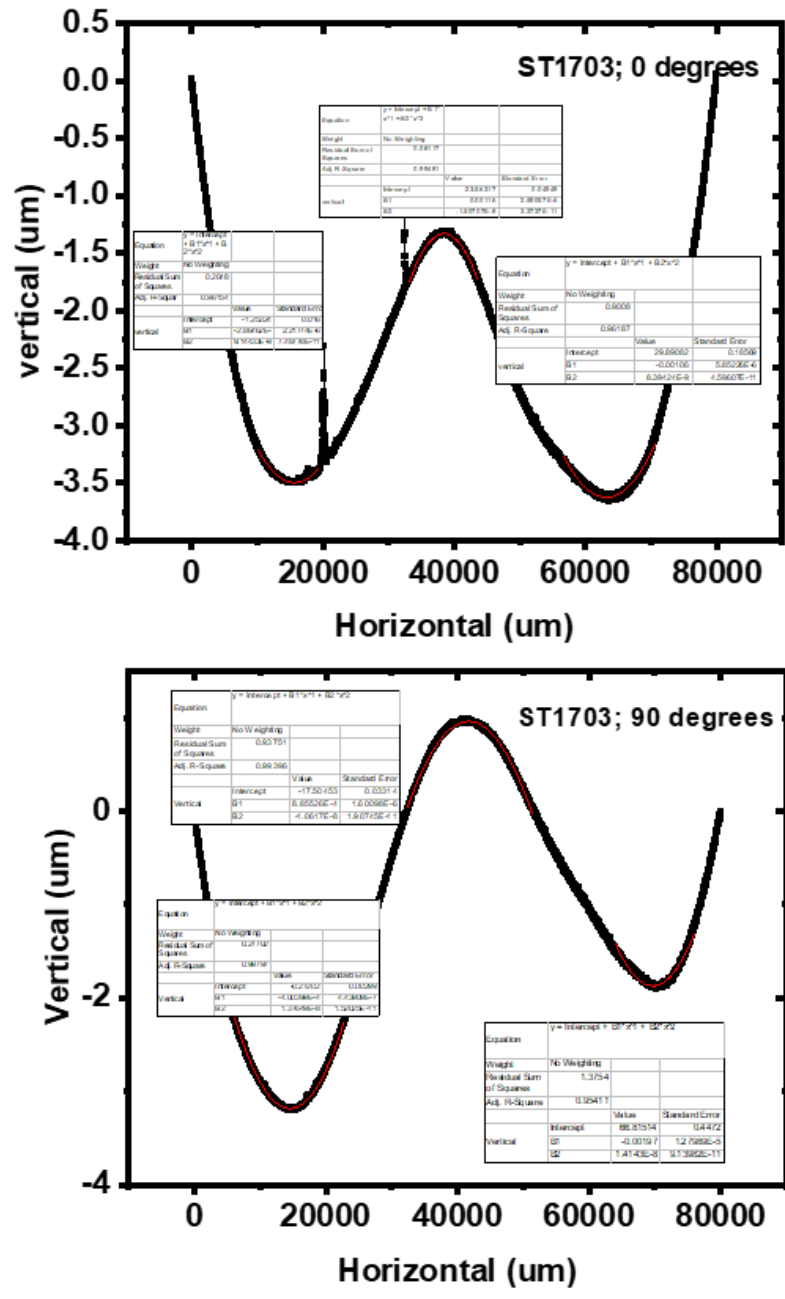


Figure 6.14. Wafer curvature measurement of the ST1703 film grown on a 4-inch silicon wafer.

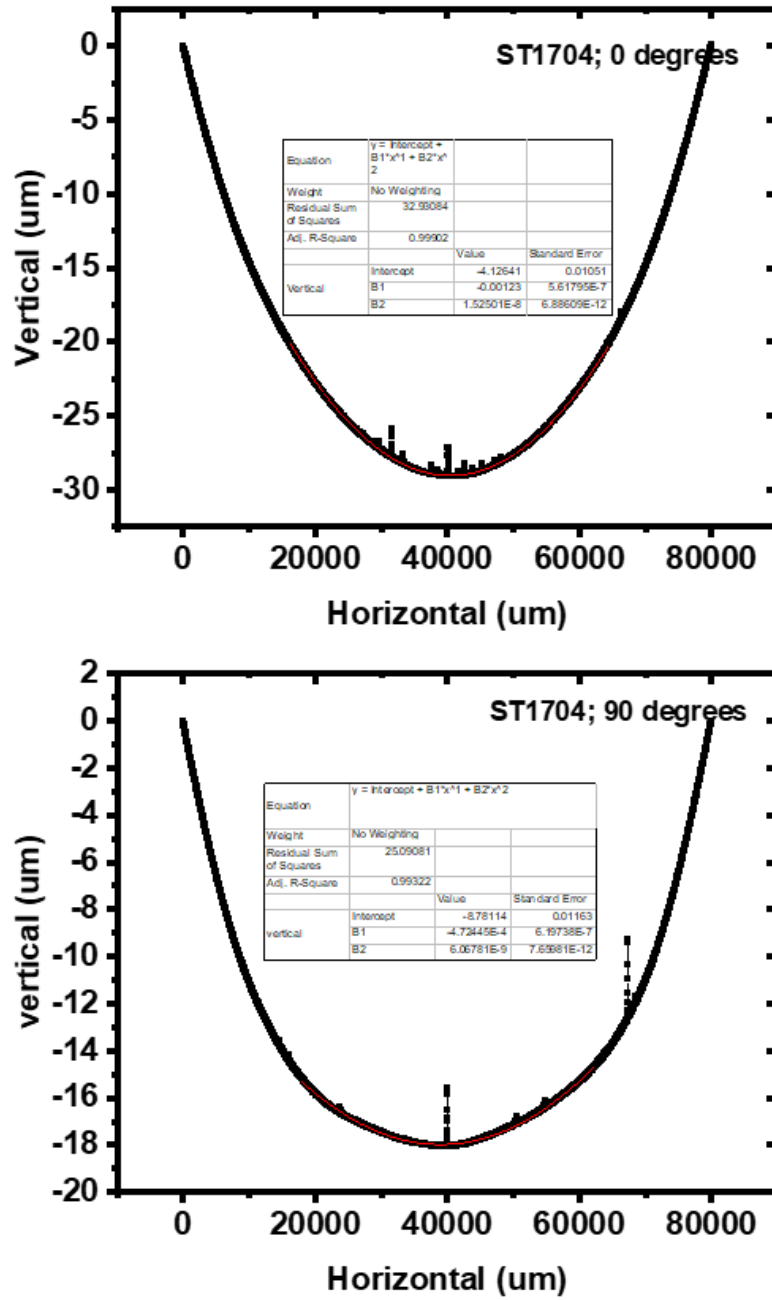


Figure 6.15. Wafer curvature measurement of the ST1704 film grown on a 4-inch silicon wafer

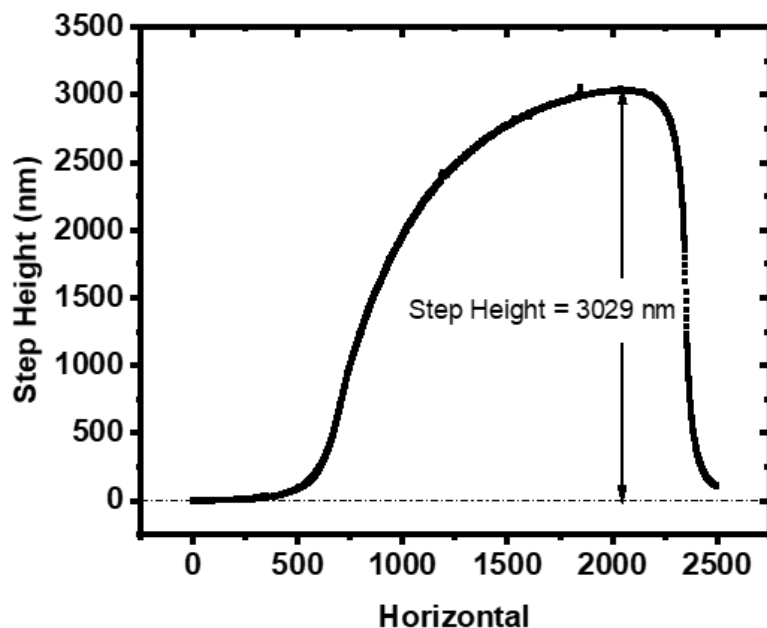


Figure 6.16. Step height measurement of the ST1705 film using KLA Tenkor P-7 profilometer.

6.3.3.2. Effect of Bottom Contact Materials

We had previously had success fabricating MIM Cu/a-BC:H/Cu heterostructures in the AB series with films on the order of 1 μm having mobility as high as $10^{-6} \text{ cm}^2 \cdot \text{V}^{-1} \text{ s}^{-1}$. Although these exhibited good I-V behavior (symmetric, reproducible across cycles, Ohmic at lower fields), they were electrically stable only up to moderately high electric fields ($<0.5 \text{ MV/cm}$), rendering these unsuitable for neutron detection measurements.

Based on previous measurements and theory (See Appendix A), we expected aluminum and copper to make injecting contacts with the a-BC:H films. Aluminum

bottom contacts sputtered on silicon and glass were electrically more stable in making MIM devices compared to the copper bottom contacts, particularly for films grown at a moderate temperature. Copper bottom contacts sputtered on silicon, however, often led to shorting of the devices. Although aluminum was stable for low-temperature PECVD growths, at high temperatures (≥ 500 °C), the sputtered aluminum layer on glass and silicon peeled off from the substrate during the deposition process, as seen in Figure 6.17, highlighting the requirement for thermally stable contact materials.

Titanium/tungsten (10% Ti and 90% Tungsten) alloy has been used to fabricate stable electric contacts in semiconductor devices [241]–[243]. Based on band alignment (Appendix A), both titanium and tungsten are expected to make neutral Ohmic contact with a-BC:H films. The Ti/W alloy is thermally stable and could allow us to grow a-BC:H films at even higher temperatures (>600 °C), which we considered an important experiment toward optimizing carrier mobility. Thus, we opted to investigate aluminum and a Ti/W alloy as bottom contacts on the devices. We also experimented with indium-doped tin oxide (ITO) and fluorine-doped tin oxide (FTO) as bottom transparent contacts, which were required for photoconductivity experiments.

Out of the films grown previously, AB15 and AB16 were sputtered with Ti/W as back contacts, both of which were stable. In the PC17 series, PC1702–PC1705 and PC1709–PC1713 were grown on ITO and FTO substrates at substrate temperatures of 300–450 °C. These films were also sputtered with Ti/W as the top contacts and were electrically stable up to 20 V (0.1 MV/cm). The films grown at 500 °C, PC1701,

PC1706, and PC1708, however, delaminated. Although the films on FTO substrates were more stable than those on ITO substrates at lower temperatures, the delamination of films on FTO substrates was worse at high temperatures, as can be seen in Figure 6.18. In addition to the delamination of the a-BC:H films on the ITO and FTO substrates, the transparent conducting layers themselves delaminated from the glass substrates at high temperatures.

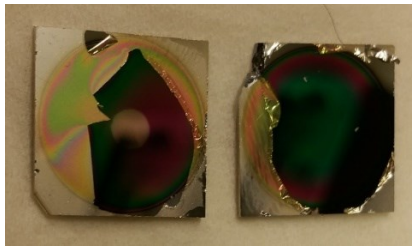


Figure 6.17. Aluminum film peeling off of silicon substrate during film growth.

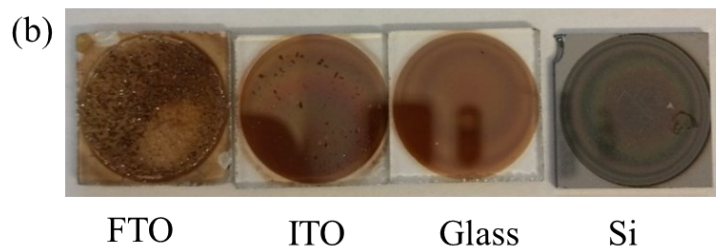
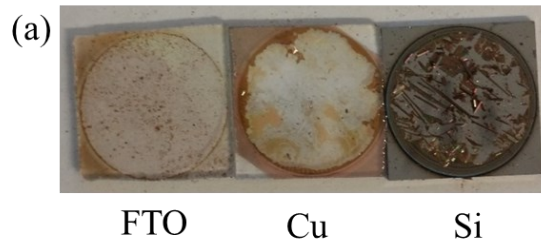


Figure 6.18. Delamination of ITO and FTO bottom contacts on films (a) PC1706 and (b) PC1708 compared to other substrates.

Because titanium–tungsten (TiW) as the back contact was stable for high-temperature films, we experimented with TiW as an alternative for the transparent contact by sputtering a thin layer of it. For the PC1707 film, TiW was used as a semi-transparent bottom contact. Although the sputtered TiW film was semi-transparent, it was hazy. The PC1707 film deposited on the semi-transparent TiW was stable mechanically, as well as electrically up to 0.6 MV/cm (Figure 6.19), confirming that even a very thin layer of TiW is stable at high temperature, unlike aluminum and copper, which both delaminated frequently.

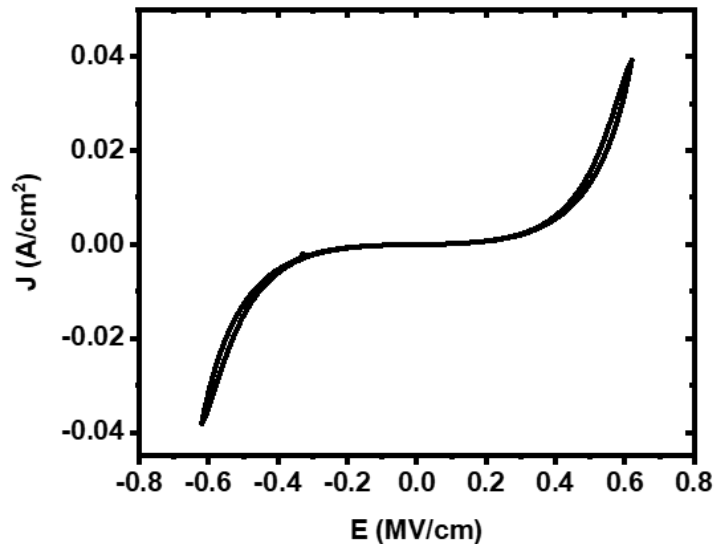


Figure 6.19. Current–voltage data of the film PC1707 grown on a glass/TiW substrate.

From the experiments on different contact materials, we concluded that TiW was the most stable bottom and top contact, and most of the films grown on TiW were electrically stable as long as the films themselves were mechanically stable, despite the possible presence of residual stress.

6.3.3.3. Effect of Hydrogen and Methane

Along with the search for better substrates to mitigate the effects of thermal expansion mismatch and/or poor adhesion, we also wanted to investigate the effect of adding hydrogen to the stability of the films and film stress because previous studies [93]–[95], [154] had shown that a-BC:H films could be grown with a wide range of hydrogen concentrations (~10–50%), and many of the film properties tracked with the amount of hydrogen in the film, which is generally explained in the context of cross-linking/density [93]. Of particular note, it was found that hydrogen concentration strongly correlates with the Urbach energy of the a-BC:H thin films, which is associated with the degree of disorder in an amorphous material. In contrast to a typical value of 50 meV found in silicon and many other amorphous solids [244], a-BC:H films showed quite high Urbach energy values on the order of 500 meV, which could indicate a high degree of disorder. In a-BC:H, it was found that the Urbach energy decreases with increasing hydrogen concentration. This same behavior has been observed in a-Si:H, and has been explained via the ability of hydrogen to relieve bond strain within the disordered lattice [245]. Importantly, the high-temperature and high-density films that we were growing and believed to have the highest mobility also possessed the lowest hydrogen concentration and highest Urbach energy. Thus, one option for potentially reducing stress while maintaining high mobility could be to introduce excess hydrogen during the growth process in the hope of relieving strain in the lattice. This addition of

hydrogen could further serve a dual purpose of enhancing charge transport properties by passivating dangling bonds and reducing electronic defects.

To investigate the effect of hydrogen on a-BC:H film stability, films in the batches PC1707 and TD1709 were grown on glass/TiW and Si, respectively, with 1% hydrogen and 99% argon as the carrier gas using the AB series growth conditions. The thickness of the PC1707 film grown for 20 minutes was measured to be 300 nm, which was very low compared to the AB series films. The film was mechanically stable, but we could not confirm whether the film was stable because of the addition of hydrogen or simply because the film was so thin. However, the TD1709 film was thick but delaminated within a few minutes after removing it from the deposition chamber, as shown in Figure 6.20. Although these two failed film growths were not sufficient to fully understand the effect of adding hydrogen in the films, and it is still worth further investigation, we did not complete additional experiment due to time constraints. Instead, we opted to investigate the incorporation of methane as an alternative strategy to incorporate hydrogen in the films.

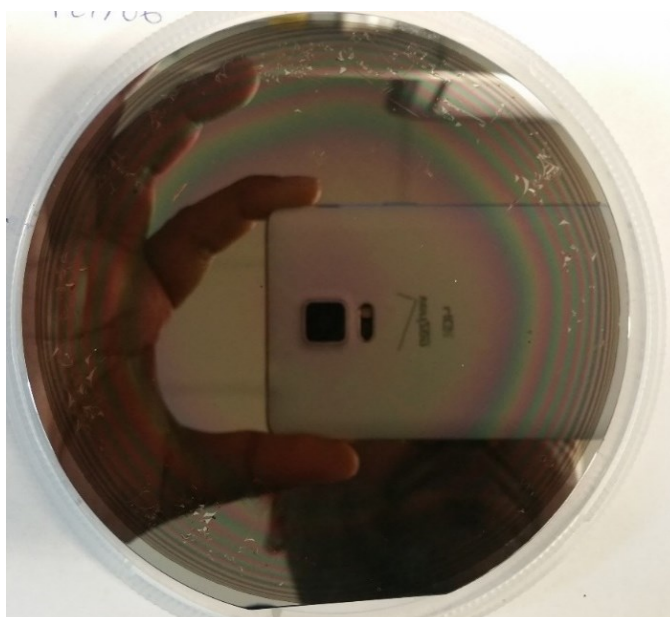


Figure 6.20. The beginning stages of delamination of the TD1709 film. The film was grown with 1% hydrogen and 99% argon as carrier gases.

A previous study [94] had produced mechanically as well electrically stable low-density a-BC:H films by incorporating methane in the PECVD process. Further, it was found that in those films, the incorporation of methane did not strongly influence charge transport mechanism at lower electric fields, but reduced the leakage current at higher electric fields, which is an important property for detector fabrication. Thus, we hypothesized that methane could potentially exhibit a similar effect to hydrogen in improving the mechanical and electrical properties of the films.

To investigate the effect of adding methane during film growth, “Methane 1” and “Methane 2” films were grown on silicon substrates using 10% methane and 90% argon as the precursor carrier gas using the AB series growth conditions for 30 and 9

minutes, respectively. However, both films delaminated during the PECVD growth process, and small ribbon-like structures could be seen on the substrate (Figure 6.21). This result was unexpected because adding methane to different low-temperature growth conditions had always resulted in stable films [94]. This delamination phenomenon was interesting in its own right in that the ribbon-type delamination pattern had never previously been observed.

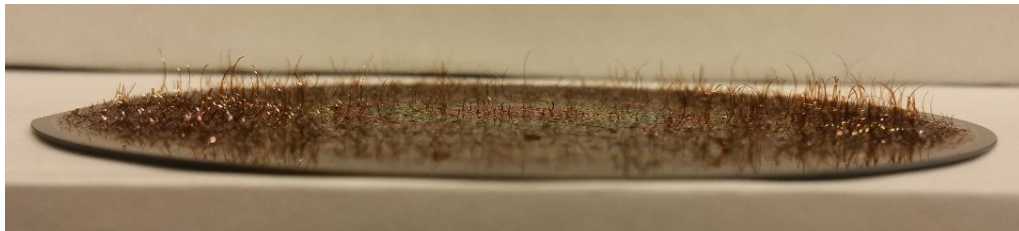


Figure 6.21. Films grown with 10% methane and 90% argon as carrier gas showing “ribbon” delamination pattern during PECVD growth.

Although the incorporation of hydrogen into a-BC:H films could still be effective in achieving higher carrier mobility by passivating the dangling bonds and thus decreasing the disorder in the material, in our experiments, both methods of incorporating hydrogen resulted in highly unstable films. While it is entirely possible that investigation of additional conditions could result in better films, we decided to prioritize other experiments in our quest to reduce film stress and obtain stable films.

6.3.3.4. Flexible Substrates

An important result we obtained from the AA, AB, and PC17 series investigations was that the films grown directly on glass substrates were more stable compared to those grown on silicon, silicon/metal, and glass/metal substrates. Because glass and silicon have similar thermal expansion coefficients of $7.6 \times 10^{-6} \text{ K}^{-1}$ [246] and $5 \times 10^{-6} \text{ K}^{-1}$ [247], respectively, which are nearly 3–4 times smaller than the thermal expansion coefficient of a-BC:H film ($20 \times 10^{-6} \text{ K}^{-1}$) [154]. It should be noted, however, that the reported thermal expansion coefficient of a-BC:H films is only for films grown at low substrate temperature, and a variation in the values can be expected for films grown using different growth conditions. Considering the reported value as a representative for a-BC:H films, the films grown on both silicon and glass substrates should have resulted in tensile stress in the films, leading to tearing and peeling, as observed in thicker high-temperature films. However, the film stability on glass substrates suggested that the thermal expansion mismatch alone is not the only critical factor in film delamination. Instead, lattice mismatch and poor film adhesion on specific substrates due to interfacial chemistry could be an additional cause of delamination. The amorphous nature of glass could have helped film stability by allowing random sites for bonding, leading to strong surface adhesion. Glass substrates, however, have a severe limitation in terms of device fabrication because they are insulators, and achieving a metal–insulator–metal (MIM) geometry required for a direct-conversion detector is

almost impossible unless the films are separated from the glass substrates as free-standing films using challenging lift-off techniques.

One way to solve all of these problems—avoiding delamination of a-BC:H films and achieving conducting contacts—was to look for different flexible conducting materials with various degrees of thermal expansion mismatch. Such substrates could help stabilize the films by offering different levels of surface adhesion with the a-BC:H based on the lattice match and interfacial chemistry, while their flexibility allows the substrates to bend and reduce the residual stress on the films. Aluminum foils were used in a previous study [94] to grow thick and wide-area films of a-BC:H where freestanding films were needed for characterization, such as in solid-state NMR. Based on the success of those films grown on aluminum, we hypothesized that different flexible metal substrates that could handle higher temperatures (>500 °C) could be used to effectively “absorb” the film stress and to grow thicker films successfully. Growing directly on metal substrates could also be a viable technology for fabricating metal–insulator–metal devices.

Among the commercially available smooth and thin metal foils, we chose aluminum, copper, tungsten, and zirconium for thick film growth for the following reasons: a) they cover a range of thermal expansion coefficients, b) they are expected to produce Ohmic and blocking contacts based on their band lineup with BC, and c) they are available at affordable cost. Among these metals, aluminum and copper have been used to make Ohmic contacts with a-BC:H films and have thermal expansion

coefficients of $23.6 \times 10^{-6} \text{ K}^{-1}$ [247] and $16.5 \times 10^{-6} \text{ K}^{-1}$ [247], respectively, which are comparable to that of a-BC:H films. Zirconium and tungsten exhibit thermal expansion coefficients of $5.8 \times 10^{-6} \text{ K}^{-1}$ [248] and $4.6 \times 10^{-6} \text{ K}^{-1}$ [247], respectively, comparable to that of glass. Tungsten was chosen because we found a titanium/tungsten (10% Ti and 90% Tungsten) alloy formed stable Ohmic contacts on a-BC:H devices, whereas zirconium was chosen as it is supposed to oxidize at high substrate temperature and form a Zr/ZrO₂/a-BC:H heterostructure, which theoretically acts as a blocking contact (See Appendix A). Table 6.17 summarizes all of the growth attempts toward achieving thick and stable films on flexible substrates with identical growth conditions to those of the AB series but with longer deposition times.

All of the films grown on the flexible metal foils were visually dark, suggesting that the films were thick as expected, and remained mechanically stable for longer times. Only the AL1705 film, which was grown for the longest time of 90 min, was measured for its thickness. The thickness measured with scanning electron microscopy was 5480 nm, as shown in Figure 6.22 (a). The CU1801 and CU1802 films were grown using an improved precursor delivery system (see Section 6.3.4.2). Thus their thicknesses (4 and 8 μm) are based on the growth rates measured on the films grown on silicon.

Table 6.17. Summary of attempted thick film growths on various substrates

Film Name	Substrate	Coefficient of Thermal Expansion (K ⁻¹)	Growth Time (min)	Thickness (nm)	Film Status
AL1701	Aluminum	23.6 × 10 ⁻⁶	45	–	Rolled up
AL1702	Aluminum		60	–	Wrinkled, rolled
AL1704	Aluminum		60	–	Wrinkled, rolled
AL1705	Aluminum		90	5480*	Wrinkled, slow delamination over time
MF1701	Zirconium	5.8 × 10 ⁻⁶	45	–	Rough film surface
MF1701	Tungsten	4.6 × 10 ⁻⁶	45	–	Rough film surface
CU1801	Copper	16.5 × 10 ⁻⁶	40	4000 [#]	Dark, shiny, rolled up, and wrinkled
CU1802	Copper		12+12+60	8000 [#]	Dark, shiny, and wrinkled

*Measured with scanning electron microscopy. [#]Based on expected growth rate.

The AL1701 film, which was grown on aluminum foil for 45 minutes rolled up with the film on the outer surface, as shown in Figure 6.22 (c), showing high residual compressive stress, which was not expected based on the thermal expansion coefficient of aluminum ($24 \times 10^{-6} \text{ K}^{-1}$) being comparable to that of a-BC:H ($20 \times 10^{-6} \text{ K}^{-1}$) [154]. However, because the CTE of the a-BC:H films referred to here was measured on low-temperature films, the residual stress in aluminum could be due to a somewhat different CTE in the high-temperature a-BC:H films. Films grown on zirconium and tungsten are shown in Figure 6.22 (d) and (e), respectively. Although the surface roughness of both of the foils purchased from MTI corporation was specified to be 5 nm, they looked

visually rough. The films grown on those foils also looked visually rough, similar to the metal foils, but they were mechanically stable.

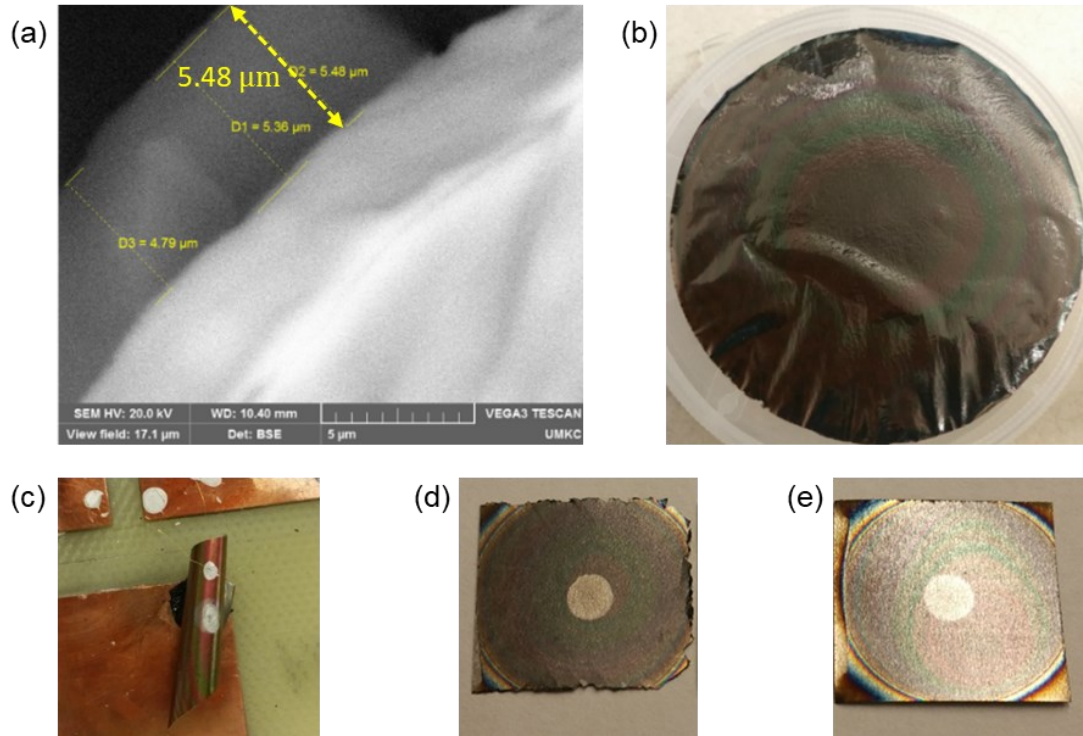


Figure 6.22. (a) Cross-sectional view of the AL1705 film obtained with scanning electron microscope, (b) Film AL1705 showing wrinkles, (c) film AL1701 rolled up after cutting from a large piece of foil, (d) film grown on tungsten, and (e) film grown on zirconium. The spots at the center of the films grown on tungsten and zirconium are sputtered top contacts.

Films grown on copper foils are shown in Figure 6.23. Among the films grown on flexible metal foils, the films grown on copper foils exhibited sustained mechanical stability, even in an open atmosphere. Both the films CU1801 and CU1802 were

visually very dark, shiny, and rolled up with the film on the outer surface, as shown in Figure 6.23 (a) and (c), suggesting thick films with high compressive stress. Both of the copper foils, however, developed wrinkles, probably during cooling, which can be seen on the backside of the CU1801 film in Figure 6.23 (b).

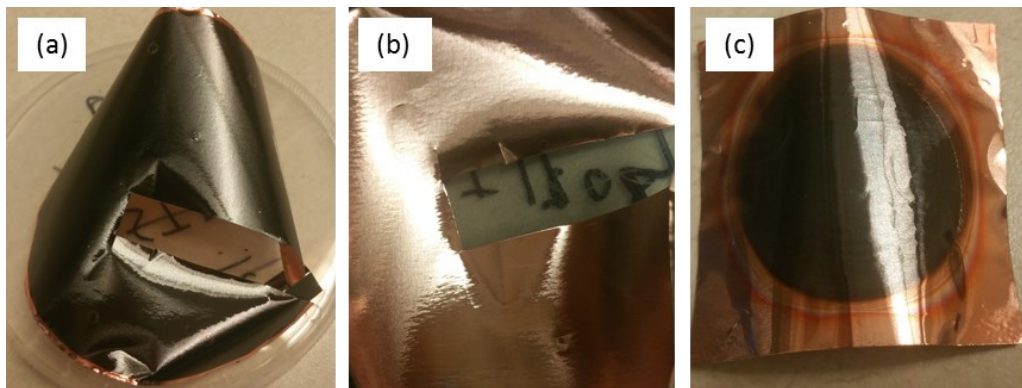


Figure 6.23. a-BC:H films grown on copper foil: a) CU1801, b) backside of CU1801 showing wrinkles on the copper foil, and c) CU1802.

Among the films grown on aluminum, only the AL1702 film was electrically stable and withstood an applied voltage of up to 100 V with a small leakage current of 2 nA. However, it also witnessed a device breakdown on the second run of IV measurements at about 40 V, as shown in Figure 6.24. All of the films grown on zirconium shorted during electrical testing and delaminated slowly over time. The film grown on tungsten, however, did not short for an applied voltage of up to 10 V. However, it produced unstable current–voltage data.

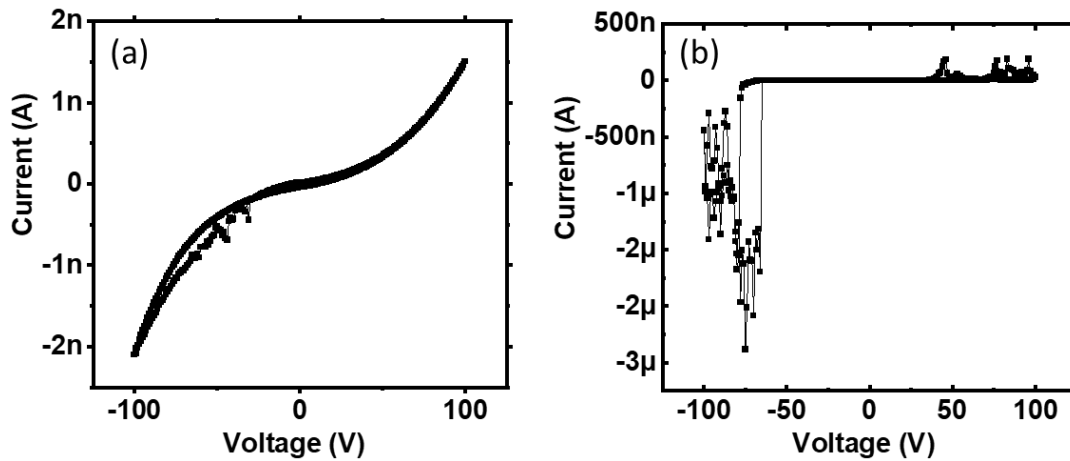


Figure 6.24. IV characteristics of film AL1702. a) The film was stable up to 100 V in the first run. b) Electrical breakdown of the device in the second run.

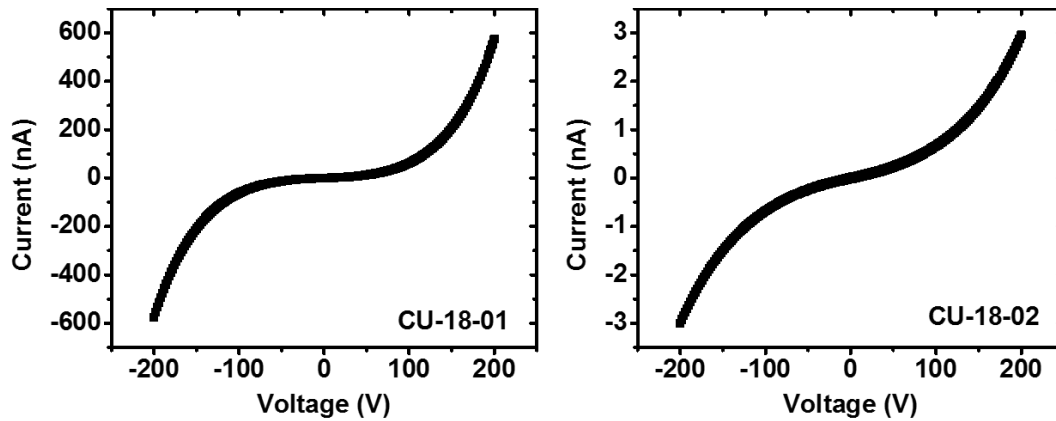


Figure 6.25. Current–voltage characteristics of CU1801 and CU1802 films grown on copper foil.

Figure 6.25 shows the resulting IV data for films CU1801 and CU1802. Both films exhibited Ohmic transport at lower applied voltage. Although we expected the film thickness of CU1802, grown for a total of 84 minutes, to be nearly double that of

CU0801, grown for 40 minutes, the measured current for CU1801 was more than two orders of magnitude higher than that for CU1802 at the maximum applied voltage of 200 V, implying that CU1802 was more resistive than CU1801. Film CU1802 was grown with three independent growth steps of 12, 12, and 60 minutes due to overheating issues with the process pump. Based on their expected thicknesses, the CU1801 and CU1802 films were expected to have resistivities in the range of 10^{11} – 10^{12} Ω -cm. The slightly higher resistivity of CU1802 might be because the film was grown in three layers, with the film exposed to atmosphere between each layer.

From the study of the flexible substrates, we found that the films deposited on aluminum and copper showed compressive stress while the stress for the films on tungsten and zirconium could not be understood. Among the flexible substrates investigated, films deposited on copper demonstrated encouraging mechanical as well as electrical stability with film resistivity in the range of 10^{11} – 10^{12} Ω -cm. The use of flexible metal foils provided a very promising direction for thick film deposition, electrical and interfacial characterization, and device fabrication. However, we had yet to achieve a consistent film thickness and property reproducibility, which are critical for the success of these experiments. Thus, we moved forward to experimenting on modifications of the precursor delivery system and growth conditions to achieve consistent precursor flow and film growth rate.

6.3.3.5. Standalone Films and Pellets

Performing electrical characterization on thick films grown at higher substrate temperatures was always a challenge because most of the films grown on conductive substrates (silicon, metal on silicon, metal on glass, ITO/FTO on glass) usually delaminated as soon as they became thicker than 1–2 μm , despite the same films deposited directly on glass substrates being relatively stable. Thus, one possibility would be to grow thick films on glass or another insulating substrate, remove the film, and then deposit electrical contacts. Alternatively, if we could produce pellets using those standalone films or film flakes, this could avoid both the issues of delamination and of growing extremely thick films.

Chemical Lift Off: Films on Glass



Figure 6.26. a-BC:H on glass after 3 h in 1% KOH (left); a-BC:H on glass (AA14) in 10% KOH after 3 days (right).

Because a-BC:H films deposited at high temperature are extremely hard, removal should involve chemical rather than mechanical means. Previous studies had

shown that low-temperature films grown on glass could be separated intact from glass with KOH etching (although these did roll up, which indicates high film stress, Figure 6.26 (left)). To test whether the films grown on glass substrates at higher temperature could be isolated, film AB5 was put in a 1% KOH solution. The film remained stable for three days without showing any etching of the glass below the film. Film AB5 along with two other films, AA14 and AB9, were then transferred to a 10% KOH solution. However, all of the films remained intact for several days (Figure 6.26, right), which was inconsistent with our previous results. It could be possible that the high-temperature films display better adhesion to glass than the lower temperature ones.

Chemical Lift Off: Films on Copper Foil

We were able to grow stable and thick films on copper foil. Thus, we attempted to separate the copper foil from the film CU-18-01 (estimated thickness of 4 μm) using dilute FeCl_3 solution, generally used by researchers to separate graphene layers grown on copper. The film grown on copper foil was covered with a thin layer of spin-coated PMMA and was heated to set the PMMA. The film was then put into an FeCl_3 solution to dissolve the copper, as shown in Figure 6.27(a). After the copper foil was etched away, the film still appeared intact, only with some sign of tearing at the edges (Figure 6.27(b)). However, as soon as the film was transferred to acetone to remove the PMMA layer, the film broke into pieces (Figure 6.27(c)). This could be because of the high stress in the film or because of the wrinkles formed on the copper foil during film growth.

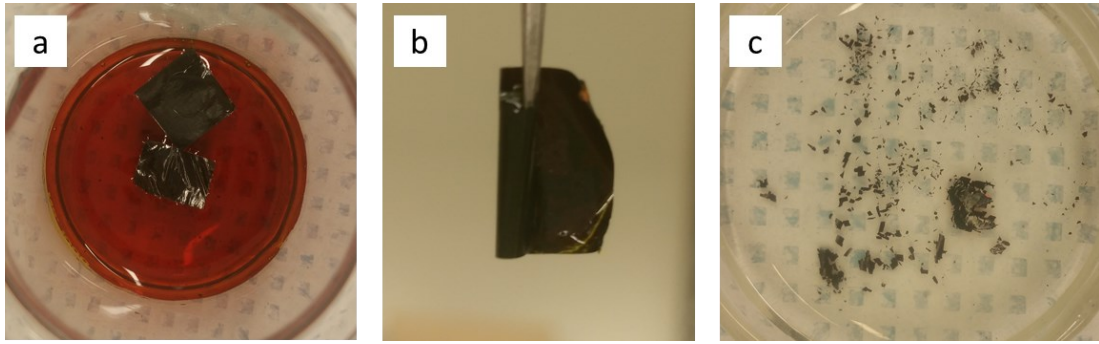


Figure 6.27. CU-18-01 film covered with PMMA in (a) FeCl_3 solution, (b) after etching the copper foil, and (c) broken into pieces when washing PMMA with acetone.

Films on NaCl Crystal

Another method to obtain a standalone film is to grow the a-BC:H film on a water-soluble crystalline salt substrate, which can then be dissolved easily to leave a freestanding film. Since films grown at high-temperature tend to delaminate often, we first tried growing a lower temperature film on a NaCl substrate because it is easily available and has a thermal expansion coefficient ($40\text{--}55 \times 10^{-6} \text{ K}^{-1}$) in the temperature range $0\text{--}500 \text{ }^\circ\text{C}$, [249] which is only double the expansion coefficient of the a-BC:H films. $10 \times 10 \times 10 \text{ mm}^3$ NaCl cubes were purchased from Ted Pella and cleaved to obtain 2 mm thick substrates. Films on the NaCl substrates were grown at a substrate temperature of $300 \text{ }^\circ\text{C}$ with 40 W of RF power for 20 minutes. However, the films delaminated quickly after removal from the growth chamber. Based on the thermal expansion coefficient, the NaCl substrate should exert compressive stress on the a-BC:H film. Although the expansion coefficient of NaCl is only double that of a-BC:H, whereas that of silicon is nearly one order of magnitude smaller than that of a-BC:H, the quick

delamination of a-BC:H films grown on NaCl substrates even at a lower temperature indicates that the thermal expansion coefficient alone is not the factor contributing to the film delamination because films grown on Si at 300 °C are generally stable.

Pressed Pellets

Another alternative to obtain standalone devices is by pressing pellets out of a-BC:H film material, for example, the flakes obtained by dissolving a film of a-BC:H grown on aluminum foil in HCl. Although it was not clear whether the pellets formed in this way would exhibit similar electrical properties to the original films, we hypothesized that densely packed pellets of this disordered amorphous material could have comparable properties to those of films.

To make a-BC:H pellets, two films grown on aluminum foil, AL1702 and AL1704, were dissolved in a 5% HCl solution, and the a-BC:H flakes were filtered and dried in a nitrogen environment for 24 hours before loading into a pellet press die of 5 mm diameter inside the nitrogen glove box. The pellets were pressed at a pressure of 3 tons, due to the die size, for one hour before removing them from the die. Figure 6.28 shows the pellet formed from the AL1702 film immediately after being taken out of the pellet press. Both pellets were very brittle and could not be handled for any tests. The resulting powder was pressed again, but that resulted in a grey color, possibly due to the powder absorbing moisture or oxygen when exposed to the atmosphere.



Figure 6.28. Pressed pellet made from a-BC:H flakes obtained by dissolving a film on aluminum foil.

Although we were limited because of the time and availability of the higher pressure and heat to make dense pellets, and the pellet formed using available resources could not be used for material characterization, pressed pellets can potentially be used to study charge transport properties in the bulk of this material, utilizing special fixtures to perform electrical characterizations while the pellet is still in the die and not exposed to the atmosphere.

6.3.4. Thickness Reproducibility

From the study of the V, AA, AB, and PC17 series films and the films on flexible substrates, we achieved a good understanding of the growth conditions that result in a-BC:H films with carrier mobility of $\sim 10^{-5} \text{ cm}^2 \cdot \text{V}^{-1} \cdot \text{s}^{-1}$ and mobility lifetime products on the order of $10^{-10} \text{ cm}^2 \cdot \text{V}^{-1}$, as well as identified substrates that tend to produce mechanically and electrically stable films. However, thickness reproducibility remained the biggest inconsistency in the film deposition process. *Ortho*-carborane ($\text{C}_2\text{B}_{10}\text{H}_{12}$) is a relatively unique PECVD precursor because it is used in a solid-state form, and thus precursor flow is more difficult to control. In our system, we sublimed *ortho*-carborane inside a custom-built bubbler from which it was carried to the PECVD chamber by a carrier gas, as explained in Section 2.1.5. As we knew that the growth rate depended significantly on the precursor flow rate [95], we hypothesized that variation in the precursor fill level, bubbler temperature, and state of the precursor (powder vs. solid chunk) could affect the evaporation and actual precursor flow rate, causing inconsistency in film thickness. In our precursor delivery system, we used two precursor bubblers to achieve greater surface area for higher precursor sublimation, and stabilized the bubbler temperatures manually in a range of 70–85 °C. However, the extent of the effect of varying temperature was not clear initially. Further, once the PECVD process was started, it was difficult to monitor the bubbler temperature due to RF interference on the thermocouples, and any possible fluctuations in the bubbler temperature remained unknown. As it was untenable to refill the bubbler for each growth, we

generally refilled the bubblers with ~15 g of *ortho*-carborane which would be sufficient for ~10 batches each of 20 minutes, when 200 sccm of carrier gas flow was used, and about 1/3 of the precursor would remain in the bubbler. While we did not notice obvious systematic changes (other than the first growth being always much thicker than later growths, which we believe was caused by the freshly prepared powdered *ortho*-carborane), it was possible that the unknown remaining amount and physical state of precursor could have greater impacts on the precursor flow rate. Thus, to remedy any inconsistency in precursor sublimation and flow rate, we decided to redesign and modify the precursor delivery system with the goal of achieving a consistent film growth rate and thickness reproducibility.

6.3.4.1. Vapor Source MFC

As a means to remedy the inconsistent precursor delivery system, we purchased and installed an MKS 1152 solid-state vapor-source mass flow controller (Figure 6.29), customized to control the precursor flow in our specific growth chamber configuration. Based on the measured vapor pressure of *ortho*-carborane (Figure 6.30, details of the experiment are beyond the scope of this dissertation), the mass flow controller was designed to operate at 150 °C with the precursor ampoule heated to 150 °C, which was required to achieve a precursor pressure of 25 Torr required to get a consistent flow from the mass flow controller.



Figure 6.29. Installed MKS 1152 solid-state vapor-source mass flow controller.

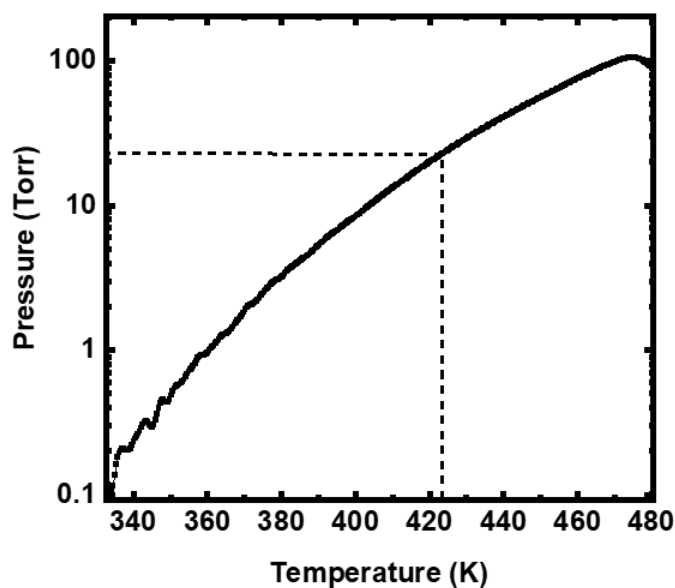


Figure 6.30. Saturated vapor pressure of *ortho*-carborane as a function of temperature determined by thermogravimetric analysis.

For the original growth procedure using the glass bubblers, we estimated, based on *ortho*-carborane usage, that approximately 1 gram of precursor was delivered to the PECVD chamber in 20 minutes with 200 sccm of argon flow. This is equivalent to an *ortho*-carborane flow rate of approximately 7 sccm. Thus, for the initial testing of the new vapor source MFC, we opted to target a flow rate of 7 sccm of *ortho*-carborane in conjunction with conditions known to produce specific film variants. As the mass flow controller allowed a burst of maximum possible precursor flow (200 sccm) briefly before stabilizing to the desired setpoint, we had to wait for ~10 seconds to stabilize the flow at the desired flow rate and an additional 30 seconds as a pre-purge to maintain a uniform precursor pressure in the deposition chamber before igniting the RF plasma.

Table 6.18. Growth conditions, film thickness, and growth rate of NS18 series films. The films were grown at 500 °C substrate temperature, 40 W RF power, and 200 sccm of carrier gas (argon) flow rate.

Film Name	Precursor Flow Rate (sccm)	Process Pressure (Torr)	Growth Time (minutes)	Thickness (nm)	Growth Rate (nm/min)
NS1801	7	0.2	3	221	74
NS1802	7	2	3	No growth	0
NS1803	7	0.2	3	306	102
NS1804	7	2	3	No growth	0
NS1805	7	1	3	No growth	0
NS1806	7	0.2	3	349	116
NS1807	7	0.2	3	Failed Growth	–
NS1808	7	0.2	3	423	141
NS1809	7	0.2	3	Failed Growth	–
NS1810	7	0.2	3	461	154
NS1811	7	0.2	3	375	125
NS1812 [#]	7	0.2	3	165	55
NS1813	7	0.2	3	259	86
NS1814	3	0.2	7	358	51
NS1815	1	0.2	15	347	23

[#]Precursor ampoule refilled with 2 g of *ortho*-carborane

Table 6.18 lists results for films in the NS18 series grown with the new vapor delivery system using AB series growth conditions, but with shorter times. Three additional growths at higher process pressures were also included. We can see that film deposition was not possible at higher process pressures, which was unexpected because a-BC:H films were successfully deposited at even higher process pressures previously in the same deposition chamber using the original precursor delivery system. In the new

system, the carrier gas line and the precursor vapor line were joined with a T-joint in which the carrier gas would flow straight while the small amount of precursor would have to flow at 90 degrees. Thus, at higher process pressure, the precursor experienced higher back pressure, resulting in a negligible amount of precursor to reach to the deposition chamber.

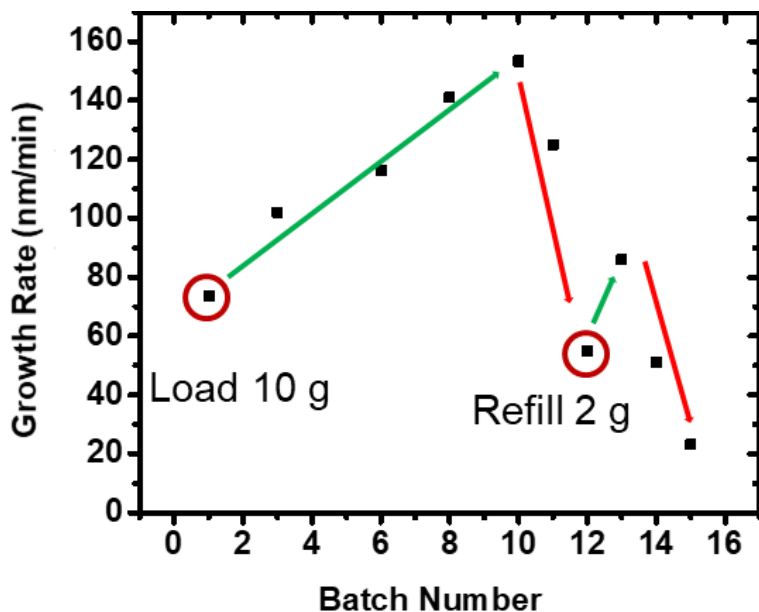


Figure 6.31. Variation of growth rate of NS18 series film. The bubbler was initially loaded with 10 g of *ortho*-carborane. The film growth rate increased, on average, by ~ 9 nm/min per sequential growth until the precursor started to deplete after the 10th growth. We observed a similar trend after refilling the bubbler with 2 g of *ortho*-carborane.

Figure 6.31 shows the growth rates of the successful growths of the NS18 series films as a function of growth number. Although these films were grown using the same growth conditions to test film thickness reproducibility, the growth rate increased for

each subsequent growth from NS1801 to NS1810 before decreasing, presumably due to precursor depletion in the ampoule. Although it is not clear why the thickness/growth rate increased as a function of growth number, we theorized that it resulted from a design flaw in the precursor delivery system. As *ortho*-carborane has very low vapor pressure, the vapor coming out from the MFC orifice could condense back due to the high back pressure of the carrier gas, resulting in buildup of solid *ortho*-carborane in the precursor line and below the flow valve above the orifice. Because we always closed the flow valve immediately after deposition, the condensed precursor would get trapped there until the valve is opened during the later growths, resulting in a higher precursor flow rate than the setpoint.

Another problem with the vapor-source mass flow controller was that the precursor depleted faster than expected based on the total flow rate and operation time, which we believe is because of the initial burst of the precursor before stabilizing the desired flow rate. This could have also altered the partial precursor pressure in the PECVD chamber as we waited for only 30 seconds to start the PECVD process after stabilizing the flow rate. A lengthy pre-purge could solve this problem but would consume a significant amount of the expensive precursor.

Although the issue of increasing growth rate could be mitigated by correcting the precursor flow line to achieve lower back pressure, correcting the precursor flow rate from the vapor-source MFC based on our precursor line design to reduce the precursor loss would require the unit to be sent back to the manufacturer, which was not

immediately possible due to time constraints. Thus, we returned to the original precursor delivery system using the solid-state bubblers, however, with an improved precursor flow system. The following sections describe the new approaches we implemented in an attempt to obtain a consistent precursor flow rate.

6.3.4.2. Stabilizing Bubbler, Carrier Line, and Substrate Temperatures

6.3.4.2.1. Effect of Bubbler and Substrate Temperature

In the original precursor delivery system, the parameters that could influence the precursor flow rate included the precursor fill level, precursor physical state (solid chunk vs. powder), bubbler temperature, and carrier line temperature. As monitoring of the precursor fill level and physical state for each growth was not tenable, the first step in regulating the precursor flow rate was to continuously monitor and stabilize the bubbler and carrier line temperatures within tighter constraints throughout the deposition time. Thus, instead of using variable transformers, we used precision PID controllers with RF shielded thermocouples to heat the solid-state bubblers. The PID controllers maintained the temperature fluctuations within a fraction of a degree with real-time temperature monitoring.

In addition to the precursor delivery system, we also optimized the substrate heating system to maintain a constant substrate temperature using the PTB SHQ-15A PID controller. After tuning the system, we achieved a temperature fluctuation within ± 0.1 °C unlike in the past where the temperature fluctuation was wide, as shown in Figure 6.32a. As we can see, especially for a substrate temperature of 500 °C,

temperature fluctuation was more than ± 25 °C with an average rise rate of 20 °C per minute, which could alter the substrate temperature by ~ 50 °C within 2.5 minutes. For these high-temperature films, this could significantly alter the film properties and, more importantly, cause variation between films. Figure 6.32(b) shows the substrate temperature as a function of time for different set temperatures after tuning the PID controller. We can see from the figure that the substrate temperature remained constant after the initial stabilization except for some oscillations at specific temperatures during the auto-tuning of the PID controller.

With the heating systems tuned, we designed an experiment to study the film reproducibility using the AB series growth conditions, but using two precursor bubblers heated at heated at 80 ± 0.1 °C. The growth time, film thickness and growth rate of the films, referred to as the PC18 series, are summarized in Table 6.19.

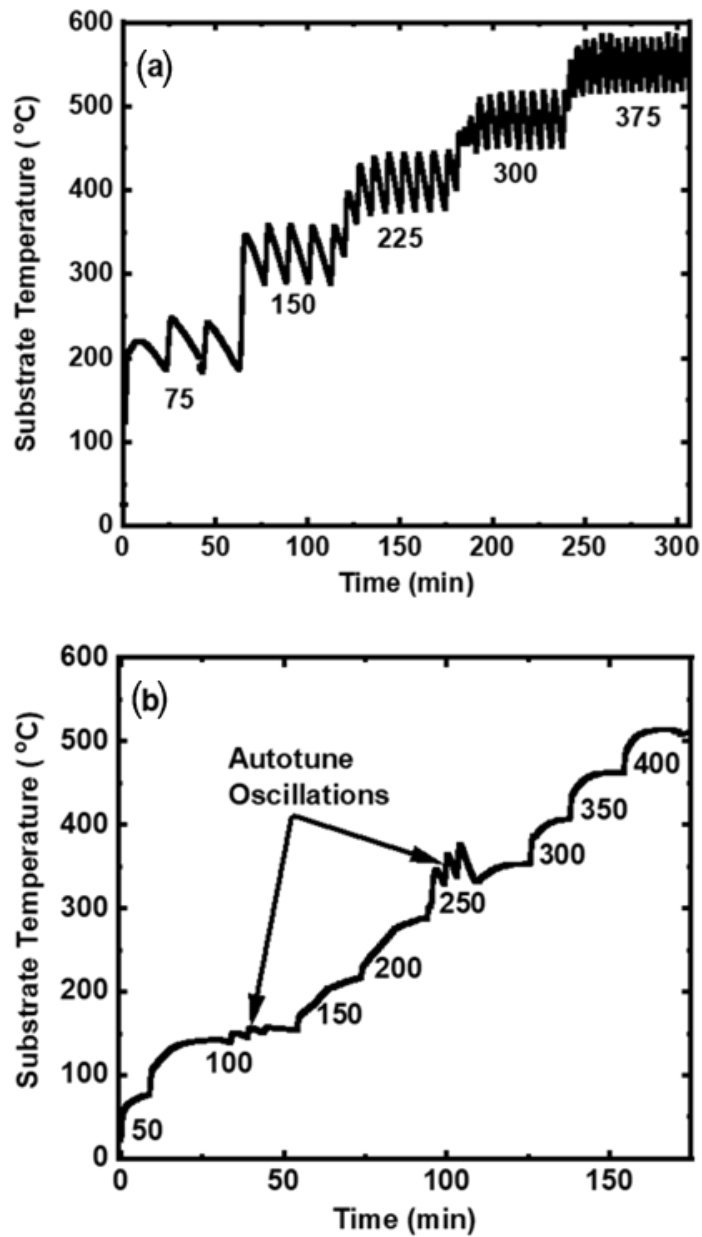


Figure 6.32. Fluctuation in substrate temperature as a function of time (a) before tuning the PID controller and (b) after tuning the PID controller. The numbers below the curves represent the set temperature, while the y-axis values represent the actual substrate temperature.

Table 6.19. Growth time, thickness, and growth rate of the PC18 series films. The films were grown at a substrate temperature of 500 °C, RF power of 40 W, total argon flow of 200 sccm, and process pressure of 0.2 Torr. Bubbler temperature was set at 80 °C.

Film	Growth Time	Thickness (nm)	Growth Rate (nm/min)
PC1801	15	Delaminated	–
PC1802	9	737	82
PC1803	9	871	97
PC1804	12	1214	101
PC1805	12	1129	94
PC1806	15	1539	103
PC1807*	20	1839	92
PC1808	15	1543	103
PC1810	10	871	87

*The substrate temperature was set at 400 °C.

We can see from Table 6.19 that the first film, PC1801, grown for 15 minutes delaminated. All the remaining films in the PC18 series demonstrated a nearly consistent growth rate of ~100 nm/min. We believe that the PC1801 film was much thicker because of being the first growth after a bubbler refill as usual, which caused it to delaminate due to high residual tensile stress. Although the PC1807 film was grown at a substrate temperature of 400 °C by an error, its growth rate did not change significantly from others, which is consistent with the findings of our previous study [95].

6.3.4.2.2. *Effect of Carrier Line Temperature and Partial Flow*

As we obtained a consistent growth rate after stabilizing the bubbler temperature, we replaced the carrier line and mixing block heaters with PID controlled heaters to minimize any possible variations in the growth rates and other properties by reducing the temperature variations. Based on the AB and NS18 series film properties, we expected the lower growth rate to produce films with higher charge carrier mobility. Thus, to study the effect of the bubbler and carrier line temperature in film growth rates and other properties, we designed a $3^1 \times 2^1$ factorial experiment using three values of bubbler temperature and two values of carrier line temperature, as summarized in Table 6.20. Instead of using two bubblers as in the past, we used only one bubbler and chose temperatures between 40–80 °C for film growths. The films, referred to as the FT18 series, were grown for 5 minutes with all other growth conditions identical to those of the AB series. In addition to the regular 15 mm × 15 mm substrates, we also deposited films on the 30 mm × 30 mm substrate that is secured at the center of the substrate holder, as shown in Figure 2.2. The films were grown in a randomized way to minimize any systematic error. Table 6.21 summarizes the growth conditions and the properties of the FT18 series films.

Table 6.20. $3^1 \times 2^1$ factorial experiment design for FT18 series film growth.

Variables	Low	Mid	High
Bubbler Temperature (°C)	40	60	80
Carrier Line Temperature (°C)	100	–	180

Table 6.21. Growth conditions, thickness, and growth rates of the FT18 series films grown according to the $3^1 \times 2^1$ factorial experiment design from Table 6.20. Films were grown for 5 minutes at a substrate temperature of 500 °C, RF power of 40 W, a total flow rate of 200 sccm, partial precursor flow of 100%, and process pressure of 0.2 Torr.

Film Name	Bubbler Temperature (°C)	Carrier Line Temperature (°C)	Thickness (nm)	Growth Rate (nm/min)
FT1801	40	100	42	8
FT1801.center	40	100	77	15
FT1802	40	180	46	9
FT1802.center	40	180	85	17
FT1803	80	100	293	59
FT1803.center	80	100	392	78
FT1804	60	180	128	26
FT1804.center	60	180	230	46
FT1805	80	180	314	63
FT1805.center	80	180	420	84
FT1806	60	100	142	28
FT1806.center	60	100	239	48
FT1807*	40	100	271	14
FT1807.center	40	100	504	25
FT1808*	40	180	215	11
FT1808.center	40	180	405	20

* Regrown for 20 minutes because the previous films were very thin.

A preliminary analysis of the results revealed that the carrier line temperature (100 °C vs. 180 °C) had a minimal effect on film growth rate. However, the bubbler temperature had substantial impacts. Thus, to further expand the factorial experiment parameter space, we included the partial precursor flow and process pressure in the study and designed a 2^3 factorial experiment, as summarized in Table 6.22. However,

in this new experiment, we kept the carrier line at 100 °C and used two new intermediate bubbler temperature values (50 °C and 70 °C). The growth conditions, film thickness, and growth rates of these films, referred to as the PP18 series, are tabulated in Table 6.23.

Table 6.22. 2³ factorial experiment design for PP18 series film growth.

Variables	Low	High
Bubbler Temperature (°C)	50	70
Partial flow (°C)	0.25	1
Process Pressure (Torr)	0.1	0.2

We can see from Table 6.21 that the film growth rates of the central films were higher than that for the regular peripheral films, which is always observed in our a-BC:H films and could be due to the lowered RF power [95] at the center of the substrate holder due to fringing effect. However, here, we observed that the effect of the lowered RF power is greater at higher process pressure.

Table 6.23. Growth conditions of PP-18 series films grown according to the 2³ factorial experiment design from Table 6.22. The films were grown for 10 minutes at a substrate temperature of 500 °C, RF power of 40 W, a total flow rate of 200 sccm, and carrier line temperature of 100 °C. The rows are shaded to separate different film batches

Film Name	Bubbler Temperature (°C)	Partial Flow	Process Pressure (Torr)	Thickness (nm)	Growth Rate (nm/min)
PP1801	70	1	0.1	416	42
PP1801.center	70	1	0.1	505	50
PP1804	70	0.25	0.2	129	13
PP1804.center	70	0.25	0.2	245	24
PP1805	50	0.25	0.1	88	9
PP1805.center	50	0.25	0.1	127	13
PP1806	70	0.25	0.1	137	14
PP1806.center	70	0.25	0.1	240	24
PP1807	50	1	0.2	213	21
PP1807.center	50	1	0.2	400	40
PP1808	50	1	0.1	223	22
PP1808.center	50	1	0.1	277	28
PP1809	70	1	0.2	484	48
PP1809.center	70	1	0.2	717	72
PP1810	50	0.25	0.2	88	9
PP1810.center	50	0.25	0.2	158	16

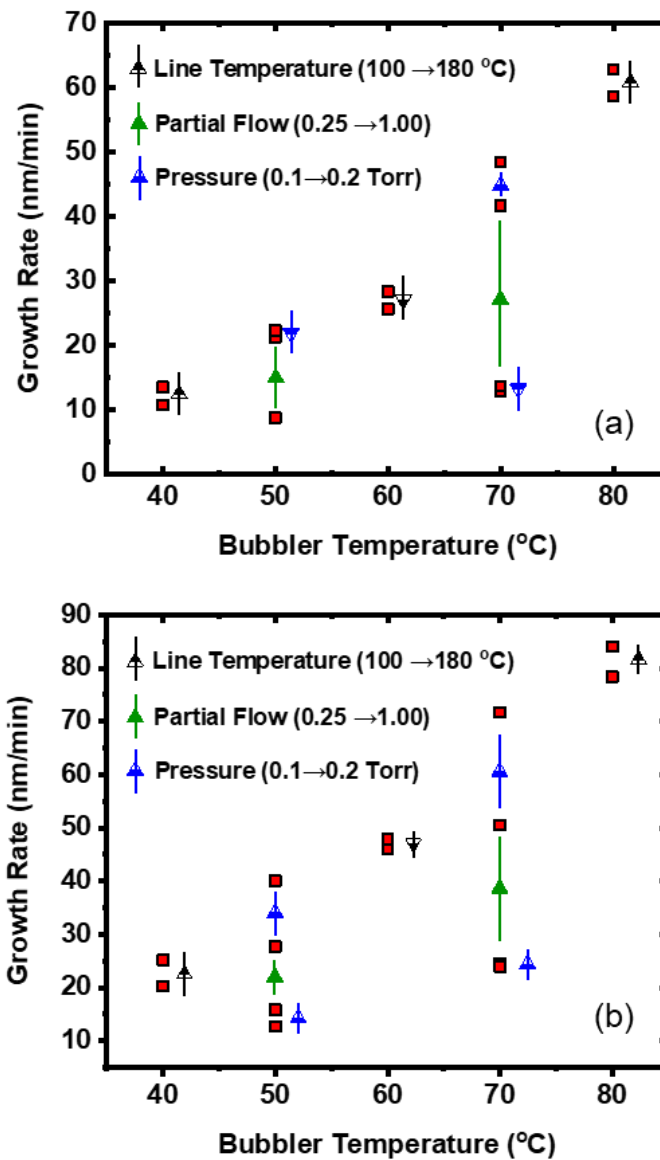


Figure 6.33. The growth rate of the FT18 and PP18 series films: (a) regular films and (b) central films, as a function of bubbler temperature. The colored arrows show the direction of increasing parameter values. Data points without corresponding arrows are obtained for carrier line temperature of 100 °C, precursor partial flow of 1.00, and process pressure of 0.2 Torr.

Figure 6.33 shows the growth rate of the FT18 and PP18 series films as a function of bubbler temperature. We can see from the figure that the bubbler temperature and partial flow of carrier gas through the bubbler had strong positive correlations to the film growth rate. We can explain this increased growth rate in terms of the increased precursor partial pressure in the chamber due to a combined effect of increased precursor sublimation rate at higher bubbler temperature and increased carrier gas flow through the bubbler. Figure 6.33 further shows that the carrier line temperature did not show a significant effect. The effect of the process pressure, however, was unusual in that it did not affect the growth rate of the regular peripheral 15×15 mm films but showed a strong positive effect on the growth rates of the central 30×30 mm films, particularly at higher precursor partial flow. Although a lowered RF power at the center is responsible for the overall increase in the growth rate of the central films, as explained previously, the strong effect of the process pressure at lower RF power and higher precursor flow rate was not expected because the process pressure individually and its interaction with any other process parameter was known to always affect the growth rate negatively [95].

At the beginning of the FT18 series film growths, the precursor bubbler was filled with ~ 10 g of *ortho*-carborane powder. As we obtained consistent growth rates for all films, starting from the FT1801 to PP1810, which were grown in a randomized sequence, the physical state of the precursor (powder vs. solid chunk) appeared to not significantly affect the growth rate. Because the total deposition time for the 18 batches

(170 min) was short and the partial flow rates were also set at lower values in a majority of the growths, the precursor might not have depleted significantly to show an effect in the growth rate. As the films in the FT18 and PP18 series were grown for 5, 10, and 20 minutes, and we observed proportional increase in film thickness, this study also revealed that the growth rate does not change as a function of the growth time, which is critical to obtaining thick films with longer growth times, unless the precursor depletes during the film growth.

The effect of bubbler temperature on the film growth rate had not previously been explicitly studied. We observe from Figure 6.33(a) that for a 10 °C change in bubbler temperature from 70 °C, the growth rate changes by ~20 nm/min at a partial flow of 100%. Thus, even a ± 5 °C variation in the set bubbler temperature could introduce nearly ± 10 nm/min fluctuation in the growth rate. This could result in the V, AA, AB, and many other films grown for 20 minutes to have a thickness difference of as much as 400 nm. It should be noted that earlier films were grown with two bubblers with the bubbler temperature set in between 75–85 °C, and any fluctuations in the bubbler temperature caused by factor, such as the change in the heating coil resistance or the mixing of hot carrier gas from the carrier line (generally heated at > 100 °C) could have added more variations in the film growth rates, thickness, and film properties.

6.3.5. Properties of the NS18, PC18, FT18 and PP18 Series Films

6.3.5.1. NS18 Series Films

The NS18 series films were deposited using the vapor-source mass flow controller to control the precursor flow in the precursor delivery system, as described in Section 6.3.4.1. The growth conditions for the films are tabulated in Table 6.18, and their optical, electronic, and electrical properties are summarized in Table 6.24.

Table 6.24. Optical and electronic properties of NS-18 series films grown using new vapor source mass flow controller.

Film Name	Growth Rate (nm/min)	Refractive Index	Dielectric Constant	E₀₄ (eV)	Urbach Energy (meV)
NS1801	74	2.44	7.4	–	–
NS1803	102	2.29	5.1	1.97	735
NS1806	116	2.28	5.4	2.11	675
NS1808	141	2.18	5.6	2.15	621
NS1810	154	2.07	5.3	2.51	552
NS1811	125	2.20	4.6	2.25	671
NS1812	55	2.35	5.1	–	–
NS1813	86	2.31	–	–	–
NS1814	51	2.39	6.5	1.94	699
NS1815	23	2.34	8.2	–	–

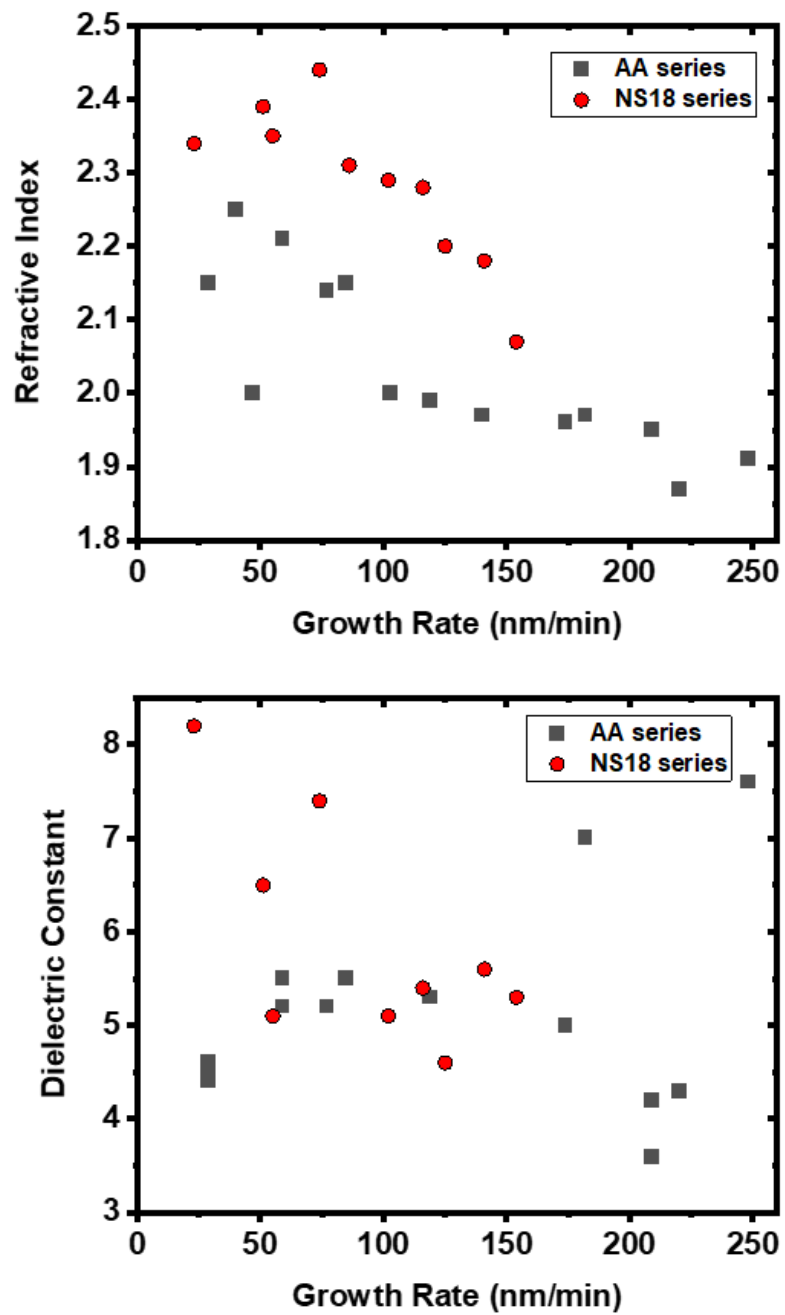


Figure 6.34. Refractive index and bandgap of NS18 series films as a function of growth rate compared to the AA series films.

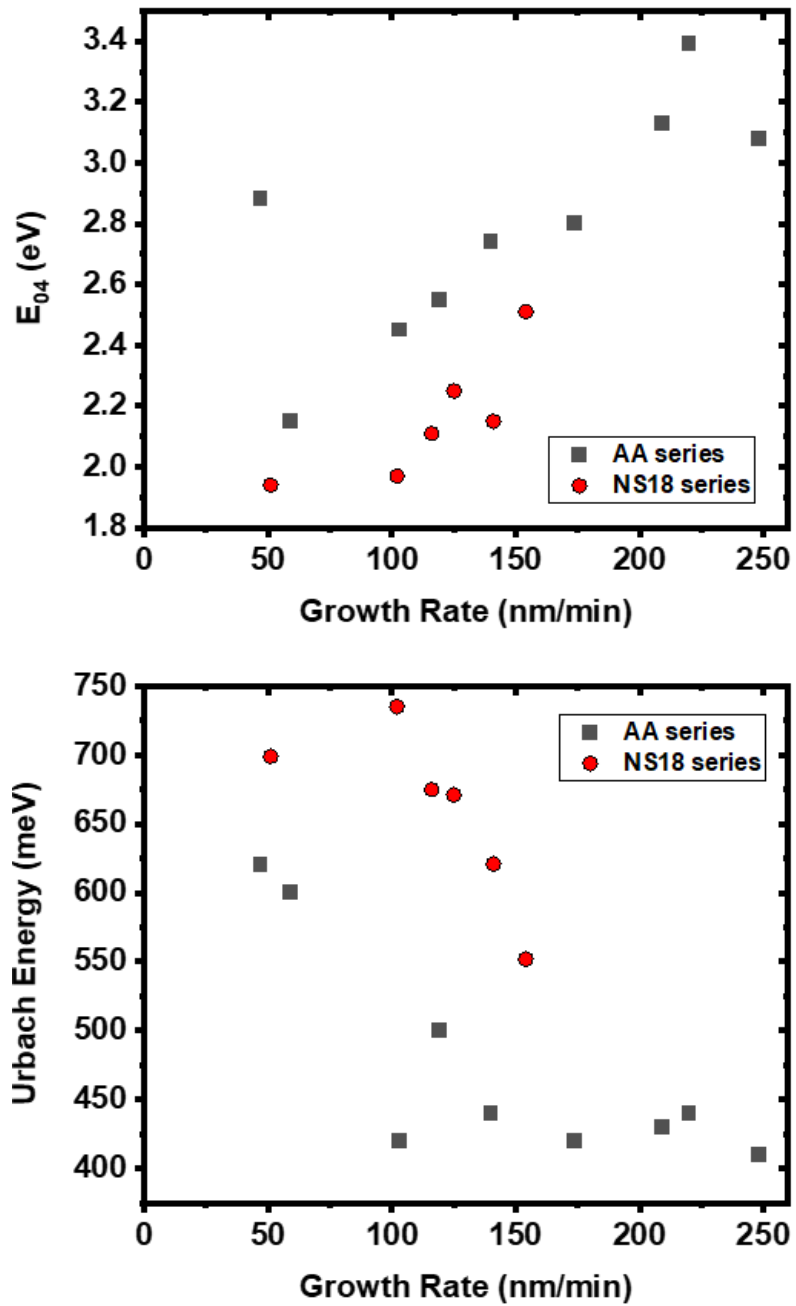


Figure 6.35. Iso-absorption energy gap (E_{04}) and Urbach energy of NS18 series films as a function of growth rate compared to the AA series films.

Although the NS18 series films were deposited using the vapor-source MFC with the expectation to achieve a reproducible film growth rate, it varied significantly. As growth rate was identified as a factor affecting the film properties in the V–AB series films, we tested for its effect in the NS18 series films. Figure 6.34 and Figure 6.35 show the optical and electrical properties of the NS18 series films as a function of growth rate. Among the NS18 series film properties, the iso-absorption energy gap (E_{04}) increased with increasing growth rate, whereas the refractive index and dielectric constant decreased. Although most of the properties of the NS18 series film followed similar trends as in the AA series film, the refractive index and the Urbach energy values were higher than those of the AA series films whereas the bandgap values were lower than those of the AA series in general. The dielectric constant values, however, were scattered with some values aligning with the AA series.

Although we measured refractive index, dielectric constant, and optical bandgap for the NS18 series films, the electrical properties (resistivity and carrier mobility) could not be evaluated because the current–voltage characteristics for the films did not show Ohmic behavior at low electric fields. This was unexpected because the a-BC:H films grown on low-resistivity silicon substrates typically showed Ohmic behavior. As we had known from previous studies [93] that films with lower bandgaps and higher Urbach energies (and consequently higher refractive indices) tend to have higher charge carrier mobility, the results from the NS18 series further suggested that films with lower growth

rates could possibly yield high carrier mobility, which is also observed in the V, AA, and AB series films.

6.3.5.2. PC18, FT18 and PP18 Series Films

The PC18, FT18, and PP18 series films were grown using the original bubbler setup, however with all of the components in the precursor delivery system and substrate temperature regulated using precision PID controllers, as discussed in Section 6.3.4.2. Among these films, films in the PC series were grown using identical growth conditions, however, for different growth times to test for the film growth rate reproducibility. Further, these films were grown using two precursor bubblers unlike the FT18 and PP18 series films which were grown using only one precursor bubbler. As we can see from the table, the PC1802–PC1806 films have nearly equal growth rates and their optical properties (refractive index and band gap) and electrical properties (resistivity and carrier mobility) are comparable. The dielectric constant, however, showed a large variation. The PC1807 film was grown at a substrate temperature of 400 °C; thus, the bandgap and the resistivity of the film was higher than those of the earlier films. Based on the bandgap, resistivity, and carrier mobility, the films PC1808 and PC1810 were probably grown at lower temperatures, although they were supposed to be grown at 500 °C.

Table 6.25. Optical, electronic, and electrical properties of PC18, FT18, and PP18 series films. The symbols RI, κ , ρ , μ_0 , E_{04} , and E_U are respectively the refractive index, dielectric constant, resistivity, low-field mobility, iso-absorption energy gap, and Urbach energy.

Film Name	Growth Rate (nm/min)	RI	κ	ρ (Ω -cm)	μ_0 ($\text{cm}^2/\text{V-s}$)	E_{04} (eV)	E_U (eV)
PC1802	82	2.11	6.5	4.4×10^{10}	1.0×10^{-8}	2.26	0.47
PC1803	97	2.15	5.8	4.2×10^{11}	1.3×10^{-9}	2.25	0.49
PC1804	101	2.06	7.0	1.4×10^{11}	2.1×10^{-9}	2.25	0.47
PC1805	94	2.15	7.0	–	1.8×10^{-8}	2.21	0.48
PC1806	103	2.04	8.4	–	1.7×10^{-8}	2.27	0.44
PC1807	92	2.03	6.4	–	5.5×10^{-11}	2.63	0.41
PC1808	103	2.00	6.6	–	1.9×10^{-11}	2.83	0.47
PC1810	87	1.96	5.4	–	3.6×10^{-12}	2.6	0.47
FT1801	8	2.03	1.7	–	–	–	–
FT1802	9	2.08	2.1	–	–	–	–
FT1803	59	2.19	5.0	2.1×10^{12}	2.0×10^{-9}	2.05	0.77
FT1804	26	2.31	4.2	1.3×10^{13}	4.2×10^{-10}	–	–
FT1805	63	2.09	4.8	6.0×10^{12}	5.0×10^{-11}	2.22	0.74
FT1806	28	2.34	4.5	4.6×10^{12}	5.5×10^{-8}	–	–
FT1807	14	2.25	4.4	3.3×10^{13}	3.3×10^{-10}	–	–
FT1808	11	2.31	–	–	–	–	–
PP1801	42	2.29	6.8	1.3×10^9	1.6×10^{-7}	1.92	0.61
PP1804	13	2.30	3.4	1.3×10^{13}	8.4×10^{-12}	–	–
PP1805	9	2.18	3.8	8.2×10^{14}	2.4×10^{-14}	–	–
PP1806	14	2.16	3.6	3.1×10^{14}	1.5×10^{-13}	–	–
PP1807	21	2.22	4.4	3.7×10^{12}	8.7×10^{-11}	–	–
PP1808	22	2.26	4.7	1.1×10^{13}	3.3×10^{-9}	–	–
PP1809	48	2.14	5.1	8.7×10^{12}	1.5×10^{-10}	2.26	0.63
PP1810	9	2.27	3.7	–	–	–	–

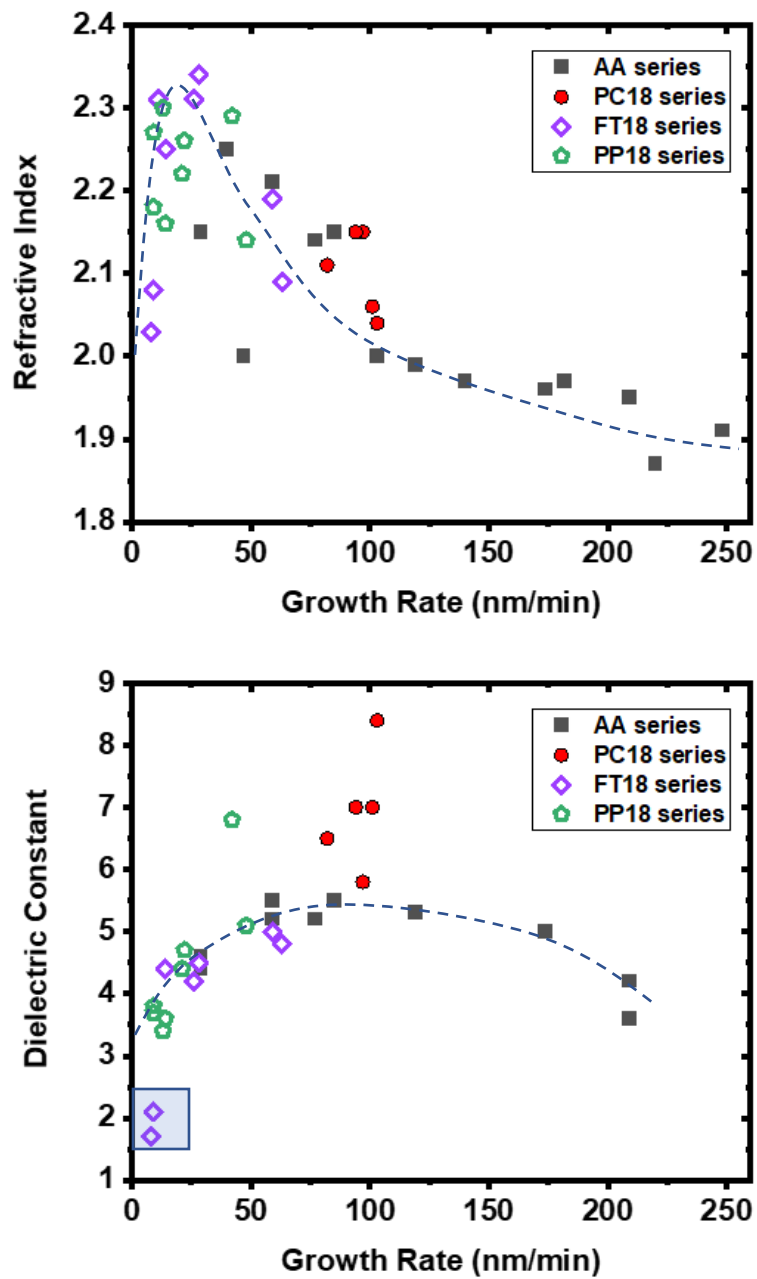


Figure 6.36. Refractive indices and dielectric constants of the AA, PC18, FT18, and PP18 series films grown at 500 °C as a function of growth rate. The dashed lines are only for visual guidance.

Figure 6.36 shows the variation of refractive index and dielectric constant of the films in the PC18, FT18, and PP18 series films grown at 500 °C as a function of growth rate compared to the AA series films grown at 500 °C. We can see from the figure that the refractive indices of the PC18, FT18, and PP18 series films first increase with increasing growth rates up to ~30–40 nm/min and then decrease following the trend of the AA series films grown previously. Similarly, the dielectric constants of the FT18 and PP18 series films followed an identical trend to the AA series with increasing dielectric constant up to ~50 nm/min and then decreasing for higher growth rates. The two data points within the square box correspond to the FT1801 and FT1802 films which were very thin (42 and 46 nm). Thus, their very low dielectric constant values may not be the representative of the series. The films in the PC18 series did not fit within the trend, which could be because the films were grown using two precursor bubblers, although the use of two bubblers was expected only to increase the precursor flow rate and thus the growth rate.

The iso-absorption energy gap (E_{04}) and Urbach energy of the PC18, FT18, and PP18 series films grown at 500 °C as a function of the growth rate compared to the AA series films are shown in Figure 6.37. We can see that the energy gap (E_{04}) shows a clear increasing trend with the growth rate while the Urbach energy, shows a decreasing trend, indicating their inverse relation, as discussed previously.

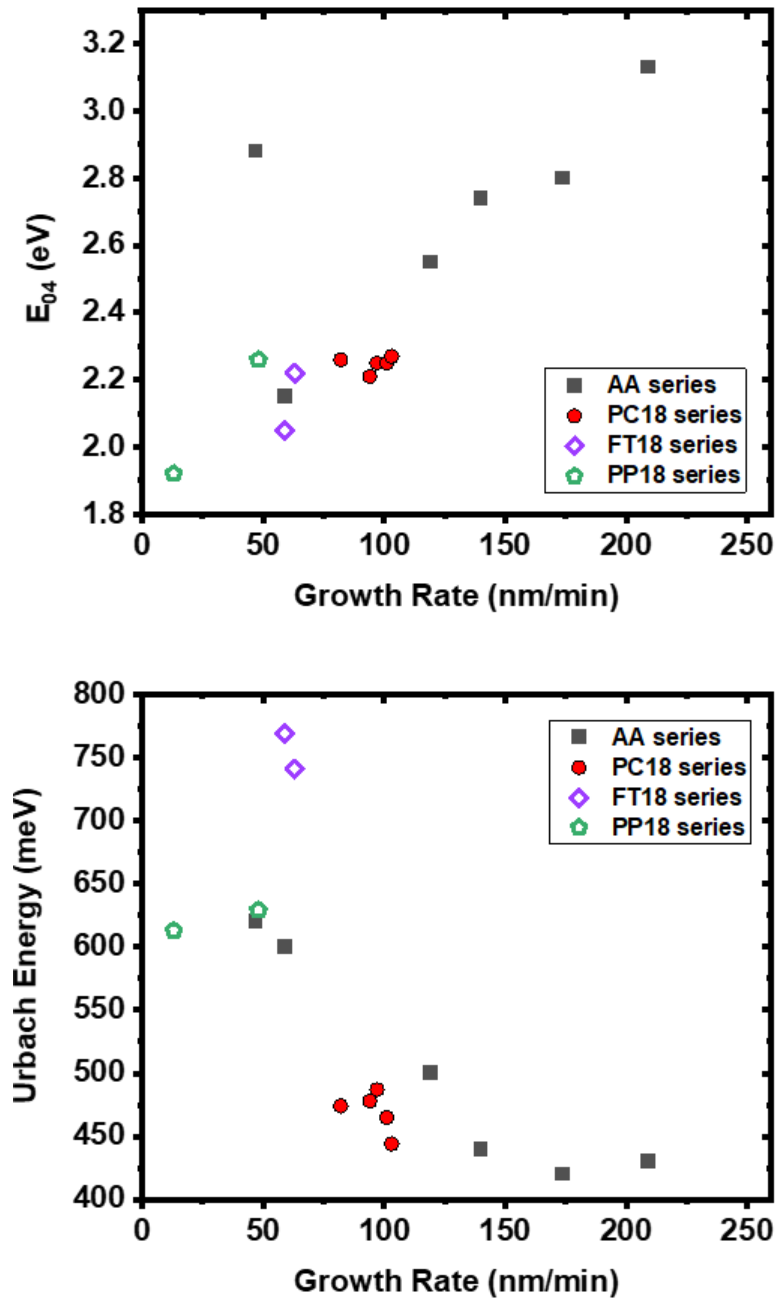


Figure 6.37. Iso-absorption energy gap and Urbach energy of the AA, PC18, FT18, and PP18 series films grown at 500 °C as a function of growth rate.

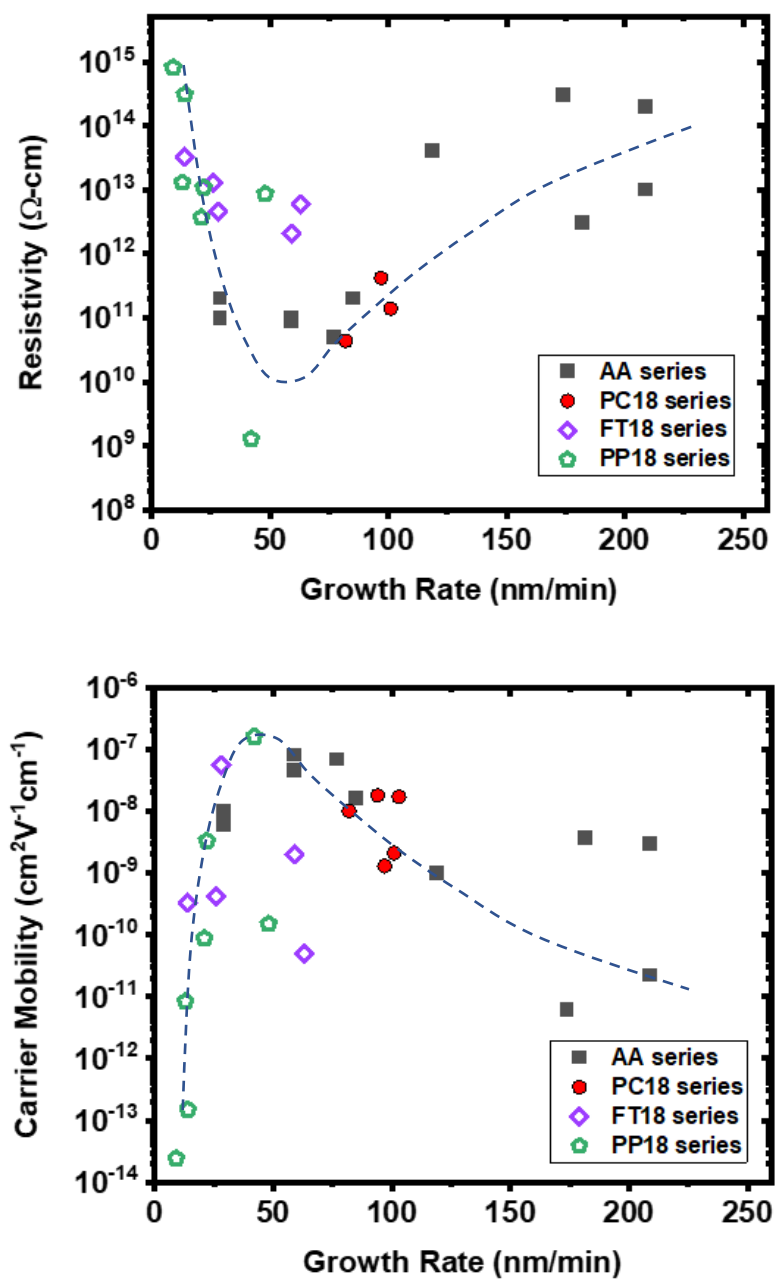


Figure 6.38 shows the electrical resistivity and carrier mobility of the PC18, FT18, and PP18 series films grown at 500 °C as a function of growth rate compared to the AA series films. The figure shows that the films demonstrated similar trend as the AA series films in the higher growth rate regimes. However, from the FT18 and PP18 series films, we found that the carrier mobility and resistivity first achieved their optimum values at growth rates ~30–50 nm/minute before respectively decreasing and increasing at higher growth rates.

6.4. Discussions: Film Properties and Correlations

We have found that growth rate significantly affects the properties of a-BC:H thin films. The precursor partial pressure was identified to be responsible for film growth rate in a previous study [95]. However, its effect on refractive index and bandgap was not found to be significant; rather, growth temperature and the power*pressure interaction were far and away the dominant process conditions. In addition, significant (i.e., moderate to high) correlations between growth rate and refractive index and bandgap were not previously evident. It could be possible that these correlations were masked by the amount of variability in the results (in particular, the variability in precursor flow) or simply overshadowed by stronger correlations. Here, however, it became clear that—all else being equal—the precursor partial pressure does have a significant effect on more than simply growth rate.

In previous studies [94], [95], it was found that the B/C ratio has the highest positive correlation with the film growth rate for <50 nm/min. For higher growth rates,

the B/C ratio was found to saturate at ~ 5 (equal to that of the *ortho*-carborane precursor). However, the hydrogen concentration was not found to correlate with the growth rate. This suggests that most of the electrical and electronic properties could be explained in terms of the film composition. As we have observed that, except for a small region below ~ 30 nm/min, the refractive index generally decreases with the growth rate. This suggests that a decreasing carbon concentration, thus a decreasing electron density with the growth rate, could be the reason behind decreasing refractive index at higher growth rates. Similarly, the lower dielectric constant at lower growth rates could be due to the formation of stiffer networks due to increased $\text{—CH}_2\text{—}$ cross-linking [94]. At higher growth rates, however, the decreased carbon concentration could result in flexible material leading to higher orientation/distortion polarization [94], giving an increasing low-frequency dielectric constant. As B/C ratio saturates at $\sim 50\text{--}75$ nm/min, it does not explain a slightly decreasing dielectric constant after $\sim 75\text{--}100$ nm/min. However, it is consistent with the observed correlation between the low-frequency dielectric constant and the refractive index. Higher orientation/distortion contribution to the polarizability of a-BC:H films grown at the gentle growth conditions is also proposed to be due to impurity oxygen, giving rise to the polar bonds such as B-O and O-H [95]. However, the growth-rate-dependence of polarizability on this basis is not consistent as the impurity oxygen concentration is found to correlate negatively with growth rate [95].

We have observed in most of our films that the iso-absorption energy gap (E_{04}) increases with the growth rate, showing a strong positive correlation, whereas the Urbach energy, which is considered as the width of band tails, decreases with growth rate. Although a negative correlation between the bandgap and Urbach energy was suggested in previous studies, the correlation between growth rate and the bandgap was not observed. As the refractive index is found to decrease with the growth rate, which can be seen in Figure 6.39, it is plausible to expect that the bandgap increases with the growth rate (the refractive index decreases in general for growth rates >30 nm/min) as refractive index generally decreases with increasing bandgap in semiconductors [157].

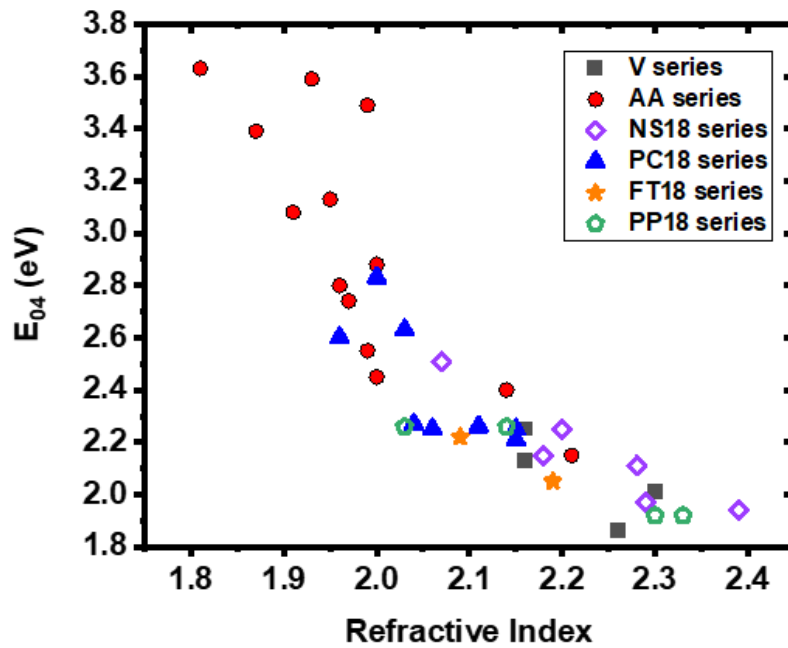


Figure 6.39. Variation of iso-absorption energy gap with the refractive index for high-temperature films.

As for the electrical properties, we initially found that electrical resistivity increases with growth rate whereas carrier mobility decreases with growth rate for growth rates above ~ 50 nm/min. However, after consistently depositing films with lower growth rates, it became apparent that both resistivity and carrier mobility reverse the trend below ~ 30 nm/min, showing an inverted V shaped graph with their optimum values at ~ 30 – 50 nm/min. The decreasing carrier mobility with increasing growth rate above 50 nm/min and the observed dependence of bandgap and Urbach energy with growth rate is consistent with the previous observation that the carrier mobility decreases with E_g/E_U ratio [93], [235]. This is also consistent with the hypothesis that the charge transport in films with lower bandgap and higher Urbach energy (lower growth rates) is due to variable range hopping (VRH) [93] as the wide localized tail states fill the narrow bandgap, providing sufficient percolation/hopping paths. As the bandgap increases and the Urbach energy decreases with increasing growth rate, the hopping between the sites becomes harder, and the charge transport shifts to a band transport with the multiple trapping of carriers by defect states [93]. However, the decrease of carrier mobility for growth rates below 30 nm/min is not consistent with the hypothesis, and further analysis, such as the role of growth rates in the structural and energetic disorder in the material could help understand the trend.

Although we had previously opted for relatively high precursor flow rates to achieve the highest possible growth rates and therefore thicker films, the above results demonstrate a clear conflict in that growth conditions that resulted in relatively low

growth rates yielded highest-mobility films. However, because both the total flow rate and pressure also interact with the partial flow rate [95], it could be possible to tune the three together to achieve a better optimum. Specifically, decreasing the total flow rate and pressure in conjunction with partial flow rate may simultaneously yield desirable electronic/electrical properties and growth rate.

6.5. Mobility and Thickness Optimization Revisited

As demonstrated by the films grown at 500 °C, lower film growth rates, specifically in the range of 30–50 nm/min, produced the highest mobility films. Thus, for optimizing the charge carrier mobility values in a-BC:H films, we decided to investigate additional batches of films with a growth rate centered at ~30 nm/min. For this, we chose a growth condition with bubbler temperature of 60 °C, carrier line temperature of 100 °C, substrate temperature of 500 °C, RF power of 40 W, process pressure of 0.2 Torr, and total carrier gas flow rate of 200 sccm through one bubbler. Among all of the alternative substrates we investigated, copper foil facilitated the deposition of the thickest and most stable films. However, they were not free from other issues such as wrinkle formation during substrate cooling and device shorting during electrical testing. Thus, we chose slightly thicker copper foil (100 µm) as the substrate, which could take advantage of substrate flexibility while hopefully eliminating wrinkle formation.

To produce a film as thick as 3 µm, we needed 100 minutes of growth time. However, because of an overheating issue related to the process pump, we deposited a

batch of films, referred to as CU1803, in five consecutive 20 minute growth cycles with more than two hours of time between each deposition cycles to produce a film approximately 3 μm thick. The substrate temperature, however, was kept at 500 $^{\circ}\text{C}$ the entire time to anneal the films during the intervals.

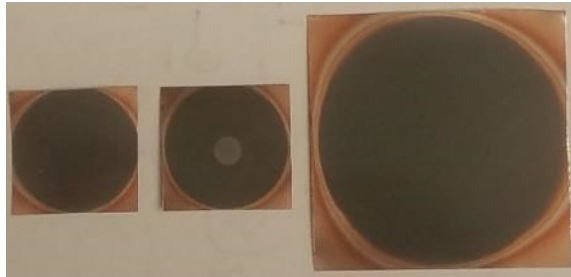


Figure 6.40. Film CU1803 deposited on 100 μm thick copper foil. The smaller films on the left were expected to be 3 μm thick, while the large film on the right was expected to be 5 μm thick based on the growth rate of films placed at the center of the substrate holder. All of the films in this batch were stable for a long time in the atmosphere.

To confirm the thickness reproducibility for these long growth times, we deposited another batch, referred to as CU1804, using the same growth condition, however, for two cycles of 20 minutes each on copper foils as well as on silicon substrates. Ellipsometry revealed that the CU1804 film was 1280 nm thick, which is very close to the expected thickness of 1200 nm based on a growth rate of 30 nm/min for 40 minutes, confirming the thickness reproducibility even for longer growth times. The films were stable on both copper and silicon substrates for the duration of electrical testing.

For the electrical characterization of the CU1803 films, a titanium/tungsten top contact was deposited on one film to form a MIM device, and a Hg probe was used to make a top contact on the other film. Figure 6.41 shows the IV characteristics of these CU1803 films. The figure shows that the film with the Ti/W contact did not exhibit shorting/electrical breakdown up to 10 V, whereas the film measured using the mercury probe achieved a breakdown voltage of ≥ 100 V. Both of the films showed perfect and stable IV symmetry, demonstrating efficient carrier injection. Both of the films produced identical IV data within the range of applied voltage.

For the CU1804 films, Ti/W bottom and top contacts were deposited on the films grown on copper foil. However, the sputtered Ti/W contact appeared black and had high resistivity, which, we later realized was due to the leakage of cooling water from the sputtering gun into the sputtering chamber. Thus, electrical characterization was performed on the film grown on silicon substrates.

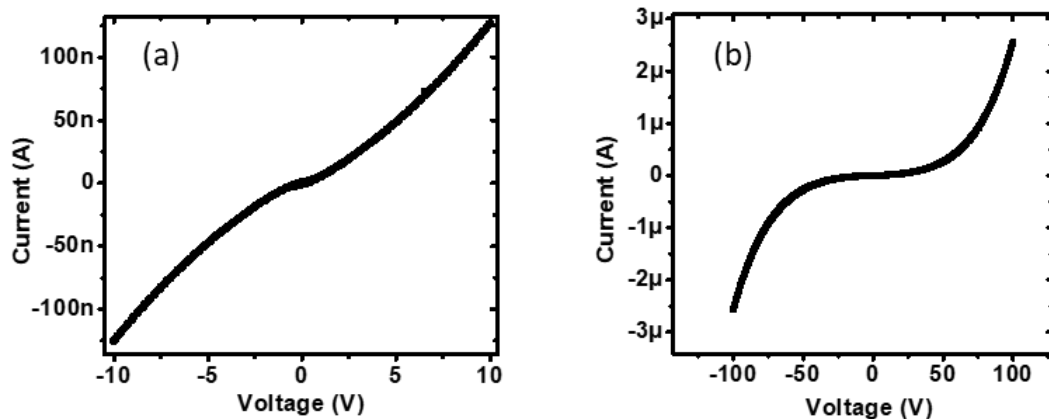


Figure 6.41. Current–voltage characteristics of CU1803 devices (a) obtained with a Ti/W top contact, and (b) obtained with Hg probe.

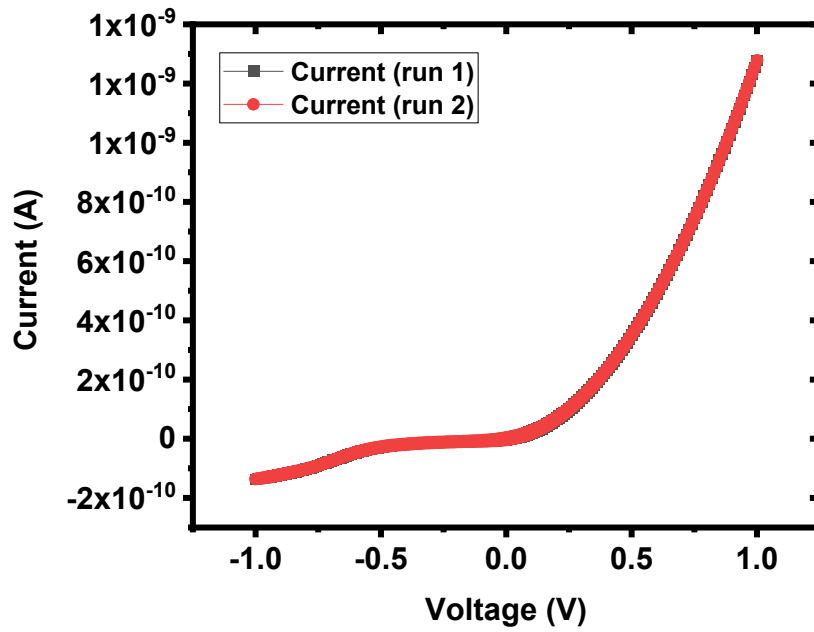


Figure 6.42. Current–voltage characteristics of the CU1804 film grown on p-type silicon.

Figure 6.42 shows the current–voltage characteristics of the CU1804 film grown on p-type silicon. The device could withstand more than 100 V of applied voltage, which corresponds to ~ 1 MV/cm with a leakage current of $55 \mu\text{A}$ without any sign of device breakdown. Because of the MIS geometry (Silicon/a-BC:H/Hg), the current–voltage characteristics were not symmetric, as was the case for the CU1803 films.

Figure 6.43 shows the current–voltage characteristics of the CU1803 and CU1804 films plotted on a log–log scale. We can see that the current–voltage data shows a sharp transition from the Ohmic charge transport regime (slope = 1) to the

SCLC charge transport regime (slope ≈ 2) at ~ 0.2 V, which corresponds to an electric field of 70 kV/cm. The charge carrier mobility values for the CU1803 and CU1804 films were extracted using steady-state SCLC analysis with negative-field-dependence. The extracted charge carrier mobility and resistivity values in the CU1803 films were $8 \times 10^{-6} \text{ cm}^2 \cdot \text{V}^{-1} \cdot \text{s}^{-1}$ and $2 \times 10^{11} \text{ } \Omega \cdot \text{cm}$, respectively, and those for the CU1804 film were $5 \times 10^{-7} \text{ cm}^2 \cdot \text{V}^{-1} \cdot \text{s}^{-1}$, and $1.5 \times 10^{12} \text{ } \Omega \cdot \text{cm}$, respectively. The higher carrier mobility and lower resistivity in the CU1803 film compared to those in the CU1804 film could be due to the fact that the former was effectively annealed for nearly 12 hours while the latter was only annealed for nearly 5 hours. The CU1803 and CU1804 films demonstrated that thick, stable, and relatively high-mobility a-BC:H films can be deposited in flexible metal substrates. This was an exciting result that the identified growth condition produced high-mobility and very high-resistivity films, both of which are very important for neutron detection. With the thickness and carrier mobility value obtained for the CU1803 film, a neutron detector using an integration time of $>5 \text{ } \mu\text{s}$ can be fabricated if the carrier lifetime in a-BC:H is $>10 \text{ } \mu\text{s}$. The maximum intrinsic detection efficiency obtainable with this detector thickness is $\sim 10\%$ for a carrier lifetime $>0.1 \text{ ms}$.

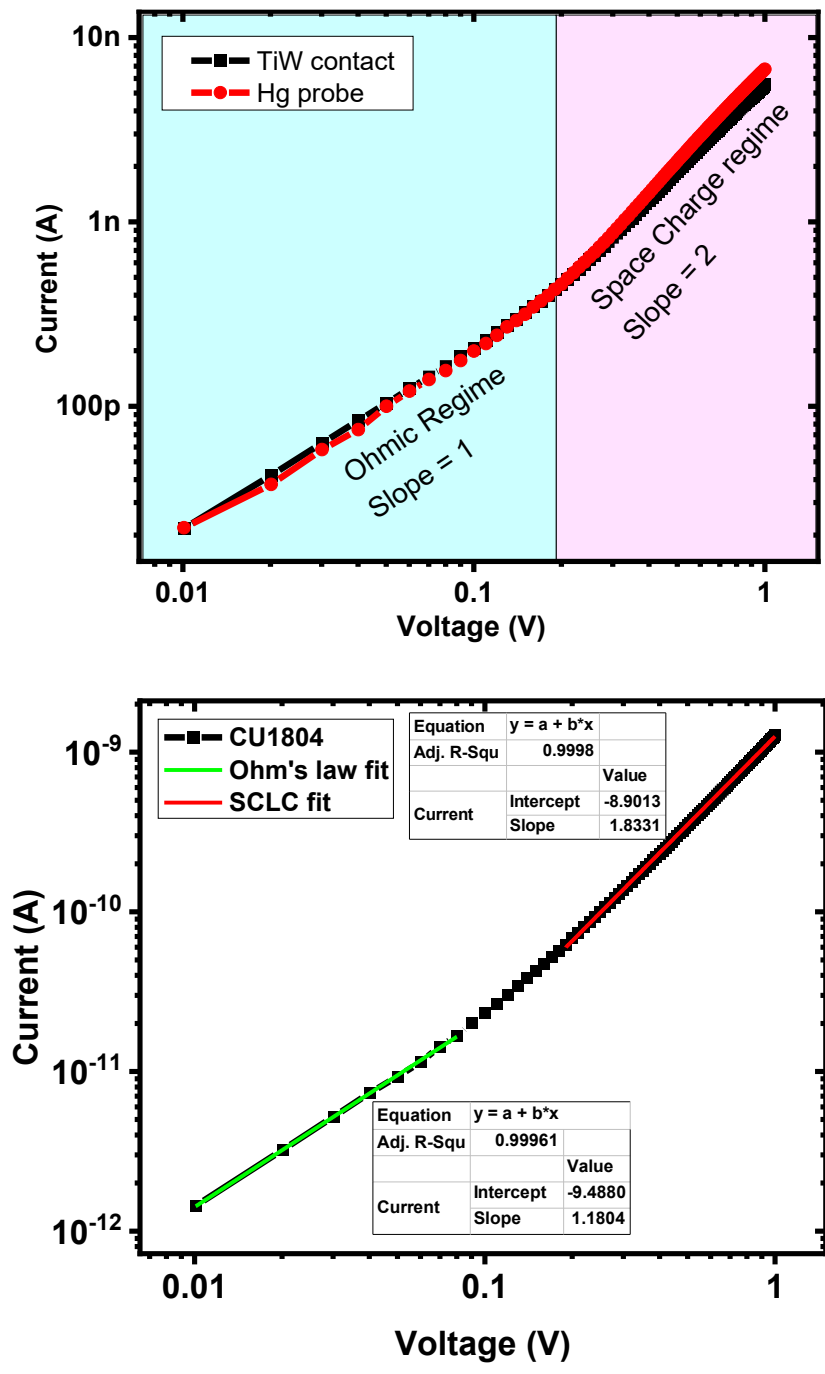


Figure 6.43. Current–voltage characteristics of the CU1803 (top) and CU1804 (bottom) films in log-log scale.

CHAPTER 7

CONCLUSION AND FUTURE WORK

Amorphous hydrogenated boron carbide (a-BC:H) has been a key player in solid-state direct-conversion neutron detection research for the last three decades due to its strong neutron absorption probability. However, very few working prototype detectors based on this material have been reported, and the reported detection efficiencies are very low. Scaling up the detection efficiency requires the ability to fabricate thick films and simultaneously optimize the charge transport properties of the material, both of which have been challenging due to limitations in growth methods and poor/poorly understood charge transport metrics: mainly the carrier mobility (μ) and carrier lifetime (τ). The objective of this work was to understand the charge transport in a-BC:H films prepared by plasma-enhanced chemical vapor deposition (PECVD) with the specific goals to (a) understand the minimum charge transport requirements to fabricate neutron detectors in relation to their thickness, (b) accurately measure the charge transport metrics in a-BC:H films using steady-state and transient current-voltage techniques, (c) optimize these metrics by improving the growth conditions, and (d) fabricate thick ($>10\ \mu\text{m}$) and mechanically stable films with good charge transport properties.

We began by investigating a basic theory of solid-state direct-conversion neutron detection, specifically focusing on materials with poor charge transport properties and single carrier transport, which we believe is the case for a-BC:H films.

By performing numerical Monte Carlo simulations of detectors of different thickness (1–25 μm), assuming a safe electric field of 1 MV/cm for a-BC:H detectors, we found that a charge carrier mobility of $>10^{-7}\text{cm}^2\cdot\text{V}^{-1}\cdot\text{s}^{-1}$ is required to achieve neutron detection with a 1 μm detector using a 1 ms integration time with a charge carrier lifetime of >1 ms. Because of the practical limitations on using long integration times, shorter integration times are desired in many cases. However, the mobility requirement increases by an order of magnitude for every order of magnitude decrease in integration time. For example, a carrier mobility $>10^{-5}\text{cm}^2\cdot\text{V}^{-1}\cdot\text{s}^{-1}$ is required if the integration time is reduced to 1 μs for a 1 μm thick detector. As the detector thickness increases, the mobility requirement further increases proportionally. In terms of mobility–lifetime product ($\mu\tau$), detection is possible with $\mu\tau >10^{-11}\text{cm}^2\cdot\text{V}^{-1}$ for a 1 μm thick detector and the requirement increases to $>10^{-10}\text{cm}^2\cdot\text{V}^{-1}$ for a 5 μm thick detector given that the mobility requirement is independently achieved.

Using the results of the numerical Monte Carlo simulation study, we developed a new theory to describe the spectral characteristics of single-carrier neutron detectors and derived new equations that can be used to extract the mobility–lifetime product ($\mu\tau$) by observing the shift of spectral peaks with an increasing electric field. We found that the usual loss of spectral characteristics in such single-carrier devices can be regained by clever manipulation of the integration time without much loss in detection efficiency. We also derived an equation that can be used to extract the $\mu\tau$ product using steady-state current–voltage measurements under steady-state neutron irradiation, which

removes the usual requirements of transparent blocking contacts in such experiments when using optical illumination. The simulation work has been published in the journal of applied physics [187].

Among the charge transport characterization methods for the PECVD-grown a-BC:H films, the charge carrier mobility extraction was the most important yet was the most difficult to carry out because conventional techniques such as Hall measurements were not appropriate due to the very high resistivity and expected low charge carrier mobility in the films. Thus, we chose to use steady-state space-charge-limited current (SCLC) analysis to extract the carrier mobility values because this method is applicable to simple device structures such as the metal–insulator–metal and metal–insulator–semiconductor devices and is sensitive to low carrier mobility. Previous studies had reported a negative field-dependence for the charge carrier mobility (i.e., decreasing carrier mobility with increasing electric field) in some a-BC:H films based on the carrier mobility extracted using transient SCLC techniques. Although negative field dependence was also shown using a conventional SCLC theory field-dependent mobility, the working equation itself was not correct for this case. Thus, to investigate it more rigorously, we extended the theory of SCLC to include the negative field dependence for mobility. The theoretical work has been published in the journal of applied physics [204].

The field-dependent SCLC theory was generally sufficient to describe the current–voltage data of a-BC:H films grown at lower substrate temperature and lower

RF power. However, for films grown at higher substrate temperature and higher RF power, the current–voltage data were inconsistent with the theory, and the extraction of carrier mobility was not possible. The field-dependent SCLC theory is valid only if the onset of the SCLC and field dependence is simultaneous or at least if the SCLC onsets before the field dependence activates. In our devices, however, we hypothesized that the field dependence (either Poole–Frenkel and/or general field-dependent mobility) was activating prior to the onset of the SCLC charge transport and were distorting/enhancing the current beyond that predicted by the field-dependent SCLC charge transport mechanism. With this assumption, we developed a theory to check the self-consistency of the charge carrier mobility extracted using field-dependent SCLC analysis. In this theory, we derived a constant, which we referred to as the “device constant,” which depends on film thickness, carrier concentration, and dielectric constant for the case of Poole–Frenkel emission, and on the field-dependent factor (γ) for the case of field-dependent mobility. For the charge carrier mobility to be consistent with the field-dependent SCLC theory, we found that the calculated device constant based on the extracted film properties should always be less than 0.736. In other words, the field-dependent SCLC mechanism dominates the charge transport only within a specific electric field range that depends on device thickness and its material properties. Beyond this electric field range, in absence of other high-field effects, the charge transport is dominated by simply Ohmic transport with Poole–Frenkel emission or field-dependent mobility, and SCLC theory is no longer applicable.

A number of films grown at higher substrate temperature and RF power were inconsistent with the theory of field-dependent SCLC in that their device constants were well beyond the limiting value. Thus, we checked for additional charge transport phenomena, such as Ohmic transport with Poole–Frenkel emission and field-dependent mobility as well as SCLC with uniform and exponential distribution of traps. Among these phenomena, SCLC with uniform trap distribution gave the best possible fit to the experimental current–voltage data. Although obtaining the absolute value of the carrier mobility was not possible using the theory, we extracted the minimum limit of the carrier mobility based on uniform distribution of traps.

On the experimental side of the work, we fabricated a large number of a-BC:H thin films with plasma-enhanced chemical vapor deposition (PECVD) using an *ortho*-carborane precursor by varying PECVD process parameters: substrate temperature, RF power, process pressure, carrier gas flow rate, and precursor partial pressure. a-BC:H thin films were deposited on different substrate materials and with different contact configurations to enable various characterization techniques. Experiments such as ellipsometry and UV-Visible spectroscopy were routinely used to measure film thickness, refractive index, band gap and Urbach energy. Capacitance–voltage and current–voltage measurements were used to extract dielectric constant, resistivity, and carrier mobility.

As our main objective was to optimize the carrier mobility and obtain stable thick films, we began the carrier mobility optimization efforts by exploring the so called

“gentle” growth conditions, which use lower substrate temperature and RF power. However, we could not achieve carrier mobility higher than $10^{-9} \text{ cm}^2 \cdot \text{V}^{-1} \cdot \text{s}^{-1}$ for these films and moved forward to explore the so called “harsh” growth conditions using higher substrate temperature and RF power. However, we encountered problems, such as inconsistent film growth, frequent film delamination, and device shorting during electrical testing.

With the less than ideal devices and frequent film delamination, we characterized a number of films grown using the harsh growth conditions. We observed from optical and electrical characterization that the film properties were related to the film growth rate. Among the measured material properties, the refractive index, Urbach energy, and carrier mobility decreased with growth rate, while the band gap and resistivity increased with growth rate. We demonstrated in a few films that a carrier mobility of $\sim 10^{-6} \text{ cm}^2 \cdot \text{V}^{-1} \cdot \text{s}^{-1}$ can be achieved in relatively thin ($< 1 \text{ }\mu\text{m}$) films grown using the harsh growth conditions. With these growth conditions, we were limited to a maximum RF power of 40 W due to system constraints, which is low in comparison to other PECVD systems. As the carrier mobility was found to be higher in films grown with high RF power, using even higher RF power in the future can be helpful in understanding whether further optimization of the material properties is possible.

Steady-state photoconductivity measurements on a few films grown at 350–400 °C yielded $\mu\tau$ product values on the order of $10^{-10} \text{ cm}^2 \cdot \text{V}^{-1}$, and quantum efficiency on the order of 10^{-3} . However, we failed to fabricate MIM devices on transparent

conducting substrates (ITO and FTO coated glass) at high substrate temperature (500 °C) as they always delaminated, which would otherwise allow us to characterize the high-mobility films using photoconductivity techniques. We obtained preliminary results with the transient photocurrent technique and observed two regimes of carrier lifetimes. An initial fast decay of photocurrent suggested a short deep trapping time on the order of 100's of ns, while a slower photocurrent decay at longer time scale suggested dispersive charge transport, frequently observed in disordered materials. We experimented with other transient techniques to extract the charge carrier mobility, such as time of flight (TOF) photoconductivity, transient SCLC (dark injection), and charge extraction by linearly increasing voltage (CELIV). However, they were not successful, primarily because of the lack of the proper device geometries, contact properties, and measurement instruments.

Because photoconductivity, and transient experiments can provide the most detailed charge transport measurements, such as carrier-specific mobility, lifetime, and mobility–lifetime product, future work should definitely focus on these experiments. Testing of devices with transient experiments that require blocking or insulating contacts was impossible. However, such experiments using thin (~10–50 nm) insulating spacers between the electrical contact and other semiconductor devices is possible. In the case of a-BC:H, the material itself is highly resistive and obtaining more insulating spacers is a problem. With recent advances in atomic layer deposition, highly insulating layer such as Al₂O₃ and HfO can be used to form insulating contacts. Further, a

Zr/ZrO₂/a-BC:H interface is expected to form a blocking contact (see Appendix A). With such contacts, experiments such as MIS-CELIV can be performed to extract carrier mobility. Photoconductivity experiments with bottom transparent contacts were not successful due to delamination of the bottom transparent conducting oxide (TCO) layer during the PECVD growth or due to device shorting, which, we believe, is also related to the unstable TCO layers. In such cases, fabricating device with a top TCO layer could solve the problem as the layer will not be exposed to high energy plasma. Other methods to obtain transparent contacts, such as by using semi-transparent metal layers and interdigitated contacts could also be used. Other than photoconductivity, some more advanced experiments, such as transient photoluminescence or time-resolved microwave conductivity (TRMC) experiments could be used in the future to know the carrier lifetime in a-BC:H films.

The delamination and shorting of films during electrical testing remained one of the most difficult challenges. Films thicker than 1 μm grown on silicon and conducting transparent substrates at high temperature frequently delaminated. The delamination of the films grown at lower temperatures was believed to be due to high compressive stress in the films based on the observed buckling-based delamination accelerated by humid conditions. However, the delamination pattern of high-temperature films suggested that these films could have high residual tensile stress. Film stress measurements on some films grown at 300–400 °C suggested that there could be a transition of stress from compressive to tensile as we increased the substrate temperature. In an attempt to reduce

the film stress and film delamination, we implemented a ramp-down protocol for substrate cooling rather than simply turning the heater off after film growth. The ramp-down protocol yielded more stable films compared to the previously grown films, however it did not completely solve the delamination problem for thick films. We also experimented with different bottom contact materials and flexible metal foils in an attempt to find materials with matching thermal expansion coefficients to reduce the residual stress. Among many sputtered bottom contact materials (Cu, Al, Ni, Ti/W alloy, ITO, and FTO), we found Ti/W to be the most stable. Among different non-flexible substrate materials, the films grown directly on glass were the most stable. However, electrical characterization of such films was not possible due to the lack of bottom electrical contact. Films grown on flexible metal foils (Al, Cu, Zr, W) were generally stable due to their ability to ‘absorb’ the film stress; the films grown on the copper foil were most stable mechanically as well as electrically. Experimenting with flexible metal foil substrates was one of the most successful experiences in this work. However, the metal foils themselves were not of the highest quality in terms of surface roughness and purity. Continuing exploring flexible metal substrates with varying coefficient of thermal expansion and better surface properties could solve both the film delamination and contact fabrication issues. As films grown at 500 °C were delaminating frequently, we could not test films grown at even higher temperatures. However, the stability of films grown on flexible metal substrates could enable the growth of films at >600 °C

to see if any significant improvement in film properties can be achieved. This work is suggested for the future.

As fabricating proper heterostructure on films grown on transparent substrates was not successful, we investigated methods to produce standalone films by depositing films on other substrates that could be washed off later. Use of washable substrates such as NaCl and copper foil failed: films on NaCl delaminated immediately after removal from the deposition chamber and films grown on copper foil broke during washing, suggesting a very high residual stress in the films even when grown on flexible substrates. Separating low-temperature films grown on glass substrates using a 2% KOH solution was achieved in previous studies; however, this approach did not work for high-temperature films even with a 10% KOH solution. We also investigated preparing pressed pellets of a-BC:H using the a-BC:H flakes prepared by dissolving aluminum from films grown on aluminum foil using HCl solution. However, the obtained pellets were very brittle, possibly due to not enough pressure applied during pellet formation due to the limitation of the pellet die, and quickly oxidized in the atmosphere. Although obtaining standalone films was not successful, fabricating pellets at high pressure and temperature in the future could lead to some important achievements, such as fabricating extremely thick devices with proper electrical contacts.

As obtaining films with consistent and reproducible film properties continued to be challenging, we purchased and installed an MKS 1152 vapor source mass flow

controller in our precursor delivery system with a hypothesis that the inconsistent precursor sublimation might be causing the film properties to vary widely. The vapor source MFC, however, did not solve the problem of inconsistent precursor flow rate due to design problems, and the films grown using the MFC showed an unusual pattern of increasing growth rate with each subsequent film growth. Although we could not extract carrier mobility values for these films, other measured optical and electronic properties suggested that the film growth rate was one key parameter determining the material properties.

As we did not have sufficient time to solve the design problem associated with the vapor source MFC, we returned to the original precursor sublimation system, which consisted of two glass bubblers. However, this time, we regulated the temperatures of all of the heating systems, including the bubblers and carrier lines, using precision PID controllers. The controlled temperature studies revealed that the bubbler temperature and the precursor partial flow were the most dominant factors in determining film growth rate, and the growth rate did not change as a function of growth time until the precursor depleted in the bubbler, which is critical in obtaining thick films by growing for extended period of time. The experiment further revealed that the film growth rate affected film properties, including carrier mobility, more significantly than it was previously believed. Interestingly, the films grown with the controlled precursor delivery system were always consistent with the field-dependent SCLC charge transport. This suggested that the fluctuating bubbler temperature, and thus fluctuating

growth rate during the growth could be interfering with the charge transport mechanism. We observed that the refractive index and the carrier mobility demonstrated an inverted V shaped trend as a function of growth rate with optimum carrier mobility for ~30–50 nm/min of growth rate.

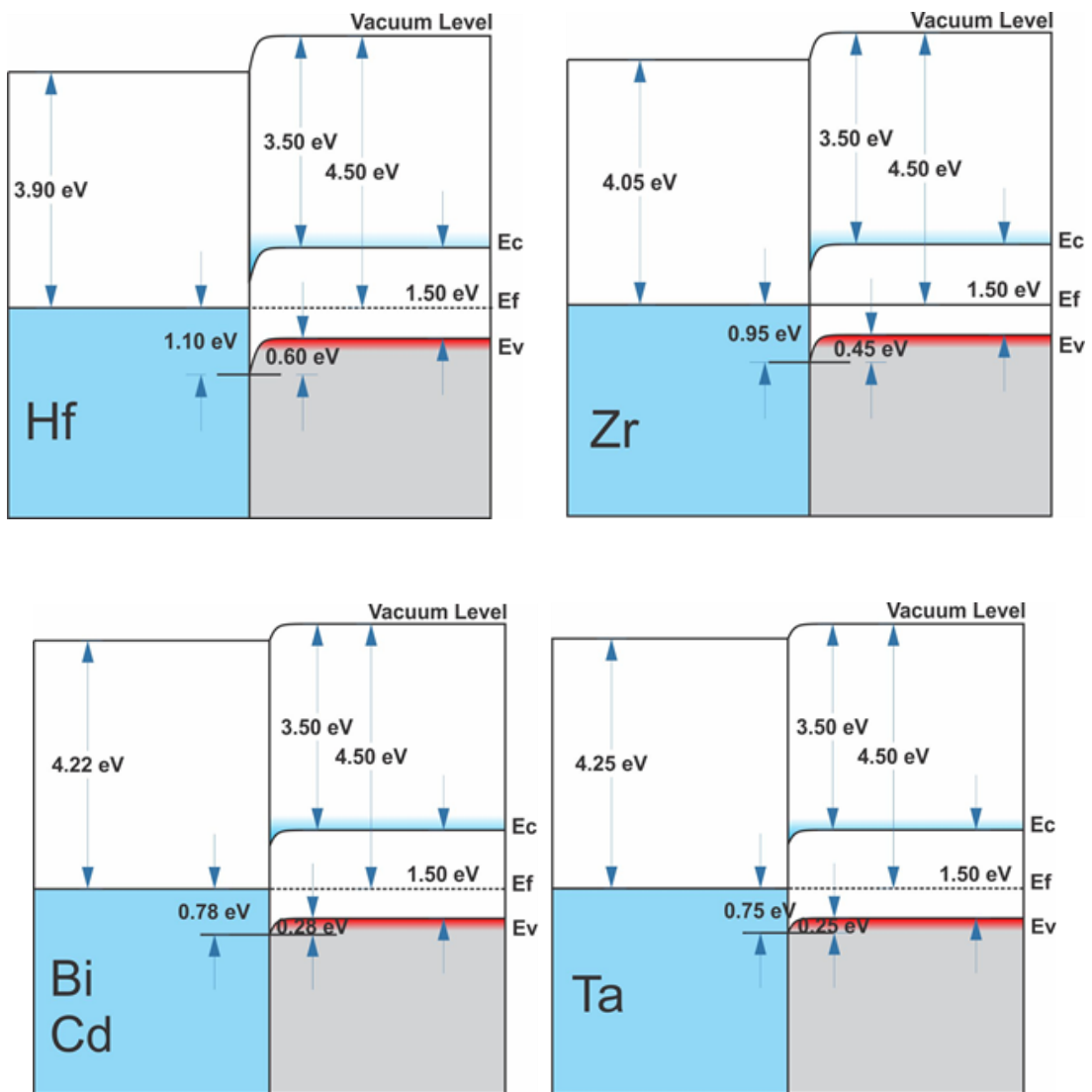
Using the optimized precursor delivery system, and with the knowledge of the target bubbler temperature required to produce a growth rate of 30 nm/min, we deposited films on copper foil as it was the most stable substrate material. We were able to demonstrate a stable ~3 μm a-BC:H device on copper foil, with mobility $8 \times 10^{-6} \text{ cm}^2 \cdot \text{V}^{-1} \cdot \text{s}^{-1}$ and resistivity $\sim 10^{12} \Omega \cdot \text{cm}$. Based on the numerical calculations we performed, the achieved film thickness and carrier mobility suggests that a neutron detector using an integration time of 5 μs or longer is viable if the carrier lifetime is 10 μs . An intrinsic detection efficiency of ~9% is possible for a carrier lifetime of 0.1 ms and longer with appropriate device size and blocking contacts to reduce the leakage current below 1 nA.

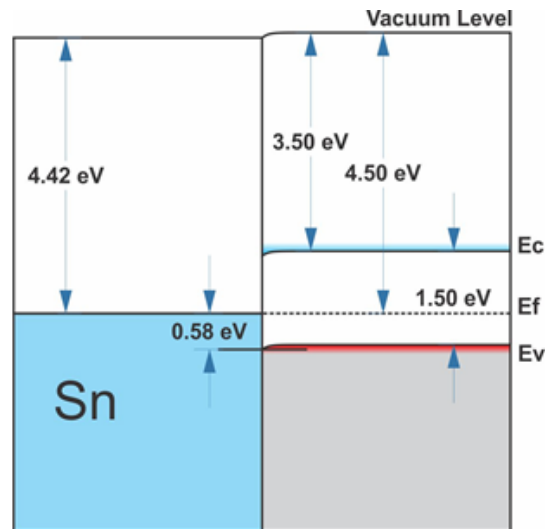
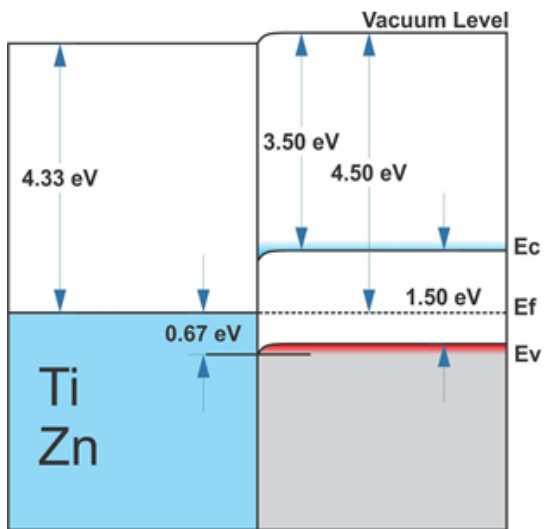
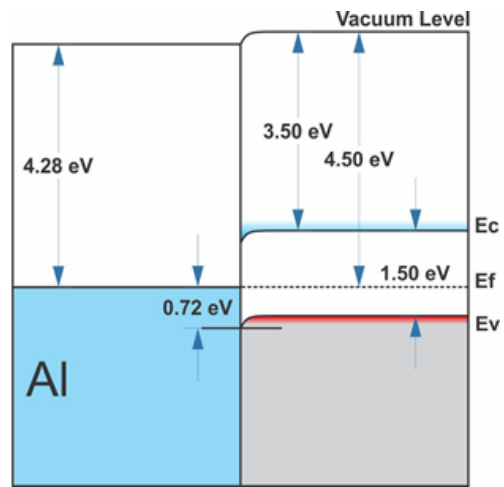
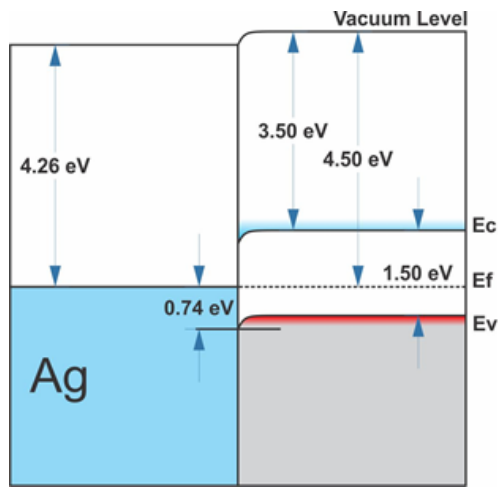
In conclusion, with continuous effort, we solved the poor reproducibility and frequent delamination of films by stabilizing the precursor flow and using flexible metal foils. By investigating the process property relations, we improved the carrier mobility by more than three orders of magnitude. With the values of charge carrier mobility demonstrated in the films deposited on copper foil, fabricating 3–5 μm detectors is possible. The fabrication and testing of a neutron detector, however, could not be completed due to time constraints, and is recommended for the future work. It would be

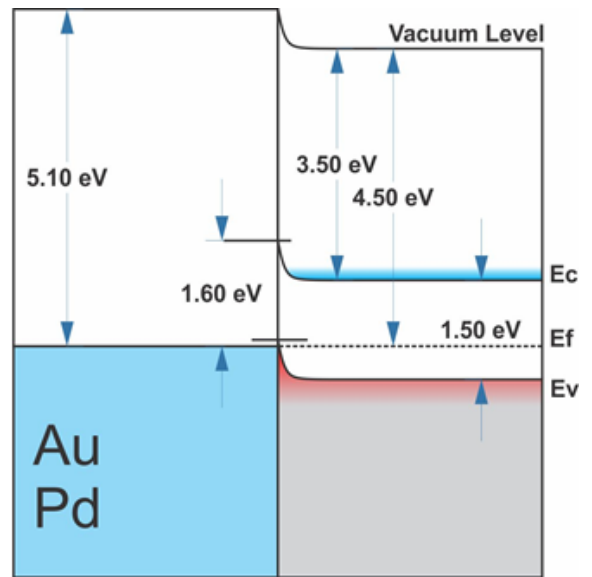
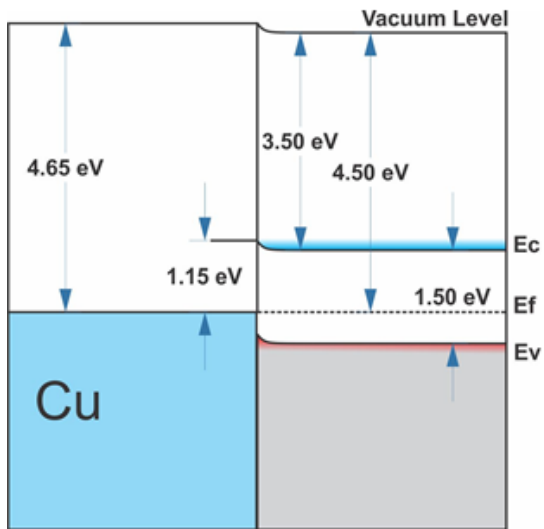
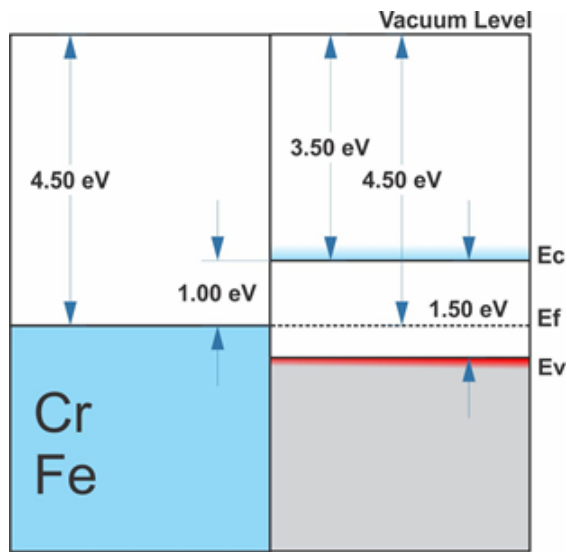
rewarding to see a working and efficient a-BC:H-based thermal neutron detector in the near future.

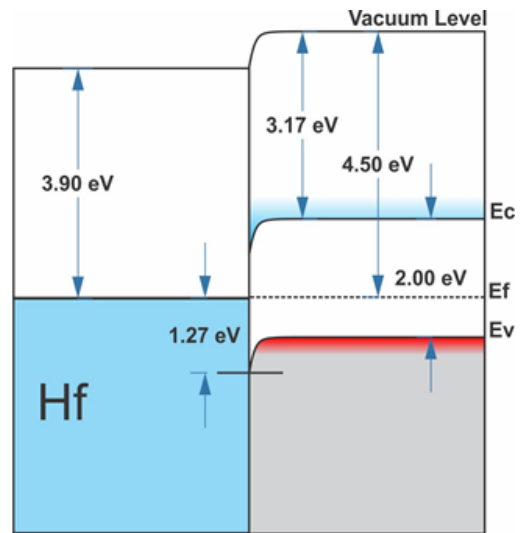
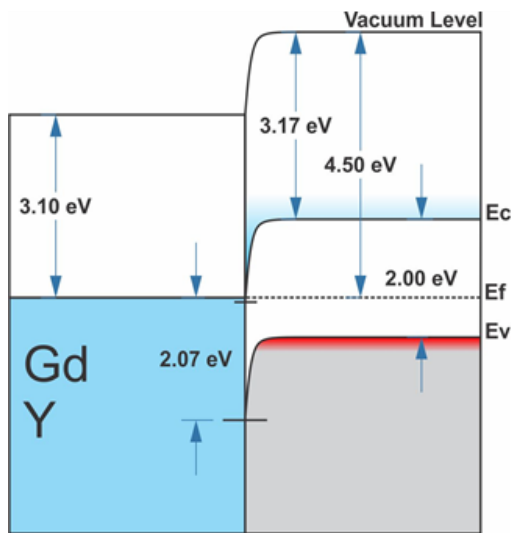
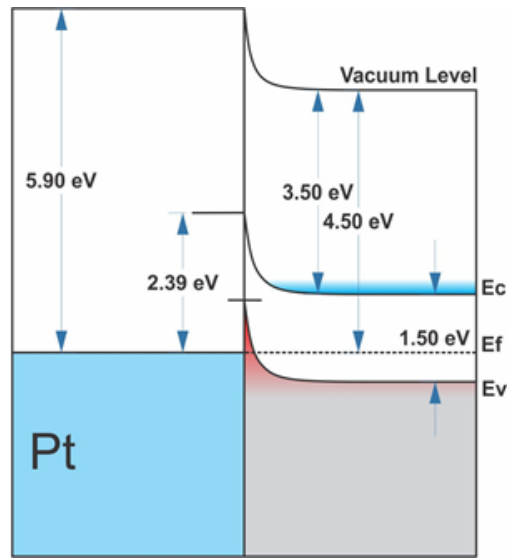
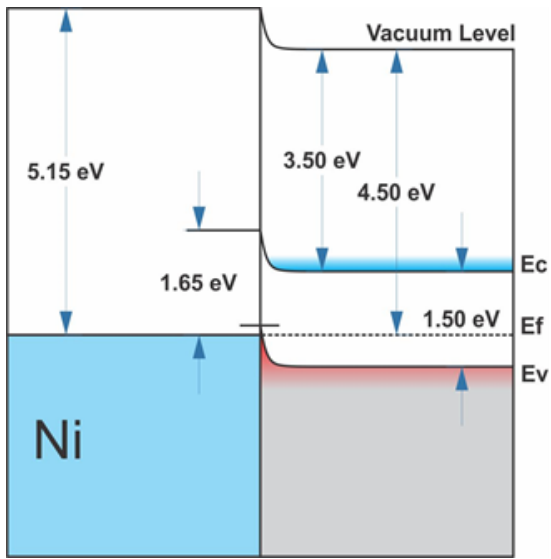
APPENDIX A

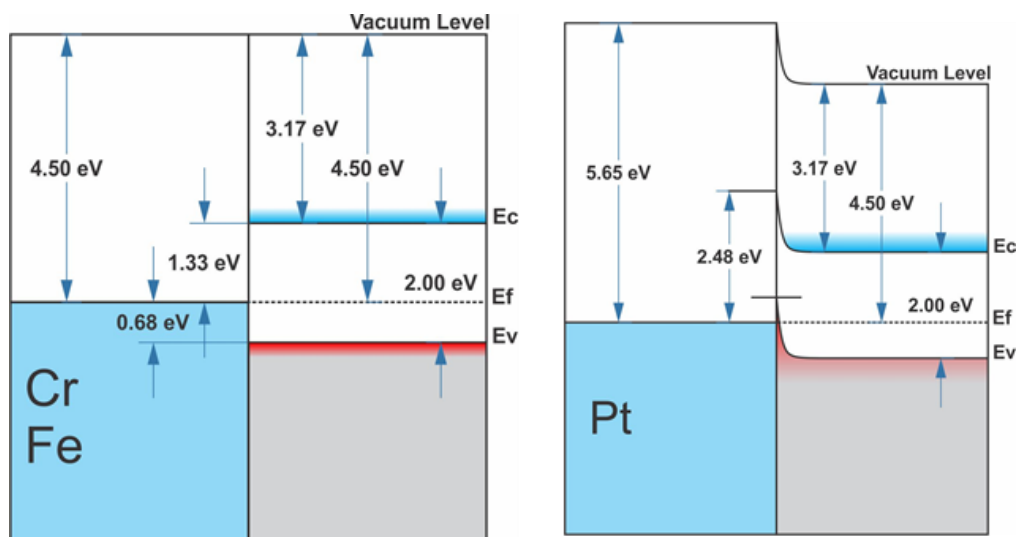
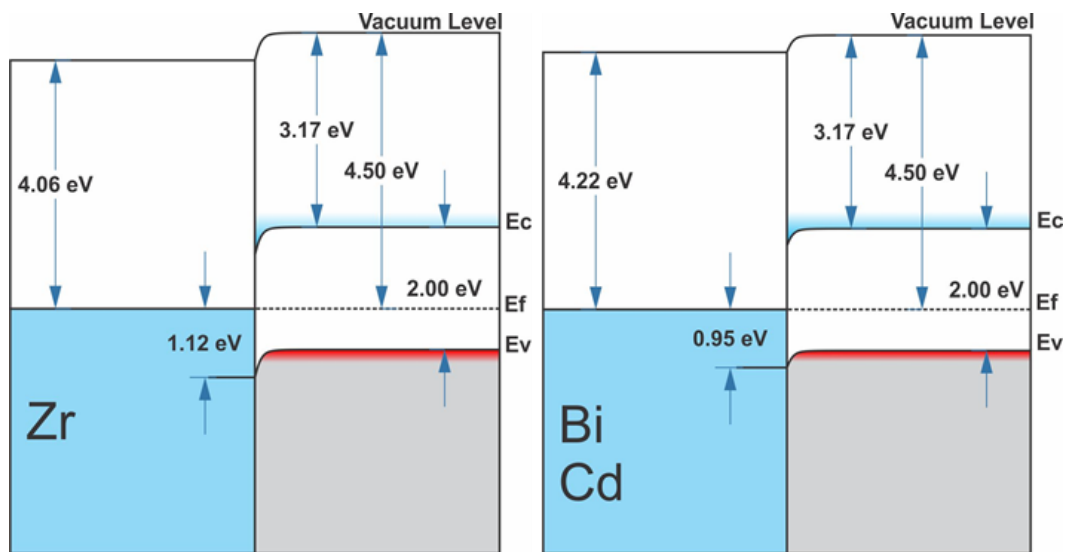
BAND ALIGNMENT OF DIFFERENT METALS WITH AMORPHOUS HYDROGENATED BORON CARBIDE FOR DIFFERENT VALUES OF BANDGAP

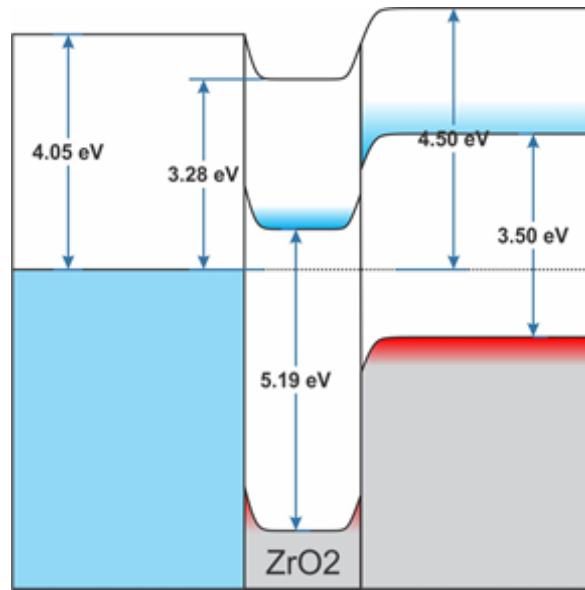












REFERENCES

- [1] T. Cole, *Democritus and the Sources of Greek Anthropology*. Western Reserve University Press, 1967.
- [2] J. Dalton, *A New System of Chemical Philosophy*. Cambridge: Cambridge University Press, 2010.
- [3] J. Chadwick, “The existence of a neutron,” *Proc. R. Soc. London. Ser. A, Contain. Pap. a Math. Phys. Character*, vol. 136, no. 830, pp. 692–708, 1932, doi: 10.1098/rspa.1932.0112.
- [4] S. S. M. Wong, *Introductory Nuclear Physics*, 2nd ed. Weinheim: Wiley-VCH Verlag GmbH & Co. KGaA, 2004.
- [5] *Nuclear Regulatory Legislation 113 th Congress ; Second Session*, vol. 1, no. 11. Washington, DC: Office of the General Counsel, United States Nuclear Regulatory Commission, 2015.
- [6] D. Henzlova *et al.*, “Current Status of Helium-3 Alternative Technologies for Nuclear Safeguards,” Los Alamos, NM (United States), 2015. doi: 10.2172/1227248.
- [7] D. A. Shea and D. Morgan, “The helium-3 shortage: Supply, demand, and options for congress,” 2010.
- [8] “Current status of neutron capture therapy,” International Atomic Energy Agency, Vienna, Austria, 2001.
- [9] M. A. Nagai and G. L. Locher, “The production of mutations in drosophila with

- neutron radiation,” *J. Franklin Inst.*, vol. 228, no. 1, pp. 101–103, 1939, doi: 10.1016/S0016-0032(39)90253-X.
- [10] S.-I. MIYATAKE *et al.*, “Boron Neutron Capture Therapy for Malignant Brain Tumors,” *Neurol. Med. Chir. (Tokyo)*., vol. 56, no. 7, pp. 361–371, 2016, doi: 10.2176/nmc.ra.2015-0297.
- [11] P. Reuss, *Neutron Physics*. Les Ulis Cedex A, France: EDP Sciences, 2008.
- [12] K. T. Bainbridge, “Trinity,” Los Alamos, NM, 1976.
- [13] “The First Reactor,” U.S. Department of Energy, Washington, DC, 1982.
- [14] “Nuclear Power in the World Today,” *World Nuclear Association*, 2020. <https://www.world-nuclear.org/information-library/current-and-future-generation/nuclear-power-in-the-world-today.aspx> (accessed May 21, 2020).
- [15] “ITER ORGANIZATION Annual Report 2018,” 2018. <https://www.iter.org/org/team/odg/comm/annualreports>.
- [16] T. E. Mason, T. J. Gawne, S. E. Nagler, M. B. Nestor, and J. M. Carpenter, “The early development of neutron diffraction: science in the wings of the Manhattan Project,” *Acta Crystallogr. Sect. A Found. Crystallogr.*, vol. 69, no. 1, pp. 37–44, 2013, doi: 10.1107/S0108767312036021.
- [17] M.-L. Mauborgne, F. Allioli, C. Stoller, M. Evans, M. Manclossi, and L. Nicoletti, “Exploring for oil with nuclear physics,” *EPJ Web Conf.*, vol. 146, p. 09009, 2017, doi: 10.1051/epjconf/201714609009.
- [18] “Gamma, X ray and Neutron Techniques for the Coal Industry,” in *Panel*

Proceedings Series - International Atomic Energy Agency, 1986, p. 232.

- [19] M. Strobl, *Neutron Imaging and Applications*. Boston, MA: Springer US, 2009.
- [20] E. Lehmann, P. Trtik, and D. Ridikas, “Status and Perspectives of Neutron Imaging Facilities,” *Phys. Procedia*, vol. 88, no. September 2016, pp. 140–147, 2017, doi: 10.1016/j.phpro.2017.06.019.
- [21] A. N. Caruso, “The physics of solid-state neutron detector materials and geometries,” *J. Phys. Condens. Matter*, vol. 22, no. 44, p. 443201, 2010, doi: 10.1088/0953-8984/22/44/443201.
- [22] W. C. Feldman, “Global Distribution of Neutrons from Mars: Results from Mars Odyssey,” *Science*, vol. 297, no. 5578, pp. 75–78, 2002, doi: 10.1126/science.1073541.
- [23] E. Drolle *et al.*, “Effect of melatonin and cholesterol on the structure of DOPC and DPPC membranes,” *Biochim. Biophys. Acta - Biomembr.*, vol. 1828, no. 9, pp. 2247–2254, 2013, doi: 10.1016/j.bbamem.2013.05.015.
- [24] J. D. Nickels *et al.*, “Dynamics of protein and its hydration water: Neutron scattering studies on fully deuterated GFP,” *Biophys. J.*, vol. 103, no. 7, pp. 1566–1575, 2012, doi: 10.1016/j.bpj.2012.08.046.
- [25] V. Valkovic, *14 MeV Neutrons*. New York: CRC Press, 2015.
- [26] T. L. Yap *et al.*, “Structural features of membrane-bound glucocerebrosidase and α -synuclein probed by neutron reflectometry and fluorescence spectroscopy,” *J. Biol. Chem.*, vol. 290, no. 2, pp. 744–754, 2015,

doi: 10.1074/jbc.M114.610584.

- [27] U. R. Shrestha *et al.*, “Generation of the configurational ensemble of an intrinsically disordered protein from unbiased molecular dynamics simulation,” *Proc. Natl. Acad. Sci. U. S. A.*, vol. 116, no. 41, pp. 20446–20452, 2019, doi: 10.1073/pnas.1907251116.
- [28] Z. B. Alfassi and C. Chung, Eds., *Prompt Gamma Neutron Activation Analysis*. Boca Raton, FL: CRC Press, 1995.
- [29] “Tritium Production,” Washington, DC, 2005.
<https://www.nrc.gov/docs/ML0325/ML032521359.pdf>.
- [30] S. Fain, M. L. Schiebler, D. G. McCormack, and G. Parraga, “Imaging of lung function using hyperpolarized helium-3 magnetic resonance imaging: Review of current and emerging translational methods and applications,” *J. Magn. Reson. Imaging*, vol. 32, no. 6, pp. 1398–1408, 2010, doi: 10.1002/jmri.22375.
- [31] A. . Shvets, “The use of liquid helium-3 to obtain temperatures down to 0.3° K,” *Cryogenics*, vol. 6, no. 6, pp. 333–337, 1966, doi: 10.1016/0011-2275(66)90130-5.
- [32] W. J. Huiskamp and O. V Lounasmaa, “Ultralow temperatures-how and why,” *Reports Prog. Phys.*, vol. 36, no. 4, pp. 423–496, 1973, doi: 10.1088/0034-4885/36/4/002.
- [33] D. Kramer, “For some, helium-3 supply picture is brightening,” *Phys. Today*, vol. 64, no. 5, pp. 20–22, 2011, doi: 10.1063/1.3591998.

- [34] R. T. Kouzes *et al.*, “Neutron detection alternatives to ^3He for national security applications,” *Nucl. Instruments Methods Phys. Res. Sect. A Accel. Spectrometers, Detect. Assoc. Equip.*, vol. 623, no. 3, pp. 1035–1045, 2010, doi: 10.1016/j.nima.2010.08.021.
- [35] T. Wilpert, “Boron trifluoride detectors,” *Neutron News*, vol. 23, no. 4, pp. 14–19, 2012, doi: 10.1080/10448632.2012.725326.
- [36] G. Gervino *et al.*, “Preliminary results of a new boron coated neutron detector,” *Nucl. Instruments Methods Phys. Res. Sect. A*, vol. 718, pp. 143–144, 2013, doi: 10.1016/j.nima.2012.08.092.
- [37] S. Mukhopadhyay, R. Maurer, P. Guss, and C. Kruschwitz, “Review of current neutron detection systems for emergency response,” vol. 9213, p. 92130T, 2014, doi: 10.1117/12.2058165.
- [38] P. Vontobel, E. H. Lehmann, R. Hassanein, and G. Frei, “Neutron tomography: Method and applications,” *Phys. B Condens. Matter*, vol. 385-386 I, pp. 475–480, 2006, doi: 10.1016/j.physb.2006.05.252.
- [39] F. Pfeiffer, C. Grünzweig, O. Bunk, G. Frei, E. Lehmann, and C. David, “Neutron phase imaging and tomography,” *Phys. Rev. Lett.*, vol. 96, no. 21, pp. 1–4, 2006, doi: 10.1103/PhysRevLett.96.215505.
- [40] R. Hassanein, H. O. Meyer, A. Carminati, M. Estermann, E. Lehmann, and P. Vontobel, “Investigation of water imbibition in porous stone by thermal neutron radiography,” *J. Phys. D. Appl. Phys.*, vol. 39, no. 19, pp. 4284–4291, 2006,

doi: 10.1088/0022-3727/39/19/023.

- [41] B. Schillinger and E. Lehmann, “Scientific Reviews: Detectors for Neutron Imaging,” *Neutron News*, vol. 17, no. 1, pp. 19–21, 2006, doi: 10.1080/10448630500517613.
- [42] S. Chong *et al.*, “High Data-Rate Neutron-Sensitive Pixelated Detector Using Silicon Photomultiplier,” in *2019 IEEE Nuclear Science Symposium and Medical Imaging Conference (NSS/MIC)*, 2019, pp. 1–4, doi: 10.1109/NSS/MIC42101.2019.9059763.
- [43] N. . Rhodes, A. . Wardle, A. . Boram, and M. . Johnson, “Pixelated neutron scintillation detectors using fibre optic coded arrays,” *Nucl. Instruments Methods Phys. Res. Sect. A Accel. Spectrometers, Detect. Assoc. Equip.*, vol. 392, no. 1–3, pp. 315–318, 1997, doi: 10.1016/S0168-9002(97)00261-1.
- [44] M. Ishikawa *et al.*, “Development of real-time thermal neutron monitor using boron-loaded plastic scintillator with optical fiber for boron neutron capture therapy,” *Appl. Radiat. Isot.*, vol. 61, no. 5, pp. 775–779, 2004, doi: 10.1016/j.apradiso.2004.05.053.
- [45] M. N. H. Comsan, “Spallation Neutron Sources for Science and Technology,” in *8th conference on Nuclear and Particle Physics*, 2011, pp. 9–22.
- [46] H. Wellker, “Semiconductor devices and methods of their manufacture,” Patent, US2798989A, 1957.
- [47] Y. Kumashiro, “Refractory semiconductor of boron phosphide,” *J. Mater. Res.*,

- vol. 5, no. 12, pp. 2933–2947, 1990, doi: 10.1557/JMR.1990.2933.
- [48] Y. Kumashiro and Y. Okada, “Schottky barrier diodes using thick, well-characterized boron phosphide wafers,” *Appl. Phys. Lett.*, vol. 47, no. 1, pp. 64–66, 1985, doi: 10.1063/1.96406.
- [49] M. A. McKay, J. Li, J. Y. Lin, and H. X. Jiang, “Anisotropic index of refraction and structural properties of hexagonal boron nitride epilayers probed by spectroscopic ellipsometry,” *J. Appl. Phys.*, vol. 127, no. 5, pp. 1–7, 2020, doi: 10.1063/1.5134908.
- [50] A. Maity, S. J. Grenadier, J. Li, J. Y. Lin, and H. X. Jiang, “Hexagonal boron nitride neutron detectors with high detection efficiencies,” *J. Appl. Phys.*, vol. 123, no. 4, 2018, doi: 10.1063/1.5017979.
- [51] A. Maity, S. J. Grenadier, J. Li, J. Y. Lin, and H. X. Jiang, “Toward achieving flexible and high sensitivity hexagonal boron nitride neutron detectors,” *Appl. Phys. Lett.*, vol. 111, no. 3, pp. 1–5, 2017, doi: 10.1063/1.4995399.
- [52] T. C. Doan, J. Li, J. Y. Lin, and H. X. Jiang, “Growth and device processing of hexagonal boron nitride epilayers for thermal neutron and deep ultraviolet detectors,” *AIP Adv.*, vol. 6, no. 7, p. 075213, 2016, doi: 10.1063/1.4959595.
- [53] T. C. Doan, J. Li, J. Y. Lin, and H. X. Jiang, “Charge carrier transport properties in layer structured hexagonal boron nitride,” *AIP Adv.*, vol. 4, no. 10, p. 107126, 2014, doi: 10.1063/1.4898630.
- [54] D. McGregor, T. C. Unruh, and W. J. McNeil, “Thermal neutron detection with

- pyrolytic boron nitride,” *Nucl. Instruments Methods Phys. Res. Sect. A Accel. Spectrometers, Detect. Assoc. Equip.*, vol. 591, no. 3, pp. 530–533, 2008, doi: 10.1016/j.nima.2008.03.002.
- [55] A. Mayo *et al.*, “Semiconducting icosahedral boron arsenide crystal growth for neutron detection,” *J. Cryst. Growth*, vol. 318, no. 1, pp. 553–557, 2010, doi: 10.1016/j.jcrysgr.2010.10.057.
- [56] C. E. Whiteley *et al.*, “Semiconducting icosahedral boron arsenide crystal growth for neutron detection,” *J. Cryst. Growth*, vol. 318, no. 1, pp. 553–557, 2011, doi: 10.1016/j.jcrysgr.2010.10.057.
- [57] R. Gul *et al.*, “Photocurrent response of B₁₂As₂ crystals to blue light, and its temperature-dependent electrical characterizations,” *AIP Adv.*, vol. 6, no. 2, p. 025206, 2016, doi: 10.1063/1.4941937.
- [58] A. Kargar, J. Tower, L. Cirignano, and K. Shah, “Boron selenide semiconductor detectors for thermal neutron counting,” in *Proc. SPIE 8852, Hard X-Ray, Gamma-Ray, and Neutron Detector Physics XV, 88521M*, 2013, p. 88521M, doi: 10.1117/12.2027078.
- [59] A. Kargar, J. Tower, H. Hong, L. Cirignano, W. Higgins, and K. Shah, “Lithium and boron based semiconductors for thermal neutron counting,” in *Proc. SPIE 8142, Hard X-Ray, Gamma-Ray, and Neutron Detector Physics XIII, 81421P*, 2011, p. 81421P, doi: 10.1117/12.899363.
- [60] A. D. Harken, E. E. Day, B. W. Robertson, and S. Adenwalla, “Boron-Rich

- Semiconducting Boron Carbide Neutron Detector,” *Jpn. J. Appl. Phys.*, vol. 44, no. No. 1A, pp. 444–445, 2005, doi: 10.1143/JJAP.44.444.
- [61] A. N. Caruso *et al.*, “The all boron carbide diode neutron detector: Comparison with theory,” *Mater. Sci. Eng. B*, vol. 135, no. 2, pp. 129–133, 2006, doi: 10.1016/j.mseb.2006.08.049.
- [62] C. Tan *et al.*, “Characterization of a boron carbide-based polymer neutron sensor,” *Nucl. Instruments Methods Phys. Res. Sect. A Accel. Spectrometers, Detect. Assoc. Equip.*, vol. 803, pp. 82–88, 2015, doi: 10.1016/j.nima.2015.09.031.
- [63] R. Bao, Z. Yan, and D. B. Chrisey, “Charge carrier lifetime in boron carbide thin films,” *Appl. Phys. Lett.*, vol. 98, no. 19, p. 192106, 2011, doi: 10.1063/1.3589816.
- [64] A. D. Harken, C. N. Lundstedt, E. E. Day, and B. W. Robertson, “Neutron Detection Efficiency and Capture Product Energy Spectra of All-Semiconducting Boron Carbide and Conversion-Layer Detectors,” *IEEE*, pp. 4585–4589, 2004.
- [65] P. B. Welsch, “Boron Carbide Films and Diodes : Electrical Characterization and Neutron Detection by Boron,” Masters Thesis, University of Nebraska, 2002.
- [66] N. Hong, L. Crow, and S. Adenwalla, “Time-of-flight neutron detection using PECVD grown boron carbide diode detector,” *Nucl. Instruments Methods Phys.*

- Res. Sect. A Accel. Spectrometers, Detect. Assoc. Equip.*, vol. 708, pp. 19–23, 2013, doi: 10.1016/j.nima.2012.12.105.
- [67] A. N. Caruso, P. A. Dowben, and J. I. Brand, “Boron carbide particle detectors,” Patent, US7368794 B2, 2008.
- [68] K. Osberg *et al.*, “A Handheld Neutron-Detection Sensor System Utilizing a New Class of Boron Carbide Diode,” *IEEE Sens. J.*, vol. 6, no. 6, pp. 1531–1538, 2006, doi: 10.1109/JSEN.2006.883905.
- [69] N. Hong, J. Mullins, K. Foreman, and S. Adenwalla, “Boron carbide based solid state neutron detectors: the effects of bias and time constant on detection efficiency,” *J. Phys. D. Appl. Phys.*, vol. 43, no. 27, p. 275101, 2010, doi: 10.1088/0022-3727/43/27/275101.
- [70] E. Echeverria *et al.*, “Semiconducting boron carbides with better charge extraction through the addition of pyridine moieties,” *J. Phys. D. Appl. Phys.*, vol. 49, no. 35, p. 355302, 2016, doi: 10.1088/0022-3727/49/35/355302.
- [71] C. Lundstedt, A. Harken, E. Day, B. Robertson, and S. Adenwalla, “Modeling solid-state boron carbide low energy neutron detectors,” *Nucl. Instruments Methods Phys. Res. Sect. A Accel. Spectrometers, Detect. Assoc. Equip.*, vol. 562, no. 1, pp. 380–388, 2006, doi: 10.1016/j.nima.2006.02.148.
- [72] A. Maity, S. J. Grenadier, J. Li, J. Y. Lin, and H. X. Jiang, “High sensitivity hexagonal boron nitride lateral neutron detectors,” *Appl. Phys. Lett.*, vol. 114, no. 22, pp. 8–11, 2019, doi: 10.1063/1.5098331.

- [73] J. E. Proctor *et al.*, “Stabilization of boron carbide via silicon doping,” *J. Phys. Condens. Matter*, vol. 27, no. 1, p. 015401, 2015, doi: 10.1088/0953-8984/27/1/015401.
- [74] K. Y. Xie *et al.*, “Breaking the icosahedra in boron carbide,” *Proc. Natl. Acad. Sci.*, vol. 113, no. 43, pp. 12012–12016, 2016, doi: 10.1073/pnas.1607980113.
- [75] V. Domnich, S. Reynaud, R. A. Haber, and M. Chhowalla, “Boron Carbide: Structure, Properties, and Stability under Stress,” *J. Am. Ceram. Soc.*, vol. 94, no. 11, pp. 3605–3628, 2011, doi: 10.1111/j.1551-2916.2011.04865.x.
- [76] J. Mazurowski, S. Baral-Tosh, G. Ramseyer, J. T. Spencer, Y.-G. Kim, and P. a. Dowben, “Novel Methods for Deposition of Boron Carbide Films,” *MRS Proc.*, vol. 190, 1990, doi: 10.1557/PROC-190-101.
- [77] S. Lee, J. Mazurowski, G. Ramseyer, and P. A. Dowben, “Characterization of boron carbide thin films fabricated by plasma enhanced chemical vapor deposition from boranes,” *J. Appl. Phys.*, vol. 72, no. 10, pp. 4925–4933, 1992, doi: 10.1063/1.352060.
- [78] I. J. T. Spencer, A. Peter, and Y. G. Kim, “Deposition of Boron-containing films from decaborane,” Patent, US4957773, 1990.
- [79] F. K. Perkins, M. Onellion, S. Lee, D. Li, J. Mazurowski, and P. a. Dowben, “Synchrotron-radiation-induced deposition of boron and boron carbide films from boranes and carboranes II: Nido-2,3-diethyl-2,3-dicarba-hexaborane,” *Appl. Phys. A Solids Surfaces*, vol. 54, no. 5, pp. 442–450, 1992,

doi: 10.1007/BF00324169.

- [80] Y. G. Kim, P. A. Dowben, J. T. Spencer, and G. O. Ramseyer, "Chemical vapor deposition of boron and boron nitride from decaborane(14)," *J. Vac. Sci. Technol. A Vacuum, Surfaces, Film.*, vol. 7, no. 4, pp. 2796–2799, 1989, doi: 10.1116/1.576181.
- [81] D. Byun, B. R. Spady, N. J. Ianno, and P. A. Dowben, "Comparison of different chemical vapor deposition methodologies for the fabrication of heterojunction boron-carbide diodes," *Nanostructured Mater.*, vol. 5, no. 4, pp. 465–471, 1995.
- [82] S. Lee *et al.*, "The structural homogeneity of boron carbide thin films fabricated plasma-enhanced chemical vapor deposition from B₅H₉ +CH₄," *J. Appl. Phys.*, vol. 74, no. 11, pp. 6919–6924, 1993, doi: 10.1063/1.355066
- [83] S. D. Hwang, D. Byun, N. J. Ianno, P. A. Dowben, and H. R. Kim, "Fabrication of boron-carbide/boron heterojunction devices," *Appl. Phys. Lett.*, vol. 68, no. 11, pp. 1495–1497, 1996, doi: 10.1063/1.116266.
- [84] S. Lee, P. A. Dowben, A. T. Wen, A. P. Hitchcock, J. A. J. Glass, and J. T. Spencer, "Structures of selected boranes and carboranes," *J. Vac. Sci. Technol. A Vacuum, Surfaces, Film.*, vol. 10, no. 4, p. 881, 1992, doi: 10.1116/1.577688.
- [85] Sunwoo Lee and P. A. Dowben, "The Properties of Boron Carbide/Silicon Heterojunction Diodes Fabricated by Plasma-Enhanced Chemical Vapor

- Deposition,” *Appl. Phys. A*, vol. 58, no. 3, pp. 223–227, 1994,
doi: 10.1007/BF00324380.
- [86] P. A. Dowben, “Forming B_{1-x}C_x Semiconductor Devices By Chemical Vapor Deposition,” 5468978, 1995.
- [87] A. A. Ahmad, N. J. Ianno, S.-D. Hwang, and P. A. Dowben, “Sputter deposition of high resistivity boron carbide,” *Thin Solid Films*, vol. 335, no. 1–2, pp. 174–177, 1998, doi: 10.1016/S0040-6090(98)00876-1.
- [88] B. W. Robertson *et al.*, “A class of boron-rich solid-state neutron detectors,” *Appl. Phys. Lett.*, vol. 80, no. 19, pp. 3644–3646, 2002,
doi: 10.1063/1.1477942.
- [89] D. McGregor and J. K. Shultis, “Spectral identification of thin-film-coated and solid-form semiconductor neutron detectors,” *Nucl. Instruments Methods Phys. Res. Sect. A Accel. Spectrometers, Detect. Assoc. Equip.*, vol. 517, no. 1–3, pp. 180–188, 2004, doi: 10.1016/j.nima.2003.09.037.
- [90] S. Hallbeck *et al.*, “Comment on ‘Spectral identification of thin film coated and solid form semiconductor neutron detectors’ by McGregor and Shultis,” *Nucl. Instruments Methods Phys. Res. Sect. A Accel. Spectrometers, Detect. Assoc. Equip.*, vol. 536, no. 1–2, pp. 228–231, 2005,
doi: 10.1016/j.nima.2004.07.210.
- [91] D. McGregor and J. Shultis, “Response to the ‘Comment’ by S. Hallbeck *et al.*,” *Nucl. Instruments Methods Phys. Res. Sect. A Accel. Spectrometers, Detect.*

- Assoc. Equip.*, vol. 536, no. 1–2, pp. 232–234, 2005,
doi: 10.1016/j.nima.2004.08.128.
- [92] E. E. Day, “Boron Carbide Devices for Neutron Detection Applications,” Ph.D Dissertation, University of Nebraska, 2006.
- [93] B. J. Nordell *et al.*, “The Influence of Hydrogen on the Chemical, Mechanical, Optical/Electronic, and Electrical Transport Properties of Amorphous Hydrogenated Boron Carbide,” *J. Appl. Phys.*, vol. 118, p. 035703, 2015,
doi: 10.1063/1.4927037.
- [94] B. J. Nordell *et al.*, “Carbon-Enriched Amorphous Hydrogenated Boron Carbide Films for Very-Low-k Interlayer Dielectrics,” *Adv. Electron. Mater.*, vol. 3, no. 12, p. 1700116, 2017, doi: 10.1002/aelm.201700116.
- [95] B. J. Nordell *et al.*, “Tuning the Properties of a Complex Disordered Material: Full Factorial Investigation of PECVD-Grown Amorphous Hydrogenated Boron Carbide,” *Mater. Chem. Phys.*, vol. 173, pp. 268–284, 2016,
doi: 10.1016/j.matchemphys.2016.02.013.
- [96] “Evaluated Nuclear Data File (ENDF).”
<https://www-nds.iaea.org/exfor/endl.htm> (accessed May 21, 2021).
- [97] G. F. Knoll, *Radiation Detection and Measurement*, 4th ed. John Wiley & Sons Inc., 2010.
- [98] G. T. Miller and S. E. Spoolman, *Living in the environment: Concepts, Connections, and Solutions*, 16th ed. Belmont, CA: Brooks/Cole, Cengage

Learning, 2009.

- [99] W. M. Deuchars and G. P. Lawrence, “Interaction of 14-MeV. Neutrons with a silicon semiconductor nuclear particle detector,” *Nature*, vol. 191, no. 4792, p. 995, 1961, doi: 10.1038/191995a0.
- [100] B. Abi *et al.*, “First results on ProtoDUNE-SP liquid argon time projection chamber performance from a beam test at the CERN Neutrino Platform,” *J. Instrum.*, vol. 15, no. 12, pp. P12004–P12004, 2020, doi: 10.1088/1748-0221/15/12/P12004.
- [101] C. L. Cowan, F. Reines, F. B. Harrison, H. W. Kruse, and A. D. McGuire, “Detection of the free neutrino: A confirmation,” *Science (80-.)*, vol. 124, no. 3212, pp. 103–104, 1956, doi: 10.1126/science.124.3212.103.
- [102] R. L. Bramblett, R. I. Ewing, and T. W. Bonner, “A new type of neutron spectrometer,” *Nucl. Instruments Methods*, vol. 9, no. 1, pp. 1–12, 1960, doi: 10.1016/0029-554X(60)90043-4.
- [103] A. Esposito and M. Nandy, “Measurement and unfolding of neutron spectra using Bonner spheres,” *Radiat. Prot. Dosimetry*, vol. 110, no. 1–4, pp. 555–558, 2004, doi: 10.1093/rpd/nch385.
- [104] K. G. McKay, “A. Germanium Counter,” *Phys. Rev.*, vol. 76, no. 10, pp. 1537–1537, 1949, doi: 10.1103/PhysRev.76.1537.
- [105] C. Petrillo, F. Sacchetti, O. Toker, and N. J. Rhodes, “Solid state neutron detectors,” *Nucl. Instruments Methods Phys. Res. Sect. A Accel. Spectrometers*,

- Detect. Assoc. Equip.*, vol. 378, no. 3, pp. 541–551, 1996,
doi: 10.1016/0168-9002(96)00487-1.
- [106] F. Foulon, P. Bergonzo, A. Brambilla, C. Jany, B. Guizard, and R. D. Marshall,
“Neutron Detectors Made From Chemically Vapour Deposited
Semiconductors,” *MRS Proc.*, vol. 487, p. 591, 1997,
doi: 10.1557/PROC-487-591.
- [107] J. K. Shultis and D. S. McGregor, “Efficiencies of coated and perforated
semiconductor neutron detectors,” *IEEE Trans. Nucl. Sci.*, vol. 53, no. 3, pp.
1659–1665, 2006, doi: 10.1109/TNS.2006.872639.
- [108] D. S. McGregor, M. D. Hammig, Y. H. Yang, H. K. Gersch, and R. T. Klann,
“Design considerations for thin film coated semiconductor thermal neutron
detectors - I: Basics regarding alpha particle emitting neutron reactive films,”
*Nucl. Instruments Methods Phys. Res. Sect. A Accel. Spectrometers, Detect.
Assoc. Equip.*, vol. 500, no. 1–3, pp. 272–308, 2003,
doi: 10.1016/S0168-9002(02)02078-8.
- [109] D. S. McGregor, W. J. McNeil, S. L. Bellinger, T. C. Unruh, and J. K. Shultis,
“Microstructured semiconductor neutron detectors,” *Nucl. Instruments Methods
Phys. Res. Sect. A Accel. Spectrometers, Detect. Assoc. Equip.*, vol. 608, no. 1,
pp. 125–131, 2009, doi: 10.1016/j.nima.2009.06.031.
- [110] S. L. Bellinger, R. G. Fronk, W. J. McNeil, T. J. Sobering, and D. S. McGregor,
“Improved High Efficiency Stacked Microstructured Neutron Detectors

- Backfilled With Nanoparticle LiF ,” *IEEE Trans. Nucl. Sci.*, vol. 59, no. 1, pp. 167–173, 2012, doi: 10.1109/TNS.2011.2175749.
- [111] S. L. Bellinger, R. G. Fronk, D. S. McGregor, and T. J. Sobering, “Arrayed High Efficiency Dual-Integrated Microstructured Semiconductor Neutron Detectors,” *2011 IEEE Nucl. Sci. Symp. Conf. Rec.*, no. 110, pp. 1281–1284, 2011.
- [112] S. L. Bellinger, R. G. Fronk, T. J. Sobering, and D. S. McGregor, “High-efficiency microstructured semiconductor neutron detectors that are arrayed, dual-integrated, and stacked,” *Appl. Radiat. Isot.*, vol. 70, no. 7, pp. 1121–4, 2012, doi: 10.1016/j.apradiso.2012.01.013.
- [113] D. S. McGregor, S. L. Bellinger, and J. K. Shultis, “Present status of microstructured semiconductor neutron detectors,” *J. Cryst. Growth*, vol. 379, pp. 99–110, 2013, doi: 10.1016/j.jcrysgr.2012.10.061.
- [114] J. K. Shultis and D. S. McGregor, “Design and performance considerations for perforated semiconductor thermal-neutron detectors,” *Nucl. Instruments Methods Phys. Res. Sect. A*, vol. 606, no. 3, pp. 608–636, 2009, doi: 10.1016/j.nima.2009.02.033.
- [115] N. LiCausi, J. Dingley, Y. Danon, J.-Q. Lu, and I. B. Bhat, “A novel solid state self-powered neutron detector,” *Hard X-Ray, Gamma-Ray, Neutron Detect. Phys. X*, vol. 7079, p. 707908, 2008, doi: 10.1117/12.797036.
- [116] Radiation Detection Technologies Inc, “Radiation Detection Technologies,

Inc.,” *MSND Technology*. https://www.radectech.com/msnd_technology
(accessed May 22, 2020).

- [117] Z. Li, “Radiation HardnesdTolerance of Si Sensors / Detectors for Nuclear and High Energy Physics Experiments,” *Energy*, vol. c, pp. 9–12, 2002.
- [118] T. Angelescu *et al.*, “Radiation hardness studies on silicon detectors in fast neutron fields,” *Nucl. Inst. Methods Phys. Res. A*, vol. 357, no. 1, pp. 55–63, 1995, doi: 10.1016/0168-9002(94)01534-1.
- [119] A. Maity, T. C. Doan, J. Li, J. Y. Lin, and H. X. Jiang, “Realization of highly efficient hexagonal boron nitride neutron detectors,” *Appl. Phys. Lett.*, vol. 109, no. 7, p. 072101, 2016, doi: 10.1063/1.4960522.
- [120] D. G. Chica *et al.*, “Direct thermal neutron detection by the 2D semiconductor ${}^6\text{LiInP}_2\text{Se}_6$,” *Nature*, vol. 577, no. 7790, pp. 346–349, 2020, doi: 10.1038/s41586-019-1886-8.
- [121] R. C. Chittick, J. H. Alexander, and H. F. Sterling, “The Preparation and Properties of Amorphous Silicon,” *J. Electrochem. Soc.*, vol. 116, no. 1, p. 77, 1969, doi: 10.1149/1.2411779.
- [122] D. E. Carlson and C. R. Wronski, “Amorphous silicon solar cell,” *Appl. Phys. Lett.*, vol. 28, no. 11, pp. 671–673, 1976, doi: 10.1063/1.88617.
- [123] D. E. Carlson, “Factors influencing the efficiency of amorphous silicon solar cells,” *J. Non. Cryst. Solids*, vol. 35–36, no. PART 2, pp. 707–717, 1980, doi: 10.1016/0022-3093(80)90287-2.

- [124] C. Braganza, S. Vepřek, and P. Groner, "Boron compound protective coatings prepared by means of low pressure plasma CVD," *J. Nucl. Mater.*, vol. 85–86, no. PART 2, pp. 1133–1137, 1979, doi: 10.1016/0022-3115(79)90413-6.
- [125] B. Meyerson and F. W. Smith, "Chemical modification of the electrical properties of hydrogenated amorphous carbon films," *Solid State Commun.*, vol. 34, no. 7, pp. 531–534, 1980, doi: 10.1016/0038-1098(80)90144-1.
- [126] S. Vepřek *et al.*, "Development of plasma CVD and feasibility study of boron carbide in-situ coatings for tokamaks," *J. Nucl. Mater.*, vol. 162–164, pp. 724–731, 1989, doi: 10.1016/0022-3115(89)90353-X.
- [127] B. Meyerson and F. W. Smith, "Thermopower of doped semiconducting hydrogenated amorphous carbon films," *Solid State Commun.*, vol. 41, no. 1, pp. 23–27, 1982, doi: 10.1016/0038-1098(82)90242-3.
- [128] D. N. McIlroy, C. Waldfried, T. McAvoy, J. Choi, P. A. Dowben, and D. Heskett, "The nonmetal to metal transition with alkali doping of films of molecular icosahedra," *Chem. Phys. Lett.*, vol. 264, no. 1–2, pp. 168–173, 1997, doi: 10.1016/S0009-2614(96)01314-0.
- [129] M. M. Abdul-Gader, U. A. Al-Binni, A. A. Ahmad, M. A. Al-Basha, and N. J. Ianno, "Low-field current transport mechanisms in rf magnetron sputter deposited boron carbide (B₅C)/p-type crystalline silicon junctions in the dark," *Int. J. Electron.*, vol. 88, no. 8, pp. 873–901, 2001, doi: 10.1080/00207210110058120.

- [130] H. Kunzli, P. Gantenbein, R. Steiner, and P. Oelhafen, "Deposition and characterization of thin boron-carbide coatings," *Fresenius. J. Anal. Chem.*, vol. 346, no. 1–3, pp. 41–44, 1993, doi: 10.1007/BF00321379.
- [131] A. A. Ahmad, N. J. Ianno, P. G. Snyder, D. Welipitiya, D. Byun, and P. A. Dowben, "Optical properties of boron carbide (B₅C) thin films fabricated by plasma-enhanced chemical-vapor deposition," *J. Appl. Phys.*, vol. 79, no. 11, p. 8643, 1996, doi: 10.1063/1.362487.
- [132] M. Saß, A. Annen, and W. Jacob, "Hydrogen bonding in plasma-deposited amorphous hydrogenated boron films," *J. Appl. Phys.*, vol. 82, no. 4, p. 1905, 1997, doi: 10.1063/1.365997.
- [133] S.-D. Hwang *et al.*, "Fabrication of n-type nickel doped B₅C(1+ δ) homojunction and heterojunction diodes," *Appl. Phys. Lett.*, vol. 70, no. 8, pp. 1028–1030, 1997.
- [134] P. A. Dowben, "Forming B_{1-x}C_x Semiconductor Layers by Chemical Vapor Deposition," Patent, US5658834, 1997.
- [135] S.-D. Hwang, "Nickel doping of boron-carbon alloy films and corresponding Fermi level shifts," *J. Vac. Sci. Technol. A Vacuum, Surfaces, Film.*, vol. 15, no. 3, p. 854, May 1997, doi: 10.1116/1.580720.
- [136] B. Sylvester, S. Lin, and B. J. Feldman, "Doping vs alloying in amorphous hydrogenated boron carbide," *Solid State Commun.*, vol. 93, no. 12, pp. 969–971, 1995, doi: 10.1016/0038-1098(94)00914-7.

- [137] D. N. McIlroy *et al.*, “The incorporation of Nickel and Phosphorus dopants into Boron-Carbon alloy thin films,” *Appl. Phys. A Mater. Sci. Process.*, vol. 67, no. 3, pp. 335–342, 1998, doi: 10.1007/s003390050780.
- [138] S. Adenwalla, P. Welsch, A. Harken, J. I. Brand, A. Sezer, and B. W. Robertson, “Boron carbide/n-silicon carbide heterojunction diodes,” *Appl. Phys. Lett.*, vol. 79, no. 26, pp. 4357–4359, 2001, doi: 10.1063/1.1426257.
- [139] A. N. Caruso, R. B. Billa, S. Balaz, J. I. Brand, and P. A. Dowben, “The heteroisomeric diode,” *J. Phys. Condens. Matter*, vol. 16, no. 10, pp. L139–L146, 2004, doi: 10.1088/0953-8984/16/10/L04.
- [140] P. Lunca-Popa *et al.*, “Evidence for multiple polytypes of semiconducting boron carbide (C2B10) from electronic structure,” *J. Phys. D. Appl. Phys.*, vol. 38, no. 8, pp. 1248–1252, 2005, doi: 10.1088/0022-3727/38/8/023.
- [141] R. B. Billa, T. Hofmann, M. Schubert, and B. W. Robertson, “Annealing effects on the optical properties of semiconducting boron carbide,” *J. Appl. Phys.*, vol. 106, no. 3, p. 033515, 2009, doi: 10.1063/1.3190679.
- [142] N. Hong, M. A. Langell, J. Liu, O. Kizilkaya, and S. Adenwalla, “Ni doping of semiconducting boron carbide,” *J. Appl. Phys.*, vol. 107, no. 2, p. 024513, 2010, doi: 10.1063/1.3284205.
- [143] A. N. Caruso *et al.*, “Surface photovoltage effects on the isomeric semiconductors of boron-carbide,” *Appl. Phys. Lett.*, vol. 84, no. 8, p. 1302, 2004, doi: 10.1063/1.1648136.

- [144] E. Day, M. J. Diaz, and S. Adenwalla, “Effect of bias on neutron detection in thin semiconducting boron carbide films,” *J. Phys. D. Appl. Phys.*, vol. 39, no. 14, pp. 2920–2924, 2006, doi: 10.1088/0022-3727/39/14/007.
- [145] M. M. Abdul-Gader, U. a. Al-Binni, A. A. Ahmad, M. a. Al-Basha, and N. J. Ianno, “Low-field current transpA critical investigation of a-Si:H photoconductivity gort mechanisms in rf magnetron sputter deposited boron carbide (B5C)/p-type crystalline silicon junctions in the dark,” *Int. J. Electron.*, vol. 88, no. 8, pp. 873–901, 2001, doi: 10.1080/00207210110058120.
- [146] D. Zhang, D. N. McIlroy, W. L. O’Brien, and G. de Stasio, “The chemical and morphological properties of boron–carbon alloys grown by plasma-enhanced chemical vapour deposition,” *J. Mater. Sci.*, vol. 33, pp. 4911–4915, 1998, doi: 10.1023/A:1004422016254.
- [147] J. Oliveira, “Laser-assisted CVD of boron carbide at atmospheric pressure,” *Appl. Surf. Sci.*, vol. 138–139, no. 1–2, pp. 159–164, 1999, doi: 10.1016/S0169-4332(98)00394-8.
- [148] H. Ahn, P. Cuong, K. Shin, and K. Lee, “Tribological behavior of sputtered boron carbide coatings and the influence of processing gas,” *Wear*, vol. 259, no. 7–12, pp. 807–813, 2005, doi: 10.1016/j.wear.2005.02.096.
- [149] E. Echeverría *et al.*, “Novel semiconducting boron carbide/pyridine polymers for neutron detection at zero bias,” *Appl. Phys. A*, vol. 118, pp. 113–118, 2014, doi: 10.1007/s00339-014-8778-4.

- [150] F. L. Pasquale, J. Liu, P. a. Dowben, and J. a. Kelber, “Novel semiconducting alloy polymers formed from ortho-carborane and 1,4-diaminobenzene,” *Mater. Chem. Phys.*, vol. 133, no. 2–3, pp. 901–906, 2012, doi: 10.1016/j.matchemphys.2012.01.114.
- [151] G. G. Peterson *et al.*, “Increased drift carrier lifetime in semiconducting boron carbides deposited by plasma enhanced chemical vapor deposition from carboranes and benzene,” *J. Vac. Sci. Technol. A Vacuum, Surfaces, Film.*, vol. 35, no. 3, p. 03E101, 2017, doi: 10.1116/1.4973338.
- [152] M. S. Driver, M. M. Paquette, S. Karki, B. J. Nordell, and A. N. Caruso, “The electronic and chemical structure of the a-B₃CO_{0.5}Hy-to-metal interface from photoemission spectroscopy: implications for Schottky barrier heights.,” *J. Phys. Condens. Matter*, vol. 24, no. 44, p. 445001, 2012, doi: 10.1088/0953-8984/24/44/445001.
- [153] R. James, F. L. Pasquale, and J. A. Kelber, “Plasma-enhanced chemical vapor deposition of ortho-carborane: structural insights and interaction with Cu overlayers.,” *J. Phys. Condens. Matter*, vol. 25, no. 35, p. 355004, 2013, doi: 10.1088/0953-8984/25/35/355004.
- [154] B. J. Nordell *et al.*, “Conquering the Low-k Death Curve: Insulating Boron Carbide Dielectrics with Superior Mechanical Properties,” *Adv. Electron. Mater.*, vol. 2, no. 7, p. 1600073, 2016, doi: 10.1002/aelm.201600073.
- [155] M. M. Paquette, B. J. Nordell, A. N. Caruso, M. Sato, H. Fujiwara, and S. W.

- King, "Optimization of amorphous semiconductors and low-/high-k dielectrics through percolation and topological constraint theory," *MRS Bull.*, vol. 42, no. 1, pp. 39–44, 2017, doi: 10.1557/mrs.2016.297.
- [156] A. F. M. Leenaars, J. A. M. Huethorst, and J. J. van Oekel, "Marangoni drying: A new extremely clean drying process," *Langmuir*, vol. 6, no. 11, pp. 1701–1703, 1990, doi: 10.1021/la00101a014.
- [157] P. Hervé and L. K. J. Vandamme, "General relation between refractive index and energy gap in semiconductors," *Infrared Phys. Technol.*, vol. 35, no. 4, pp. 609–615, 1994, doi: 10.1016/1350-4495(94)90026-4.
- [158] J. Tauc and A. Menth, "States in the gap," *J. Non. Cryst. Solids*, vol. 8–10, pp. 569–585, 1972.
- [159] G. G. Stoney, "The Tension of Metallic Films Deposited by Electrolysis," *Proc. R. Soc. A Math. Phys. Eng. Sci.*, vol. 82, no. 553, pp. 172–175, 1909, doi: 10.1098/rspa.1909.0021.
- [160] G. C. a. M. Janssen, M. M. Abdalla, F. van Keulen, B. R. Pujada, and B. van Venrooy, "Celebrating the 100th anniversary of the Stoney equation for film stress: Developments from polycrystalline steel strips to single crystal silicon wafers," *Thin Solid Films*, vol. 517, no. 6, pp. 1858–1867, 2009, doi: 10.1016/j.tsf.2008.07.014.
- [161] M. A. Lampert and P. Mark, *Current Injection in Solids*, Illustrate. Academic Press, 1970.

- [162] R. H. Bube, *Photoconductivity of Solids*. New York: John Wiley & Sons, 1982.
- [163] N. F. MOT and R. W. Gurney, *Electronic Processes in Ionic Crystals*, Second Edition. Oxford University Press, 1950.
- [164] J. Frenkel, “On Pre-Breakdown Phenomena in Insulators and Electronic Semiconductors,” *Phys. Rev.*, vol. 54, no. 8, pp. 647–648, 1938, doi: 10.1103/PhysRev.54.647.
- [165] S. M. Sze and K. K. Ng, *Physics of Semiconductor Devices*. Hoboken, NJ, John Wiley & Sons, 2007.
- [166] S. D. Baranovskii, “Theoretical description of charge transport in disordered organic semiconductors,” *Phys. Status Solidi*, vol. 251, no. 3, pp. 487–525, 2014, doi: 10.1002/pssb.201350339.
- [167] L. J. van der Pauw, “A method of measuring the resistivity and Hall coefficient on lamellae of arbitrary shape,” *Philips Technical Review*, vol. 20, pp. 220–224, 1958, doi: 537.723.1:53.081.7+538.632:083.9.
- [168] D. K. Schroder, *Semiconductor Material and Device Characterization*. Hoboken, New Jersey: John Wiley & Sons, 2006.
- [169] A. Rose, “Space-Charge-Limited Currents in Solids,” *Phys. Rev.*, vol. 97, no. 6, pp. 1538–1544, 1955, doi: 10.1103/PhysRev.97.1538.
- [170] J. C. Blakesley, F. A. Castro, W. Kylberg, and G. F. A. Dibb, “Protocol for extracting a space-charge limited mobility benchmark from a single hole-only or electron-only current-voltage curve Version 2,” no. March, 2014.

- [171] A. Rose, *Concepts in photoconductivity and allied problems*, vol. 1. Interscience Publishers, 1963.
- [172] K. von Hecht, "Zum Mechanismus des lichtelektrischen Primärstromes in isolierenden Kristallen," *Zeitschrift für Phys.*, vol. 77, pp. 235–245, 1932, doi: 10.1007/BF01338917.
- [173] A. Many, "High-field effects in photoconducting cadmium sulphide," *J. Phys. Chem. Solids*, vol. 26, pp. 575–578, 1965.
- [174] H. H. Fong, K. C. Lun, and S. K. So, "Hole transports in molecularly doped triphenylamine derivative," *Chem. Phys. Lett.*, vol. 353, no. February, pp. 407–413, 2002.
- [175] B. C. Hen *et al.*, "Improved Time-of-Flight Technique for Measuring Carrier Mobility in Thin Films of Organic Electroluminescent Materials" vol. 39, no. 3, pp. 1190–1192, 2000.
- [176] E. Lebedev, T. Dittrich, V. Petrova-Koch, S. Karg, and W. Brütting, "Charge carrier mobility in poly(p-phenylenevinylene) studied by the time-of-flight technique," *Appl. Phys. Lett.*, vol. 71, no. 18, p. 2686, 1997, doi: 10.1063/1.120179.
- [177] M. Brinza, J. Willekens, M. L. Benkhedir, E. V. Emelianova, and G. J. Adriaenssens, "Photoconductivity methods in materials research," *J. Mater. Sci. Mater. Electron.*, vol. 16, no. 11–12, pp. 703–713, 2005. doi: 10.1007/s10854-005-4972-7..

- [178] P. J. Sellin, A. W. Davies, A. Lohstroh, M. E. Özsan, and J. Parkin, “Drift Mobility and Mobility-Lifetime Products in CdTe : Cl Grown by the Travelling Heater Method,” *IEEE Trans. Nucl. Sci.*, vol. 52, no. 6, pp. 3074–3078, 2005.
- [179] S. Baranovski, *Charge transport in disordered solids with applications in electronics*. West Sussex, United Kingdom: John Wiley & Sons, Ltd, 2006.
- [180] B. A. Khan, M. A. Kastner, and D. Adler, “Time-of-flight and photoconductivity studies of a-As₂Se₃ films,” *Solid State Commun.*, vol. 45, no. 2, pp. 187–189, 1983, doi: 10.1016/0038-1098(83)90373-3.
- [181] H. Scher and E. W. Montroll, “Anomalous transit-time dispersion in amorphous solids,” *Phys. Rev. B*, vol. 12, pp. 2455–2477, 1975, doi: 10.1103/PhysRevB.12.2455.
- [182] R. a. Street, “Trapping parameters of dangling bonds in hydrogenated amorphous silicon,” *Appl. Phys. Lett.*, vol. 41, no. 11, p. 1060, 1982, doi: 10.1063/1.93400.
- [183] R. Zallen, *The Physics of Amorphous Solids*. New York: John Wiley & Sons Inc., 1998.
- [184] S. Ramo, “Currents Induced by Electron Motion,” *Proc. IRE*, vol. 27, no. 9, pp. 584–585, 1939, doi: 10.1109/JRPROC.1939.228757.
- [185] W. Shockley, “Currents to conductors induced by a moving point charge,” *J. Appl. Phys.*, vol. 9, no. 10, pp. 635–636, 1938, doi: 10.1063/1.1710367.
- [186] A. Many, “High-field effects in photoconducting cadmium sulphide,” *J. Phys.*

Chem. Solids, vol. 26, no. 3, pp. 575–578, 1965,

doi: 10.1016/0022-3697(65)90133-2.

- [187] G. Bhattarai, A. N. Caruso, and M. M. Paquette, “Single-carrier charge collection in thin direct-conversion semiconductor neutron detector: A numerical simulation,” *J. Appl. Phys.*, vol. 129, no. 19, p. 194502, 2021, doi: 10.1063/5.0039034.
- [188] E. Tupitsyn *et al.*, “Lithium containing chalcogenide single crystals for neutron detection,” *J. Cryst. Growth*, pp. 1–5, 2013, doi: 10.1016/j.jcrysgro.2013.10.054.
- [189] I. S. Anderson *et al.*, *Neutron Imaging and Applications*. Boston, MA: Springer US, 2009.
- [190] F. Hippert, E. Geissler, J. L. Hodeau, E. Lelièvre-Berna, and J.-R. Regnard, Eds., *Neutron and X-ray Spectroscopy*. Dordrecht: Springer Netherlands, 2006.
- [191] B. A. Brunett, J. C. Lund, J. M. Van Scyoc, N. R. Hilton, E. Y. Lee, and R. B. James, “Low-Cost Cadmium Zinc Telluride Radiation Detectors Based on Electron-Transport-Only Designs,” Sandia National Laboratories, 1999.
- [192] A. H. Goldan and K. S. Karim, “Unipolar charge sensing using Frisch grid technique for amorphous selenium radiation detectors,” in *Hard X-Ray, Gamma-Ray, and Neutron Detector Physics X*, 2008, vol. 7079, p. 70790P, doi: 10.1117/12.796211.
- [193] D. S. McGregor and R. A. Rojas, “High-Resolution Ionization Detector and

Array of Such Detectors,” Patent, US6175120B1, 2001.

- [194] P. N. Luke, “Single-polarity charge sensing in ionization detectors using coplanar electrodes,” *Appl. Phys. Lett.*, vol. 65, no. 22, pp. 2884–2886, 1994, doi: 10.1063/1.112523.
- [195] C. Szeles, E. E. Eissler, D. J. Reese, and S. E. Cameron, “Radiation Detector Performance of CdTe Single Crystals Grown by the Conventional Vertical Bridgman Technique,” *SPIE Conf. Hard X-Ray, Gamma-Ray Neutron Detect. Phys.*, no. July, 1999.
- [196] N. Hong, “An Exploration of Neutron Detection in Semiconducting Boron Carbide,” Ph.D. Dissertation, University of Nebraska - Lincoln, 2012.
- [197] J. F. Ziegler, J. P. Biersack, and M. D. Ziegler, *The Stopping and Range of Ions in Matter*. Chester, Maryland: www. SRIM.org, 2008.
- [198] F. Thevenot, “Boron carbide—A comprehensive review,” *J. Eur. Ceram. Soc.*, vol. 6, no. 4, pp. 205–225, 1990, doi: 10.1016/0955-2219(90)90048-K.
- [199] James F. Ziegler, “The Stopping and Range of Ions in Matter.” <http://www.srim.org/>.
- [200] C. a. Klein, “Bandgap Dependence and Related Features of Radiation Ionization Energies in Semiconductors,” *J. Appl. Phys.*, vol. 39, no. 4, p. 2029, 1968, doi: 10.1063/1.1656484.
- [201] Y. Cui, M. Groza, D. Hillman, A. Burger, and R. B. James, “Study of surface recombination velocity of Cd(1-x)Zn(x)Te radiation detectors by direct current

- photoconductivity,” *J. Appl. Phys.*, vol. 92, no. 5, p. 2556, 2002,
doi: 10.1063/1.1497696.
- [202] S. L. Bellinger, R. G. Fronk, W. J. McNeil, T. J. Sobering, and D. S. McGregor, “Enhanced variant designs and characteristics of the microstructured solid-state neutron detector,” *Nucl. Instruments Methods Phys. Res. Sect. A Accel. Spectrometers, Detect. Assoc. Equip.*, vol. 652, no. 1, pp. 387–391, 2011, doi: 10.1016/j.nima.2010.08.049.
- [203] A. Ruzin and Y. Nemirovsky, “Methodology for evaluation of mobility-lifetime product by spectroscopy measurements in CdZnTe spectrometers,” *J. Appl. Phys.*, vol. 82, no. 9, p. 4166, 1997, doi: 10.1063/1.366218.
- [204] G. Bhattarai, A. N. Caruso, and M. M. Paquette, “Steady-state space-charge-limited current analysis of mobility with negative electric field dependence,” *J. Appl. Phys.*, vol. 124, no. 4, p. 045701, 2018, doi: 10.1063/1.5038578.
- [205] A. C. Arias, J. D. MacKenzie, I. McCulloch, J. Rivnay, and A. Salleo, “Materials and Applications for Large Area Electronics: Solution-Based Approaches,” *Chem. Rev.*, vol. 110, no. 1, pp. 3–24, 2010,
doi: 10.1021/cr900150b.
- [206] M. Kaltenbrunner *et al.*, “An ultra-lightweight design for imperceptible plastic electronics,” *Nature*, vol. 499, no. 7459, pp. 458–463, 2013, doi: 10.1038/nature12314.
- [207] C. Wang, H. Dong, W. Hu, Y. Liu, and D. Zhu, “Semiconducting π -Conjugated

- Systems in Field-Effect Transistors: A Material Odyssey of Organic Electronics,” *Chem. Rev.*, vol. 112, no. 4, pp. 2208–2267, 2012, doi: 10.1021/cr100380z.
- [208] J. C. Blakesley *et al.*, “Towards reliable charge-mobility benchmark measurements for organic semiconductors,” *Org. Electron.*, vol. 15, no. 6, pp. 1263–1272, 2014, doi: 10.1016/j.orgel.2014.02.008.
- [209] A. Kokil, K. Yang, and J. Kumar, “Techniques for characterization of charge carrier mobility in organic semiconductors,” *J. Polym. Sci. Part B Polym. Phys.*, vol. 50, no. 15, pp. 1130–1144, 2012, doi: 10.1002/polb.23103.
- [210] R. P. Rocha and J. a. Freire, “The time-of-flight experiment and the average transit-time,” *J. Appl. Phys.*, vol. 112, no. 8, p. 083717, 2012, doi: 10.1063/1.4759357.
- [211] A. Many and G. Rakavy, “Theory of Transient Space-Charge-Limited Currents in Solids in the Presence of Trapping,” *Phys. Rev.*, vol. 126, no. 6, pp. 1980–1988, 1962, doi: 10.1103/PhysRev.126.1980.
- [212] G. Juška, K. Arlauskas, M. Viliūnas, and J. Kočka, “Extraction Current Transients: New Method of Study of Charge Transport in Microcrystalline Silicon,” *Phys. Rev. Lett.*, vol. 84, no. 21, pp. 4946–4949, May 2000, doi: 10.1103/PhysRevLett.84.4946.
- [213] P. N. Murgatroyd, “Theory of space-charge-limited current enhanced by Frenkel effect,” *J. Phys. D. Appl. Phys.*, vol. 3, no. 2, p. 308, 1970,

doi: 10.1088/0022-3727/3/2/308.

- [214] J. L. Hartke, “The three-dimensional poole-frenkel effect,” *J. Appl. Phys.*, vol. 39, no. 10, pp. 4871–4873, 1968, doi: 10.1063/1.1655871.
- [215] D. F. Barbe, “Space-charge-limited current enhanced by Frenkel effect,” *J. Phys. D. Appl. Phys.*, vol. 4, no. 11, p. 427, 1971, doi: 10.1088/0022-3727/4/11/427.
- [216] A. J. Mozer and N. S. Sariciftci, “Negative electric field dependence of charge carrier drift mobility in conjugated, semiconducting polymers,” *Chem. Phys. Lett.*, vol. 389, no. 4–6, pp. 438–442, May 2004, doi: 10.1016/j.cplett.2004.04.001.
- [217] S. Raj Mohan, M. P. Joshi, and M. P. Singh, “Negative electric field dependence of mobility in TPD doped Polystyrene,” *Chem. Phys. Lett.*, vol. 470, no. 4–6, pp. 279–284, 2009, doi: 10.1016/j.cplett.2009.01.066.
- [218] V. Kažukauskas, M. Pranaitis, V. Čyras, L. Sicot, and F. Kajzar, “Negative mobility dependence on electric field in poly(3-alkylthiophenes) evidenced by the charge extraction by linearly increasing voltage method,” *Thin Solid Films*, vol. 516, no. 24, pp. 8988–8992, 2008, doi: 10.1016/j.tsf.2007.11.076.
- [219] A. K. Tripathi and Y. N. Mohapatra, “Mobility with negative coefficient in Poole–Frenkel field dependence in conjugated polymers: Role of injected hot electrons,” *Org. Electron.*, vol. 11, no. 11, pp. 1753–1758, 2010, doi: 10.1016/j.orgel.2010.07.019.

- [220] G. Juška, K. Genevičius, K. Arlauskas, R. Österbacka, and H. Stubb, “Charge transport at low electric fields in π -conjugated polymers,” *Phys. Rev. B*, vol. 65, no. 23, p. 233208, 2002, doi: 10.1103/PhysRevB.65.233208.
- [221] O. J. Weiß, R. K. Krause, and A. Hunze, “Hole mobility of 1-NaphDATA,” *J. Appl. Phys.*, vol. 103, no. 4, p. 043709, 2008, doi: 10.1063/1.2841362.
- [222] A. Rose, “Space-Charge-Limited Currents in Solids,” *Phys. Rev.*, vol. 97, no. 6, pp. 1538–1544, 1955.
- [223] J. Bisquert, J. M. Montero, H. J. Bolink, E. M. Barea, and G. Garcia-Belmonte, “Thickness scaling of space-charge-limited currents in organic layers with field- or density-dependent mobility,” *Phys. status solidi*, vol. 203, no. 15, pp. 3762–3767, 2006, doi: 10.1002/pssa.200622248.
- [224] H. Bässler, “Charge Transport in Disordered Organic Photoconductors a Monte Carlo Simulation Study,” *Phys. status solidi*, vol. 175, no. 1, pp. 15–56, 1993, doi: 10.1002/pssb.2221750102.
- [225] A. Hirao, H. Nishizawa, and M. Sugiuchi, “Diffusion and drift of charge carriers in molecularly doped polymers,” *Phys. Rev. Lett.*, vol. 75, no. 9, pp. 1787–1790, 1995, doi: 10.1103/PhysRevLett.75.1787.
- [226] A. Mozer *et al.*, “Charge carrier mobility in regioregular poly(3-hexylthiophene) probed by transient conductivity techniques: A comparative study,” *Phys. Rev. B*, vol. 71, no. 3, p. 035214, 2005, doi: 10.1103/PhysRevB.71.035214.

- [227] I. Fishchuk, A. Kadashchuk, H. Bässler, and M. Abkowitz, “Low-field charge-carrier hopping transport in energetically and positionally disordered organic materials,” *Phys. Rev. B*, vol. 70, no. 24, p. 245212, 2004, doi: 10.1103/PhysRevB.70.245212.
- [228] I. I. Fishchuk, A. Kadashchuk, and H. Bässler, “Theory of low-field hopping mobility in organic solids with energetic and positional disorder,” *Phys. status solidi*, vol. 3, no. 2, pp. 271–274, 2006, doi: 10.1002/pssc.200562722.
- [229] P. N. Murgatroyd, “Theory of space-charge-limited current enhanced by Frenkel effect,” *J. Phys. D. Appl. Phys.*, vol. 3, no. 2, pp. 151–156, 1970, doi: 10.1088/0022-3727/3/2/308.
- [230] R. Ongaro and A. Pillonnet, “Poole-Frenkel (PF) effect high field saturation,” *Rev. Phys. Appliquée*, vol. 24, no. 12, pp. 1085–1095, 1989, http://hal.archives-ouvertes.fr/docs/00/24/61/46/PDF/ajp-rphysap_1989_24_12_1085_0.pdf.
- [231] S. Habermehl and R. T. Apodaca, “Dielectric breakdown and Poole-Frenkel field saturation in silicon oxynitride thin films,” *Appl. Phys. Lett.*, vol. 86, no. 7, pp. 1–3, 2005, doi: 10.1063/1.1865338.
- [232] X.-G. Zhang and S. T. Pantelides, “Theory of Space Charge Limited Currents,” *Phys. Rev. Lett.*, vol. 108, no. 26, p. 266602, 2012, doi: 10.1103/PhysRevLett.108.266602.
- [233] B. A. Gregg, S. E. Gledhill, and B. Scott, “Can true space-charge-limited currents be observed in ?? -conjugated polymers?,” *J. Appl. Phys.*, vol. 99, no.

- 11, pp. 10–13, 2006, doi: 10.1063/1.2201859.
- [234] B. J. Nordell *et al.*, “The Influence of Hydrogen on the Chemical, Mechanical, Optical/Electronic, and Electrical Transport Properties of Amorphous Hydrogenated Boron Carbide,” *J. Appl. Phys.*, vol. 118, no. October, p. 035703, 2015, doi: 10.1063/1.4927037.
- [235] C. L. Keck, “Electrical Carrier Mobility Measurements of Amorphous Hydrogenated Boron Carbide Using Space-Charge-Limited Current Techniques,” Masters Thesis, University of Missouri - Kansas City, 2015.
- [236] M. Brinza and G. J. Adriaenssens, “The time-of-flight photocurrent analysis revisited,” *J. Optoelectron. Adv. Mater.*, vol. 8, no. 6, pp. 2028–2034, 2006.
- [237] M. Hecker and R. Hubner, “Diffusion Barriers,” in *Advanced Interconnects for ULSI Technology*, M. R. Baklanov, P. S. Ho, and E. Zschech, Eds. John Wiley & Sons, Ltd., 2012, pp. 221–262.
- [238] I.-H. Kim, S.-H. Kim, and K.-B. Kim, “Delamination mechanism in relation to adhesion of cubic boron nitride,” *J. Vac. Sci. Technol. A Vacuum, Surfaces, Film.*, vol. 16, no. 4, pp. 2295–2299, 1998.
- [239] J. Möller, D. Reiche, M. Bobeth, and W. Pompe, “Observation of boron nitride thin film delamination due to humidity,” *Surf. Coatings Technol.*, vol. 150, pp. 8–14, 2002.
- [240] P. Waters and a. a. Volinsky, “Stress and Moisture Effects on Thin Film Buckling Delamination,” *Exp. Mech.*, vol. 47, no. 1, pp. 163–170, 2007, doi:

10.1007/s11340-006-9346-4.

- [241] B. Notes, “~ O ~ S ~ O ~ ’ S ; O,” vol. 27, no. 12, pp. 354–356, 1997.
- [242] S. K. Lee, C. M. Zetterling, and M. Östling, “Titanium tungsten (TiW) for Ohmic contacts to n-and p-type 4H-SiC,” *Mater. Res. Soc. Symp. - Proc.*, vol. 640, pp. 1–6, 2001, doi: 10.1557/proc-640-h7.2.
- [243] S. E. Babcock and K. N. Tu, “Titanium-tungsten contacts to Si: The effects of alloying on Schottky contact and on silicide formation,” *J. Appl. Phys.*, vol. 53, no. 10, pp. 6898–6905, 1982, doi: 10.1063/1.330031.
- [244] K. Tanaka, “Minimal Urbach energy in non-crystalline materials,” *J. Non. Cryst. Solids*, vol. 389, pp. 35–37, 2014, doi: 10.1016/j.jnoncrysol.2014.02.004.
- [245] G. Cody, T. Tiedje, B. Abeles, B. Brooks, and Y. Goldstein, “Disorder and the Optical-Absorption Edge of Hydrogenated Amorphous Silicon,” *Phys. Rev. Lett.*, vol. 47, no. 20, pp. 1480–1483, 1981, doi: 10.1103/PhysRevLett.47.1480.
- [246] P. Hidnert, “Thermal Expansion of Five Selected Optical Glasses,” *J. Res. Natl. Bur. Stand. (1934)*, vol. 52, no. 6, pp. 311–312, 1954, doi: 10.6028/jres.052.044.
- [247] A. Technologies, “Agilent Laser and Optics User ’ s Manual , Volume I,” vol. I.
- [248] P. Hidnert and W. T. Sweeney, “Thermal Expansion of Tungsten,” 1925.
- [249] A. S. M. Rao, “Thermophysical Properties of NaCl, NaBr and NaF by γ -Ray

Attenuation Technique,” *J. Mod. Phys.*, vol. 04, no. 02, pp. 208–214, 2013,
doi: 10.4236/jmp.2013.42029.

VITA

Gyanendra Bhattarai was born in Jhapa, Nepal. He completed B.Sc. and M.Sc. in Physics from Tribhuvan University, Nepal. He joined the University of Missouri-Kansas City in the Fall of 2013 as a M.S. student in Physics. After completing his M.S. in 2015, he continued to pursue PhD degree in Physics, working as a graduate research assistant in Caruso–Paquette Research Group. Gyanendra Bhattarai plans to continue working in physics research after graduation.